# Hydrogels as Biofunctional Coatings and Thiol-Ene Clickable Bioinks for Biofabrication

Dissertation zur Erlangung des
naturwissenschaftlichen Doktorgrades
der Julius-Maximilians-Universität Würzburg

vorgelegt von
Sarah Bertlein
aus Neustadt a.d. Aisch

Würzburg 2018

Eingereicht bei der Fakultät für Chemie und Pharmazie am

_____

Gutachter der schriftlichen Arbeit

1. Gutachter: _____

2. Gutachter: _____

Prüfer des öffentlichen Promotionskolloquiums

1. Prüfer: _____

2. Prüfer: _____

3. Prüfer: _____

Datum des öffentlichen Promotionskolloquiums

_____

Doktorurkunde ausgehändigt am

_____

This work was conducted from September 2012 till June 2017 at the Department for Functional Materials in Medicine and Dentistry, University of Würzburg, Würzburg, Germany under supervision of Prof. Dr. Jürgen Groll.

"…make yourself proud,
you are all you will ever be…"
Chad I. Ginsburg

# Acknowledgements

I would like to thank everyone who directly and also indirectly contributed to the success of this work.

First I would like to express my gratitude to my supervisor Prof. Dr. Jürgen Groll for offering me the opportunity to work at the Department for Functional Materials in Medicine and Dentistry (University of Würzburg), the financial support as well as for the interesting research topics. His supervision gave me the freedom to explore on my own and at the same time his guidance and experience helped me to overcome experimental difficulties.

Moreover, I would especially like to thank Dr. Jörg Teßmar for all the countless and more than helpful discussions, his patience and encouraging words.

Additionally I would like to thank my collaboration partners Prof. Dr. Tim Woodfield, Dr. Gabriella Brown and Dr. Khoon S. Lim from the Christchurch Regenerative Medicine and Tissue Engineering group (Department of Orthopaedic Surgery and Musculoskeletal Medicine, University of Otago in Christchurch, New Zealand) and Prof. Dr. Mitsuru Akashi, Prof. Dr. Michiya Matsusaki and Daichi Hikimoto from the Department of Frontier Biosciences (Graduate School of Forntier Biosciences, Osaka University, Japan). In the context of collagen-related topics I was blessed to participitate at the Gordon Research Conference (New London, NH, USA) and to meet Dr. Nuno Coelho, Dr. Anita Capalbo and Dr. António Santos only to name a few who provided very helpful discussions on this topic. Moreover, Prof. Dr. Michael Raghunath (Institute of Chemistry and Biotechnology, Center for Cell Biology and Tissue Engineering, Zurich University of Applied Sciences, Wädenswil, Switzerland) helped with his profound knowledge about collagen. Additionally colleagues from the Deparment of Prof. Dr. Jürgen Groll supported me with PCL scaffolds for cell culture experiments (Dr. Gernot Hochleitner), the construction of and the introduction to the MEW device (Tomasz Jüngst) and cell culture for bioink experiments in Würzburg (Dr. Thomas Böck).

Dr. Andrea Ewald, Maria Aniolek, Simone Werner and Kathrin Knorr always provided me with insightful discussions for the biological aspects of my work.

In my daily work I have been blessed with a friendly, cheerful and continuously growing FMZ group. I want to especially thank Isabell Biermann, Julia Blöhbaum, Dr. Thomas Böck, Dr. Theresa Brückner, Prof. Dr. Paul Dalton, Tanja Dambach, Dr. Eva Esser, Judith Friedlein, Prof. Dr. Uwe Gbureck, Stefanie Hauck, Johannes Herbig, Dr. Gernot Hochleitner, Tomasz Jüngst, Dr. Martina Keßler, Johanna Lutz, Susanne and Markus Meininger, Dr. Claus Moseke, Michaela Rödel, Dr. Ana Sancho, Dr. Martha Schamel, Dr. Katrin Schlegelmilch, Dr. Michael Schmitz, Willi Smolan and Laura Wistlich for their time, the scientific but also non-scientific discussions and their patience. All in all the reliability, the collegiality and the entertaining times we spent together rendered this a memorable journey for me.

Furthermore, I would like to thank Carina Blum, Susanne Feineis, Simone Schäfer, Verena Schill, Dr. Kai Stuckensen, Dr. Matthias Kuhlmann and Ilona Zilkowski for (at least partially) sharing the office, their kindness and support but most importantly for becoming way more than just colleagues during the last years. Thank you Matthias for your endless support, your humor and the time we spent together.

I would also like to thank Anton Hofmann and Harald Hümpfer for their help with constructional matters, solutions for computer-related problems and for continously offered coffee brakes.

The support and care of my friends helped me to stay focused on my study and I greatly value their friendship and deeply appreciate their belief in me. In this context I would like to especially thank Dr. Isabell Kenkel, Johanna Letzner, Dr. Stefanie Fehler, Gurki, Gudrun & Horst and the rest of the Steiner-family. One could simply not wish for better friends or an extended family.

Above all, I would like to thank my parents Petra and Dr. Gerhard Bertlein. They raised, supported, taught, loved and most importantly respected me. I am very grateful for their understanding, endless patience and encouragement when it was most needed.

# Publications

1. R. Wedmann, S. Bertlein, I. Macinkovic, S. Böltz, J. Lj. Miljkovic, L. E. Muñoz, M. Herrmann, M. R. Filipovic, Working with "$H_2S$": Facts and Apparent Artifacts, Nitrite Oxide, 41 (2014) 85-96.

2. S. Bertlein*, G. Brown*, K. S. Lim, T. Jungst, T. Boeck, T. Blunk, J. Tessmar, G. J. Hooper, T. B. F. Woodfield, J. Groll, Thiol-Ene Clickable Gelatin: a Platform Bioink for Multiple 3D Biofabrication Technologies, Advanced Materials, 29 (2017) 1703404.

3. S. Bertlein*, D. Hikimoto*, G. Hochleitner, J. Hümmer, T. Jungst, M. Matsusaki, M. Akashi, J. Groll, Development of Endothelial Cell Networks in 3D-Tissues by Combination of Melt Electrospinning Writing with Cell-Accumulation Technology, Small, 14 (2017) 1701521.

4. S. Stichler, S. Bertlein, J. Tessmar, T. Jungst, J. Groll, Thiol-Ene Cross-Linkable Hydrogels as Bioinks for Biofabrication, Macromolecular Symposia, 372 (2017) 102.

5. S. Stichler, T. Böck, N. Paxton, S. Bertlein, R. Levato, V. Schill, W. Smolan, J. Malda, J. Teßmar, T. Blunk, J. Groll, Double Printing of Hyaluronic Acid/Poly(Glycidol) Hybrid Hydrogels with Poly(ε-Caprolactone) for MSC Chondrogenesis, Biofabrication, 9 (2017) 044108.

6. M. Glogger, S. Stichler, I. Subota, S. Bertlein, M.-C. Spindler, J. Tessmar, J. Groll, M. Engstler, S. F. Fenz, Live-Cell Super-Resolution Imaging of Intrinsically Fast Moving Flagellates, Journal of Physics D. Applied Physics, 50 (2017) 074004.

* shared first authorship

# Table of Contents

# List of abbreviations and symbols

| Abbreviation | Meaning |
|---|---|
| 3D | Three-dimensional |
| a.u. | Arbitrary units |
| AFSA | Alexa Fluor™ 647 labelled streptavidin |
| AGE | Allyl glycidyl ether |
| AM | Additive manufacturing |
| APS | Ammonium persulfate |
| Arom. | Aromatic |
| AsAp | L-ascorbic acid-2-phosphate sesquimagnesium salt |
| ATR-FT-IR | Attenuated Total Reflection-Fourier Transform Infrared |
| $BaCl_2$ | Barium chloride |
| BSA | Bovine serum albumin |
| CAD | Computer aided designs |
| calcein-AM | Calcein acetoxymethyl ester |
| cm | Centimeter |
| C-C | Carbon-carbon bond |
| $CDCl_3$ | Deuterated chloroform |
| C-H | Carbon-hydrogen bond |
| $CO_2$ | Carbon dioxide |
| CNC | Computerized Numerical Control |
| d | Day, doublet (for NMR assignment) |
| DDR | Discoidin Domain Receptor |
| DLP | Digital light processing |
| DMAB | 4-(dimethylamino)benzaldehyde |
| DMEM | Dulbecco´s Modified Eagle´s Medium |
| DMF | Dimethylformamide |
| DMSO-*d6* | Deuterated dimethyl sulfoxide |
| DNA | Deoxyribonucleic acid |
| $D_2O$ | Deuterium oxide |
| DTP | Dithiobis(propanoic dihydrazide) |
| DTT | Dithiothreitol |
| EDC | 1-Ethyl-3-(3-dimethylaminopropyl)carbodiimide |
| EDX | Energy dispersive X-ray |
| e.g. | Exempli gratia (for example) |
| Ene | Carbon-carbon double bond |
| *et al.* | Et alii (and others) |
| EthD-1 | Ethidium homodimer 1 |
| EtOH | Ethanol |
| FCS | Fetal calf serum |
| FDA | U.S. Food and Drug Administration |
| FIB | Focused Ion Beam |

| | |
|---|---|
| g | Gram |
| G | Gauge |
| GelAGE | Gelatin modified with allyl glycidyl ether |
| GelMA | Gelatin methacryloyl |
| GMIA | Gelatin handbook of the Gelatin Manufacturer's Institute of America |
| h | Hour(s) |
| H | High, protons (for NMR assignment) |
| HA | Hyaluronic acid |
| HAc | Acetic acid |
| hACh | Human articular chondrocytes |
| HAMA | Methacrylated hyaluronic acid |
| HAPA | Pentenoate-modified hyaluronic acid |
| HASH | Thiol-modified hyaluronic acid |
| HCl | Hydrochloric acid |
| HHA | High molecular weight hyaluronic acid |
| HHAPA | High molecular weight pentenoate-modified hyaluronic acid |
| hMSCs | Human mesenchymal stromal cells |
| -HN-CO-NH- | Urea bridge |
| $H_2O$ | Water |
| Hyp | Hydroxyproline |
| $I_2$ | Iodine |
| I2959 | 2-hydroxy-1-[4-(hydroxyethoxy)-phenyl]-2-methyl-1-propanone |
| ICH | Individual collagen helices |
| i.e. | Id est (that is) |
| IPDI | Isophorone diisocyanate |
| IR | Infrared |
| kDa | Kilodalton |
| keV | Kiloelectron Volt |
| kPa | Kilopascal |
| kV | Kilovolt |
| L | Low |
| LAP | 2,4,6-trimethylbenzoylphosphinate |
| LHA | Low molecular weight hyaluronic acid |
| LHAPA | Low molecular weight pentenoate-modified hyaluronic acid |
| LHASH | Low molecular weight thiol-modified hyaluronic acid |
| m | Multiplett (for NMR assignment), middle (for IR assignment) |
| M | Medium |
| M | Molar |
| MA | Methacrylic anhydride |
| MALDI-ToF | Matrix-assisted laser desorption/ionization time-of-flight |
| MALS | Multi-angle light scattering |

| | |
|---|---|
| MDa | Megadalton |
| MEW | Melt electrowriting |
| mg | Milligram |
| µg | Microgram |
| MHz | Megahertz |
| min | Minute |
| mL | Milliliter |
| µL | Microliter |
| mM | Millimolar |
| mm | Millimeter |
| µm | Micrometer |
| mmol | Millimol |
| µmol | Micromol |
| MMP | Matrix Metalloproteinase |
| ms | Millisecond |
| mW | Milliwatt |
| $M_w$ | Weight-averaged molar mass |
| MWCO | Molecular-weight cut off |
| mV | Millivolt |
| N | Newton |
| $N_2$ | Nitrogen |
| NaCl | Sodium chloride |
| $NaHCO_3$ | Sodium hydrogen carbonate |
| $Na_2HPO_4$ | Disodium phosphate |
| $NaNO_3$ | Sodium nitrate |
| NaOH | Sodium hydroxide |
| NCO | Isocyanate |
| n.d. | Not detectable |
| $NH_2$ | Amine |
| nm | Nanometer |
| NMR | Nuclear Magnetic Resonance |
| OD | Optical Density |
| O-H | Oxygen-hydrogen bond |
| OH | Hydroxyl group |
| pA | Pikoampere |
| Pa | Pascal |
| PA | Pentenoic anhydride |
| PAAm | Poly(allylamine) |
| PBS | Phosphate buffered saline |
| pCh | Porcine chondrocytes |
| PCL | Poly-ε-caprolactone |
| PDLA | Poly D,L-lactides |
| PAA | Poly(acrylic acid sodium salt) |

| | |
|---|---|
| PEG | Poly(ethylene glycol) |
| PEO | Poly(ethylene oxide) |
| PGA | Polyglycolide |
| pH | Negative logarithm of the $H^+$ concentration |
| PLGA | Poly(lactic-*co*-glycolic acid) |
| PMMA | Poly(methacrylic acid sodium salt) |
| POX | Poly(2-oxazoline) |
| ppm | Parts per million |
| PPO | Poly(propylene oxide) |
| PVA | Poly(vinyl alcohol) |
| q | Mass swelling ratio |
| qASA | Quantitative amino acid analysis |
| RGD | Arginine-glycine-aspartic acid |
| RI | Refractive Index |
| RT | Room temperature |
| Ru | Tris(2,2´-bipyridyl)dichlororuthenium(II) hexahydrate |
| s | Second, strong (for IR assignment) |
| SA | Streptavidin |
| SCA | Supramolecular collagen aggregates |
| SD | Substitution degree |
| SDS | Sodium dodecyl sulfate |
| SDS-PAGE | Sodium dodecyl sulfate polyacrylamide gel electrophoresis |
| SEC | Size-exclusion chromatography |
| SEM | Scanning electron microscopy |
| SH | Thiol |
| SLA | Stereolithography |
| sPEGSH | Eight-armed star-shaped PEG thiol (hexaglycerol core) |
| sP(EO-*stat*-PO) | Six-armed star-shaped NCO-poly(ethylene oxide-*stat*-propylene oxide) |
| SPS | Sodium persulfate |
| t | Time, triplet (for NMR assignment) |
| TCEP | Tris(2-carboxyethyl)phosphine |
| TEM | Transmission electron microscopy |
| TEMED | *N,N,N',N'*-Tetramethylethylenediamine |
| TMS | Tetramethylsilane |
| TNBSA | 2,4,6-trinitrobenzene sulfonic acid |
| TRBSA | Texas Red™ labelled bovine serum albumin |
| UV | Ultraviolet |
| Vis | Visible |
| $V_{ret}$ | Retention volume |
| v/v | Volume/volume |
| w | Weak (for IR assignment) |
| wt.-% | Weight percentage |

| | |
|---|---|
| w/w | Mass/mass |
| w/v | Mass/volume |
| XPS | X-ray photoelectron spectroscopy |

| **Symbol** | **Meaning** |
|---|---|
| ° | Degree |
| °C | Degree Celsius |
| Ø | Diameter |
| γ | Shear rate |
| δ | Chemical shift (NMR spectroscopy), bending or deformation vibrations (for IR assignment) |
| Δ | Difference |
| ν | Printing velocity, stretching or bonding vibrations (for IR assignment) |

# 1. Introduction

## 1. Introduction

Organ and tissue failure are often consequences of diseases, injuries or accidents and can ultimately lead to loss of damaged or diseased tissue. The most common therapeutic strategy to treat patients suffering from these incidents is the transplantation of donor tissues, but unfortunately this approach is limited by the availability of suitable donor tissues. Each year nearly 100 000 patients are awaiting transplants in the United States with an averaged waiting time of more than three years. Although 77 patients receive transplants on a daily basis, almost 20 patients die because of donor shortages. Intricacy of tissue matching and low donor rates are crucial factors reducing the applicability of donor organs.[1, 2]

Tissue Engineering aims at offering alternatives to the current therapeutic approaches, though the complexity and versatility of native tissues and organs are fundamental challenging criteria that have to be met.[1, 2] In this research field solid support structures (scaffolds) or matrices (e.g. hydrogels) are combined with cells and/or biologically active molecules to form tissue engineered constructs (TECs). These TECs should promote repair or ideally regenerate the damaged tissues[3, 4] and should consequently consist of biocompatible and bioresorbable materials with controllable degradation and resorption rates, matching cell and tissue growth *in vitro* and *in vivo*.[5] Moreover, control over the surface properties of TECs is fundamental as these influence e.g. cellular attachment, proliferation and differentiation. TEC development usually aims to closely mimic native tissues with respect to mechanical properties, origin-derived materials and, most importantly, complex architectures.[5] Shape and complexity of native tissues demand fabrication techniques enabling the sophisticated production of three-dimensional (3D) constructs.

Additive manufacturing (AM) techniques address this criteria through the automated layer-by-layer deposition of materials according to computer aided designs (CAD) and benefit from minimum waste of material.[3, 6] The automated production ensures precisely controlled architectures with a high reproducibility and simultaneously allows to fabricate customized constructs by 3D model data derived from e.g. X-ray computed tomography[7] and magnetic resonance imaging[8].[3] AM methods offer the outmost important possibility to precisely fabricate high resolution architectures which ensures the production of interconnected porous networks. This open network structure facilitates cellular ingrowth, diffusion of nutrients and metabolic waste and eventually allows vascularization and host-TEC integration.[4, 6] Not only control of the construct architecture in the micrometer-range

is important for biomimicry, instead it is already acknowledged that sub-micron fibers govern key cellular processes and pathways.[9, 10]

These ultrafine fibers were recently obtained via a relatively new subclass of AM techniques, namely melt electrowriting (MEW).[11] Up to now the most commonly used material for melt electrowritten scaffolds is a rather hydrophobic and inert material. The first aspect is crucial for unspecific protein adsorption from cell media during *in vitro* experiments and could eventually falsify the biological readout. Additionally, the inertness of this material is not sufficient to meet the required biocompatibility, as this is often described as "…the applicability of a material to perform with an appropriate host response in a specific application"[12] and hence requires further optimization by e.g. surface post-modifications via hydrogel coatings. Melt electrowritten scaffolds can be applied to gain insight into the fundamental underlying interactions between different cells with bioactive compounds and/or with dependence on scaffold architectures. This knowledge ultimately will help to develop advanced suitable tissue substitutes.

Typically MEW-derived scaffolds are seeded with cells in a post-fabrication manner[11, 13] as processing temperatures, required to obtain polymer melts, are one of the main hurdles to simultaneously process materials with embedded cells. To allow the concurrent processing of materials with cells, referred to as "biofabrication", extrusion-based bioprinting is often used and offers the advantage to gain control over the cell distribution.[6, 14] A reasonable class of materials for this technique is represented by hydrogels and extrusion-based bioprinting allows to produce constructs in clinically relevant sizes for transplantation purposes.[14, 15]

**Aim of this thesis** was the development of functionalizable hydrogel coatings for cell-material interaction studies and of bioprintable hydrogels for biofabrication. Melt electrowritten scaffolds were fabricated with a synthetic polymer and coated via a functionalizable hydrogel layer to obtain control over the surface properties and to enable investigation of cell-material interactions with bioactive compounds in minimal unspecific protein adhesive environments. Bioprintable hydrogels were based on natural polymers, which were functionalized to allow for cytocompatible thiol-ene crosslinking into mechanically stable hydrogels. These materials were further optimized regarding the mechanical performance and suitability for extrusion-based printing.

**Chapter 2** provides a literature-based overview over different AM techniques together with general requirements for, and properties of, suitable materials.

**Chapter 3** covers the syntheses and material characteristics of the developed materials and constructs. **Chapter 3.1** describes the fabrication of high resolution 3D scaffolds based on a hydrophobic synthetic thermoplast. These scaffolds were subsequently coated with hydrophilic star-shaped crosslinkable polymers to control the surface chemistry and to guarantee minimal protein adhesive environments. The coating protocol was developed with respect to scaffold pre-treatment, coating solution concentrations and coating durations. Biofunctionalization was achieved via two different reaction routes and a new photosensitive route allowed for a pH independent biofunctionalization to obtain a versatile platform for further coupling substances such as e.g. collagen functionalized scaffolds.
**Chapter 3.2** covers the synthesis and thorough characterization of allyl-modified gelatin and the production of hydrogels via thiol-ene crosslinking. Control and optimization of the hydrogel properties were gained via application of different functional group ratios and photoinitiators. Moreover, combinations with various crosslinker molecules improved the mechanical and rheological properties of the hydrogels for extrusion-based bioprinting, while maintaining the viability of encapsulated cells.
In **Chapter 3.3** hyaluronic acid was modified with suitable groups for thiol-ene crosslinking. Optimization of the hydrogel properties and the processability for extrusion-based bioprinting was accomplished. Post-fabrication cytocompatibility of this system was demonstrated with embedded cells.

**Chapter 4** summarizes the thesis in English and German language.

**Chapter 5** depicts the experimental section with detailed information about the individual experiments and characterizations.

# 2. Background

## 2.1. Additive manufacturing for Tissue Engineering

As already outlined in the introduction of this thesis, the research field of Tissue Engineering, dating back to the early 1990`s[16], aims to mimic native tissue to ultimately restore, maintain or improve tissue function. In order to resemble the complex hierarchical structure of tissues, additive manufacturing (AM) methodologies are more and more exploited. These techniques have the automated layer-by-layer deposition in common, which enables to individually customize the constructs.[3, 6] Fused deposition modeling, selective laser sintering, stereolithography (SLA) and extrusion-based printing are among the most commonly used AM methods.[15] In the scope of this study, special emphasis will be given to extrusion-based AM approaches with the examples of MEW and extrusion-based printing, and to SLA. Besides a variety of available AM methods, the choice of materials also plays a crucial role and will be highlighted in detail for the distinct AM techniques.

Generally, natural and synthetic polymers can be used for AM technologies. Natural polymers are generally acknowledged to possess superior cell triggering properties than synthetic materials. Moreover, an inherent biocompatibility is usually associated with not only the educts but also for the degradation products of these polymers.[17, 18] However, potential immunogenicity accompanies some of these polymers[19] and often insufficient mechanical properties of final constructs restrict the applicability of this class of biomaterials for Tissue Engineering approaches.[17, 18] Furthermore, polymers sourced from tissues are often subject to large batch-to-batch variations.[17]

Synthetic polymers, on the other hand, provide good control over molecular weight distributions and reproducible production without significant batch-to-batch variations.[20] Synthesis of these polymers allows to adjust the product properties by means of e.g. molecular weight distributions and substitution degrees (SD). Potentially cytotoxic degradation products and remaining educts have to be excluded and often complicate the application of synthetic polymers for Tissue Engineering approaches. Moreover, in many cases suitable bioactivities are missing and synthetic polymers represent rather inert systems[2, 6] that do not meet the required biocompatibility, which is described as "…the applicability of a material to perform with an appropriate host response in a specific application"[12] and often require further optimization.

A promising approach to overcome the drawbacks of purely natural or synthetic materials relies on their modification and combination. Synthetic polymers can be modified with

natural moieties such as peptides, to increase biodegradability and render polymers more biocompatible or even trigger specific cell responses.[21-23] As well combinations of synthetic and natural polymers to hybrid systems have been described to increase cellular adhesion.[24]

Hence, the choice of suitable materials for AM products needs to be carefully and individually evaluated depending on the intended fabrication method and the to-be-engineered tissue associated requirements.

## 2.2. Additive manufacturing via melt electrowriting

Polymer solutions can be spun into fibers and result in high resolution scaffolds by exploitation of high voltages e.g. via solution electrospinning (**Figure 1 A**). Therefore, polymers are dissolved in organic solvents, loaded into a syringe and application of high voltages at the needle tip generates an electrified liquid polymer jet launching from the Taylor cone. Solvent evaporation allows to collect solidified fibers on a grounded target and repulsion of surface charges, overcoming the surface tension of the jet, induces jet stretching.[25] These electrical instabilities, often referred to as "whipping"[4, 11, 25], are crucial to reduce fiber diameters to the sub-micron scale but also result in randomly distributed fibers.[4] Especially for small fiber diameters, this random fiber orientation results in rather small and broadly distributed pore sizes. Solution electrospinning is generally not considered as AM since control over fiber deposition and accurate scaffold architecture are missing.[26] For Tissue Engineering approaches and the mimicry of native tissues, not only the fiber diameter, but also final pore sizes are important for scaffold design. Lack of pore size control associated with solution electrospinning renders this technique not considered as an AM method, but on the other hand also prone to fabricate constructs with sub-micron fibers that could comprise cell barrier functions. Pham *et al*. proved for solution electrospinning that larger pore sizes, as resulting from increased fiber diameters, contribute to the interconnectivity of scaffolds and cell infiltration. Solution spun scaffolds were found to require fiber diameters of 4 µm to obtain pore sizes of at least 20 µm to promote cellular invasion and ingrowth.[27] In other words, not only the fiber diameter determines cell infiltration, the final pore sizes resembling the interconnectivity, cannot be neglected for scaffold design.

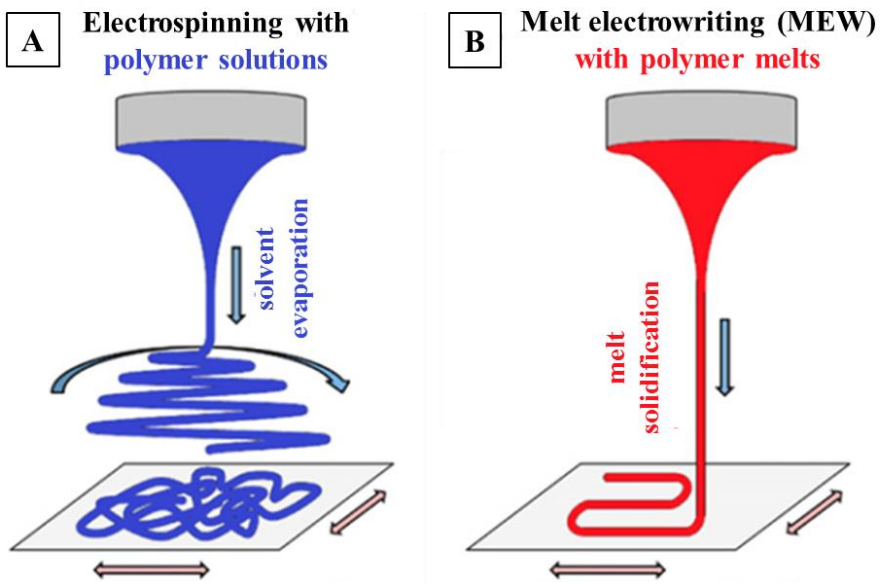


**Figure 1:** Illustration of solution electrospinning (**A**) and melt electrowriting (**B**). Solution electrospinning leads to an uncontrolled deposition of fibers that solidify via solvent evaporation, whereas polymer melts result in a stabilized jet and allow to deposit strands in a direct writing fashion. Adapted from Hochleitner and coworkers.[11]

Precise control over polymer deposition and, hence, scaffold architectures can be achieved via MEW (**Figure 1 B**). For MEW approaches a polymer melt, instead of a solution, is electrostatically drawn to the collector. This tremendously reduces the fiber diameter compared to other melt-extrusion-based methods.[28] Cooling of the jet is accompanied by solidification, in dependence on the spinneret distance, and enables to draw straight jets over long distances. Hence, smaller collector distances can result in depositing slightly molten fibers, further enhancing structural integrity and stability of the scaffolds.[4] As proven by Brown *et al.*[28] matching collector- to the jet-speed generates the possibility of a direct writing mode. Suitable low-conductive polymers have to possess a viscosity that decreases the probability of strand breakages.[4] Technical parameters controlling the fiber diameter include spinneret diameter, voltage, polymer flow-rate and collector distance. Material parameters tremendously governing the fiber diameter are the melt temperature and the polymers molecular weight, as both contribute to the polymer melt viscosity.[4, 11, 29] Fiber diameters associated with MEW are usually in the range of 5 – 30 µm[28-30] and comparably larger than for solution spun fibers, which was attributed to the missing whipping effects.[4] However, recently sub-micron fibers with sizes of 817 ± 165 nm were achieved with MEW through adjusted voltages, flow rates and spinneret diameters.[11] Control over scaffold architecture, porosity and resolution of the scaffolds enhance rapid

and homogenous infiltration of cells for subsequent *in vitro* studies.[31]

Whereas MEW allows to produce higher resolution fibers than extrusion-based printing approaches, the production is restricted to scaffolds in non-clinically relevant sizes but it is yet a promising AM technique for cell-material interaction studies. Though the beneficial absence of any organic and potentially cytotoxic solvents renders MEW promising, high polymer melting temperatures exclude direct processing with encapsulated cells for biofabrication purposes. Moreover, the inherent rather low mechanical stability of melt electrowritten scaffolds, associated to small fiber diameters, restrict the applicability of these to mimic native high load bearing tissues such as cartilage. To overcome these hurdles, melt electrowritten scaffolds were combined with hydrogels as provided by Visser *et al.*[32] Here, reinforcement of soft cell-laden hydrogels with melt electrowritten scaffolds resulted in stiffness and elasticity of the hybrid constructs that almost match that of articular cartilage.[32] Nevertheless, melt electrowritten scaffolds provide also a platform to study the underlying interactions of cells with different materials and ultra-fine scaffold architectures.

### 2.2.1. Materials for melt electrowriting

The MEW process parameters require low conductive polymers that possess a distinct viscosity ensuring the deposition of continuous strands without scaffold architecture defects.[4] Similar to other melt-based AM methods, polymers for MEW have to be thermally stable at the melting point without the need of buffers or any other solvents. Natural polymers often lack these requirements and can be denatured upon heating.[4] Denaturation and degradation compromises the applicability and potentially require process parameter adjustments during the fabrication process. Hence, biocompatible synthetic thermoplastic materials are often applied for MEW, such as poly-ε-caprolactone (PCL)[11, 28, 30, 33] and poly(2-oxazoline)s (POX)[34]. These thermoplastics render the MEW fabrication of scaffolds free of additional crosslinkers to ensure high shape fidelity scaffolds.

Since its first synthesis in the 1930´s[35], the degradable PCL has been broadly applied both in biomedical and Tissue Engineering approaches[36-41], most often for solution electrospinning[17, 42-44] and MEW[11, 28, 30, 33]. PCL is hydrophobic, soluble in a variety of solvents ranging from chloroform, dichloromethane and benzene to toluene and approved by the U.S. Food and Drug Administration (FDA) for drug-delivery devices.[45] Lam *et al.*

confirmed the short- and long-term biocompatibility of PCL in animal models.[46] Besides its low-price and the low melting point of around 59 – 64 °C, the rheological and viscoelastic properties render this polymer suitable for multiple AM techniques.[45]
PCL is in many cases used to fabricate scaffolds via MEW[11, 28, 30, 33] though these scaffolds per se often have insufficient mechanical properties to be applied for high load bearing Tissue Engineering approaches such as e.g. cartilage regeneration.[45] An intriguing approach by Visser *et al*. showed GelMA hydrogel reinforcement with highly structured MEW-derived PCL scaffolds matching the mechanical stiffness and elasticity of articular cartilage.[32] Another important study elucidating the general suitability of PCL-based scaffolds for application in cartilage defects was performed by Li and coworkers.[47] Herein, chondrocytes seeded on solution spun PCL scaffolds could maintain the chondrogenic phenotype in contrast to flat and well spread cell morphologies on polystyrene controls.[47] Hence, PCL-derived scaffolds can serve as a promising platform to study their applicability for demanding native tissues such as cartilage.

Keeping the general requirements of suitable materials for 3D scaffold formation in the context of Tissue Engineering in mind, special emphasis has to be given to the degradability of synthetic polymers. In particular, the degradation and resorption of naturally-derived polyglycolides (PGA) and poly D,L-lactides (PDLA) is completed after 2 – 4 months, whereas PCL as synthetic thermoplast degrades over a period of up to 4 years depending on the molecular weight and fiber diameter dimensions, which dictates the use for long-term applications. It is acknowledged that higher molecular weight PCL generally degrade slower as a consequence of longer polymer chains which require a higher number of ester bond cleavages to generate water-soluble oligomers.[45] Importantly, PCL is known to be non-biodegradable in the human body as no suitable enzymes are present[48], instead the degradation involves non-enzymatic hydrolytic cleavage of ester groups followed by intracellular degradation.[45] The latter occurs for oligomers below molecular weights of 3 kDa and generally may allow for complete resorption of PCL.[49] Morphologically, hydrolytic cleavage of poly(hydroxy) esters can generally proceed either via surface or bulk degradation as depicted in **Figure 2** and is dependent on the dimensions of the scaffold fibers.
The specific degradation pathway is dictated via by-product diffusion.[50] When hydrolytic chain scission and diffusion of oligo- and monomers into the surrounding area are more

pronounced than the rate of water penetrating into the polymer bulk, surface degradation and erosion occur. Polymeric structure thinning, without affecting the molecular weight of internal bulk material can be observed (**Figure 2 A**). When the relationship of chain scission, by-product diffusion and incoming water is vice versa, bulk degradation results with hydrolysis throughout the polymer matrix. Random chain scission decreases the overall molecular weight of the polymer material and oligo- and monomers readily diffuse into the surrounding until reaching an equilibrium (**Figure 2 B**).[45]

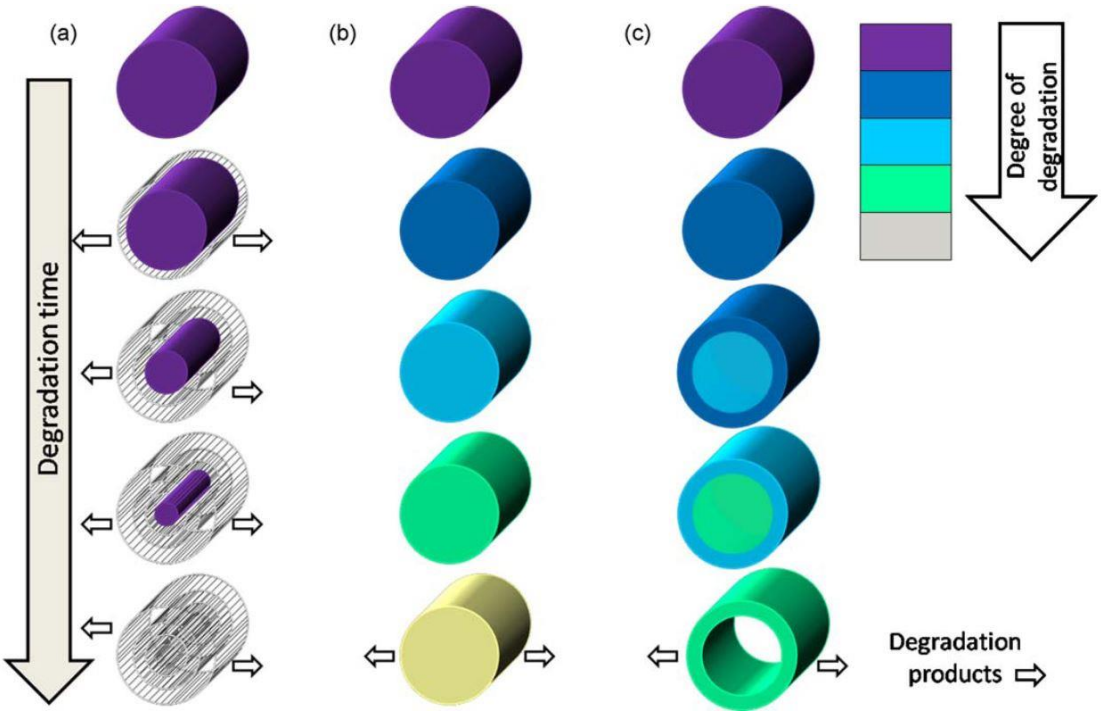


**Figure 2:** Comparison of surface erosion (**a**), bulk degradation (**b**) and autocatalytic bulk degradation (**c**) of degradable poly(hydroxy) esters. Reprinted from Hutmacher *et al.*[45], with permission from Elsevier.

In unbalanced bulk degrading systems the by-products can accumulate within the polymer interior leading to an acidic gradient due to carboxylated oligo- and monomers, resulting in autocatalytic ester bond cleavages. This speeds up the degradation and results in polymeric structures with an outer high molecular weight layer and an interior with lower molecular weight products (**Figure 2 C**).[45] Critical for bulk degrading materials is the state when oligomers are small enough to rapidly diffuse out of the bulk into surrounding tissue as inflammation reactions often occur.[51]

The general relationship between loss of polymer mass and molecular weight for resorbable polymers is depicted in **Figure 3** and accompanies the aforementioned observations.[5, 52]

Polymer degradation proceeds first via mass loss and ultimately results in declining molecular weights of the degraded products which allows to resorb or metabolize the oligo- and monomers.

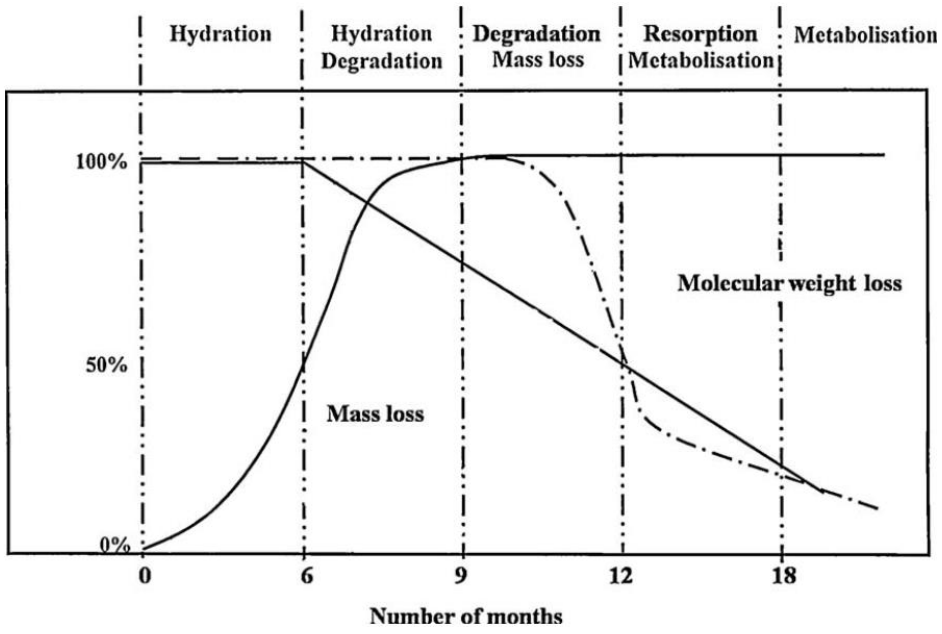


**Figure 3:** Overview of the degradation time course of a resorbable polymer regarding polymer mass loss and decreasing molecular weight. Reproduced from Hutmacher *et al.*[5] with permission from Taylor & Francis.

To speed up time-consuming long-term experiments regarding PCL degradation, an accelerated degradation system (5 M NaOH, 37 °C) was developed from Hutmacher and coworkers and compared to simulated physiological conditions with PBS at 37 °C.[53] However, PCL scaffolds were subject to different degradation pathways for both experimental setups. Whereas surface degradation occurred for accelerated conditions, detectable via thinning polymer strands, physiological conditions resulted generally in bulk degradation with a significant lower degradation rate (**Figure 4**).[53] Furthermore, the artificial accelerated degradation of PCL cannot be correlated to studies mimicking physiological conditions and it has to be noted that prolonged alkaline treatments of PCL scaffolds tremendously influence the degradability.

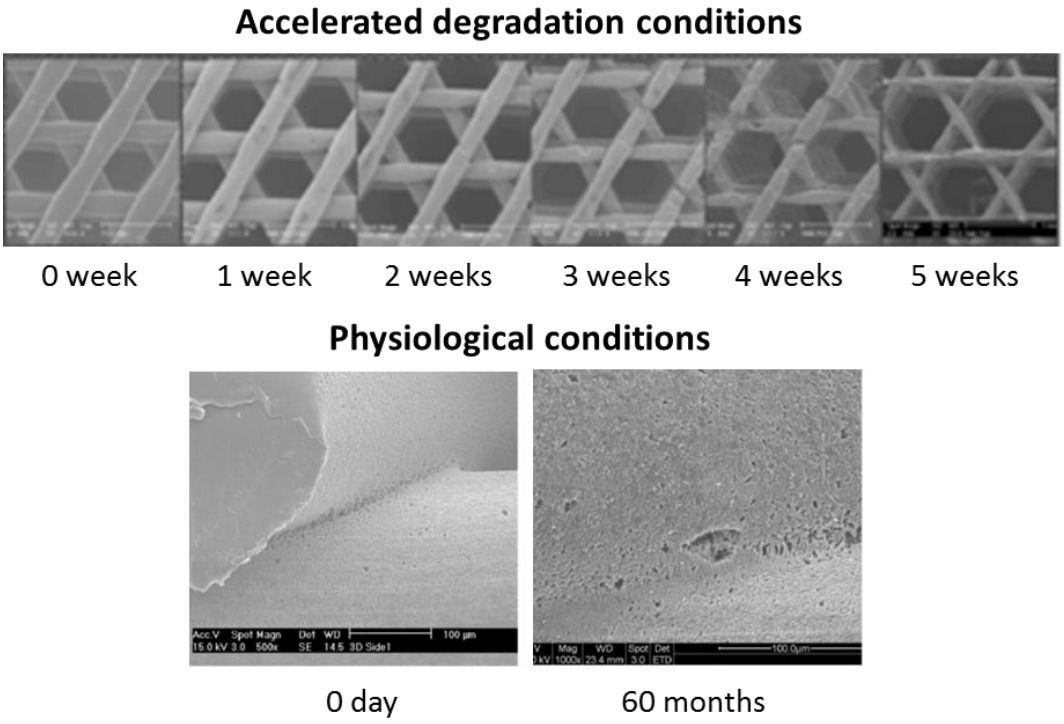


**Figure 4:** Comparison of microscopic pictures of PCL scaffolds which were treated with accelerated degradation conditions (5 M NaOH, 37 °C) for up to 5 weeks or with physiological conditions (PBS, 37 °C) up to 60 months. Surface degradation occurs for accelerated degradation conditions as indicated by thinning polymer strands, whereas at physiological conditions no changes in the surface structure were observable after 60 months and suggest bulk degradation accompanied by a lower degradation rate. Reproduced from Hutmacher *et al*.[53].

### 2.2.2. Coating of hydrophobic polymers with linear and star-shaped PEG

For simplification, solely the term poly(ethylene glycol) (PEG) is used in this chapter, except for six-armed star-shaped NCO-poly(ethylene oxide-*stat*-propylene oxide) (sP(EO-*stat*-PO)), though poly(ethylene oxide) (PEO) is often used to indicate molecular weights higher than 20 kDa.[54]

Hydrophobic synthetic biomaterials are often coated with linear PEG to increase the hydrophilicity and thereby reducing unspecific protein adsorption. This adsorption can ultimately result in denaturation of the proteins and induce inflammation cascades and needs to be circumvented.[55-57] On top, PEG provides several additional advantageous properties, which contribute to its broad application, namely being neutral, hydrophilic, non-immunogenic, non-toxic and moreover already approved by the FDA.[54, 55, 58]

The protein repellent property of PEG coated surfaces was both theoretically[57, 59, 60] and experimentally[61-65] addressed and correlated to a combination of chain molecular weight

with a high grafting density of PEG chains. For steric repulsion of proteins, the surface grafting density is more important than the PEG chain length.[63, 66] However, a high surface grafting density is not straight forward achievable as steric repulsions between grafted linear polymer chains are limiting the overall grafting density. An alternative to linear PEG molecules and limitations thereof is represented by more complex star-shaped architectures for which multiple PEG arms are connected via a central core molecule.[61, 67-71] These molecules were expected to enhance the overall surface grafting density compared to linear PEG chains, since they provide a higher polymer segment density,[66, 68, 72] which would also contribute to the protein repellency as a consequence of increased steric repulsive forces against adsorbing proteins.[60]

Sofia *et al.*[70] investigated the protein repellent properties of hydroxyl-terminated star-shaped PEG molecules with 20 and 70 arms attached to a poly(divinylbenzene) core and final molecular weights of 200 and 350 kDa, respectively. Star-shaped PEG coated surfaces demonstrated increased protein repellency for high molecular weight proteins. However, smaller proteins (~ 12 kDa) were capable to adsorb onto star-shaped PEG coated surfaces but not on surfaces coated with linear PEG molecules. Spherical star-shaped PEG molecules did not homogeneously coat the surface, instead gaps between individual grafted star-shaped PEGs remained which were hypothesized to be large enough to trigger adhesion of relatively small proteins.[70] This further underlined that not only the architecture, molecular weight and hydrophilicity of PEGs are crucial for the protein repellent properties, but the surface grafting density seemed to represent one of the main contributing forces. The difference in grafting densities of linear and star-shaped PEGs is schematically represented in **Figure 5 A** and **B** with the additional option of crosslinked six-armed star-shaped NCO-poly(ethylene oxide-*stat*-propylene oxide) (sP(EO-*stat*-PO)) (**Figure 5 C**), which will be discussed in the following section. For simplification only one crosslinked sP(EO-*stat*-PO)-layer is schematically represented in **Figure 5 C**.

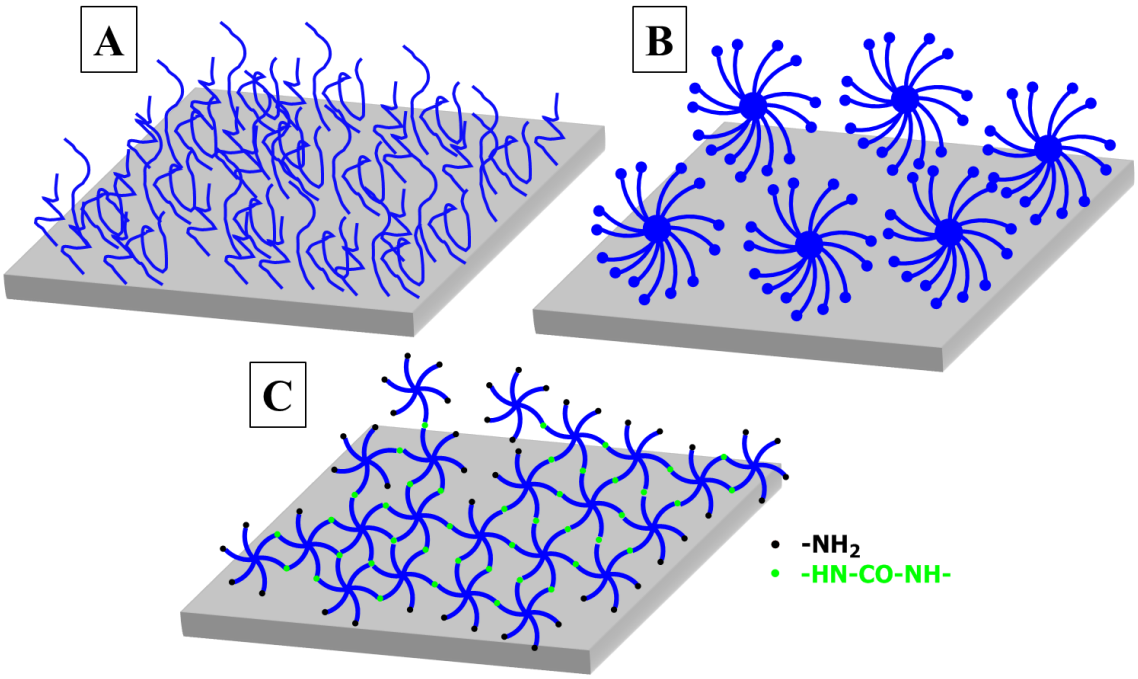


**Figure 5:** Comparison of the grafting densities of linear PEG (**A**), star-shaped uncrosslinked PEG (**B**) and one representative layer of crosslinked six-armed star-shaped NCO-poly(ethylene oxide-*stat*-propylene oxide) (sP(EO-*stat*-PO)) (**C**). Redrawn with permission from Gasteier *et al.*[72]. Copyright (2007) John Wiley and Sons.

### 2.2.2.1. Coatings with crosslinkable star-shaped molecules

To improve surface grafting densities simultaneously to protein repellency, star-shaped molecules with lower arm molecular weights, a reduced arm number and more flexible core molecules were examined. It was hypothesized that the higher flexibility reduces the sphere like structures, improves the gap size between star-shaped molecules and eventually enhances the protein repellent properties. NCO-terminated star-shaped molecules successfully addressed this concept and intermolecular crosslinking reduced the gaps between adjacent star-molecules. The crosslinked molecules demonstrated more homogenous grafting density profiles, a higher surface coverage and functional end groups near the top of the star polymer molecules and generated layer thicknesses higher than monolayers.[68]

The six-armed star-shaped polymer used for these studies is based upon a 4:1 statistical copolymer of poly(ethylene oxide) (PEO) with poly(propylene oxide) (PPO) attached to a sorbitol core (**Scheme 1**).[67] This six-armed star-shaped NCO-poly(ethylene oxide-*stat*-propylene oxide) polymer is referred to as "sP(EO-*stat*-PO)".

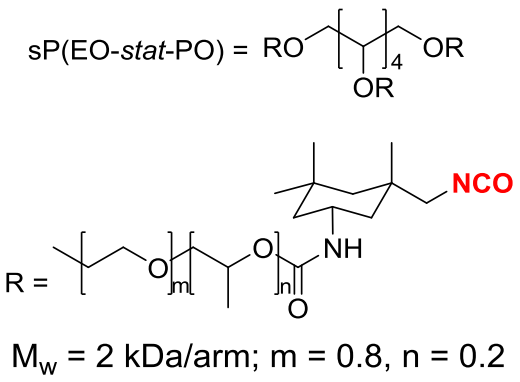


**Scheme 1:** Molecular structure of six-armed star-shaped NCO-poly(ethylene oxide-*stat*-propylene oxide) (sP(EO-*stat*-PO)). Six copolymer arms, consisting of a 4:1 ratio of PEO:PPO, are attached to the sorbitol core. Adapted from Heyes *et al*.[73] with permission of The Royal Society of Chemistry.

Each arm possesses a molecular weight of 2 kDa resulting in a total molecular weight of 12 kDa for sP(EO-*stat*-PO). Terminal NCO-groups were introduced by reacting OH-terminated star PEGs with isophorone diisocyanate (IPDI). As secondary NCO-groups from IPDI are higher reactive and form urethane bonds within sP(EO-*stat*-PO), the less reactive primary NCO-groups determine the functional groups at the distal sP(EO-*stat*-PO) arm ends.[74] Due to the hydrophilic PEO, the hydrophobic PPO and cyclohexane rings of IPDI the resulting sP(EO-*stat*-PO) polymer possesses an amphiphilic character.[75]

The aqueous hydrolysis of NCO-groups enables surface coatings with sP(EO-*stat*-PO) or hydrogels thereof. Mechanistically, the aqueous NCO-hydrolysis generates carbaminic acid, which is unstable at neutral pH values, and instantly decarboxylates to amines. These nucleophilic groups are more NCO-reactive than water and form stable and biocompatible urea bridges with yet unhydrolyzed NCO-groups (**Scheme 2**).[65]

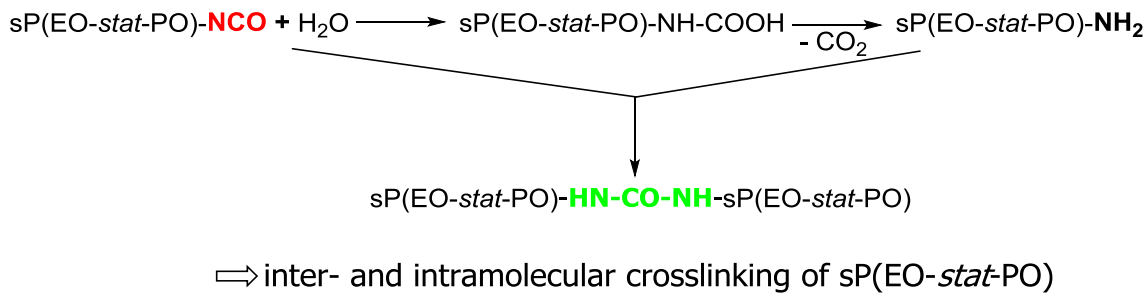


**Scheme 2:** Schematic illustration of aqueous induced crosslinking of sP(EO-*stat*-PO). Carbaminic acid decarboxylates to amines (black) and the subsequent reaction of amines with yet unhydrolyzed NCO-groups (red) intra- or intermolecularly crosslinks sP(EO-*stat*-PO) via urea bridges (green).

The rate determining step of this reaction is the NCO-hydrolysis, rather than the fast aminolysis[76], and autocatalytic crosslinking of sP(EO-*stat*-PO) occurs. Steric restrictions finally lower the reaction rate[72] and due to crosslinking of low molecular weight arms with little steric repulsions, a dense polymeric network of oligomeric sP(EO-*stat*-PO)s is formed. The flexibility of sP(EO-*stat*-PO) arms sterically allows all NCO-groups to react with amines and results, due to arm multivalence, in good contact to NCO-reactive surfaces. Oligomer formation and the concurrent steric demand induces three-dimensionally crosslinked (EO-*stat*-PO) layers and increases coating thicknesses higher than monolayers.[75] This layer thickness additionally aids the protein repellent properties of sP(EO-*stat*-PO) coated surfaces and improves the long-term stability.[77] A kinetic energy barrier is provided by the network density and contributes together with hydrophilicity and high surface grafting density to the extremely efficient protein repellent properties of sP(EO-*stat*-PO).[77] SP(EO-*stat*-PO) coated substrates were proven cell repellent under standard cell culture conditions for up to six weeks for a variety of different cells, such as MSCs, SaOS-2 cells[78], HaCaT keratinocytes and human skin derived fibroblasts[79]. As the reactive and cytotoxic NCO-groups hydrolyze with time, cytocompatible, NCO-hydrolyzed sP(EO-*stat*-PO) layers result without the need for additional blocking steps.[78, 79]

#### 2.2.2.2. Biofunctionalization of sP(EO-*stat*-PO) coated surfaces

A balance of coating density, reactivity and final cytocompatibility, allows biological effect studies of molecules covalently linked to the sP(EO-*stat*-PO) layer in minimal unspecific protein adhesive environments. Modification with bioactive compounds, e.g. peptides or proteins, can easily be achieved via different possibilities and sP(EO-*stat*-PO)s diverse reactive groups.[58, 71, 78, 80] These include the direct reaction with NCO-groups in solution (1), before complete hydrolysis in freshly prepared layers (2) and reaction with amine groups in completely crosslinked sP(EO-*stat*-PO) layers (3).[72] Based on the changing reactivity of sP(EO-*stat*-PO) upon NCO-hydrolysis a variety of compounds can be incorporated. Whilst NCO-reactive groups such as amines, alcohols and thiols are suitable for approaches (1) and (2), the amine groups for the last modification (3) can be reacted with aldehydes, epoxides or active esters. Often peptides already possess relevant functional groups for approaches (1) and (2) and do not require additional functionalization.[73] The multivalence of star shaped polymers not only provides good

contact to substrate surfaces with high surface grafting densities, but also high functional group quantities and binding capacities per molecule.[72, 73] This latter aspect is important to trigger sufficient cellular adhesion and ultimately biological readout as a consequence of highly functionalized surfaces. Moreover, immobilized proteins on sP(EO-*stat*-PO) were proven to maintain their native conformation a crucial factor for proteins function.[71] Not only planar surfaces were coated with sP(EO-*stat*-PO), but also more complex substrate architectures derived from solution electrospun poly(lactic-*co*-glycolic acid) (PLGA)[80-83] or PCL[58] meshes.

Hence, sP(EO-*stat*-PO) coating represents a powerful tool enabling the investigation of bioactive compounds in their native and functional state in minimal unspecific protein adhesive environments and thereby allow to investigate cell-material interactions in dependence on immobilized substances.

## 2.3. Biofabrication via extrusion-based printing

Biofabrication techniques, such as extrusion-based printing or SLA, offer the advantage to simultaneously process materials with embedded cells and are capable to produce TECs in centimeter ranges but with lower fiber resolutions, than compared to e.g. MEW-based approaches. Both extrusion-based printing and SLA allow fabrication of constructs in biomedical relevant size ranges with reasonable processing times.[14, 15] A comparison of both techniques is given in **Figure 6** with the example of post-fabrication fixation of materials via irradiation with UV- or Vis-light.

Extrusion-based printing allows the deposition of continuous strands either pneumatically or mechanically (**Figure 6 A**). The ability to apply high pressures renders pneumatically driven extrusion favorable for high viscous materials compared to mechanically driven systems. Extrusion of cell-laden polymer solutions, so called “bioinks”, in a layer-by-layer fashion forms 3D constructs via an automated movement of the nozzle and the printing stage. Deposition of continuous strands allows for structural integrity of the constructs and the final resolution is mostly predetermined by the nozzle diameter.[14, 84] Furthermore, a non-Newtonian fluid shear thinning behavior of bioinks is beneficial, meaning that viscosity decreases as shear rates increase, and thermo-gelling materials, such as e.g. gelatin, are often exploited.[6, 14, 85, 86]

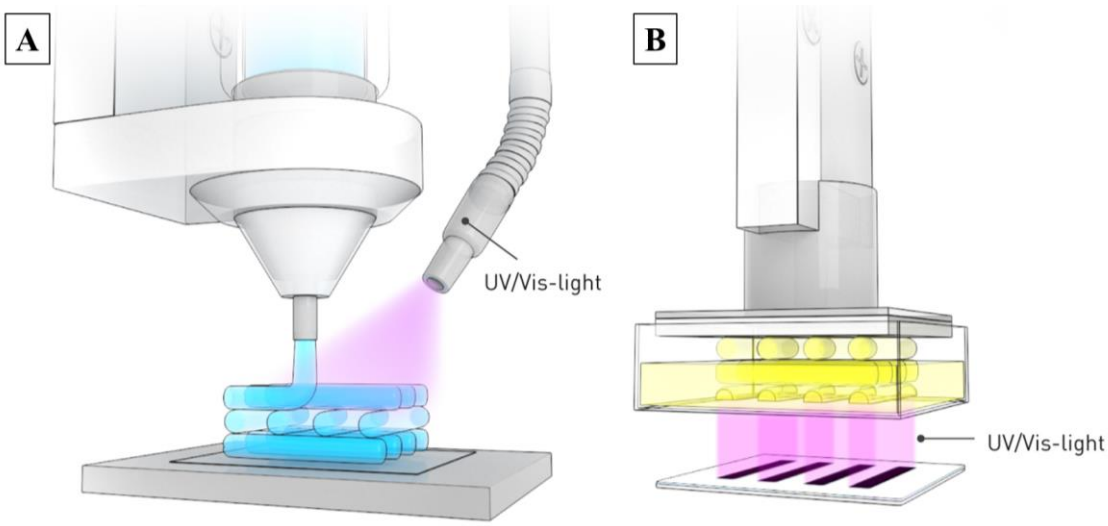


**Figure 6:** Schematic representations of extrusion-based printing (**A**) and stereolithography (SLA) with digital light processing (DLP) (**B**). Fixation of the constructs is achieved by irradiation with UV- or Vis-light.

The layer-by-layer fabrication of SLA-derived constructs is either bottom-up or top-down oriented. A laser scans and irradiates continuously the top layer of a bioresin reservoir and the movable platform is afterwards either lowered (bottom-up) or lifted (top-down) which pulls the construct out of the bioresin.[14] Combining SLA with digital light processors enables to speed up the fabrication process, as the complete layer can be cured at once (**Figure 6 B**).[15]

Reasonable temperature ranges render both AM techniques applicable to process bioinks for biofabrication approaches. Nonetheless, these approaches often require post-crosslinking, for construct-architecture fixation to ensure high shape fidelities as depicted in **Figure 6** with irradiation-induced crosslinking. It should be noted that low viscous Newtonian fluids with distinct flow properties are preferred for SLA approaches to generate high print fidelities[86] with resolutions between 80 – 125 µm.[87] For higher viscous materials, extrusion-based printing is more suitable, and allows resolutions of around 100 µm.[14]

### 2.3.1. Materials for extrusion-based printing

For extrusion-based printing approaches, solvents for bioinks should be composed of buffers or ideally cell media to resemble physiological conditions. Additionally, cytocompatible materials as well as crosslinking chemistries are crucial.[14] A reasonable class of materials for this technique is represented by hydrogels, which are highly hydrated

3D crosslinked polymer networks capable of taking up to 99 % (w/w) water of the dry weight of polymers.[88] Two classes of hydrogels are typically distinguished, namely physically or chemically crosslinked networks.

The dynamic nature of physical crosslinks based upon hydrophobic or electrostatic interactions and hydrogen bonds, is in contrast to the irreversible covalent network formation resulting from chemically crosslinked networks.[14, 89] Different chemically induced crosslinked hydrogels will be introduced with the example of gelatin-based materials in **Chapter 2.3.1.1**.

Hydrogel precursor solutions for extrusion-based printing with embedded cells require homogeneous cell distributions and often post-fabrication crosslinking to ensure mechanical stability and shape fidelity of the constructs. For bioink formulations, a low viscous material is preferred allowing to homogeneously distribute cells with low shear stress, though a distinct viscosity is crucial to prevent blocking of the nozzle by cell sedimentation. Furthermore, the bioink formulation has to remain uncrosslinked and stable in the printing reservoir to ensure constant processing parameters throughout the fabrication process.[14] Due to the beneficial properties especially with respect to cytocompatibility common materials for bioprinting are based on natural polymers such as alginate and gelatin.[89]

### 2.3.1.1. Chemical crosslinking of hydrogels

Cell-laden hydrogels for biofabrication processed by AM techniques require not only biocompatible materials but also cytocompatible crosslinking chemistries to form covalent networks. One common method to crosslink bioinks is by irradiation of the precursor formulations in the presence of photoinitiators. This photopolymerization offers spatial and temporal control over the crosslinking process and has found various applications to crosslink printable hydrogels post-fabrication.[90, 91] To allow photocrosslinking in the presence of suitable initiators, polymers are often modified with acrylic or methacrylic moieties.[6] The radical initiated process starts a free radical polymerization of the (meth)acrylic groups to crosslink the polymers. An alternative method to crosslink polymers is based on the dimerization of thiol- and allyl-functional polymers and is termed "thiol-ene click chemistry".[91, 92]

In case of free radical random chain-growth polymerizations, dissociation of the initiator into radicals is followed by the radical transfer to monomer units and creates a growing

polymer chain end (**Scheme 3**).[93]

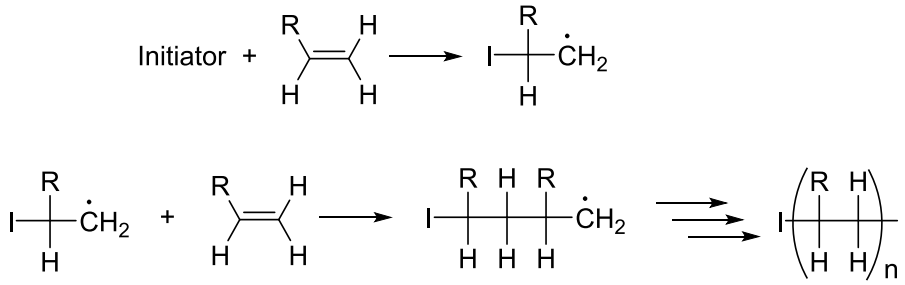


**Scheme 3:** Free radical chain-growth polymerization of acrylic groups initiated by suitable initiators (I). Radicals derived from dissociating initiator molecules are transferred to monomers and result in growing polymer chains.

Albeit its cytocompatible crosslinking, the free radical random chain-growth polymerization is known to result in rather heterogeneous polymer networks with crosslinking oligomeric chains of varying, unknown and uncontrollable lengths.[90, 94]
The thiol-ene click chemistry leads to controlled dimerization of thiols with "enes" (carbon-carbon double bonds) associated with distinct advantages compared to common free radical polymerizations. Mechanistically, the initiator dissociation is followed by transforming the thiol to a thiyl radical, which subsequently reacts with ene-functionalities. After radical transfer to another thiol group, the thioether bearing product is obtained (**Scheme 4**). A step-growth radical mechanism governs this reaction with generally high functional group conversions.[91]

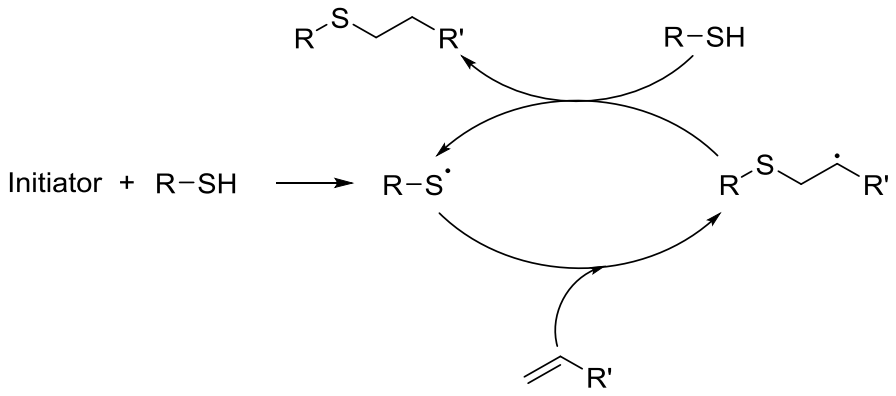


**Scheme 4:** Schematic representation of the thiol-ene click reaction. The initiator (I) dissociates into radicals which transform thiols to thiyl radicals that react with ene-groups. The subsequent reaction with another thiol group yields dimerized products that are bridged via thioethers. Adapted with permission from Kade and coworkers[92]. Copyright (2010) John Wiley and Sons.

Lower radical initiator concentrations and low polymerization shrinkage, and stress, are also beneficial properties of the thiol-ene click reaction. Compared to free radical polymerizations, more homogeneous networks are formed that are predetermined via the educts.[91, 92, 94-96] Besides these advantages the thiol-ene click chemistry is known to proceed rapid[91, 97] with gel points for thiol-ene crosslinked systems in the range of around 4 s for PEG-norbornenes, in contrast to the free radical polymerization of e.g. PEG-diacrylates with around 130 s.[98]

### 2.3.1.2. Photoinitiators

Irradiation of hydrogel precursor solutions in the presence of suitable photoinitiators, with UV- or Vis-light, induces the crosslinking process for both free radical polymerizations and thiol-ene click reactions. Generally, photoinitiators encompass a high absorption at a specific wavelength to dissociate into radicals.[99]

Especially for biofabrication approaches the photoinitiators have to be biocompatible, soluble in aqueous conditions and non-cytotoxic.[100, 101] The most commonly used photoinitiator for UV-light curing under aqueous conditions is 2-hydroxy-1-[4-(hydroxyethoxy)-phenyl]-2-methyl-1-propanone (Irgacure 2959 or I2959).[102-105] This initiator is cleaved into benzoyl and ketyl radicals upon exposure to UV light[106] (**Scheme 5**) and is known to be cytocompatible with concentrations up to 0.05 wt.-%.[107-109]

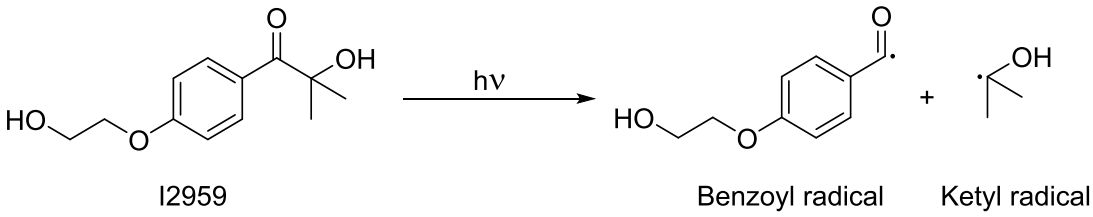


**Scheme 5:** Photolysis of 2-hydroxy-1-[4-(hydroxyethoxy)-phenyl]-2-methyl-1-propanone (I2959) upon UV irradiation. The photoinitiator I2959 dissociates into benzoyl and ketyl radicals. Redrawn from Phillips *et al*.[106] with permission from The Journal of Physical Chemistry A.

Since irradiation with UV-light is known to potentially damage cellular DNA[110-112], Vis-light initiation is a promising alternative to decrease the potential of cellular damages and to overcome the limited penetration depth associated with UV-irradiation of larger

constructs.[113]

Different Vis-light photoinitiators such as eosin-Y[114] and LAP (2,4,6-trimethylbenzoylphosphinate)[115] were already applied to fabricate cell-laden hydrogels. Another promising Vis-light initiator system is based on the combination of tris(2,2-bipyridyl)dichlororuthenium(II) hexahydrate (Ru) with sodium persulfate (SPS).[113] Compared to the one-step radical production of I2959, the Ru/SPS system includes two steps, in which the metal complex is photooxidized from $Ru^{2+}$ to $Ru^{3+}$ and subsequently transfers electrons to SPS.[116] This system was already proven cytocompatible up to concentrations of 1/10 mM Ru/SPS and demonstrated advantageous properties compared to I2959 by decreasing oxygen inhibiting effects of free radical polymerizations and therefore improving the crosslinking efficacy as indicated by lower mass swelling ratios after equilibrium swelling.[113]

### 2.3.2. Gelatin-based hydrogels

Gelatin and hyaluronic acid are among the most widely used natural polymers for polymerizing hydrogels due to their cell-interactive properties and biodegradability.[6, 117, 118]

Gelatin can be obtained by treating collagen at different pH-conditions and can be subdivided into type A or type B gelatin depending on the pH values during hydrolysis. Type A gelatin is obtained with acidic conditions, whereas type B gelatin represents the product of alkaline treated collagen.[105] In contrast to collagen, gelatin possesses an increased water solubility and a lower antigenicity, both being consequences of the denaturation process.[19, 119] Gelatin contains the repetitive collagen-derived cell binding motif arginine-glycine-aspartic acid (RGD) and is enzymatically degradable through matrix metalloproteinase (MMP) sensitive cleavage sites.[94] Whereas collagen is resistant to most proteases and requires specific enzymes to be cleaved, gelatin is susceptible to most proteases.[19] At temperatures below 30 °C gelatin can form physical crosslinked hydrogels.[120, 121] However, this property cannot be exploited for Tissue Engineering approaches as physiological temperatures of around 37 °C are required for *in vitro* experiments. Accordingly, gelatin has to be modified with additional functional groups enabling chemical crosslinking and thus irreversible covalent network formation to stable hydrogels.

One of the most frequently used modifications is based upon introducing methacryloyl

groups resulting in gelatin methacryloyl (GelMA). GelMA is also referred to as gelatin methacrylate[102, 122], methacrylated gelatin[123, 124] or methacrylamide gelatin[125-127]. Recent literature suggests the term "gelatin methacryloyl" to be most suitable, as GelMA possesses more methacrylamide than methacrylate groups.[93] These functional groups enable the photo-cured crosslinking of GelMA into mechanically stable hydrogel constructs. Currently existing GelMA synthesis protocols are all slight modifications of the first synthesis report from Van den Bulcke *et al*.[125] back in 2000. Briefly, gelatins amine and hydroxyl group bearing amino acids are modified by the reaction with methacrylic anhydride (MA) in PBS at 50 °C. The ratios of MA to gelatin controls substitution degree (SD) values and ultimately triggers the physico-chemical properties of the obtained hydrogels besides the possibility to tune these properties by increasing the overall hydrogel polymer content. Typically less than 5.0 % in molar ratio of amino acid residues are modified with methacryloyl groups and limit loss of amino acid motif function.[125] Free radical random chain-growth polymerization of GelMA is initiated at mild and most importantly cytocompatible conditions (e.g. RT, neutral pH and aqueous environments).[93, 102, 121-123, 125, 126] Hence, GelMA hydrogels are widely used for different biofabrication techniques such as photopatterned GelMA hydrogels[102, 128], self-assembled hydrogels[129, 130] or for microfluidics[131-133] and bioprinted constructs[85, 121, 134, 135].

### 2.3.3. Hyaluronic acid-based hydrogels

Hyaluronic acid (HA) can be found throughout the human body in various tissues and e.g. represents besides collagen the major component of the extracellular matrix of cartilage.[136, 137]

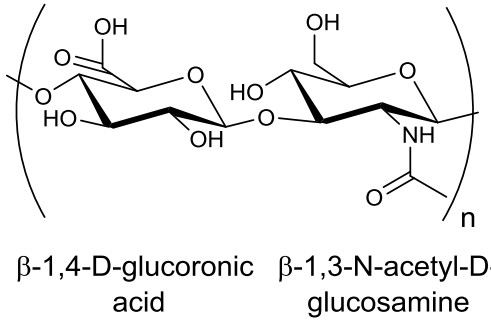


**Scheme 6:** Molecular structure of the repeating β-1,4-D-glucoronic acid and β-1,3-N-acetyl-D-glucosamine disaccharide unit of hyaluronic acid (HA). Redrawn with permission from Peppas *et al*.[2]. Copyright (2009) John Wiley and Sons.

The non-immunogenic and linear polysaccharide HA consists of repeating β-1,4-D-glucoronic acid and β-1,3-*N*-acetyl-D-glucosamine disaccharide units (**Scheme 6**).[2, 136] This non-sulfated glycosaminoglycan possesses a polyanionic character which results in a high hydration that contributes to the lubrication of joints. High molecular weight HA with molecular weights of 100 – 8000 kDa is biodegraded into smaller oligosaccharide fragments via hyaluronidases and also susceptible to reactive oxygen species.[2, 136-138] As degradation of HA proceeds with half lifetimes of a few hours to days[136], a prerequisite to prolong enzymatic degradation is the introduction of synthetic crosslinks.

HA displays beneficial rheological features rendering it suitable for demanding biofabrication techniques such as extrusion-based printing. Here, the viscosity of HA solutions[139, 140] is being exploited either simply as additive to increase the printability of low-viscous bioinks with unmodified HA[20, 121] or additionally as thiol-ene crosslinker post-fabrication[141]. For the latter system, crosslinking of poly(glycidol) with thiol-modified HA was proven to result in printable and biocompatible hydrogels. Thiol-modified HA represents a versatile hydrogel platform either by means of thiol-ene click chemistry[141] or by simple reoxidation, i.e. disulfide-bridging[142, 143]. Synthesis of the thiol-bearing HA precursor is based on the introduction of disulfide bridged dihydrazides which can reductively be cleaved to thiols (**Scheme 7**).[142]

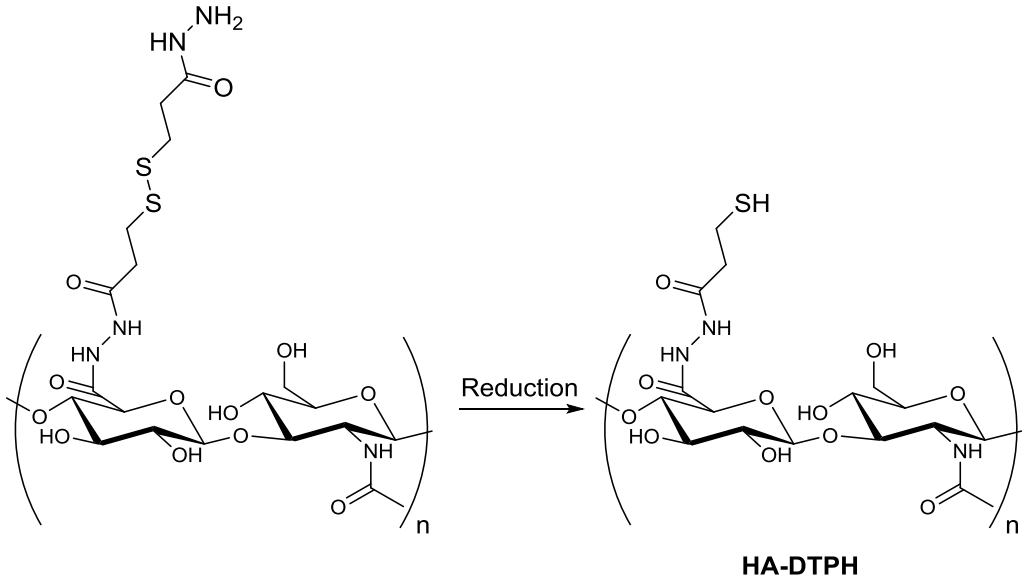


**Scheme 7:** Molecular structure of thiol-modified hyaluronic acid (HA). Reduction of the disulfide bridged precursor yields the thiol bearing product (HA-DTPH). Redrawn from Prestwich *et al.*[142] with permission from Biomacromolecules.

Prestwich *et al.*[142] conducted a comparison of air-oxidized versus $H_2O_2$-oxidized hydrogels and found improved oxidation efficacies for the latter option. Nevertheless, the fast gelation under physiological conditions rendered this system suitable for *in vitro* studies with murine fibroblasts. Only 5 % dead cells were detectable after 96 h of culture and underlined the cytocompatibility of this system.[142]

### 2.3.4. Gelatin- and hyaluronic acid-based hybrid hydrogels

Biocompatibility, availability and ease of modification render gelatin- and HA-based hydrogels promising as biofabrication and Tissue Engineering platforms. Nonetheless, the combination of these materials with other polymers has gained interest to improve certain aspects compared to hydrogels based on only one of both polymers. For GelMA-based systems combinations with other biomaterials improved e.g. mechanical properties[144, 145] or swelling ratios[145]. Besides the combination with synthetic polymers, special interest gained the combination with hyaluronic acid. The mechanical properties of these hybrid hydrogels, copolymerized with methacrylated hyaluronic acid (HAMA), were more than doubled (72 kPa) compared to GelMA hydrogels alone (32 kPa).[146] Furthermore, the addition of unmodified HA was demonstrated to increase the printability of rather low viscous GelMA solutions for extrusion-based bioprinting as demonstrated by Schuurman *et al.*[121] For HA-based systems, cellular adhesion on previously mentioned oxidized HA-DTPH hydrogels could be enhanced by hybrid hydrogels with gelatin-DTPH. This system was either crosslinked via oxidation[143] or in combination with PEGDA[147] and both studies proved superior cell adhesion on gelatin containing hydrogels.

The intrinsic advantages of gelatin, such as increased cellular adhesion rates, and of HA, e.g. enhanced viscosities, demonstrate that combining both natural polymers to hybrid hydrogels provides a highly versatile, flexible and attractive biofabrication platform.

# 3. Results and Discussion

## 3.1. Biofunctionalization of PCL scaffolds via hydrogel surface coatings

In this chapter box-structured poly-ε-caprolactone (PCL) scaffolds with filament spacing and fibers in the micron scale range were produced via the solvent-free additive manufacturing technique of melt electrowriting (MEW). Control over the initial scaffold properties was obtained by purely aqueous coating these scaffolds with six-armed star-shaped NCO-poly(ethylene oxide-*stat*-propylene oxide) (sP(EO-*stat*-PO)). This coating simultaneously enabled biofunctionalization of the scaffolds in minimal protein adhesive environments, which is a prerequisite for exactly controlled cell-material interaction studies. Furthermore, a generic platform was developed which enabled a photo-induced time-independent biofunctionalization of scaffolds. The herein obtained biofunctionalized scaffolds were investigated for their cell adhesiveness.

Tomasz Jungst from the Department for Functional Materials in Medicine and Dentistry of Prof. Dr. Jürgen Groll at the University of Würzburg constructed and built the MEW device.

Dr. Gernot Hochleitner from the Department for Functional Materials in Medicine and Dentistry of Prof. Dr. Jürgen Groll at the University of Würzburg provided PCL scaffolds for cell culture experiments.

All experiments were performed in triplicate ($n = 3$) and statistical evaluation was assessed by one-way ANOVA with post hoc Tukey (SigmaPlot 12.5). All values are presented as the mean ± standard deviation. Significant differences between represented groups are assigned with * ($p < 0.05$) and ** ($p < 0.001$).

### 3.1.1. Scaffold production and hydrogel coating with sP(EO-*stat*-PO)

PCL scaffolds (4.2 x 4.2 $cm^2$) with a total of 32 layers and defined geometries with filament spacing of 200 µm and fiber diameters of 5 – 7 µm were produced via the solvent-free process of MEW. The samples box-structure was achieved by alternating layer deposition at 0° and 90° similar to previously fabricated PCL scaffolds.[11, 148] An overview of these scaffolds is depicted in **Figure 7 A** and **B**.

Additionally scaffolds for cell culture experiments (100 layers, 300 µm filament spacing and 6 µm fiber diameters) were provided from Gernot Hochleitner (**Figure 7 C**). The scaffolds were cut via a custom-built device into 1.2 x 1.2 $cm^2$ pieces (**Figure 7 D**).

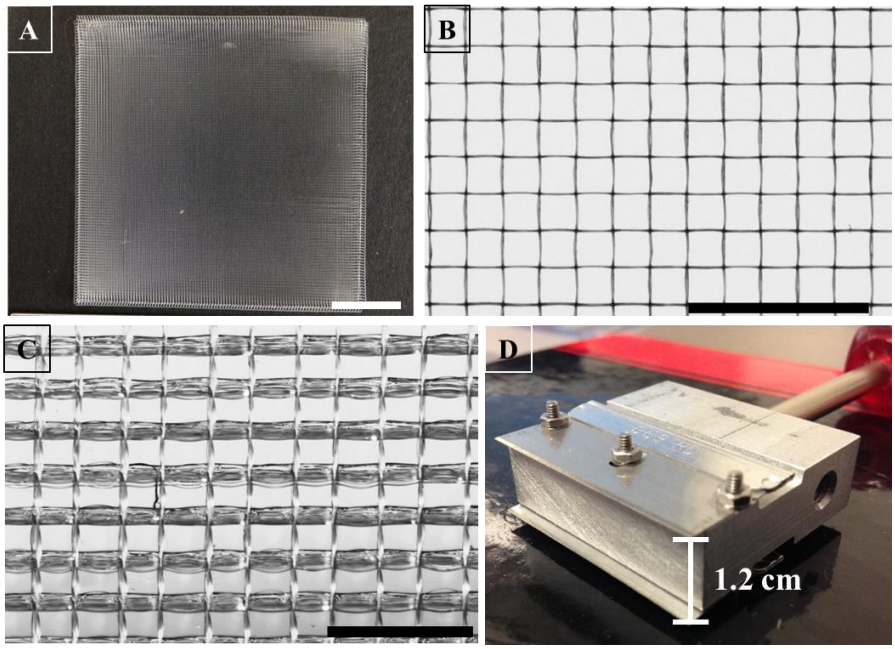


**Figure 7:** Representative overview of a 200 µm filament spaced scaffold (**A**) and a stereomicroscopic magnification thereof (**B**). Stereomicroscopic magnification of a scaffold provided by Dr. Gernot Hochleitner with 300 µm filament spacing (**C**). Scaffolds possessed fiber diameters of around 5 – 7 µm. Scale bars represent 1 cm (**A**) and 1 mm (**B** and **C**). Custom built cutting-device for scaffolds, for which two razor blades were mounted on a stainless steel block (1.2 cm width), equipped with a handle (**D**).

The aim of this chapter was to generate homogenous but thin biofunctionalizable sP(EO-*stat*-PO) hydrogel coatings on PCL scaffolds. Hence, a crucial factor to later ensure sufficient homogeneously sP(EO-*stat*-PO) coated PCL fibers is represented by an optimized concentration of the sP(EO-*stat*-PO) coating solution. Increasing this concentration raises the probability of bulk gelation[149], whereas too low concentrated solutions may lead to insufficient PCL surface coverage. To determine the lowest bulk

gelation limit different weight percentages of aqueous sP(EO-*stat*-PO) solutions were investigated. An overview of the experimental observations is given in **Table 1**.

**Table 1:** Representative observations on bulk gelation of aqueous sP(EO-*stat*-PO) solutions ranging from 0.3 – 7.5 wt.-%.

| **sP(EO-*stat*-PO) [wt.-%]** | **0.3** | **0.5** | **1.0** | **2.0** | **4.0** | **7.5** |
|---|---|---|---|---|---|---|
| Dissolution [min] | 2 | 2 | 2 | 3 | 3 | 5 |
| Bulk gelation [min] | n.d. | n.d. | n.d. | n.d. | n.d. | 20 |

n.d. = not detectable

Even after 24 h no bulk gelation was detectable for sP(EO-*stat*-PO) concentrations in the range of 0.3 – 4.0 wt.-%. Only the highest sP(EO-*stat*-PO) amount of 7.5 wt.-% resulted in the formation of macroscopic hydrogels after 20 min and was consequently not included for following experiments (**Table 1**). This is slightly different to the results from Dalton *et al.*[149], for which homogeneous hydrogels above 10 wt.-% sP(EO-*stat*-PO) and particle formation or heterogeneous hydrogels with 7.0 wt.-% sP(EO-*stat*-PO) were obtained. Although the same sP(EO-*stat*-PO) structures were used, namely six-armed star-shaped isocyanate-terminated sP(EO-*stat*-PO) with 12 kDa, the differences to this study could probably be correlated to distinct batches of sP(EO-*stat*-PO) with slightly different residual amounts of free IPDI.

For the subsequent sP(EO-*stat*-PO) coating of PCL scaffolds, 1.0 – 4.0 wt.-% sP(EO-*stat*-PO) solutions were used to ensure homogeneous and thin hydrogel layers around PCL fibers. An overview of the workflow for sP(EO-*stat*-PO) coating of the scaffolds is depicted in **Figure 8**.

Scaffolds were always firstly pre-wetted with water to remove entrapped air bubbles after which a water or an alkaline pre-treatment of the scaffolds followed. This alkaline pre-treatment can cleave ester bonds of PCL[150, 151] and thereby could raise the scaffold hydrophilicity due to increased hydrogen bond interaction possibilities and anionic acid groups. Hence, this pre-treatment could prevent the formation of a sP(EO-*stat*-PO) monolayer in which all star-arms are in contact to the PCL surface. Otherwise the hydrophobic PPO and IPDI parts of the star molecules would readily attach to the hydrophobic PCL surface and thereby could result in these specific monolayers, which would limit an efficient protein repellency and restrict the biofunctionalization possibility

of sP(EO-*stat*-PO) hydrogel layers. Therefore, a comparison of solely water to alkaline pre-treated PCL and sP(EO-*stat*-PO) coated samples was included.

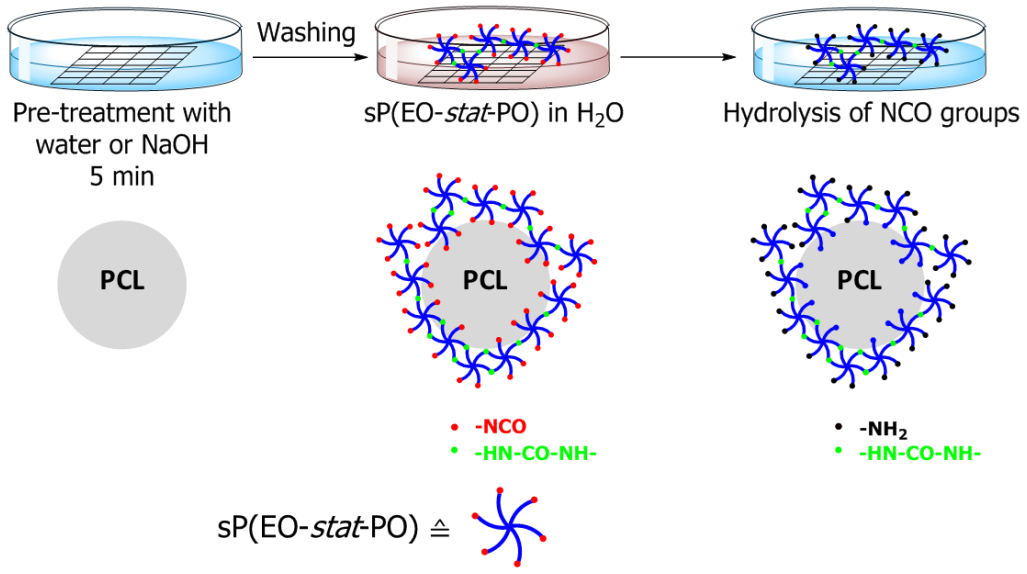


**Figure 8:** Workflow of the sP(EO-*stat*-PO) coating procedure for PCL scaffolds. Aqueous pre-wetting of scaffolds (not depicted) was followed by either a water or an alkaline pre-treatment with NaOH for 5 min. After washing the scaffolds, differently concentrated aqueous sP(EO-*stat*-PO) solutions were added for distinct times and were replaced by water to allow overnight crosslinking and complete NCO hydrolysis to amines.

The alkaline pre-treatment was followed by washing steps and melt electrowritten scaffolds were placed in between two serological pipette rings to ensure entirely sP(EO-*stat*-PO) coated PCL fibers. Aqueous sP(EO-*stat*-PO) solutions were added to allow the crosslinking to sP(EO-*stat*-PO) layers around the PCL fibers via urea bridge formation. A balance of adsorption and covalent bonds between PCL-OH- and sP(EO-*stat*-PO)-NCO-groups is hypothesized to contribute to the sP(EO-*stat*-PO) attachment.[58] Complete hydrolysis of reactive NCO-groups to amines was achieved by placing sP(EO-*stat*-PO) coated scaffolds in water for an overnight incubation. Herein, the aqueous step additionally decreases the hydrophobic interactions in between sP(EO-*stat*-PO) layers and, hence, improves the prevention of sP(EO-*stat*-PO) layers in which all star-arms are crosslinked to the underlying layers. This is important to later allow for a biofunctionalization of coated scaffolds via uncrosslinked sP(EO-*stat*-PO)-NCO-groups. A crucial factor to restrict negative effects on cells arising from the reactive and cytotoxic NCO-groups, is represented by completely hydrolyzed NCO-groups.

IR spectroscopy was used to analyze the presence of sP(EO-*stat*-PO) on coated PCL scaffolds. Prior to complete NCO-hydrolysis, prominent NCO peaks in the region of 2280 – 2240 $cm^{-1}$[152] are hypothesized to allow the detection of bound sP(EO-*stat*-PO). Simultaneously, the presence of these groups is essential for the later biofunctionalization of coated PCL scaffolds. Therefore, alkaline pre-treated (1 M NaOH, 5 min) scaffolds were coated for 15 min with sP(EO-*stat*-PO) solutions (1.0 – 4.0 wt.-%) and immediately dried prior to IR analyses. Additionally, successful NCO-hydrolysis was investigated with aqueous overnight incubated sP(EO-*stat*-PO) coated scaffolds.

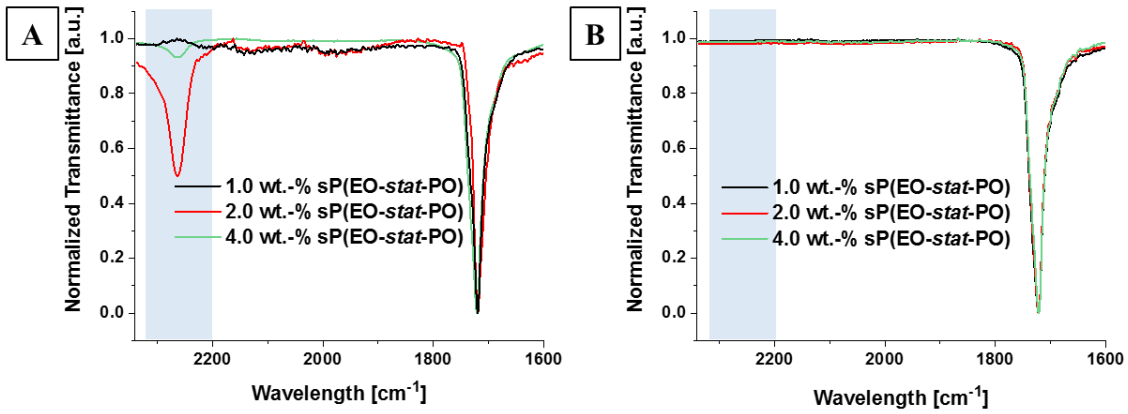


**Figure 9:** Representative normalized IR spectra of sP(EO-*stat*-PO) coated scaffolds with 1.0 wt.-% (black line), 2.0 wt.-% (red line) and 4.0 wt.-% (green line) sP(EO-*stat*-PO) (**A**) and the corresponding overnight NCO-hydrolyzed samples (**B**). SP(EO-*stat*-PO) coating was performed for 15 min on aqueous pre-wetted, alkaline pre-treated scaffolds (1 M NaOH, 5 min) and washed scaffolds. Samples were dried before IR analysis. Spectra were normalized to the carbonyl peak at 1720 $cm^{-1}$. Blue boxes highlight the wavelength area of NCO of around 2260 $cm^{-1}$.

The obtained IR spectra were normalized to the carbonyl peak at around 1720 $cm^{-1}$ and the peak around 2260 $cm^{-1}$ was assigned to NCO-functionalities (**Figure 9**, blue boxes). Scaffolds coated with 1.0 wt.-% sP(EO-*stat*-PO) solution did not display this characteristic peak (**Figure 9 A**, black line). This can either be a sign of completely hydrolyzed or crosslinked NCO-groups on the scaffolds or of an absent sP(EO-*stat*-PO) layer around the PCL fibers as consequence of too low sP(EO-*stat*-PO) amounts. Therefore, the investigation of lower sP(EO-*stat*-PO) concentrations (0.3 – 0.5 wt.-% sP(EO-*stat*-PO)) was neglected as scaffold biofunctionalizations require these groups.

Coating with 2.0 wt.-% sP(EO-*stat*-PO) resulted in the most prominent NCO peak (**Figure 9 A**, red line), whereas 4.0 wt.-% sP(EO-*stat*-PO) yielded a comparable smaller

peak (**Figure 9 A**, green line). This was attributed to the increased probability of crosslinked NCO-groups for higher sP(EO-*stat*-PO) concentrations, thereby reducing the amount of remaining NCO-groups. More pronounced hydrophobic interactions, as a consequence of a higher sP(EO-*stat*-PO) layer number, could as well contribute to smaller NCO signals. In this case, star shaped molecules could be arranged so that in the outer sP(EO-*stat*-PO) layer the molecules are completely crosslinked to the previous layer and adjacent molecules. Moreover, besides the hydrogel formation around PCL fibers, higher concentrated coating solutions could also lead to particle formation and contribute to the reduction of sP(EO-*stat*-PO) on the scaffolds.

Complete NCO-hydrolysis, after an overnight incubation in water, was confirmed by disappearing peaks at 2264 $cm^{-1}$ for all investigated sP(EO-*stat*-PO) concentrations (**Figure 9 B**). This is in accordance to literature stated NCO-hydrolysis intervals of 12 h[72-74] or 24 h[78, 80].

Thus, 2.0 wt.-% sP(EO-*stat*-PO) solutions represented the most suitable composition for coating purposes, considering the later biofunctionalization via sP(EO-*stat*-PO)-NCO-groups and following experiments were conducted solely with this concentration.

#### 3.1.1.1. Hydrophilicity and protein repellency

Next, the final scaffold hydrophilicity and, hence, protein repellency was investigated. The necessity of an alkaline etching prior to sP(EO-*stat*-PO) coating and the effect of increasing NaOH molarities on the aforementioned scaffold properties was assessed. Therefore, different pre-treatments prior to sP(EO-*stat*-PO) coating were investigated. Scaffolds were either pre-treated solely with water or via the alkaline etching with 1 M or 5 M NaOH for 5 min. SP(EO-*stat*-PO) coating was limited to 10 min to evaluate if this coating time would sufficiently increase the final hydrophilicity and protein repellency of sP(EO-*stat*-PO) coated scaffolds while restricting the time-dependent NCO-hydrolysis. Analysis of these approaches was conducted with completely NCO-hydrolyzed sP(EO-*stat*-PO) coated scaffolds. To elucidate a shift towards increased hydrophilicities, resulting from the pre-treatments and/or the sP(EO-*stat*-PO) coating, contact angle measurements were performed by placing water droplets on dried scaffolds, which were placed in Eppendorf lids, and measuring the contact angles 2 s after deposition.

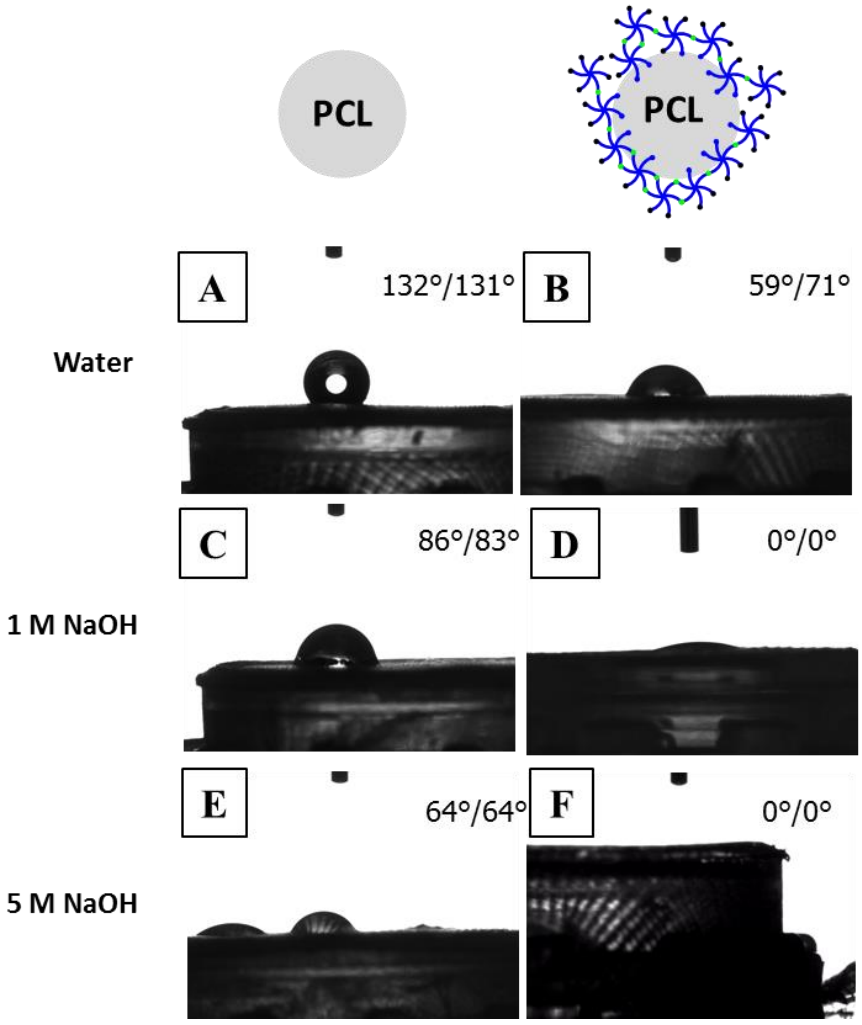


**Figure 10:** Representative images of the contact angles of PCL control (**A**, **C** and **E**) and sP(EO-*stat*-PO) coated scaffolds (**B**, **D** and **F**). After aqueous pre-wetting, the scaffolds were pre-treated for 5 min with water (**A** and **B**), 1 M NaOH (**C** and **D**) or 5 M NaOH (**E** and **F**) and washed prior to sP(EO-*stat*-PO) coating with 2.0 wt.-% sP(EO-*stat*-PO) for 10 min for **B**, **D** and **F**. All samples were incubated in water overnight. Images were taken 2 s after depositing water droplets on the dried scaffold surfaces.

Water pre-treated scaffolds, with a rather hydrophobic PCL surface (**Figure 10 A**), were rendered more hydrophilic upon sP(EO-*stat*-PO) coating (**Figure 10 B**) with a concurrent decrease of the contact angles from ~ 132° to ~ 65°. A correlation to contact angles derived from e.g. solution electrospun scaffolds[58] was not conducted as the contact angles strongly depend on the scaffold geometry and structure, hence, a direct comparison would be prone to misinterpretations.

For alkaline pre-treated PCL scaffolds with 1 M NaOH (**Figure 10 C**) or 5 M NaOH (**Figure 10 E**) an increased initial scaffold hydrophilicity was detectable, correlating to the alkaline induced cleavage of ester bonds. The higher the molarity of the alkaline solution,

the lower the observed contact angles with ~ 85° for 1 M NaOH and ~ 64 °C for 5 M NaOH. For alkaline pre-treated sP(EO-*stat*-PO) coated scaffolds an extremely high hydrophilicity was observable as the water droplets were immediately soaked into the scaffolds (**Figure 10 D** (1 M NaOH) and **Figure 10 F** (5 M NaOH)).

These results demonstrate the advantageous alkaline etching pre-treatment of PCL scaffolds by increasing the initial scaffold hydrophilicity, which could in turn increase the interaction between PCL and sP(EO-*stat*-PO). The comparison of water versus alkaline pre-treated sP(EO-*stat*-PO) coated samples further underline the aforementioned hypothesis of the hydrophobic interactions dependent star-molecule arrangement. Only with the alkaline pre-treatment completely hydrophilic sP(EO-*stat*-PO) coated scaffolds were obtained. Generally these results are in accordance to the well-known hydrophilic properties of sP(EO-*stat*-PO) and derived coatings thereof.[17, 55, 75, 80]

The same pre-treatments and sP(EO-*stat*-PO) coating procedures were applied to investigate the effect on the protein-repellency of the scaffolds. After sP(EO-*stat*-PO) coating and NCO-hydrolysis overnight, the scaffolds were incubated with Texas Red™ labelled bovine serum albumin (TRBSA) for 3 h under exclusion of light, afterwards extensively washed and finally analyzed with fluorescence microscopy. All images were taken with the same exposure time of 500 ms to enable qualitative comparisons.

The relatively high TRBSA adsorption for water pre-treated scaffolds (**Figure 11 A**) was reduced upon sP(EO-*stat*-PO) coating (**Figure 11 B**), as suggested by declining fluorescence signals.

Considering alkaline pre-treated PCL scaffolds, the fluorescence intensities of 1 M NaOH (**Figure 11 C**) and 5 M NaOH (**Figure 11 E**) revealed no clear improvements for higher NaOH molarities. The same conclusions were drawn for alkaline pre-treated and sP(EO-*stat*-PO) coated scaffolds for which no fluorescence was detectable independent on the NaOH molarities (**Figure 11 D**, 1 M NaOH; **Figure 11 F**, 5 M NaOH). Clearly reduced TRBSA adsorption was obtained by sP(EO-*stat*-PO) coatings, which is in good accordance to previously published data for combinations of solution electrospun PCL with sP(EO-*stat*-PO)[58] and to sP(EO-*stat*-PO) coatings or hydrogels in general.[74, 80, 153, 154]

The sP(EO-*stat*-PO) coating for the water pre-treated control was not as efficient in increasing the protein repellency as compared to the alkaline pre-treated scaffolds. This further underlined the importance of this pre-treatment, as only etched and sP(EO-*stat*-PO)

coated scaffolds were capable to completely inhibit TRBSA adsorption. Solely for these samples a sufficient and homogeneous hydrophilicity was ensured, which avoided unspecific protein adsorption and demonstrate the close relationship between surface hydrophilicity and protein repellency.

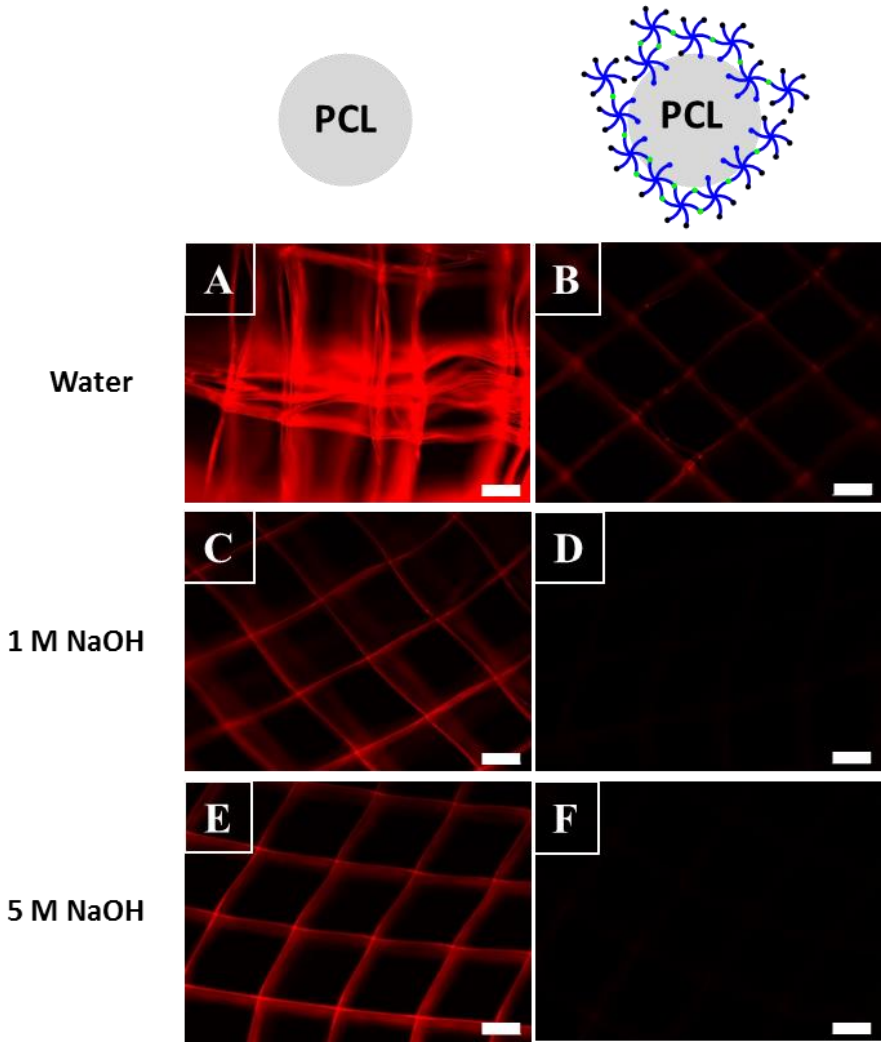


**Figure 11:** Representative fluorescence images of TRBSA adsorption on PCL control (**A**, **C** and **E**) and on sP(EO-*stat*-PO) coated scaffolds (**B**, **D** and **F**). After aqueous pre-wetting, the scaffolds were pre-treated with water (**A** and **B**), 1 M NaOH (**C** and **D**) or 5 M NaOH (**E** and **F**) and washed for 5 min prior to sP(EO-*stat*-PO) coating with 2.0 wt.-% sP(EO-*stat*-PO) for 10 min for **B**, **D** and **F**. All samples were incubated in water overnight prior to incubation with TRBSA (50 µg $mL^{-1}$ in PBS for 3 h under light exclusion). Scaffolds were washed with PBS and dried prior to fluorescence analysis. Exposure times of 500 ms and scale bars represent 100 µm.

Nonetheless, it should be noted that the alkaline etching also significantly influences the scaffold degradation by cleaving ester bonds[150, 151] and to reduce this, the following

experiments were conducted with 1 M NaOH. The sP(EO-*stat*-PO) coating time of 10 min seemed sufficient to increase the scaffold hydrophilicity concurrent with the protein-repellency and was applied for all subsequent experiments. With this coating a functionalizable minimal unspecific protein adhesive environment is obtained that allows to study interactions between cells and coupled biomolecules.

### 3.1.1.2. Limited time frame for biofunctionalizations

A prerequisite for later biofunctionalization is the presence of NCO-groups. Hence, sP(EO-*stat*-PO) coating intervals of up to 2 h were investigated in order to optimize the coating via knowledge of the duration of NCO-presence on sP(EO-*stat*-PO) coated scaffolds. Therefore, alkaline pre-treated (1 M NaOH, 5 min) PCL scaffolds were coated with 2.0 wt.-% sP(EO-*stat*-PO), immediately dried and analyzed with IR spectroscopy.

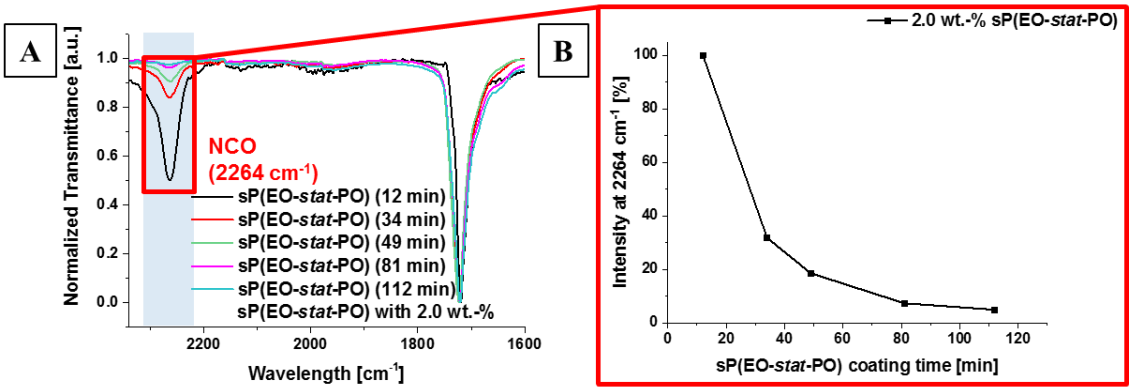


**Figure 12:** Representative time dependent and normalized IR spectra of aqueous pre-wetted and alkaline pre-treated (1 M NaOH, 5 min) PCL scaffolds coated with 2.0 wt.-% sP(EO-*stat*-PO) for 12 – 112 min (**A**). Spectra were recorded immediately after drying the sP(EO-*stat*-PO) coated scaffolds and normalized to the carbonyl peak at 1720 $cm^{-1}$. The blue box highlights the wavelength area of NCO at around 2260 $cm^{-1}$. Representative corresponding correlation of NCO signal intensity at 2264 $cm^{-1}$ (t = 12 min equals 100 %) to the progression of signal intensity for different sP(EO-*stat*-PO) coating times (**B**).

Present NCO-groups were correlated to characteristic peaks at around 2260 $cm^{-1}$ (**Figure 12 A**, blue box). The initial most intense NCO peak for 12 min sP(EO-*stat*-PO) coating decreased concurrent with the progression in sP(EO-*stat*-PO) coating time. After around 80 min this peak almost disappeared, suggesting the NCO-hydrolysis to amines together with urea bridge formation[65, 75, 149] of these groups. Decreasing NCO-peak intensity was plotted against sP(EO-*stat*-PO) coating time and the signal intensity for

12 min sP(EO-*stat*-PO) coating was set to 100 %. This plot supported the aforementioned observations by a reduction below 10 % signal intensity after 80 min (**Figure 12 B**). Only 5.0 % of the initial peak intensity were detectable after 112 min and complete NCO-hydrolysis was hypothesized after approximately 130 – 150 min. These results suggested a time frame of maximum 80 min for concurrent biofunctionalizations of these scaffolds.

The investigation of immediately dried scaffolds after sP(EO-*stat*-PO) coating was expanded to a washing cycle, after sP(EO-*stat*-PO) coating, with deionized water changes (5 times) for a total of 3 min. This was performed as the complete removal of unreacted sP(EO-*stat*-PO) molecules prior to the addition of to-be-coupled biomolecules would be favorable to overcome a potential scavenging by unbound sP(EO-*stat*-PO)-NCO-groups. The stated time points correlate to the time of sP(EO-*stat*-PO) coating (5 min, 25 min and 75 min) neglecting the time for the subsequent washing cycle and the drying process (1 min).

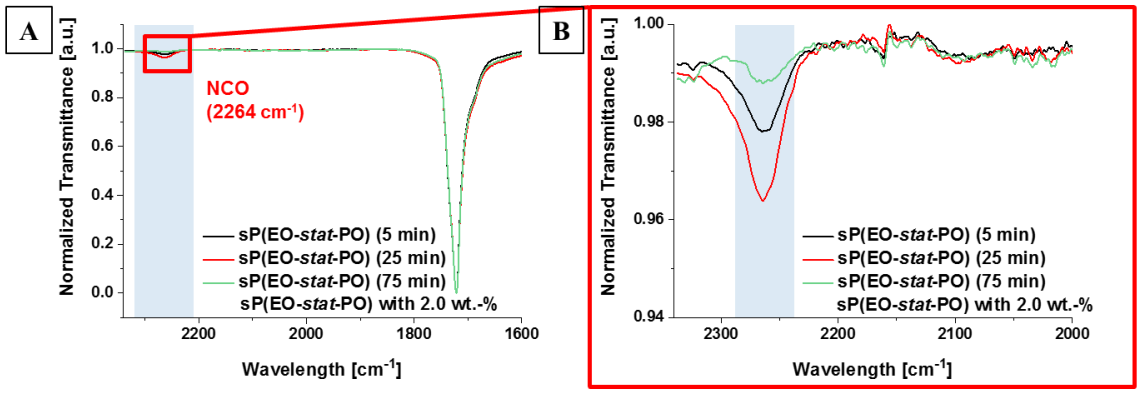


**Figure 13:** Representative normalized IR spectra of different sP(EO-*stat*-PO) (2.0 wt.-% sP(EO-*stat*-PO)) coating times (5 – 75 min) with a subsequent washing cycle prior to IR analyses of dried scaffolds (**A**). SP(EO-*stat*-PO) coatings were performed on aqueous pre-wetted, alkaline pre-treated (1 M NaOH, 5 min) and washed PCL scaffolds. Inset represents the magnification of the area from 2340 – 2000 $cm^{-1}$ (**B**). SP(EO-*stat*-PO) coating was performed for 5 min (black line), 25 min (red line) or 75 min (green line). Spectra were normalized to the carbonyl peak at 1720 $cm^{-1}$. Blue boxes highlight the wavelength area of NCO at around 2260 $cm^{-1}$.

In general, NCO peaks at 2264 $cm^{-1}$ were less intense for experiments that included washing cycles (**Figure 13 A**), than compared to previous results (**Figure 12 A**), probably due to the removal of unbound sP(EO-*stat*-PO) and a faster NCO-hydrolysis as a consequence of the water excess. The magnification from 2340 – 2000 $cm^{-1}$ demonstrated the highest NCO peak intensity for 25 min sP(EO-*stat*-PO) coating (red line), followed by

5 min (black line) and hardly any signal was detectable for the longest sP(EO-*stat*-PO) coating time of 75 min (**Figure 13 B**, green line). Due to the general very low signal intensities and the extremely slight difference in between NCO signal of sP(EO-*stat*-PO) coating times ($\Delta_{max}$ = 0.02 a.u.), further conclusions about the available time frame of NCO presence for biofunctionalization experiments were not drawn.

Instead, an additional experimental setup was conducted with the same sP(EO-*stat*-PO) coating times but without the subsequent washing after sP(EO-*stat*-PO) coating. This was performed to obtain more detailed information on the previous determined time frame of maximum 80 min especially for shorter coating times. For this approach more intense signal intensities and, hence, a better correlation to the presence of NCO-groups were hypothesized.

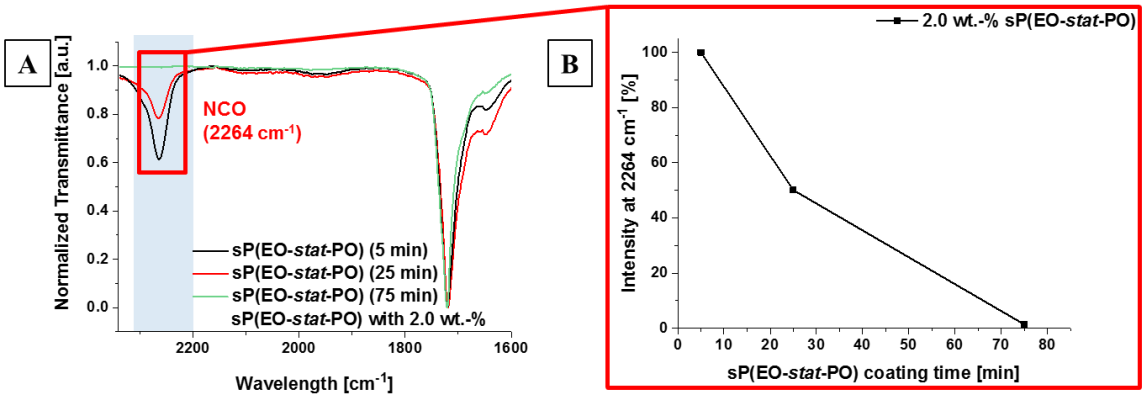


**Figure 14:** Representative normalized IR spectra of distinct sP(EO-*stat*-PO) (2.0 wt.-% sP(EO-*stat*-PO)) coating times (5 – 75 min) without subsequent washing of the scaffolds prior to IR analyses of dried scaffolds (**A**). SP(EO-*stat*-PO) coating for 5 min (black line), 25 min (red line) and 75 min (green line) was performed for aqueous pre-wetted, alkaline pre-treated (1 M NaOH, 5 min) and washed PCL scaffolds. Spectra were normalized to the carbonyl peak at 1720 $cm^{-1}$. The blue box highlights the wavelength area of NCO at around 2260 $cm^{-1}$. Representative correlation of NCO signal intensity at 2264 $cm^{-1}$ (t = 5 min equals 100 %) to the progression of signal intensity for sP(EO-*stat*-PO) coating times (**B**).

For this experimental setup more intense signals were detected (**Figure 14 A**) compared to results with the washing cycle (**Figure 13**), due to the fact that unbound sP(EO-*stat*-PO) was neither removed nor diluted, and were comparable to the experiments without the washing cycle (**Figure 12 A**). The highest NCO peak intensity at 2264 $cm^{-1}$ was detectable for 5 min sP(EO-*stat*-PO) coating (**Figure 14 A**, black line). This peak decreased after 25 min to 50.0 % signal intensity (**Figure 14 A**, red line) and almost disappeared after

75 min (**Figure 14 A**, green line and **Figure 14 B**, 2.0 % signal intensity). Decreasing NCO signal intensities for longer sP(EO-*stat*-PO) coating times were correlated to a lower amount of NCO-groups as a consequence of higher crosslinked sP(EO-*stat*-PO) layers in combination with progressive NCO-hydrolysis. After 75 – 80 min the hydrolysis and crosslinking was complete as suggested by the almost completely diminished NCO peak, which is in accordance to the previous determined time frame.

This experiment elucidated that an efficient scaffold biofunctionalization can only be achieved within the first 20 min (65 % NCO signal intensity) to 40 min (26 % NCO signal intensity), hence, a fast working procedure is mandatory (**Figure 14 B**). Following experiments were conducted with 10 min sP(EO-*stat*-PO) coating times to ensure a balance of sP(EO-*stat*-PO) coating and presence of NCO-groups to enable biofunctionalization experiments.

Furthermore, these results suggested that an intense washing of freshly sP(EO-*stat*-PO) coated scaffolds is unsuitable for biofunctionalization experiments. Consequently, the sP(EO-*stat*-PO) solutions is removed after 10 min coating and immediately replaced by the to-be-coupled biomolecule solutions without additional washing steps. Removing excessive sP(EO-*stat*-PO) after the coating, minimizes the scavenging of to-be-coupled molecules by yet unbound sP(EO-*stat*-PO).

### 3.1.1.3. Quantification of sP(EO-*stat*-PO) hydrogel layers on PCL scaffolds

SEM analysis was exploited to obtain detailed information about the sP(EO-*stat*-PO) coating homogeneity and PCL scaffolds served as controls.

PCL fiber surfaces (**Figure 15 A**, **C** and **E**) appeared slightly more porous compared to rather smooth sP(EO-*stat*-PO) coated fibers (**Figure 15 B**, **D** and **F**). The sP(EO-*stat*-PO) coating was successfully visualized via SEM analysis and could be correlated to web-like structures in between adjacent fibers without obvious coating defects (**Figure 15 B**, **D** and **F**). These results further support the sP(EO-*stat*-PO) coating homogeneity, as already suggested by protein adsorption experiments.

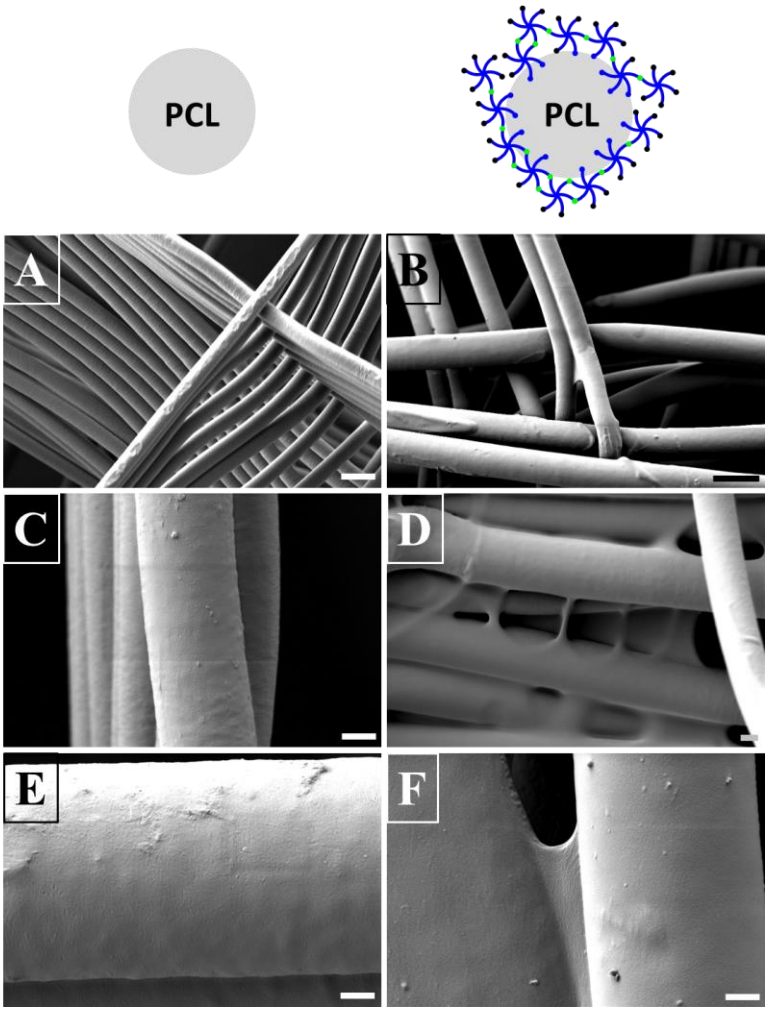


**Figure 15:** Representative SEM images of PCL control (**A**, **C** and **E**) and sP(EO-*stat*-PO) coated scaffolds (**B**, **D** and **F**). After aqueous pre-wetting, the scaffolds were pre-treated with 1 M NaOH for 5 min (**A** – **F**) and washed prior to sP(EO-*stat*-PO) coating (2.0 wt.-%, 10 min) for **B**, **D** and **F**. All samples were incubated in water overnight and washed with water prior to analyses. Dried scaffolds were sputtered with 4 nm platinum. Scale bars represent 10 µm (**A** and **B**), 2 µm (**C** and **D**) and 1 µm (**E** and **F**).

Not only the homogeneity of the sP(EO-*stat*-PO) coating, but also the sP(EO-*stat*-PO) layer thickness around PCL fibers, was of interest. To gain information about the sP(EO-*stat*-PO) layer thickness, PCL control and sP(EO-*stat*-PO) coated fibers were cut with a focused ion beam (FIB) tool equipped to the SEM device.

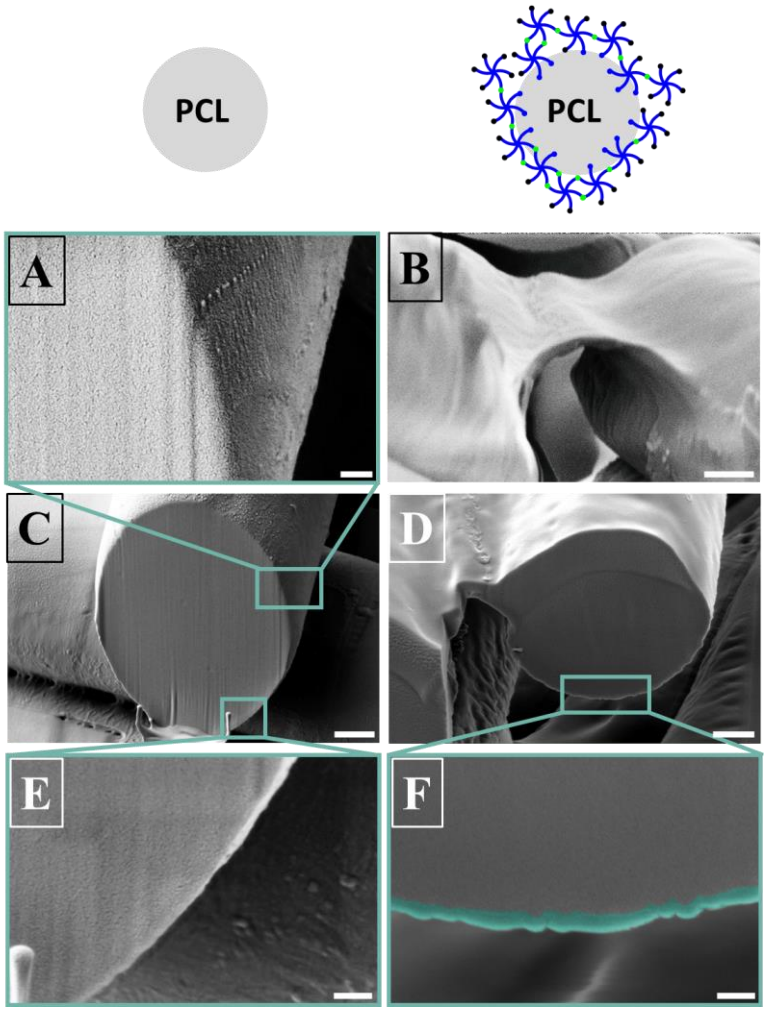


**Figure 16:** Representative SEM images of cut fibers from PCL control (**A**, **C** and **E**) and sP(EO-*stat*-PO) coated scaffolds (**B**, **D** and **F**). After aqueous pre-wetting, the scaffolds were pre-treated with 1 M NaOH for 5 min (**A** – **F**) and washed prior to sP(EO-*stat*-PO) coating with 2.0 wt.-% sP(EO-*stat*-PO) for 10 min for **B**, **D** and **F**. All samples were incubated in water overnight and washed with water prior to analyses. Dried scaffolds were cut with a Ga-beam (30 kV and beam currents of 10 – 50 pA). Insets display corresponding magnifications of the area of interest (turquoise). Scale bars represent 200 nm (**A**, **E** and **F**) and 1 µm (**B** – **D**).

PCL fibers (**Figure 16 A**, **C** and **E**) did not display any structures at the cutting edges compared to sP(EO-*stat*-PO) coated fibers (**Figure 16 D** and **F**) and suggested the structures on sP(EO-*stat*-PO) coated fibers not to derive from cutting artefacts. Hence, observable structures at the edges were correlated to the sP(EO-*stat*-PO) layer around the PCL fibers with an estimated hydrogel thickness of 100 nm (**Figure 16 F**, colored in turquoise). The sP(EO-*stat*-PO) layer thickness in between two adjacent fibers was determined to be around 240 nm (**Figure 16 B**). The herein obtained values for the sP(EO-*stat*-PO) hydrogel layer thickness are in accordance to sP(EO-*stat*-PO) spin coated glass

substrates.[65]

To additionally ensure the structures at the cutting edges not to derive from cutting artefacts, energy dispersive X-ray spectroscopy (EDX) was performed for PCL scaffolds, sP(EO-*stat*-PO) (2.0 wt.-%) and sP(EO-*stat*-PO) coated PCL scaffolds (2.0 wt.-% sP(EO-*stat*-PO)), 10 min). The elemental content of the fiber surfaces was analyzed, as the difference in nitrogen content of PCL and sP(EO-*stat*-PO) was hypothesized to allow distinguishing both polymers.

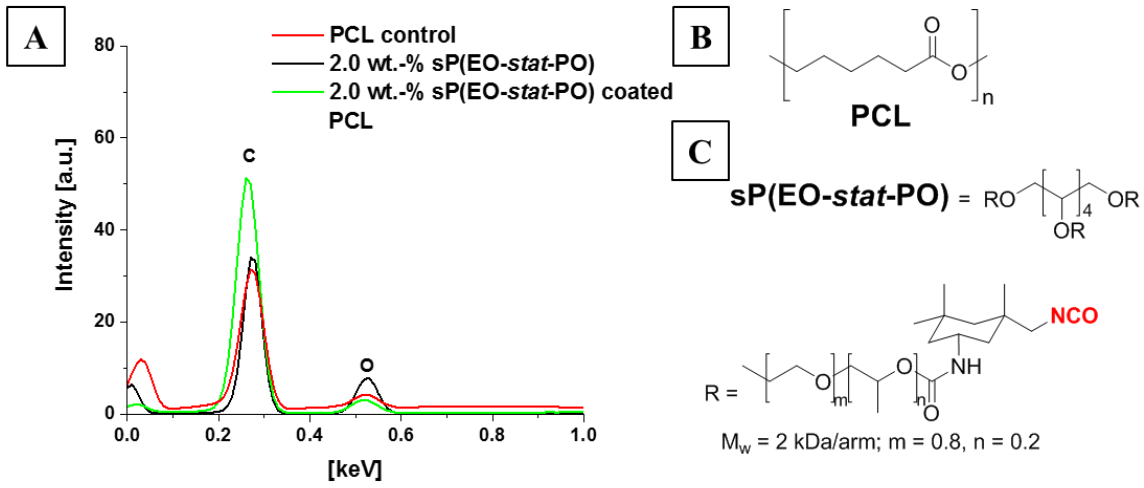


**Figure 17:** Representative EDX results for PCL scaffolds (red line), 2.0 wt.-% sP(EO-*stat*-PO) controls (black line) and sP(EO-*stat*-PO) coated scaffolds (2.0 wt.-% sP(EO-*stat*-PO)) (green line) (**A**). After aqueous pre-wetting, scaffolds were pre-treated with 1 M NaOH for 5 min and washed prior to sP(EO-*stat*-PO) coating with 2.0 wt.-% sP(EO-*stat*-PO) for 10 min. Scaffolds were incubated in water overnight and washed with water prior to analyses. Molecular structures of PCL (**B**) and sP(EO-*stat*-PO) (**C**).

As expected, carbon as well as oxygen were detectable for the samples without detectable differences in elemental compositions (**Figure 17 A**). Contrary to the expectations based on the elemental compositions of PCL (**Figure 17 B**) and sP(EO-*stat*-PO) (**Figure 17 C**), nitrogen was not detectable in the sP(EO-*stat*-PO) containing samples. Especially in the case of pure sP(EO-*stat*-PO), nitrogen detection was expected but the EDX detection limit of 0.1 wt.-% probably restricted this.[155] Moreover, the nitrogen peak is often overlapped by the carbon peak and common polymer compositions with high carbon- and oxygen- but rather low nitrogen-content further contribute to obstacles in nitrogen detection.[156] Hence, this method was suggested unsuitable to further support the sP(EO-*stat*-PO) layer thicknesses derived from SEM analysis.

To overcome the hurdles associated with EDX-based nitrogen detection, a barium iodide-polymer-complex-formation[157, 158] was tested. This complex-formation was already used to distinguish PEGylated from non-PEGylated proteins via SDS-PAGE analysis[159] and was also used to spectrophotometrically quantify the amounts of PEGylation.[160] It was of interest whether a selective barium iodide-polymer-complex-formation would occur and consequently would allow differentiation of PCL and sP(EO-*stat*-PO) via detection of barium and iodide. Therefore, a sP(EO-*stat*-PO) coated scaffold was exemplarily cut via FIB and analyzed with EDX.

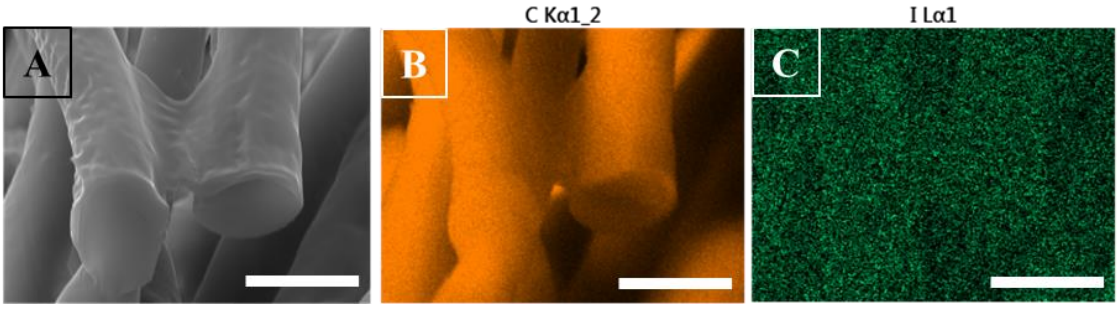


**Figure 18:** Representative SEM image of the cut region of sP(EO-*stat*-PO) coated PCL fibers depicting a visible sP(EO-*stat*-PO) layer in between two adjacent fibers (**A**). After aqueous pre-wetting, the scaffold was pre-treated with 1 M NaOH for 5 min and washed prior to sP(EO-*stat*-PO) coating with 2.0 wt.-% sP(EO-*stat*-PO) for 10 min. The scaffold was incubated in water overnight and washed with water prior to analyses. The sample was cut with a Ga-beam (30 kV and beam currents of 10 – 50 pA). Carbon (**B**) and iodide distribution (**C**) within this sample. Scale bars represent 5 µm.

The investigated cut fiber interface is depicted in **Figure 18 A**. As expected, the carbon distribution revealed no detectable differences among the polymers (**Figure 18 B**). Elemental mapping did not detect barium, however, iodide was evenly distributed within and around the fibers (**Figure 18 C**). These observations were correlated to an unsuccessful barium iodide-polymer-complex formation and thus unsuitable to distinguish between the polymers.

In addition to the sP(EO-*stat*-PO) layer thickness determination with SEM analysis, the amount of sP(EO-*stat*-PO) on coated PCL scaffolds was spectrophotometrically investigated. The trinitrobenzenesulfonic acid (TNBSA) assay was used to quantify sP(EO-*stat*-PO) on the scaffolds via the detection of primary amines as NCO-hydrolysis product of sP(EO-*stat*-PO). The sulfonic acid group of TNBSA as good leaving group enables a

nucleophilic substitution reaction on the tri-nitro functionalized and, hence, electron deficient aromatic ring. The colored trinitrophenyl derivative product can be quantified via its absorbance at 335 nm and correlated to the amine content of the sample (**Scheme 8**).

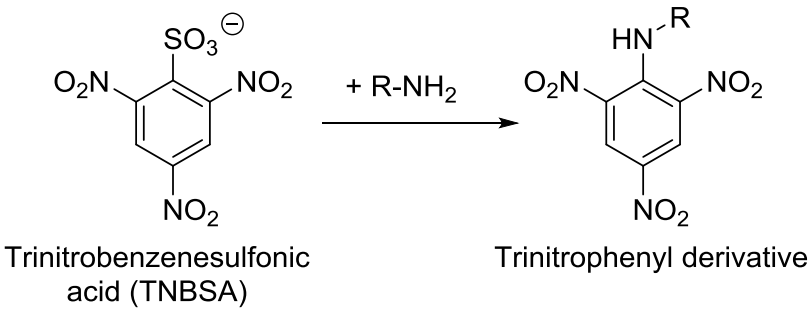


**Scheme 8:** Reaction of trinitrobenzenesulfonic acid (TNBSA) with primary amines to yield a colored trinitrophenyl derivative.

In order to spectrophotometrically quantify amines, solutions are required and therefore PCL and sP(EO-*stat*-PO) coated scaffolds were completely hydrolyzed with 6 M HCl (2 h, 65 °C). To distinguish between hydrolysis of NCO-groups and acid-induced scaffold hydrolysis, the latter is referred to as "acid-hydrolysis" and "acid-hydrolyzed".

For ethanolamine, as standard for amine quantification, common assay conditions with 0.1 M $NaHCO_3$ were compared to pre-treatments with harsh acidic conditions to ensure correct amine quantifications under these conditions.

**Table 2:** Representative TNBSA assay results for ethanolamine which was either treated with a pre-treatment with 6 M HCl at 65 °C for 2 h or under common TNBSA assay conditions with 0.1 M $NaHCO_3$, RT and pH 8.5. The slope and intercept were determined by linear regression.

| Treatment | Slope | Intercept |
|---|---|---|
| 0.1 M $NaHCO_3$, RT, pH 8.5 | 2.5 | 0.016 |
| 6 M HCl, 65 °C, 2 h | 2.1 | 0.044 |

The slope and intercept values, which were derived from the linear regression, were in similar ranges independent on different treatments (**Table 2**). This ruled out possible influences on the amine quantification arising from harsh acidic pre-treatments.

Ethanolamine was not used to indirectly quantify sP(EO-*stat*-PO) based on the amine amount. The indirect correlation was suggested unsuitable as the sP(EO-*stat*-PO) crosslinking density may cover a broad and unknown range that influences the quantities of amines per sP(EO-*stat*-PO) molecules, as exemplarily depicted in **Figure 19**.

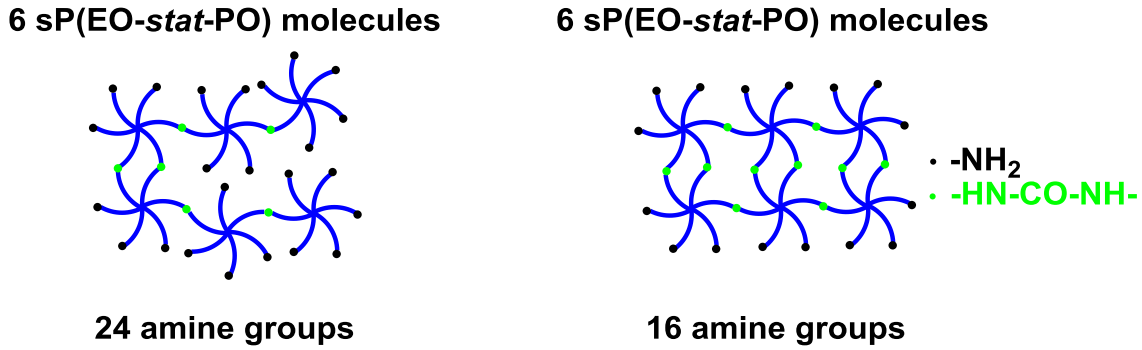


**Figure 19:** Schematic representation of different crosslinking densities of sP(EO-*stat*-PO) molecules and the effect on the amine content.

To quantify the amount of sP(EO-*stat*-PO) on coated scaffolds, scaffold-free sP(EO-*stat*-PO) solutions served as calibration standards. Therefore, different concentrations of coating solutions were allowed to hydrolyze overnight and were subsequently acid-hydrolyzed with 6 M HCl prior to the TNBSA assay (**Figure 20**).

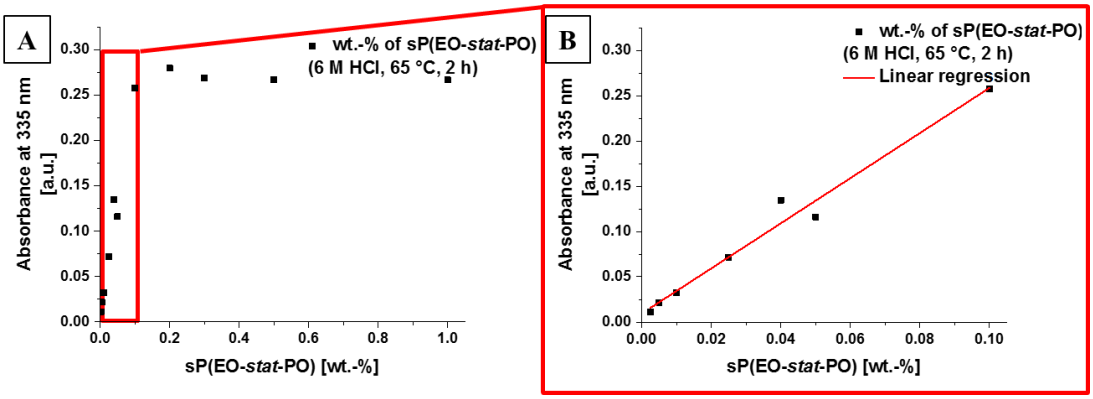


**Figure 20:** Representative correlation of the absorbance at 335 nm to different concentrations of sP(EO-*stat*-PO) (0.0025 – 1.0 wt.-%) as result of the TNBSA assay (**A**) and the inset displays the linear dependent region from 0.0025 – 0.1 wt.-% sP(EO-*stat*-PO) (**B**). After an overnight incubation in water the sP(EO-*stat*-PO) solutions were acid-hydrolyzed with 6 M HCl at 65 °C prior to the TNBSA assay procedure.

Concentrations above 0.1 wt.-% sP(EO-*stat*-PO) reached an absorbance plateau (**Figure 20 A**), suggesting the upper assay detection limit for the herein used TNBSA concentration. Thus, the linear dependent region in the range of 0.0025 – 0.1 wt.-% sP(EO-*stat*-PO) was used for calibration purposes (**Figure 20 B**). The hereby obtained slope was 2.5 and the intercept 0.01 and were both comparable to the ethanolamine calibration (compare **Table 2**).

To analyze whether prolonged sP(EO-*stat*-PO) coating times would increase sP(EO-*stat*-PO) amounts on the scaffolds, two different coating times (10 min and overnight) were compared and PCL scaffolds were included as controls. Both sP(EO-*stat*-PO) coated samples were allowed to completely hydrolyze overnight prior to acid-hydrolysis. Results for the amine and sP(EO-*stat*-PO) content on coated scaffolds is given in **Table 3**.

**Table 3:** TNBSA assay results for PCL control and sP(EO-*stat*-PO) coated scaffolds (10 min or overnight sP(EO-*stat*-PO) coating). The amine content was obtained from the ethanolamine calibration, whereas the sP(EO-*stat*-PO) content of coated scaffolds was derived from the sP(EO-*stat*-PO) calibration.

| **Samples** | **Amine content [µmol mL$^{-1}$]** | **sP(EO-*stat*-PO) [µmol mL$^{-1}$]** |
|---|---|---|
| PCL scaffold | not detectable | not detectable |
| sP(EO-*stat*-PO) coated scaffold (10 min) | 0.32 ± 0.08 | 0.11 ± 0.021 |
| sP(EO-*stat*-PO) coated scaffold (overnight) | 0.19 ± 0.003 | 0.07 ± 0.001 |

As expected, PCL controls did neither contain detectable amounts of amines nor of sP(EO-*stat*-PO) (**Table 3**). Interestingly, shorter coated scaffolds (10 min) displayed higher amounts of amines (0.32 µmol mL$^{-1}$) and sP(EO-*stat*-PO) (0.11 µmol mL$^{-1}$) as compared to the overnight sP(EO-*stat*-PO) coating with 0.19 µmol mL$^{-1}$ amines and 0.07 µmol mL$^{-1}$ sP(EO-*stat*-PO).

For the short incubation, the sP(EO-*stat*-PO) solution is removed after 10 min and replaced by water which removes unbound sP(EO-*stat*-PO) and dilutes the remaining solution, thereby further reducing the probability of urea bridge formations inter- and intra-molecularly. This could account for an overall higher detected sP(EO-*stat*-PO) amount for 10 min coating times, since the less NCO-groups are used for crosslinking, the higher the number of NCO-groups that hydrolyze. The overnight sP(EO-*stat*-PO) coating was not further diluted and the probability of forming highly urea crosslinked networks was

increased and in turn decreases the amount of detectable amines and sP(EO-*stat*-PO).

For both sP(EO-*stat*-PO) coated scaffolds the TNBSA results suggest approximately three amine groups per sP(EO-*stat*-PO) molecule as obtained by correlating amine content to sP(EO-*stat*-PO) content, which is in good accordance to previous findings.[161] These results indicate the top layer of sP(EO-*stat*-PO) to consist of molecules for which three star-arms are inter- or intramolecularly crosslinked, while the other three star-arms remain uncrosslinked. Hence, approximately three NCO-groups per sP(EO-*stat*-PO) molecule could be later used for biofunctionalization on coated scaffolds. Furthermore, the long coating duration is unsuitable to biofunctionalize sP(EO-*stat*-PO) layers around PCL fibers via NCO-groups as it was already proven with previous IR experiments that these groups are completely hydrolyzed to amines after 24 h. This coating duration was consequently neglected in the following experiments.

### 3.1.2. Biofunctionalization via NCO-groups

Biofunctionalizations of sP(EO-*stat*-PO) coated scaffolds were based on the reaction of sP(EO-*stat*-PO)-NCO-groups with suitable moieties of the coupling molecules. Functionalities therefore are e.g. amines or alcohols.[65, 72-74] The biofunctionalization via sP(EO-*stat*-PO)-NCO-groups was first evaluated with model substances for low and high molecular weight components. As low molecular weight component biocytin was chosen and Alexa Fluor™ 647 labelled streptavidin (AFSA) for high molecular weight components.

#### 3.1.2.1. Biofunctionalization with biocytin

Biotin (**Scheme 9 A**) could not be used as a model substance due to the lack of suitable NCO-reactive groups, whereas biocytin (**Scheme 9 B**) is an amide derived form of lysine coupled to biotin and already used for biofunctionalizations.[71, 162]

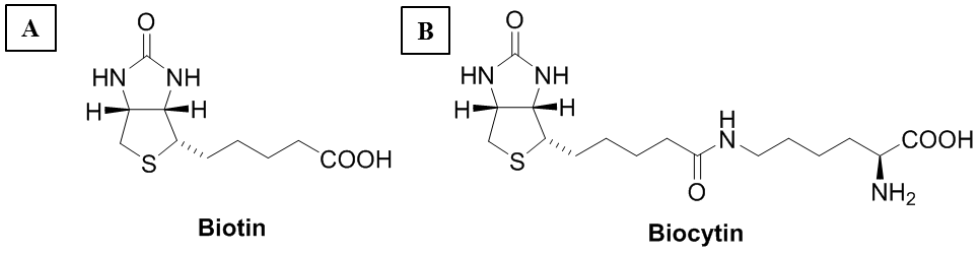


**Scheme 9:** Molecular structures of biotin (**A**) and biocytin (**B**).

The ease of detection via fluorescently labelled streptavidin[71] and the suitable NCO-reactive primary amine, render biocytin a reasonable model substance. Streptavidin (SA) can bind simultaneously up to four biotin molecules due to the tetrameric quaternary structure of SA, and the resulting streptavidin-biotin bond is acknowledged as one of the strongest non-covalent biological bindings.[163-165] Similarly biocytin can be bound from SA and enables the visualization of biocytin biofunctionalization on sP(EO-*stat*-PO) coated scaffolds via fluorescently labelled streptavidin.

The general workflow for the biofunctionalization of sP(EO-*stat*-PO) coated scaffolds with biocytin and the subsequent visualization with AFSA is depicted in **Figure 21**.
After pre-treating PCL scaffolds as previously described, the sP(EO-*stat*-PO) coating was conducted for 10 min. Afterwards sP(EO-*stat*-PO) solutions were replaced by distinct concentrated biocytin solutions ($5.37 \times 10^{-7}$ mol, $2.68 \times 10^{-6}$ mol and $1.34 \times 10^{-5}$ mol in PBS) and incubated overnight. Scaffolds were extensively washed and incubated in an AFSA solution overnight for visualization of adsorbed or bound biocytin. For simplification AFSA is displayed with only one binding site for biotin/biocytin. Comparably diluted AFSA solutions ($1.67 \times 10^{-10}$ mol in PBS) were used due to the aforementioned high affinity of streptavidin to biotin/biocytin. The scaffolds were finally washed and analyzed with fluorescence microscopy. Equal exposure times were used to enable qualitative comparisons.
PCL and NCO-hydrolyzed sP(EO-*stat*-PO) coated scaffolds were included as controls to firstly evaluate possible interferences arising from unspecifically adsorbed biocytin. Therefore, the controls were incubated in biocytin solutions and subsequently treated equal to the biofunctionalization approach. These controls are termed “treated scaffolds” in the context of this study, whereas the biofunctionalization is referred to as “functionalized sP(EO-*stat*-PO) scaffolds”. These terms also apply to controls and biofunctionalizations with other molecules.

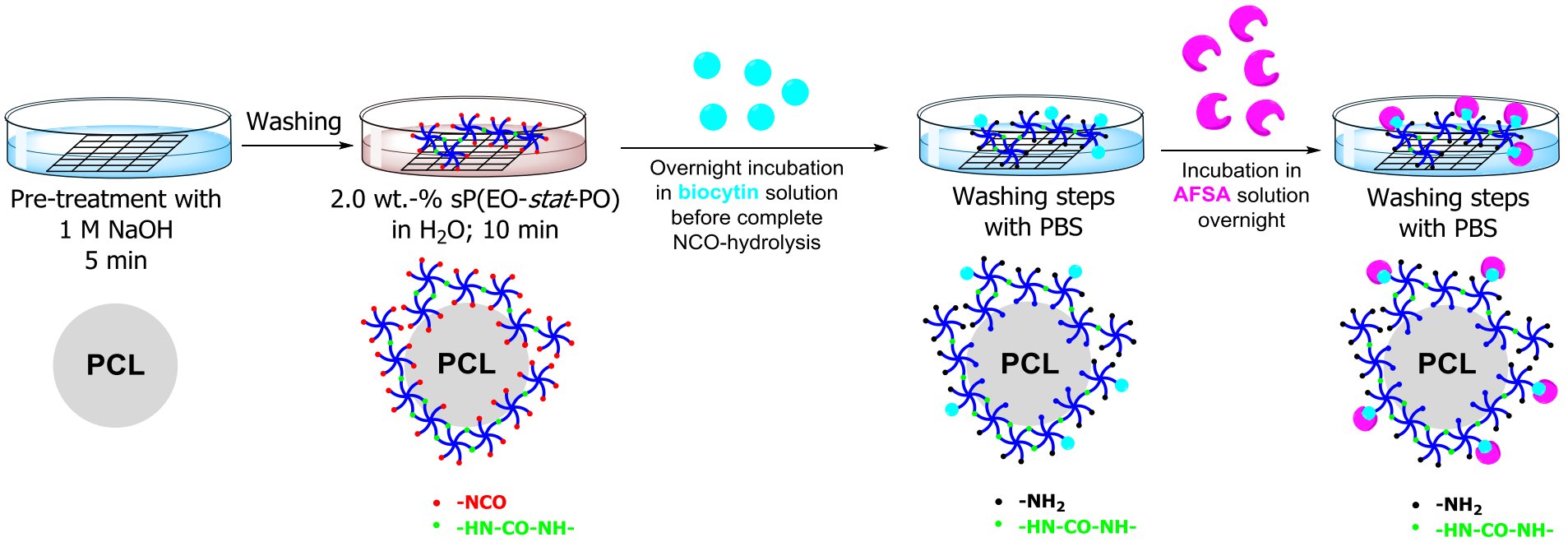


**Figure 21:** Workflow for the biofunctionalization of sP(EO-*stat*-PO) coated scaffolds with biocytin based upon the reaction with sP(EO-*stat*-PO)-NCO-groups. Aqueous pre-wetting of scaffolds (not depicted) was followed by an alkaline pre-treatment with 1 M NaOH for 5 min and subsequent washing steps. Aqueous sP(EO-*stat*-PO) solutions (2.0 wt.-%, 1.67 x $10^{-6}$ mol sP(EO-*stat*-PO), 1.0 x $10^{-5}$ mol NCO) were used to coat scaffolds for 10 min. Biocytin solutions with different concentrations ranging from 5.37 x $10^{-7}$ mol, 2.68 x $10^{-6}$ mol to 1.34 x $10^{-5}$ mol in PBS replaced the sP(EO-*stat*-PO) solution after 10 min for an overnight incubation. After washing with PBS, AFSA solutions (1.67 x $10^{-10}$ mol in PBS) were added for an overnight incubation. Prior to analyses the scaffolds were intensively washed with PBS.

For biocytin treated PCL (**Figure 22 A**, **C** and **E**) and biocytin treated NCO-hydrolyzed sP(EO-*stat*-PO) coated scaffolds (**Figure 22 B**, **D** and **F**) no fluorescence was detectable regardless of the applied biocytin amounts, suggesting that neither biocytin nor AFSA were unspecifically adsorbed. This ensured the following biofunctionalization experiments to be selectively occurring as a result of the reaction between amine groups of biocytin and sP(EO-*stat*-PO)-NCO-groups.

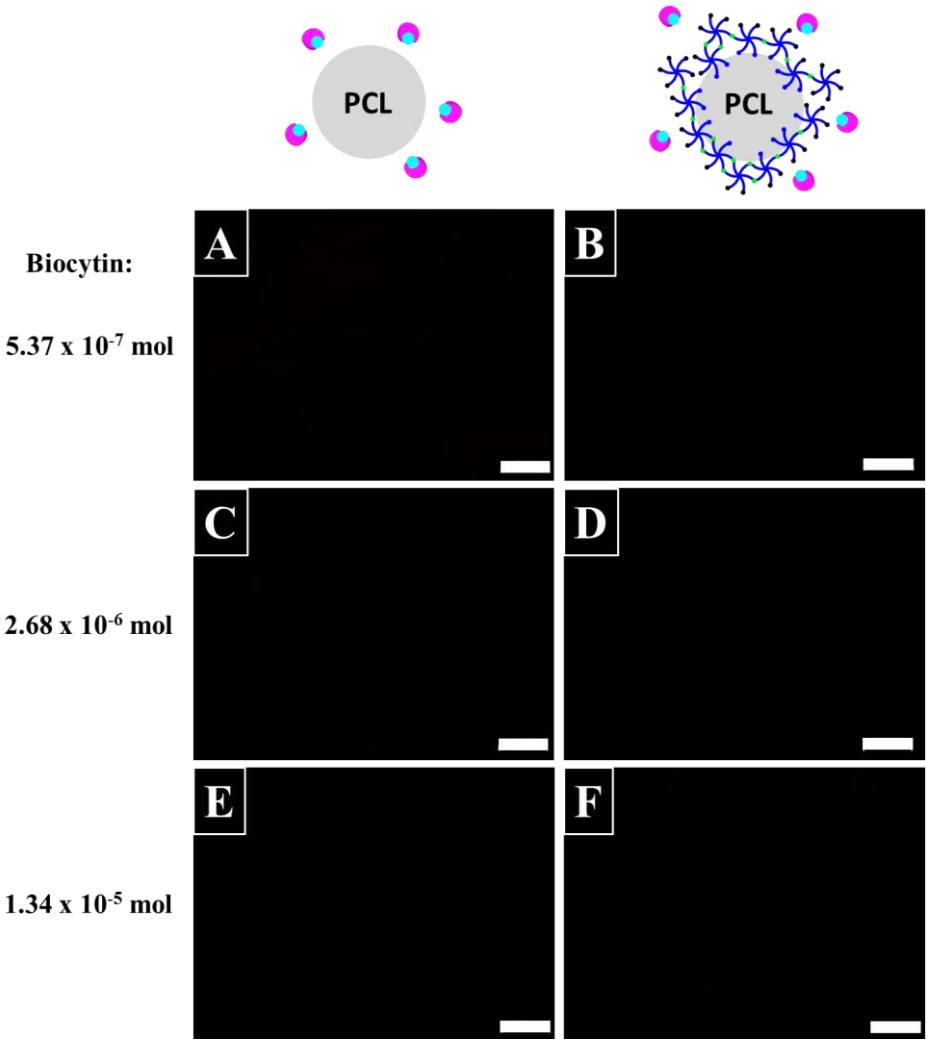


**Figure 22:** Representative fluorescence images of biocytin treated PCL control (**A**, **C** and **E**) and biocytin treated NCO-hydrolyzed sP(EO-*stat*-PO) coated scaffolds (**B**, **D** and **F**). After aqueous pre-wetting, the pre-treatment of scaffolds was performed with 1 M NaOH for 5 min prior to washing the scaffolds (**A** – **F**). Different concentrations of biocytin were then applied (5.37 x $10^{-7}$ mol in **A** and **B**, 2.68 x $10^{-6}$ mol in **C** and **D**; and 1.34 x $10^{-5}$ mol in **E** and **F**; all in PBS) and replaced the sP(EO-*stat*-PO) solution (2.0 wt.-%, 10 min) after an aqueous overnight incubation (**B**, **D** and **F**). After overnight incubation in biocytin solutions, the scaffolds were washed with PBS and incubated in AFSA (1.67 x $10^{-10}$ mol in PBS) overnight. Prior to analysis the scaffolds were washed with PBS. Exposure times of 4 ms and the scale bars represent 100 µm.

The biofunctionalization with biocytin via NCO-groups of sP(EO-*stat*-PO) coated scaffolds was successful and could be visualized with AFSA, as proven by the fluorescence for all samples in **Figure 23**. It seemed that with increasing biocytin concentrations from 5.37 x $10^{-7}$ mol (**Figure 23 A**) to 2.68 x $10^{-6}$ mol (**Figure 23 B**) and 1.34 x $10^{-5}$ mol (**Figure 23 C**) the fluorescence concurrently increased. Quantification based only upon fluorescence images remains a hurdle, hence, only qualitative conclusions about the efficacy of biocytin biofunctionalization in dependence on biocytin concentrations were drawn.

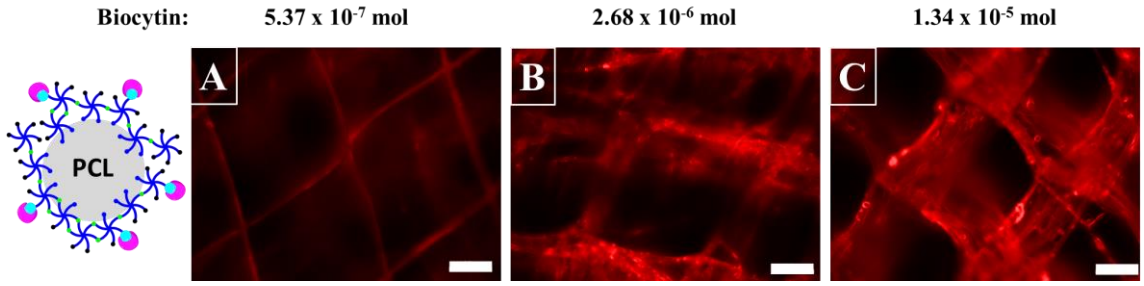


**Figure 23:** Representative fluorescence images of biocytin functionalized sP(EO-*stat*-PO) coated scaffolds. After aqueous pre-wetting, the pre-treatment of scaffolds with 1 M NaOH for 5 min followed, the scaffolds were washed and the sP(EO-*stat*-PO) coating was performed (2.0 wt.-% sP(EO-*stat*-PO), 10 min) and the solution was replaced by different concentrations of biocytin (5.37 x $10^{-7}$ mol in **A**, 2.68 x $10^{-6}$ mol in **B** and 1.34 x $10^{-5}$ mol in **C** in PBS) for an overnight incubation. After washing with PBS, visualization of bound biocytin was achieved by incubating the samples overnight in AFSA solutions (1.67 x $10^{-10}$ mol in PBS). Prior to analysis the scaffolds were washed with PBS. Exposure times of 4 ms and the scale bars represent 100 µm.

IR spectroscopy was conducted with biocytin functionalized sP(EO-*stat*-PO) coated scaffolds and NCO-hydrolyzed sP(EO-*stat*-PO) coated scaffolds to further underline the successful modification. Therefore the scaffolds were completely dried prior to analyses and the spectra were normalized to the carbonyl peak at 1720 $cm^{-1}$.

Even for the highest biocytin amount of 1.34 x $10^{-5}$ mol, no differences between IR spectra of NCO-hydrolyzed sP(EO-*stat*-PO) coated scaffolds (**Figure 24**, black line) and biocytin functionalized sP(EO-*stat*-PO) coated scaffolds (**Figure 24**, red line) were observable and IR spectroscopy could not be used to further support the success of this biofunctionalization.

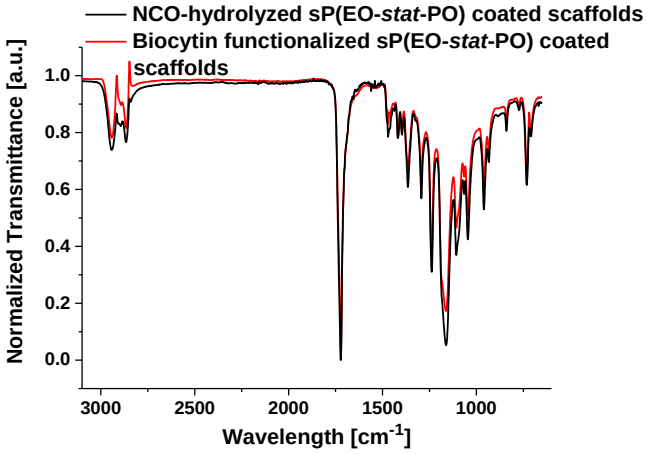


**Figure 24:** Representative IR spectra of NCO-hydrolyzed sP(EO-*stat*-PO) coated scaffolds (black line) and biocytin functionalized sP(EO-*stat*-PO) coated scaffolds (red line). After aqueous pre-wetting, the pre-treatment of scaffolds with 1 M NaOH (5 min), washing of scaffolds and the sP(EO-*stat*-PO) coating followed (2.0 wt.-% sP(EO-*stat*-PO), 10 min). For biocytin functionalized sP(EO-*stat*-PO) coated scaffolds the solutions were replaced by the highest biocytin concentration (1.34 x $10^{-5}$ mol in PBS) for an overnight incubation. Prior to IR analyses the scaffolds were washed with PBS. Spectra were normalized to the carbonyl peak at 1720 $cm^{-1}$.

### 3.1.2.2. Biofunctionalization with streptavidin

To further determine whether high molecular weight components, such as AFSA, could directly be incorporated via sP(EO-*stat*-PO)-NCO-functionalities, the same experimental setup as for biocytin functionalization of sP(EO-*stat*-PO) coated scaffolds was used. Identical controls, namely PCL and NCO-hydrolyzed sP(EO-*stat*-PO) coated scaffolds, were included to ensure the selective AFSA functionalization.

The general workflow for the biofunctionalization of sP(EO-*stat*-PO) coated scaffolds with AFSA is demonstrated in **Figure 25**.

After pre-treating the PCL scaffolds as already described, the sP(EO-*stat*-PO) coating was conducted for 10 min. Then sP(EO-*stat*-PO) solutions were replaced by AFSA (1.67 x $10^{-10}$ mol in PBS) and incubated overnight. After intensive washing steps, the analysis with fluorescence microscopy was conducted. Equal exposure times ensured the qualitative comparison within the following experiments.

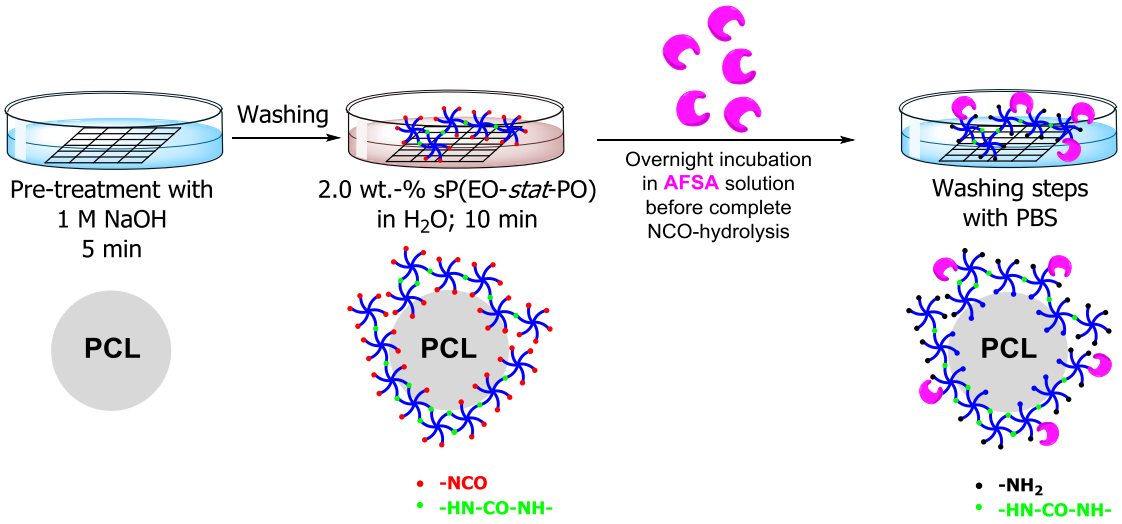


**Figure 25:** AFSA biofunctionalization workflow for sP(EO-*stat*-PO) coated scaffolds based upon the reaction with sP(EO-*stat*-PO)-NCO-groups. Aqueous pre-wetting of scaffolds (not depicted) was followed by a pre-treamtnet with 1 M NaOH for 5 min and subsequent washing steps. Aqueous sP(EO-*stat*-PO) solutions (2.0 wt.-%, 1.67 x $10^{-6}$ mol sP(EO-*stat*-PO), 1.0 x $10^{-5}$ mol NCO) were used to coat scaffolds for 10 min. AFSA solutions (1.67 x $10^{-10}$ mol in PBS) were added after 10 min for an overnight incubation. Prior to analysis the scaffolds were intensively washed with PBS.

The results for AFSA treated PCL and AFSA treated NCO-hydrolyzed sP(EO-*stat*-PO) coated scaffolds together with AFSA functionalized sP(EO-*stat*-PO) coated scaffolds are depicted in **Figure 26**.

AFSA was neither adsorbed to AFSA treated PCL controls (**Figure 26 A**) nor to AFSA treated NCO-hydrolyzed sP(EO-*stat*-PO) coated scaffolds (**Figure 26 B**) as proven by the absence of any fluorescence. Moreover, the biofunctionalization of sP(EO-*stat*-PO) coated scaffolds with AFSA via sP(EO-*stat*-PO)-NCO-groups was unsuccessful (**Figure 26 C**). This could be explained by the sterically relative high demand of AFSA (~ 60 kDa) together with a rather complex amino acid composition[165] rendering the biofunctionalization not as straight forward as for biocytin.

Whereas AFSA was not adsorbed on PCL, TRBSA was adsorbed as already proven via the protein adsorption experiments. This could be explained by the well-known unspecific binding properties of BSA which accounts for its use as blocking substance for immunoassays.[166, 167] Streptavidin on the other hand possesses more restricted specific binding properties.[163-165]

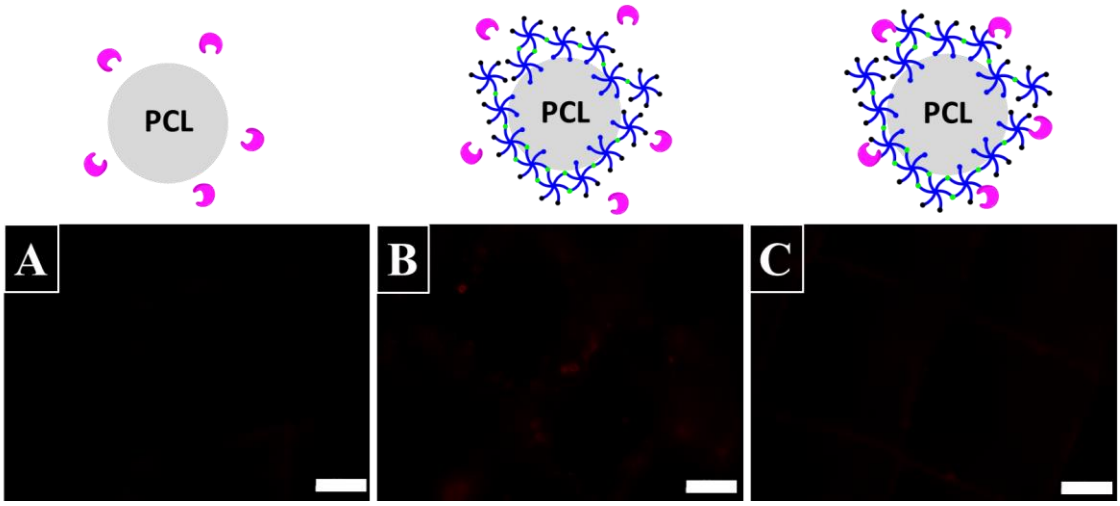


**Figure 26:** Representative fluorescence images of AFSA treated PCL control (**A**), AFSA treated NCO-hydrolyzed sP(EO-*stat*-PO) coated scaffolds (**B**) and AFSA functionalized sP(EO-*stat*-PO) coated scaffolds (**C**). After aqueous pre-wetting, the pre-treatment of scaffolds with 1 M NaOH for 5 min (**A** – **C**) followed, prior to washing the scaffolds and the sP(EO-*stat*-PO) coating (2.0 wt.-% sP(EO-*stat*-PO)) for 10 min (**B** and **C**). AFSA solutions (1.67 x $10^{-10}$ mol in PBS) replaced the sP(EO-*stat*-PO) solutions after 10 min (**C**) or after an overnight incubation in water (**B**) for an overnight incubation (**A** – **C**). Prior to analysis the scaffolds were washed with PBS. Exposure times of 44 ms and the scale bars represent 100 µm.

### 3.1.3. Photo-induced streptavidin biofunctionalization

The successful immobilization of low molecular weight components via the reaction between primary amines and sP(EO-*stat*-PO)-NCO-groups was successful but unsuitable for higher molecular weight molecules. To allow biofunctionalization of sP(EO-*stat*-PO) coated scaffolds with more complex substances, an alternative approach with diazirine bearing components was developed. The latter moieties were hypothesized to enable a pH independent photo-induced covalent biofunctionalization of sP(EO-*stat*-PO) coated scaffolds. Additionally, this photoreaction enables the decoupling of the biofunctionalization from the limited time frame associated with biofunctionalization via NCO-groups.

Photoleucine was chosen as diazirine bearing model component as it possesses a NCO-reactive amine group, which is crucial for biofunctionalization of sP(EO-*stat*-PO) coated scaffolds. The photo-induced modification of sP(EO-*stat*-PO) coated scaffolds is based upon a pH independent, yet unspecific, photolysis of diazirine moieties[168-173] and is schematically represented in **Scheme 10**.

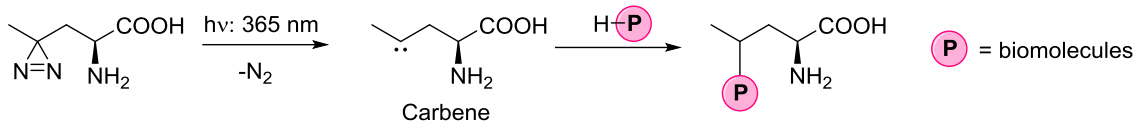


**Scheme 10:** Photolysis of photoleucines diazirine group into carbene and $N_2$ upon UV-irradiation at 365 nm and the subsequent coupling of biomolecules.

Diazirines decompose into $N_2$ and highly reactive carbenes upon UV-irradiation at 365 nm. These carbenes can then couple to e.g. peptides or proteins via covalent C-C, C-H and O-H bond insertions (**Scheme 10**).[168-173] The advantages of this system are based upon the lack of any required functional groups of the to-be-coupled molecules and the pH independency. The general workflow for the biofunctionalization of sP(EO-*stat*-PO) coated scaffolds with photoleucine is depicted in **Figure 27**. Pre-treatment of the scaffolds was conducted as previously described and followed by the sP(EO-*stat*-PO) coating for 10 min. SP(EO-*stat*-PO) solutions were replaced by photoleucine ($1.34 \times 10^{-5}$ mol in PBS) after 10 min and incubated overnight. After washing the scaffolds an incubation in AFSA ($1.67 \times 10^{-10}$ mol) followed in which the scaffolds were irradiated (30 min, 365 nm) to allow to visualized bound photoleucine. The pH independency of the photoreaction was assessed with neutral (PBS) or acidified (0.5 M HAc) AFSA solutions. Finally, the scaffolds were washed and analyzed with fluorescence microscopy at constant exposure times.

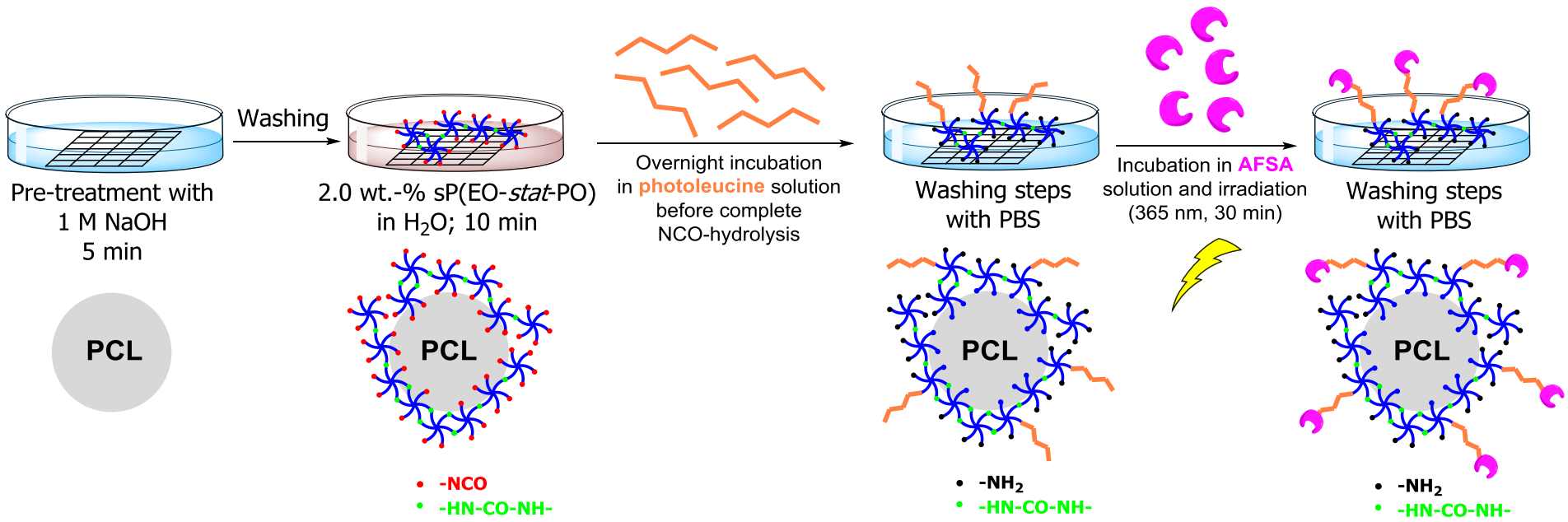


**Figure 27:** Workflow for the biofunctionalization of sP(EO-*stat*-PO) coated scaffolds with photoleucine based upon the reaction with sP(EO-*stat*-PO)-NCO-groups. The subsequent photoreaction is used to enable the covalent incorporation of AFSA. Aqueous pre-wetting of scaffolds (not depicted) was followed by an alkaline pre-treatment with 1 M NaOH for 5 min and subsequent washing steps. Aqueous sP(EO-*stat*-PO) solutions (2.0 wt.-%, 1.67 x $10^{-6}$ mol, 1 x $10^{-5}$ mol NCO) were used to coat scaffolds for 10 min. Photoleucine solutions (1.34 x $10^{-5}$ mol in PBS) replaced the sP(EO-*stat*-PO) solution after 10 min for an overnight incubation. After washing with PBS, AFSA solutions (1.67 x $10^{-10}$ mol in PBS or 0.5 M HAc) were added and the irradiation was performed for 30 min at 365 nm. Prior to analysis the scaffolds were intensively washed with PBS.

The 30 min irradiation of diazirines was performed based on results obtained by Susanne Feineis (doctoral thesis at the Department for Functional Materials in Medicine and Dentistry at the University of Würzburg). To detect the photobleaching scaffold-free neutral and acidified AFSA solutions ($1.67 \times 10^{-10}$ mol in PBS or 0.5 M HAc) were irradiated for different times (0 min, 15 min and 30 min) and correlated to the fluorescence signal at 665 nm, which represents the emission wavelength of Alexa Fluor™ 647.

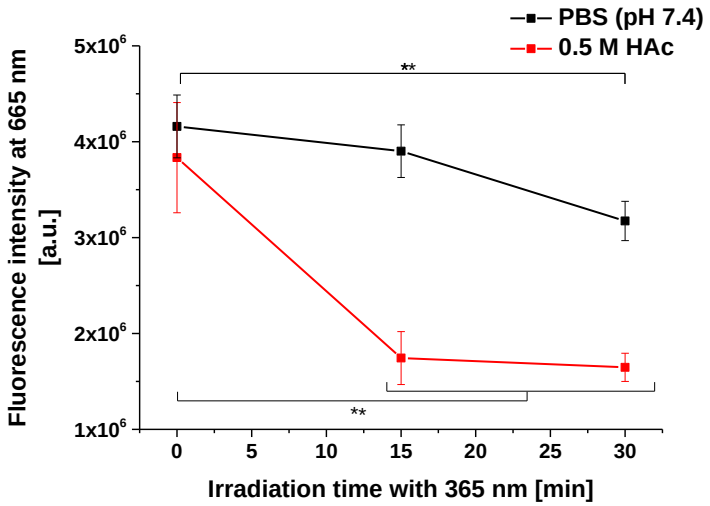


**Figure 28:** Correlation of the fluorescence signal intensity at 665 nm to the irradiation time at 365 nm of neutral (PBS; black dots) and acidified (0.5 M HAc; red dots) AFSA solutions ($1.67 \times 10^{-10}$ mol).

Slightly lower initial fluorescence intensities were found for acidified AFSA solutions (**Figure 28**, red line) than for neutral conditions (**Figure 28**, black line). The photobleaching was more pronounced for acidic conditions and significantly decreased within the first 15 min. Prolonged irradiations only slightly further decreased the fluorescence intensities. Protonation of Alexa Flour™ 647 and the reconfiguration of the fluorophores´ π-electron system were hypothesized to account for decreased fluorescence intensities. Additionally the acidic conditions could probably also induce the hydrolysis of the amide bond between streptavidin and Alexa Fluor™ 647[174] resulting in lower fluorescence quantum yields (**Scheme 11**). It has to be considered that for later visualization of AFSA on the scaffolds, this hydrolysis could eventually result in fluorophore removal which further decreases the detectable fluorescence and circumvents the possibility to draw conclusions about the efficacy of AFSA scaffold functionalization in pH dependency.

Within the following experiments the exposure times for the fluorescence microscopic analyses were increased to 44 ms due to the photobleaching of AFSA during the irradiation.

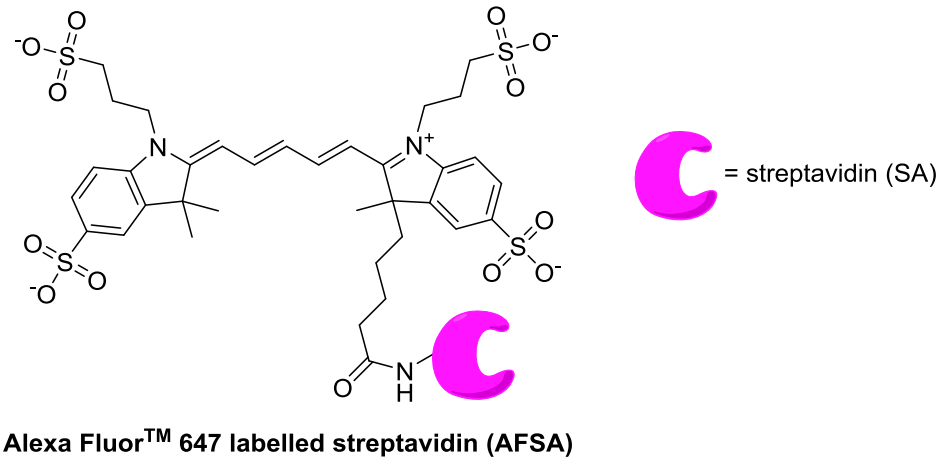


**Alexa Fluor™ 647 labelled streptavidin (AFSA)**

**Scheme 11:** Molecular structure of Alexa Fluor™ 647 conjugated to streptavidin (AFSA). Streptavidin (SA) is schematically represented in magenta with one binding site for biotin/biocytin.

To ensure no interferences from adsorbed photoleucine, photoleucine treated PCL scaffolds were included as controls. After this incubation the PCL scaffolds were washed and irradiated for 30 min at 365 nm in neutral (PBS) or acidified (0.5 M HAc) AFSA solutions with $1.67 \times 10^{-10}$ mol. To additionally exclude unspecific adsorption from AFSA to photoleucine functionalized sP(EO-*stat*-PO) coated scaffolds, these scaffolds were incubated in neutral and acidified AFSA solutions but not irradiated and are termed "AFSA treated photoleucine functionalized sP(EO-*stat*-PO) coated scaffolds".

No fluorescence was detectable for photoleucine treated PCL controls after irradiation in neutral (**Figure 29 A**) or acidified AFSA solutions (**Figure 29 B**). This suggested that photoleucine and AFSA were not adsorbed onto PCL scaffolds.
AFSA treated photoleucine functionalized sP(EO-*stat*-PO) coated scaffolds also displayed no fluorescence for neutral (**Figure 29 C**) or acidic conditions (**Figure 29 D**) implying that AFSA was not unspecifically adsorbed on these scaffolds.

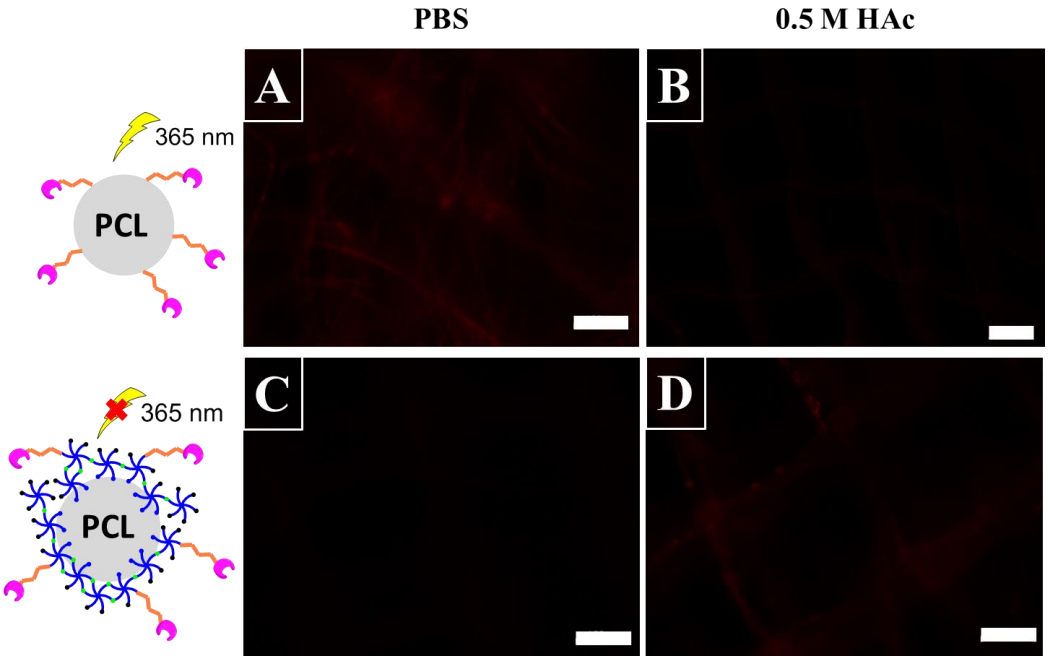


**Figure 29:** Representative fluorescence images of photoleucine treated PCL controls followed by the irradiation for 30 min at 365 nm in neutral (**A**) or acidic AFSA solutions (**B**). AFSA treated photoleucine functionalized sP(EO-*stat*-PO) coated controls without irradiation in neutral (**C**) or acidic AFSA solutions (**D**). After aqueous pre-wetting, the pre-treatment of all scaffolds with 1 M NaOH for 5 min and washing of scaffolds followed. SP(EO-*stat*-PO) coating was performed with 2.0 wt.-% sP(EO-*stat*-PO) for 10 min (**C** and **D**). Photoleucine solutions (1.34 x $10^{-5}$ mol in PBS) were applied on PCL scaffolds (**A** and **B**) or replaced sP(EO-*stat*-PO) solutions after 10 min (**C** and **D**) for an overnight incubation. Finally the scaffolds were washed with PBS and incubated in AFSA with 1.67 x $10^{-10}$ mol in PBS (**A** and **C**) or in 0.5 M HAc (**B** and **D**). Irradiation was performed at 365 nm for 30 min (**A** and **B**). Prior to analysis the scaffolds were washed with PBS. Exposure times of 44 ms and the scale bars represent 100 µm.

Positive controls for AFSA functionalized sP(EO-*stat*-PO) coated scaffolds were conducted as previously described and schematically presented in **Figure 27**.

Successful biofunctionalization of sP(EO-*stat*-PO) coated scaffolds with photoleucine were indirectly proven via visualization with AFSA, as demonstrated by detectable fluorescence signals in **Figure 30**. Moreover, the pH independency of this photoreaction was proven for pH 7.4 (**Figure 30 A**) and for pH 2.5 with 0.5 M HAc (**Figure 30 B**). Although both samples seemed to display comparable fluorescence intensities, no conclusions about the efficacy of the photoreaction in pH dependency were drawn due to the aforementioned enhanced photobleaching of AFSA under acidic conditions.

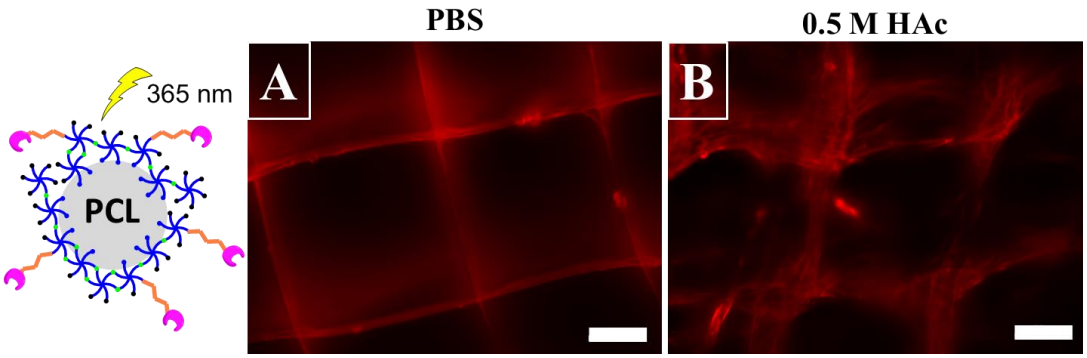


**Figure 30:** Representative fluorescence images of the irradiation for 30 min at 365 nm of photoleucine functionalized sP(EO-*stat*-PO) coated scaffolds in neutral (**A**) or acidic AFSA solutions (**B**). After aqueous pre-wetting, the pre-treatment of PCL scaffolds with 1 M NaOH for 5 min and washing of scaffolds followed, prior to sP(EO-*stat*-PO) coating (2.0 wt.-% sP(EO-*stat*-PO), 10 min). Photoleucine solutions ($1.34 \times 10^{-5}$ mol in PBS) replaced the sP(EO-*stat*-PO) solutions after 10 min for an overnight incubation. The scaffolds were washed with PBS, incubated in AFSA solutions ($1.67 \times 10^{-10}$ mol in PBS in **A** or in 0.5 M HAc in **B**) and irradiated (365 nm, 30 min). Prior to analysis the scaffolds were washed with PBS. Exposure times of 44 ms and the scale bars represent 100 µm.

Though relatively diluted AFSA concentrations were used, the protein was successfully incorporated to photoleucine functionalized sP(EO-*stat*-PO) coated scaffolds. This was not possible in case of the AFSA functionalization of sP(EO-*stat*-PO) coated scaffolds via sP(EO-*stat*-PO)-NCO-groups. Thus, the photoreaction provides an alternative to biofunctionalize sP(EO-*stat*-PO) coated scaffolds with minimal required protein concentrations independent on pH values. These AFSA functionalized sP(EO-*stat*-PO) coated scaffolds demonstrate the successful decoupling of the biofunctionalization from the limited time frame of NCO-presence and could furthermore be used as a versatile platform to bind any biotinylated molecule.

### 3.1.4. Photo-induced collagen biofunctionalization

Based upon photoleucine functionalized sP(EO-*stat*-PO) coated scaffolds, the time and pH independent biofunctionalization with AFSA at pH 2.5 and pH 7.4 was enabled. These scaffolds potentially also allow the incorporation of other coupling substances, which specifically require acidified conditions, such as collagen type I.

Collagen type I was chosen as biofunctionalization agent for photoleucine functionalized sP(EO-*stat*-PO) coated scaffolds in order to allow the investigation of cell adhesion. Generally, cell adhesion is mediated either via cellular integrins and the recognition of e.g.

arginine-glycine-aspartic acid (RGD) sequences[56, 175] or via discoidin domain receptors (DDR) upon collagen recognition[176, 177]. Two types of these receptors are known, namely DDR1 and DDR2, and expressed in different cells, such as hMSCs[178, 179] or MCF7-[180, 181] and MDA-cell lines[180]. For example DDR2 is only activated via exposure to fibrillary collagens such as collagen type I and type III.[182, 183] Upon exposure to native collagen these receptors are phosphorylated, which equals their activation, and this can be analyzed with Western Blot analysis.[182] Collagen type I functionalized sP(EO-*stat*-PO) coated scaffolds would help to elucidate whether cells would preferentially adhere to individual collagen helices or to supramolecular collagen aggregates and if this would be reflected by a more pronounced activation of DDR receptors.

Importantly, the biofunctionalization of sP(EO-*stat*-PO) coated scaffolds with collagen via sP(EO-*stat*-PO)-NCO-groups was not further investigated as previous results demonstrated failure of AFSA functionalization of sP(EO-*stat*-PO) coated scaffolds. The only possibility to biofunctionalize sP(EO-*stat*-PO) coated scaffolds with AFSA was represented via the photoreaction with diazirines. Moreover, collagen possesses a higher molecular weight (~ 300-345 kDa)[184, 185] compared to streptavidin (~ 60 kDa)[186] and, hence, is sterically even more demanding. As the steric demand and the complex amino acid composition of AFSA were hypothesized to attribute to the failure of the NCO-modification approach the possibility of incorporating collagen to sP(EO-*stat*-PO)-NCO-groups further decreases.

In order to evaluate the presence of NCO groups, IR spectroscopy of pre-wetted and pre-treated PCL scaffolds incubated in acidified sP(EO-*stat*-PO) solutions with and without a subsequent neutralization were performed.

However, in this approach no characteristic NCO peaks in the region of 2280 – 2240 $cm^{-1}$ (**Figure 31**, blue box) on PCL scaffolds were detectable (**Figure 31**, black line). Even after the short sP(EO-*stat*-PO) coating time of 5 min, NCO peaks were not observable, for which previously strong NCO peak signals were detected with aqueous sP(EO-*stat*-PO) solutions. This could be a result of a faster NCO-hydrolysis to protonated amine-groups under acidic conditions or of the absence of sP(EO-*stat*-PO) on the PCL scaffolds. SP(EO-*stat*-PO) crosslinking between NCO and amine groups is trapped under acidic conditions due to the rather unreactive protonated amine-groups.

To elucidate if a subsequent neutralization would allow the detection of NCO-groups, the acidified sP(EO-*stat*-PO) solutions were subsequently neutralized prior to IR spectroscopy

(**Figure 31**, red line). But this, as well, resulted in the absence of NCO peaks and was correlated to the fact that under acidic conditions a fast NCO-hydrolysis occurred and consequently no crosslinking of sP(EO-*stat*-PO) molecules was possible.

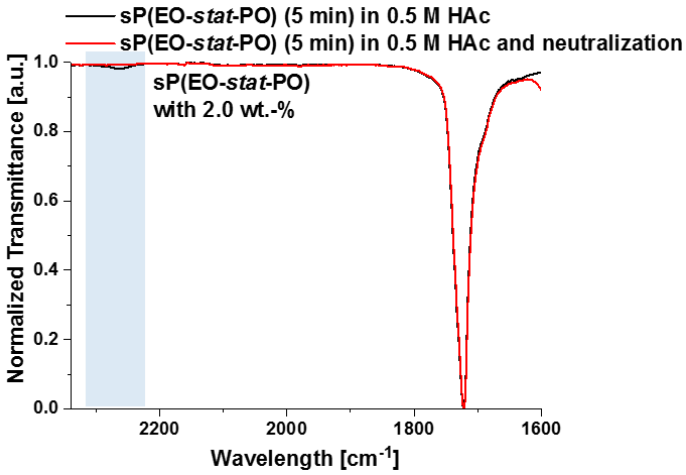


**Figure 31:** Representative normalized IR spectra of dried scaffolds for the incubation of scaffolds with acidified sP(EO-*stat*-PO) solutions (2.0 wt.-% in 0.5 M HAc) for 5 min (black line) together with the subsequent neutralization of this solution with 1 M NaOH (red line). After aqueous pre-wetting, the pre-treatment of scaffolds with 1 M NaOH for 5 min and washing of the scaffolds followed, prior to sP(EO-*stat*-PO) coating (2.0 wt.-% sP(EO-*stat*-PO) in 0.5 M HAc for 5 min). Spectra were normalized to the carbonyl peak at 1720 $cm^{-1}$. Blue box highlights the wavelength area of NCO at around 2260 $cm^{-1}$.

Since collagen type I is only soluble under acidic conditions, the pH-independent photoreaction seemed reasonable for following biofunctionalization experiments.

### 3.1.4.1. Collagen conformations

Collagen type I was immobilized on photoleucine functionalized sP(EO-*stat*-PO) coated scaffolds according to the workflow (**Figure 32**), which is in accordance to AFSA functionalization of sP(EO-*stat*-PO) coated scaffolds via photoleucine. After pre-wetting, pre-treating, a sP(EO-*stat*-PO) coating (10 min) followed and scaffolds were biofunctionalized with photoleucine as previously described. Then the scaffolds were washed with PBS and incubated in collagen type I solution (200 µg $mL^{-1}$ in 0.5 M HAc), in which the scaffolds were irradiated for 30 min at 365 nm. Finally, immobilized collagen was visualized via successive antibody detections. The primary anti-collagen antibody was detected by a suitable biotinylated secondary antibody to indirectly visualize collagen type I with AFSA.

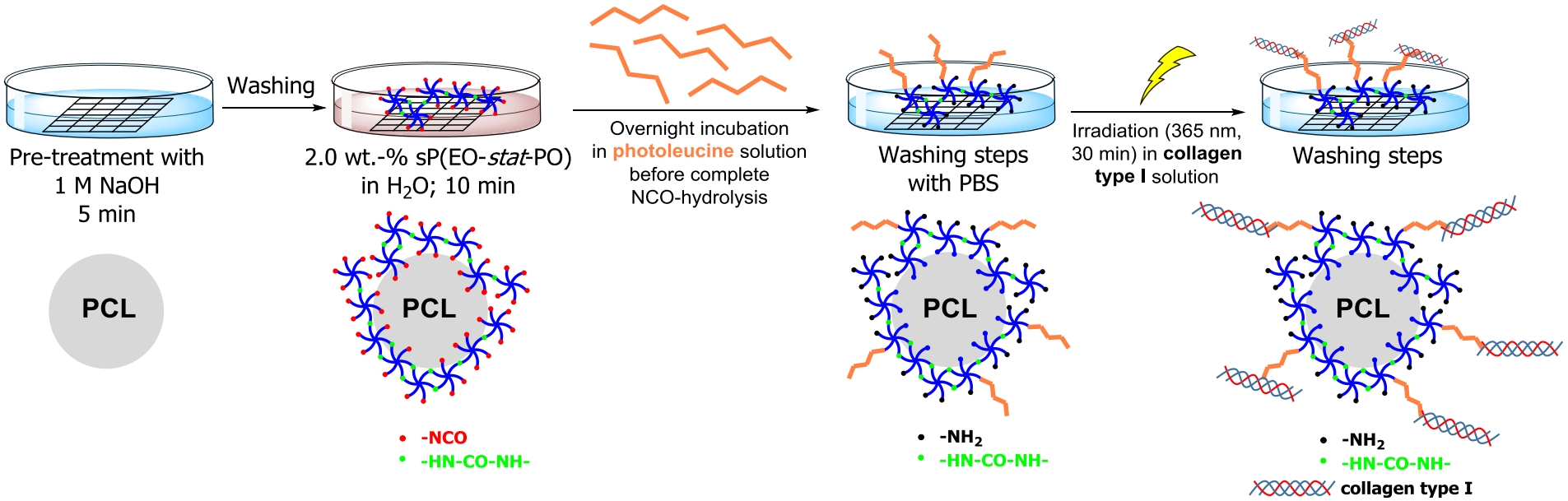


**Figure 32:** Workflow for the biofunctionalization of sP(EO-*stat*-PO) coated scaffolds with photoleucine based upon the reaction with sP(EO-*stat*-PO)-NCO-groups. The subsequent photoreaction is used to enable the covalent incorporation of collagen type I (200 µg $mL^{-1}$; 1.67 x $10^{-9}$ mol in 0.5 M HAc). Aqueous pre-wetting of scaffolds (not depicted) was followed by an alkaline pre-treatment with 1 M NaOH for 5 min and subsequent washing steps. Aqueous sP(EO-*stat*-PO) solutions (2.0 wt.-%; 1.67 x $10^{-6}$ mol, 1.0 x $10^{-5}$ mol NCO) were used to coat scaffolds for 10 min. Photoleucine solutions (1.34 x $10^{-5}$ mol in PBS) replaced the sP(EO-*stat*-PO) solution after 10 min for an overnight incubation. After washing with PBS, collagen type I solutions were added and the irradiation was performed for 30 min at 365 nm. Prior to analysis the scaffolds were intensively washed with PBS.

Two different approaches were investigated after the immobilization of collagen via the photo-induced biofunctionalization of photoleucine functionalized sP(EO-*stat*-PO) coated scaffolds (**Figure 33**). While one approach was based on individual collagen triple helices (ICH), the other approach induced collagen fibril formation to supramolecular collagen aggregates (SCA) upon a pH switch to neutral conditions and incubation at 37 °C.[187, 188] These approaches were investigated to ultimately allow the investigation of the influence of different collagen conformations on cell adhesion.

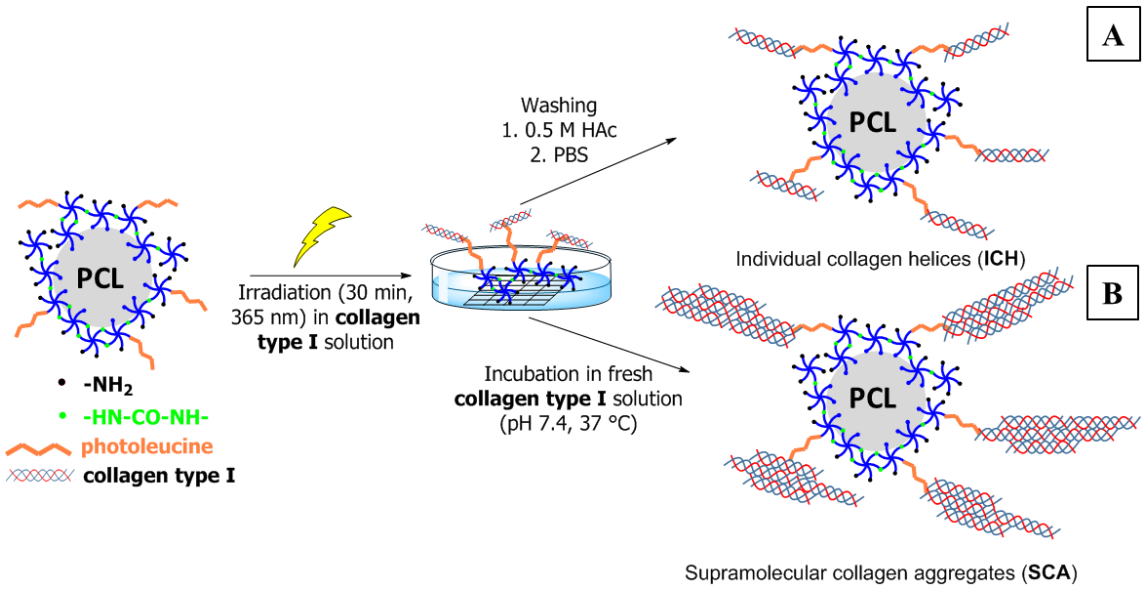


**Figure 33:** Schematic representation of different collagen conformation approaches on collagen functionalized sP(EO-*stat*-PO) coated scaffolds. After aqueous pre-wetting, the pre-treatment of PCL scaffolds with 1 M NaOH for 5 min and washing of scaffolds followed, prior to sP(EO-*stat*-PO) coating (2.0 wt.-% sP(EO-*stat*-PO), 10 min). Photoleucine solutions (1.34 x $10^{-5}$ mol in PBS) replaced the sP(EO-*stat*-PO) after 10 min for an overnight incubation. The scaffolds were washed with PBS. Only the following steps are depicted in this scheme. Scaffolds were incubated in collagen type I solutions with 200 µg $mL^{-1}$ (1.67 x $10^{-9}$ mol in 0.5 M HAc) and irradiated (365 nm, 30 min). After the irradiation, the samples were either washed with 0.5 M HAc and PBS to obtain individual collagen helices (ICH in **A**) or incubated in fresh collagen type I solutions (pH 7.4 at 37 °C) to achieve supramolecular collagen aggregates (SCA in **B**). Prior to analysis the scaffolds were intensively washed with PBS (not depicted).

In order to obtain immobilized ICH, the irradiation of photoleucine functionalized sP(EO-*stat*-PO) coated scaffolds was performed in a collagen type I solution (1.67 x $10^{-9}$ mol in 0.5 M HAc) with a subsequent washing under acidic conditions (0.5 M HAc) to remove excess of unbound collagen (**Figure 33 A**). Then the scaffolds were washed with PBS for subsequent visualization with antibodies.

SCA were achieved by the same photoreaction step, but followed by incubation of collagen functionalized sP(EO-*stat*-PO) coated scaffolds in a fresh collagen solution ($1.67 \times 10^{-9}$ mol in 0.5 M HAc). This solution was then neutralized and incubated at 37 °C for different time intervals (**Figure 33 B**) after which the scaffolds were washed with PBS prior to antibody incubations. Herein, the collagen molecules which were bound during the photoreaction are hypothesized to function as nucleation anchors for the later collagen fibril formation.

Different collagen conformations on collagen functionalized sP(EO-*stat*-PO) coated scaffolds are referred to as "ICH-" or "SCA functionalized sP(EO-*stat*-PO) coated scaffolds".

Firstly the extent of fibril formation was followed with turbidity measurements, as increasing turbidity correlates to SCA formation.[189-191] This was performed to obtain suitable incubation intervals for SCA functionalized sP(EO-*stat*-PO) coated scaffolds. Therefore, scaffold-free collagen type I solutions (5.0 mg $mL^{-1}$ in 0.5 M HAc) were neutralized, incubated at 37 °C and the absorption at 313 nm was continuously measured every minute for a total of 3 h.

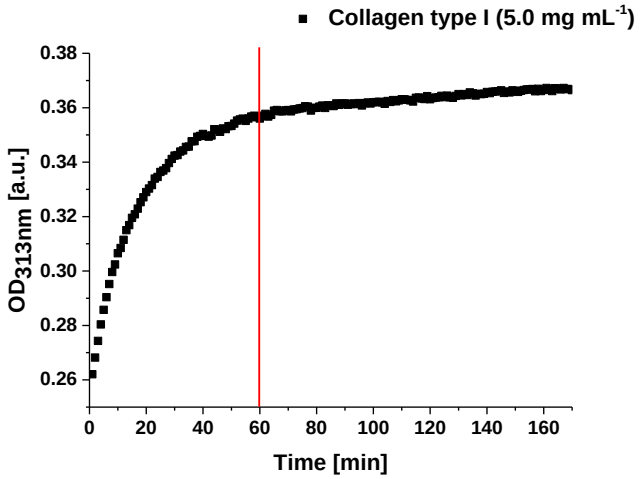


**Figure 34:** Representative correlation of the turbidity (313 nm) of freshly neutralized collagen type I solutions (5.0 mg $mL^{-1}$ in 0.5 M HAc) to the fibril formation time at 37 °C. Collagen fibril formation is indicated by increasing turbidity.[189-191] Red line at 60 min represents completion of the main part of fibril formation. Spectra were recorded every minute for a total of 3 h.

The turbidity at 313 nm of neutralized collagen solutions continuously increased with time, which correlated to collagen fibril formation (**Figure 34**). After 60 min the main part of

SCA formation seemed to be almost complete, thus this was chosen as the shortest incubation time for the following scaffold biofunctionalization experiments.
However, a slight increasing turbidity from 60 – 180 min was detectable. To later ensure complete fibril formation on the scaffolds a prolonged incubation of 4 h was chosen. Generally, these results were comparable to previous studies with collagen type I solutions which demonstrated as well that fibrillogenesis proceeded longer than 160 min.[191]
For following studies the terms "SCA1h" and "SCA4h" correspond to 1 h and 4 h fibril formation times, respectively. All following microscopic images were recorded with the same exposure time to ensure qualitative comparisons between the samples.

### 3.1.4.2. Fluorescence microscopic analyses

Control experiments for the collagen modification were conducted to eliminate interferences with adsorbed collagen. Exemplarily these control experiments were performed accordingly to the ICH approach and are termed "ICH/photoleucine treated PCL scaffolds" and "ICH treated unirradiated photoleucine functionalized sP(EO-*stat*-PO) coated scaffolds".

An intense fluorescence was detectable on ICH/photoleucine treated PCL scaffolds (**Figure 35 A**), whereas only a slight signal was detectable for ICH treated unirradiated photoleucine functionalized sP(EO-*stat*-PO) coated samples (**Figure 35 B**). This could imply a higher amount of ICH on ICH/photoleucine treated PCL scaffolds, as a result of different scaffold hydrophilicities. Whereas PCL scaffolds were already proven to be rather hydrophobic, even after alkaline pre-treatments, sP(EO-*stat*-PO) coated scaffolds possessed an increased hydrophilicity (**Figure 10**). However, the distribution of the fluorescence signal of this sample (**Figure 35 A**) was hypothesized to arise due to interactions of the primary antibody with PCL fibers, rather than to represent immobilized ICH. Due to the homogeneous distribution throughout the scaffold structure and the similar sizes to PCL fibers, the visualized structures were correlated to PCL fibers. In case of detected ICH, the fluorescence signal was expected to represent thinner and smaller structures than PCL fibers.
For ICH treated unirradiated photoleucine functionalized sP(EO-*stat*-PO) control scaffolds the slight detectable fluorescence could probably be correlated to ICH along the PCL fibers (**Figure 35 B**).

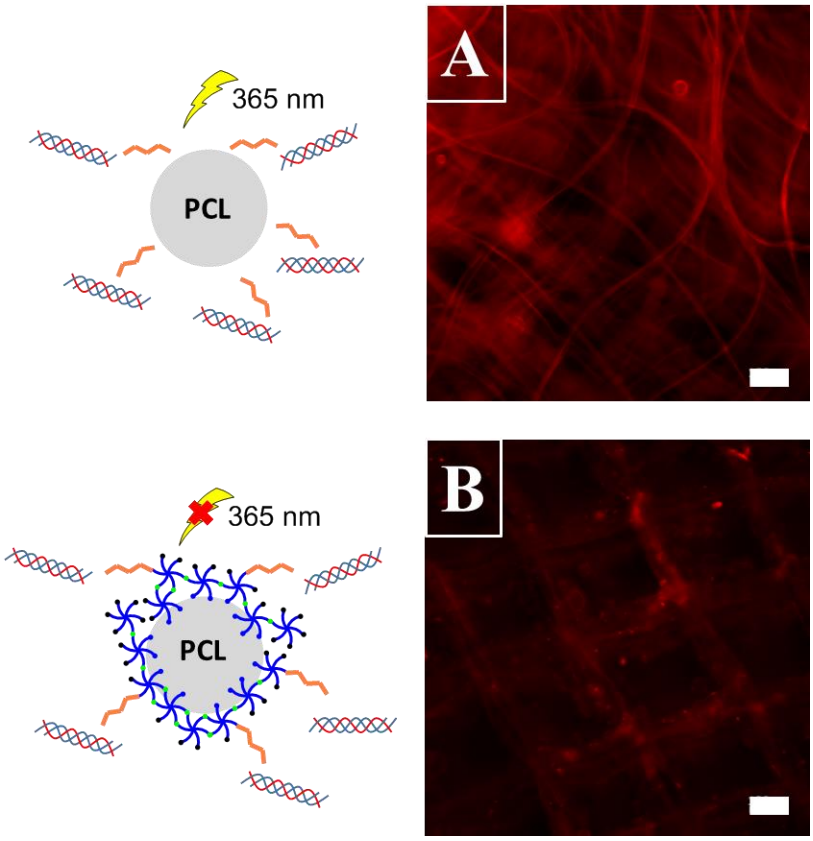


**Figure 35:** Representative fluorescence images of ICH/photoleucine treated PCL scaffolds followed by a subsequent irradiation in collagen type I solution for 30 min at 365 nm (**A**). Control for ICH treated unirradiated photoleucine functionalized sP(EO-*stat*-PO) coated scaffolds (**B**). After aqueous pre-wetting, the pre-treatment of PCL scaffolds with 1 M NaOH for 5 min and washing of the scaffolds followed (**A** and **B**), prior to sP(EO-*stat*-PO) coating (2.0 wt.-% sP(EO-*stat*-PO), 10 min for **B**). Photoleucine solutions ($1.34 \times 10^{-5}$ mol in PBS) either replaced the sP(EO-*stat*-PO) after 10 min for an overnight incubation (**B**) or were applied without a sP(EO-*stat*-PO) coating (**A**). The scaffolds were washed with PBS and incubated in collagen type I solutions with 200 µg $mL^{-1}$ ($1.67 \times 10^{-9}$ mol in 0.5 M HAc) and irradiated (365 nm, 30 min for **A**) or left unirradiated (**B**). Both samples were washed with 0.5 M HAc and PBS after collagen immobilization accordingly to the ICH approach. Primary (1:500, 4 h, RT) and secondary antibody (1:1666, overnight, 4 °C) incubations were performed in TBST. After washing the scaffolds, indirect visualization of collagen was achieved by an overnight incubation in AFSA solutions ($1.67 \times 10^{-10}$ mol in PBS) at 4 °C. Prior to analysis the scaffolds were washed with PBS. Exposure times of 44 ms and the scale bars represent 100 µm.

However, in this experimental setup the scaffolds were not blocked before being incubated in antibody solutions and thus could lead to interferences from unspecifically adsorbed antibodies that falsify the visualization.

To analyze the effect of blocked scaffolds on the visualized structures, this experiment was repeated with blocking with TBST (pH 8.0) supplemented with 5.0 wt.-% milk powder

prior to the antibody incubations.

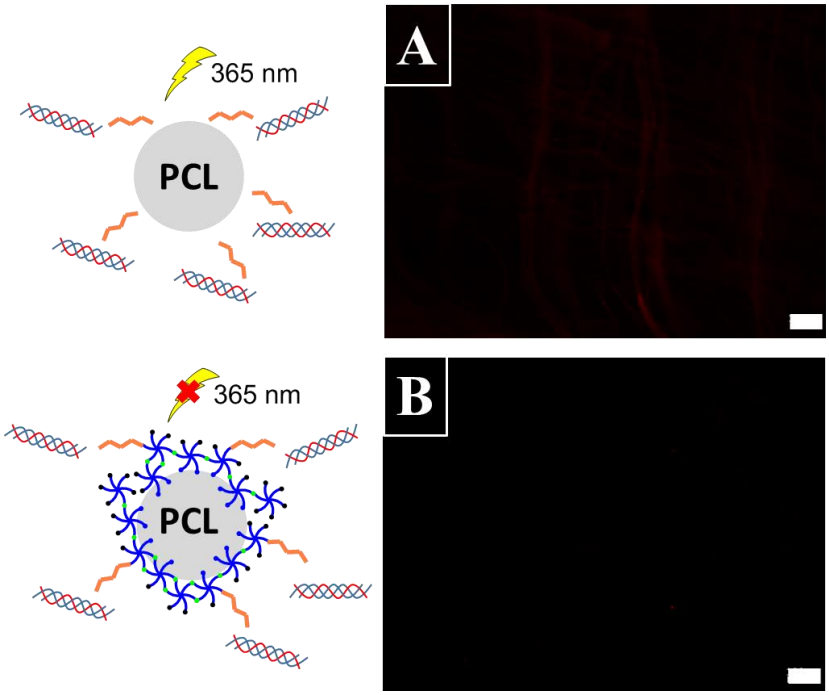


**Figure 36:** Representative fluorescence images of controls for the ICH approach with blocking (5.0 wt.-% milk powder in TBST) prior to scaffold incubations in antibody solutions. ICH/photoleucine treated PCL scaffolds with the subsequent irradiation in collagen type I (**A**). The corresponding control for ICH treated unirradiated photoleucine functionalized sP(EO-*stat*-PO) coated scaffolds (**B**). After aqueous pre-wetting, the pre-treatment of PCL scaffolds with 1 M NaOH for 5 min and washing of the scaffolds followed, prior to sP(EO-*stat*-PO) coating (2.0 wt.-% sP(EO-*stat*-PO), 10 min for **B**). Photoleucine solutions ($1.34 \times 10^{-5}$ mol in PBS) either replaced the sP(EO-*stat*-PO) after 10 min for an overnight incubation (**B**) or were applied without a sP(EO-*stat*-PO) coating (**A**). The scaffolds were washed with PBS and incubated in collagen type I solutions with 200 µg $mL^{-1}$ ($1.67 \times 10^{-9}$ mol in 0.5 M HAc) and irradiated (365 nm, 30 min for **A**) or left unirradiated (**B**). Both samples were washed with 0.5 M HAc and PBS after collagen immobilization accordingly to the ICH approach. Overnight blocking of the scaffolds with TBST (pH 8.0) supplemented with 5.0 wt.-% milk powder at 4 °C was followed by primary (1:500, 4 h, RT, TBST) and secondary antibody (1:1666, overnight, 4 °C, TBST) incubations. After washing the scaffolds indirect visualization of ICH was achieved by an overnight incubation in AFSA solution ($1.67 \times 10^{-10}$ mol in PBS) at 4 °C. Prior to analysis the scaffolds were washed with PBS. Exposure times of 44 ms and the scale bars represent 100 µm.

For neither ICH/photoleucine treated PCL (**Figure 36 A**) nor ICH treated unirradiated photoleucine functionalized sP(EO-*stat*-PO) coated scaffolds (**Figure 36 B**) a fluorescence was detectable. This implied no unspecific interactions between the blocked controls and the primary antibody and consequently prevented a visualization. Hence, falsification of

the results due to visualization of PCL fibers instead of ICH was successfully circumvented. These results also suggested that ICH was not immobilized on these controls.
In general, the blocking prior to antibody incubations seemed crucial in reducing unspecific primary antibody adsorption on the scaffolds. In the course of the following experiments, the scaffolds were consequently blocked prior to the scaffold incubations in antibody solutions.

Moreover, it was also tested whether the secondary antibody could unspecifically interact with collagen functionalized sP(EO-*stat*-PO) coated scaffolds. Both collagen conformation approaches were included and blocking of collagen functionalized sP(EO-*stat*-PO) coated scaffolds was directly followed by secondary antibody incubations. For SCA, the fibril formation times were matched to the observation from the turbidity measurements and set to 1 h (SCA1h) and 4 h (SCA4h) at 37 °C.

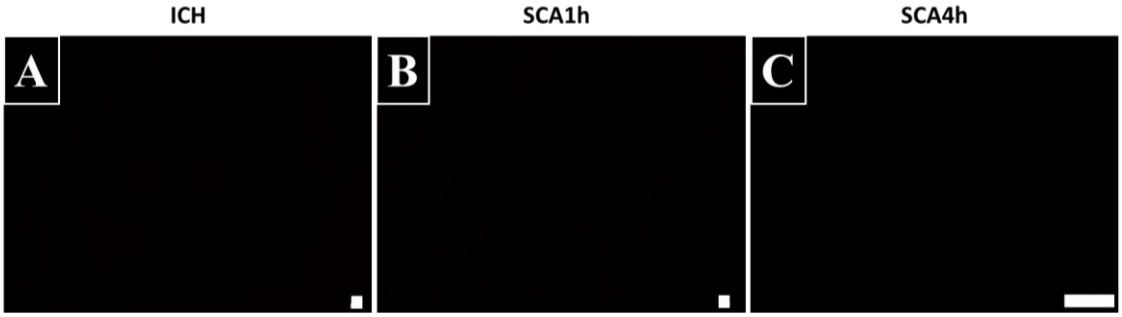


**Figure 37:** Representative fluorescence images of the secondary antibody controls for ICH (**A**) compared to SCA1h (**B**) and SCA4h approach (**C**) on photoleucine functionalized sP(EO-*stat*-PO) coated scaffolds. After aqueous pre-wetting, the pre-treatment of PCL scaffolds with 1 M NaOH for 5 min and washing of the scaffolds followed, prior to sP(EO-*stat*-PO) coating (2.0 wt.-% sP(EO-*stat*-PO), 10 min). Photoleucine solutions ($1.34 \times 10^{-5}$ mol in PBS) replaced the sP(EO-*stat*-PO) after 10 min for an overnight incubation. The scaffolds were washed with PBS and incubated in collagen type I solutions with 200 µg $mL^{-1}$ ($1.67 \times 10^{-9}$ mol in 0.5 M HAc) and irradiated (365 nm, 30 min). Afterwards the samples were treated accordingly to the different collagen conformation approaches. Overnight blocking of the scaffolds with TBST (pH 8.0) supplemented with 5.0 wt.-% milk powder at 4 °C was followed solely by secondary antibody (1:1666, overnight, 4 °C) incubations. After washing the scaffolds indirect visualization of collagen was achieved by an overnight incubation in AFSA solution ($1.67 \times 10^{-10}$ mol in PBS) at 4 °C. Prior to analysis the scaffolds were washed with PBS. Exposure times of 44 ms and the scale bars represent 200 µm.

The absence of any fluorescence signal for ICH (**Figure 37 A**) and SCA approaches (**Figure 37 B** for SCA1h; **Figure 37 C** for SCA4h) suggested no unspecific interactions of the secondary antibody with collagen on photoleucine functionalized sP(EO-*stat*-PO) coated scaffolds. These results and the blocking of the scaffolds, ensured a selective detection of collagen without cross-reactions arising from the applied antibodies.
Circumventing of any potential interferences of collagen detection via the applied antibodies allowed to further expand the controls to both collagen conformation approaches. First, the adsorption potential of collagen to PCL fibers was assessed and included collagen treated PCL scaffolds and collagen/photoleucine treated PCL scaffolds. These samples were irradiated whilst being incubated in collagen solutions and afterwards treated accordingly to the different collagen conformation approaches. For simplification purposes the schemes depicted in **Figure 38** represent both collagen conformation approaches and are distinguished through the individual panels.

No fluorescence was detectable for ICH treated PCL (**Figure 38 A**) and for ICH/photoleucine treated PCL scaffolds (**Figure 38 B**), thus implied no immobilized ICH. However, it seemed possible to attach SCA1h directly onto PCL scaffolds (**Figure 38 C**). An additional structure next to the scaffold was observable and correlated to SCA1h as suggested by the slight fluorescence. The corresponding SCA1h/photoleucine treated PCL scaffold (**Figure 38 D**) displayed as well a slight fluorescence.
With increasing fibril formation time to 4 h, the adsorption of SCA4h to PCL scaffolds (**Figure 38 E**) did not concurrently increase, further suggesting the absence of covalently attached SCA4h. Additionally, SCA4h were also detectable on SCA4h/photoleucine treated PCL scaffolds, but not homogenously distributed throughout the scaffolds but instead more accumulated on one side and linked to only a few specific points (**Figure 38 F**). This was also observable upon handling and correlated to aggregated collagen which was physically entrapped into the scaffold upon neutralization.[187, 188]
For these controls the advantageous protein-repellent surface of sP(EO-*stat*-PO) is lacking and explains the presence of collagen at only a few spots within the samples and the inconsistency of collagen presence. Moreover, these samples could not enable the cellular adhesion exclusively mediated by collagen. Instead an interference of adsorbed proteins from cell media with the collagen induced cellular response is suggested and is, hence, unsuitable for later cell-material interaction studies.

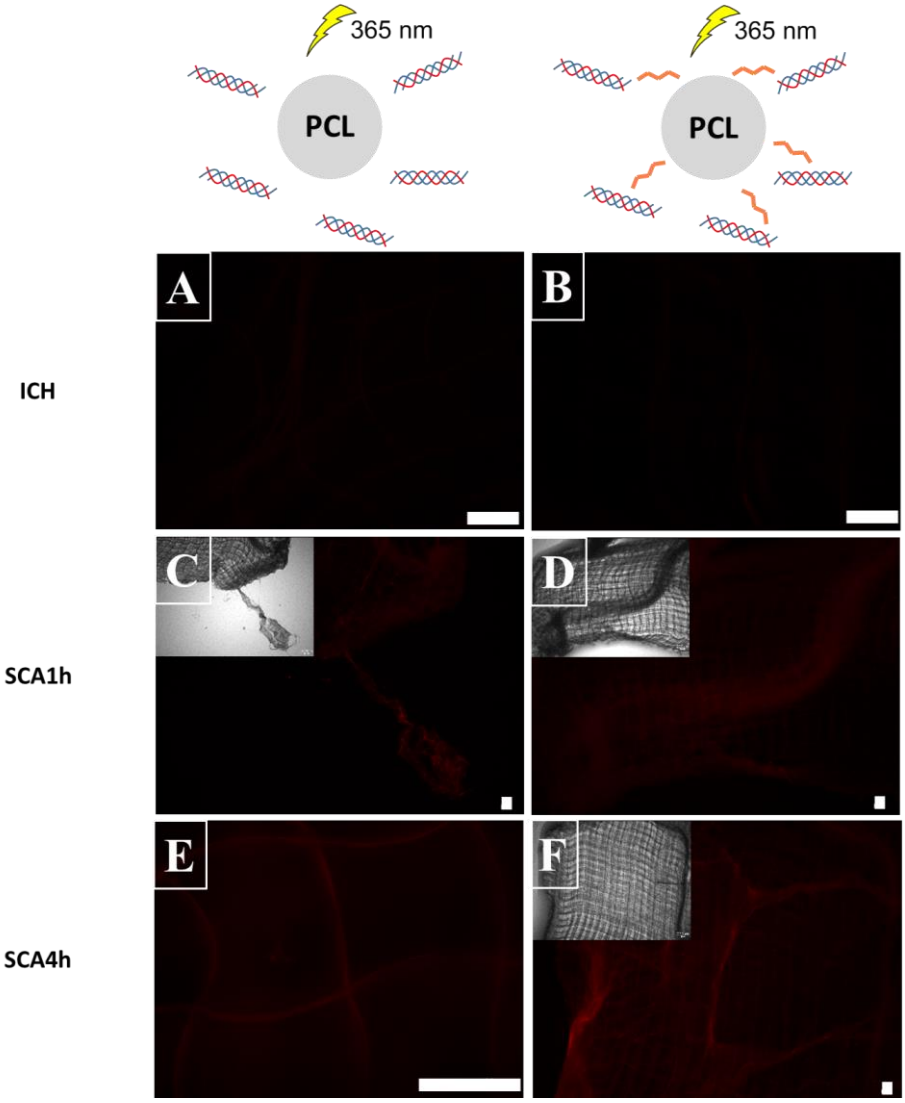


**Figure 38:** Representative fluorescence images of collagen treated PCL control (**A**, **C** and **E**) and collagen/photoleucine treated PCL scaffolds (**B**, **D** and **F**). These controls were either treated following the ICH (**A** and **B**) or the SCA approach (SCA1h in **C** and **D**; SCA4h in **E** and **F**). After aqueous pre-wetting, the pre-treatment of PCL scaffolds with 1 M NaOH for 5 min and washing of the scaffolds followed. Photoleucine solutions (1.34 x $10^{-5}$ mol in PBS) were added for an overnight incubation (**B**, **D** and **F**). All scaffolds were washed with PBS and incubated in collagen type I solutions with 200 µg $mL^{-1}$ (1.67 x $10^{-9}$ mol in 0.5 M HAc) and irradiated (365 nm, 30 min). Afterwards the samples were treated accordingly to the different collagen conformation approaches. Overnight blocking of the scaffolds with TBST (pH 8.0) supplemented with 5.0 wt.-% milk powder at 4 °C was followed by primary (1:500, 4 h, RT) and secondary antibody (1:1666, overnight, 4 °C) incubations. After washing the scaffolds an indirect visualization was achieved via overnight incubations in AFSA solution (1.67 x $10^{-10}$ mol in PBS) at 4 °C. Prior to analysis the scaffolds were washed with PBS. Exposure times of 44 ms and the scale bars represent 200 µm. Insets in **C**, **D** and **F** display transmission images with same magnifications.

Another set of controls included collagen treated NCO-hydrolyzed sP(EO-*stat*-PO) coated and collagen treated unirradiated photoleucine functionalized sP(EO-*stat*-PO) coated samples. The schemes depicted in **Figure 39** represent both collagen conformation approaches and are further distinguished through the individual panels.

For ICH on collagen treated NCO-hydrolyzed sP(EO-*stat*-PO) coated scaffolds (**Figure 39 A**) and on collagen treated unirradiated photoleucine functionalized sP(EO-*stat*-PO) coated scaffolds (**Figure 39 B**) no fluorescence signals were detectable, implying no unspecifically adsorbed ICH.

The same observations were made for SCA1h treated NCO-hydrolyzed sP(EO-*stat*-PO) coated scaffolds (**Figure 39 C**) and on SCA1h treated unirradiated photoleucine functionalized sP(EO-*stat*-PO) coated scaffolds (**Figure 39 D**) and suggested the absence of SCA1h on these samples.

However, an intense fluorescence was observable for SCA4h treated NCO-hydrolyzed sP(EO-*stat*-PO) coated scaffolds (**Figure 39 E**). But again no homogenous SCA4h distribution within the scaffolds was found but SCA4h was rather attached at few anchor spots (**Figure 39 E**, inset). This suggested a possible incorporation of SCA4h without the photoreaction on NCO-hydrolyzed sP(EO-*stat*-PO) coated scaffolds, similar to the results of SCA treated PCL- and photoleucine treated PCL-fibers (**Figure 38 C** for SCA1h; **Figure 38 F** for SCA4h). This was probably mediated by the aforementioned physical entrapment of collagen. For the corresponding SCA4h treated unirradiated photoleucine functionalized sP(EO-*stat*-PO) coated scaffolds, however, no fluorescence signal was evident (**Figure 39 F**).

The comparison of SCA1h treated NCO-hydrolyzed sP(EO-*stat*-PO) coated (**Figure 39 C** and **Figure 39 E** for SCA4h) and SCA treated unirradiated photoleucine functionalized sP(EO-*stat*-PO) coated scaffolds (**Figure 39 D** for SCA1h; **Figure 39 F** for SCA4h) proved the physically entrapped collagen to occur only by chance and not reproducible, and to result in inhomogeneously distributed collagen which was only loosely attached to the scaffolds. These conditions are not suitable for cell-material interaction studies.

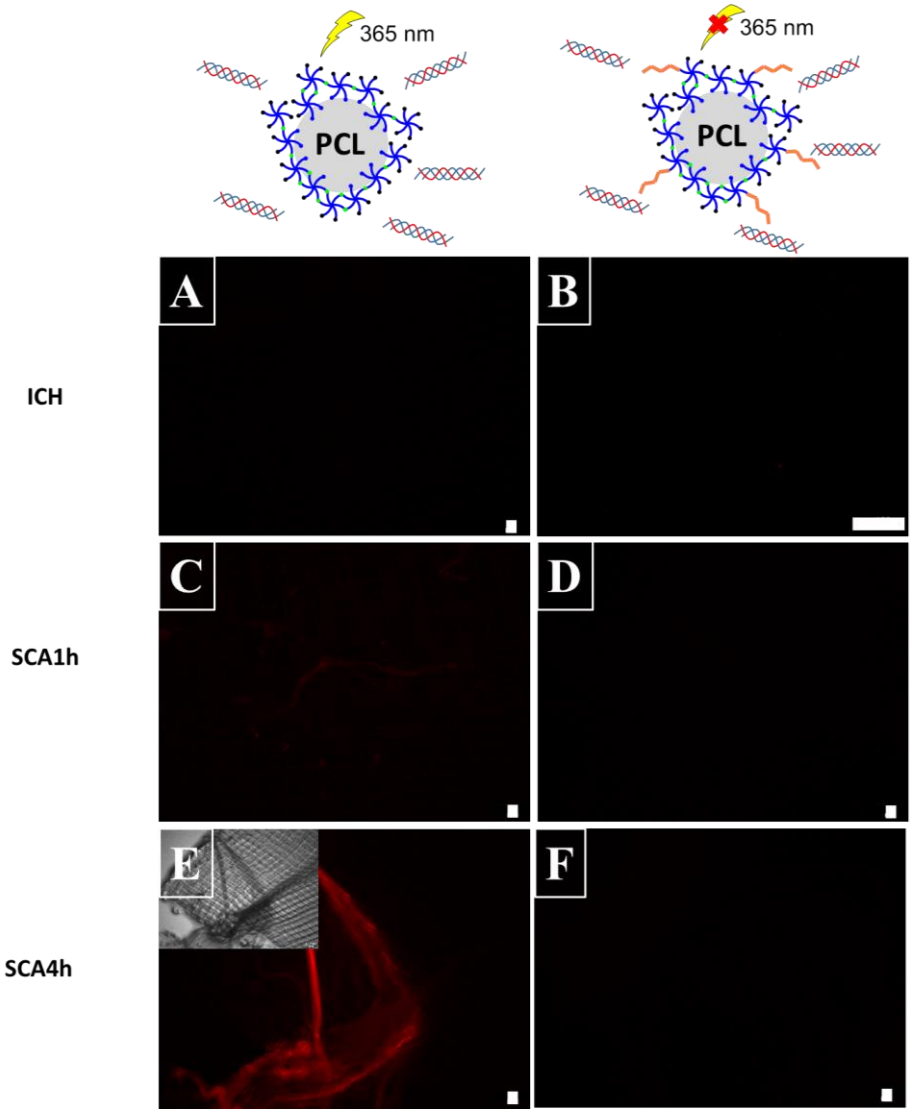


**Figure 39:** Representative fluorescence images of collagen treated NCO-hydrolyzed sP(EO-*stat*-PO) coated scaffolds (**A**, **C** and **E**) compared to collagen treated unirradiated photoleucine functionalized sP(EO-*stat*-PO) coated scaffolds (**B**, **D** and **F**). Controls were treated according to ICH (**A** and **B**) or to SCA approach (SCA1h in **C** and **D**; SCA4h in **E** and **F**). After aqueous pre-wetting, the pre-treatment of PCL scaffolds (1 M NaOH for 5 min) and washing of the scaffolds followed, prior to sP(EO-*stat*-PO) coating (2.0 wt.-% sP(EO-*stat*-PO), for 10 min). Water (**A**, **C** and **E**) or photoleucine ($1.34 \times 10^{-5}$ mol in PBS) was added after the coating for an overnight incubation (**B**, **D** and **F**). Scaffolds were washed with PBS and incubated in collagen type I solutions with 200 µg $mL^{-1}$ ($1.67 \times 10^{-9}$ mol in 0.5 M HAc) and irradiated (365 nm, 30 min for **A**, **C** and **E**) or left unirradiated (**B**, **D** and **F**). Then samples were treated accordingly to the collagen conformation approaches. Overnight blocking of the scaffolds with TBST (pH 8.0) supplemented with 5.0 wt.-% milk powder at 4 °C was followed by primary (1:500, 4 h, RT) and secondary antibody (1:1666, overnight, 4 °C) incubations. After washing the scaffolds an indirect visualization was achieved via overnight incubations in AFSA solution ($1.67 \times 10^{-10}$ mol in PBS) at 4 °C. Prior to analysis the scaffolds were washed with PBS. Exposure times of 44 ms and the scale bars represent 200 µm. Inset displays transmission image with same magnification (**E**).

Finally, positive controls for collagen functionalized sP(EO-*stat*-PO) coated scaffolds were investigated for both collagen formation approaches and are termed "ICH" or "SCA functionalized sP(EO-*stat*-PO) coated scaffolds". Herein, the direct comparison of non-blocked versus blocked scaffolds was conducted to evaluate possible interferences from blocked samples to the fluorescence intensities. For ICH only low incorporated collagen amounts were expected and hypothesized to be completely blocked by TBST with 5.0 wt.-% milk powder.

Fluorescence signals for ICH functionalized sP(EO-*stat*-PO) coated scaffolds were only detected for non-blocked scaffolds and correlated to ICH within the filaments and on PCL fibers, due to the sizes and distributions thereof (**Figure 40 A**). The non-detectable fluorescence for blocked scaffolds could probably be attributed to the rather small amount of immobilized ICH, which was completely blocked by TBST supplemented with 5.0 wt.-% milk powder (**Figure 40 B**).

The fluorescence intensities and structures for SCA functionalized sP(EO-*stat*-PO) coated scaffolds were comparable for both fibril formation times on non-blocked scaffolds (**Figure 40 C** for SCA1h; **Figure 40 E** for SCA4h) and similar to blocked scaffolds (**Figure 40 D** for SCA1h; **Figure 40 F** for SCA4h). These signals were correlated to collagenous structures in between the scaffold fibers due to their distribution and sizes compared to PCL fibers, similar to ICH (**Figure 40 A**). For these samples a relatively high background signal, probably arising from interferences with the transparency of PCL fibers, was as well detectable independent of blocked or non-blocked samples (**Figure 40 C – F**). But this background was less pronounced for blocked ICH as the interference with PCL transparency was reduced by blocking of any fluorescence signal (**Figure 40 B**).

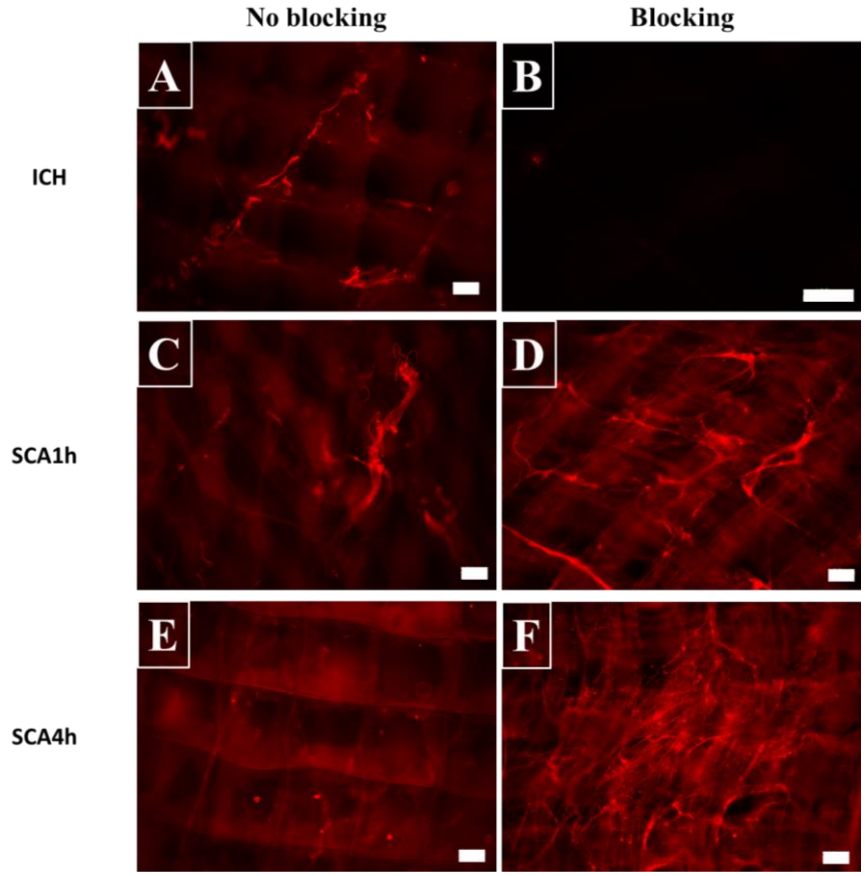


**Figure 40:** Representative comparison of fluorescence images of non-blocked blocked versus blocked scaffolds prior to antibody incubations for ICH (**A** and **B**) and SCA (SCA1h in **C** and **D**; SCA4h in **E** and **F**) both on collagen functionalized sP(EO-*stat*-PO) coated scaffolds. After aqueous pre-wetting, the pre-treatment of PCL scaffolds with 1 M NaOH for 5 min and washing of scaffolds followed, prior to sP(EO-*stat*-PO) coating (2.0 wt.-% sP(EO-*stat*-PO), 10 min). Photoleucine solutions ($1.34 \times 10^{-5}$ mol in PBS) replaced the sP(EO-*stat*-PO) after 10 min for an overnight incubation. The scaffolds were washed with PBS and incubated in collagen type I solutions with 200 µg $mL^{-1}$ ($1.67 \times 10^{-9}$ mol in 0.5 M HAc) and irradiated (365 nm, 30 min). Afterwards the samples were treated accordingly to the different collagen conformation approaches. Overnight blocking of the scaffolds with TBST (pH 8.0) supplemented with 5.0 wt.-% milk powder at 4 °C was performed for **B**, **D** and **F**. All samples were incubated in primary (1:500, 4 h, RT) and secondary antibody solutions (1:1666, overnight, 4 °C). After washing the scaffolds indirect visualization was achieved by an overnight incubation in AFSA solution ($1.67 \times 10^{-10}$ mol in PBS) at 4 °C. Prior to analysis the scaffolds were washed with PBS. Exposure times of 44 ms and the scale bars represent 100 µm.

To investigate the collagenous structure distribution within and around the fibers, confocal fluorescence microscopy was exemplarily applied for SCA1h functionalized sP(EO-*stat*-PO) coated scaffolds. It was of interest whether the hypothesized collagen anchors set during the photoreaction, would dictate fibril formation orientation along the PCL fibers.

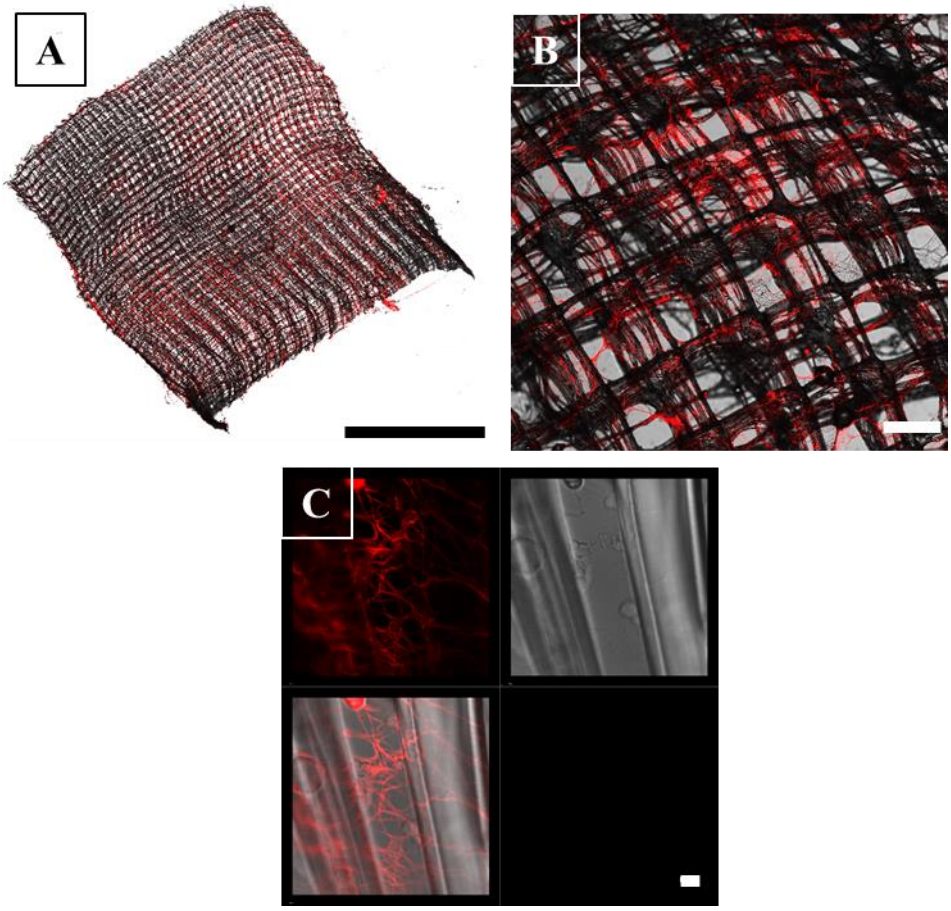


**Figure 41:** Representative overlap of fluorescence and transmission confocal microscopic images of SCA1h functionalized sP(EO-*stat*-PO) coated scaffolds with different magnifications. After aqueous pre-wetting, the pre-treatment of PCL scaffolds with 1 M NaOH for 5 min and washing of the scaffolds followed, prior to sP(EO-*stat*-PO) coating (2.0 wt.-% sP(EO-*stat*-PO), 10 min). Photoleucine solutions ($1.34 \times 10^{-5}$ mol in PBS) replaced the sP(EO-*stat*-PO) after 10 min for an overnight incubation. The scaffolds were washed with PBS and incubated in collagen type I solutions with 200 µg $mL^{-1}$ ($1.67 \times 10^{-9}$ mol in 0.5 M HAc) and irradiated (365 nm, 30 min). The sample was treated accordingly to the SCA1h approach. Overnight blocking of the scaffolds with TBST (pH 8.0) supplemented with 5.0 wt.-% milk powder at 4 °C was followed by primary (1:500, 4 h, RT) and secondary antibody incubations (1:1666, overnight, 4 °C). After washing the scaffolds indirect visualization was achieved by an overnight incubation in AFSA solution ($1.67 \times 10^{-10}$ mol in PBS) at 4 °C. Prior to analysis the scaffold was washed with PBS. Scale bars represent 5 mm (**A**), 200 µm (**B**) and 5 µm (**C**).

An overview over the homogeneous SCA1h distribution on the investigated scaffold is represented in **Figure 41 A**. More detailed images depicting the collagenous fibers within the scaffold filaments and around individual fibers further complemented the microscopic analyses (**Figure 41 B** and **C**). A directed fibril formation parallel to the PCL fibers was not predominantly observable as the collagen fibrils were also spread within the filaments.

### 3.1.4.3. Quantification and collagen morphology

To further compare the collagen conformation approaches, not only the presence or absence of collagen was evaluated, but the amount of immobilized collagen was assessed with a hydroxyproline (Hyp) assay. Collagen is among the small group of proteins possessing this amino acid and the Hyp amount can directly be converted to the total collagen amount[192]. This assay is based on the oxidation of Hyp via chloramine T and the subsequent reaction of pyrrole with 4-(dimethylamino)benzaldehyde (DMAB) (**Scheme 12**).

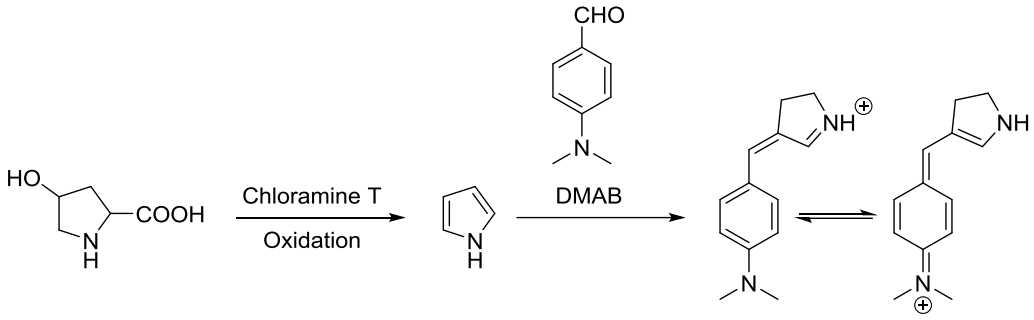


**Scheme 12:** Simplified reaction mechanism of the hydroxyproline (Hyp) assay. Hyp is oxidized via the addition of chloramine T and the chromophoric compound is obtained by the reaction of pyrrole with 4-(dimethylamino)benzaldehyde (DMAB).

For this assay collagen functionalized sP(EO-*stat*-PO) coated scaffolds were incubated under acidic conditions (6 M HCl, 95 °C, 12 h) to ensure protein hydrolysis and completely acid-hydrolyzed scaffolds. Trans-4-hydroxy-L-proline was included for calibration purposes and after the assay procedure the adsorption at 560 nm was measured. To obtain the percentage of immobilized collagen, the total amount of collagen in the fibril formation solution was correlated to the detected values of collagen on the scaffolds.

**Table 4:** Hydroxyproline (Hyp) assay results for the comparison of ICH- and SCA-functionalized sP(EO-*stat*-PO) coated scaffolds (with 1 h and 4 h fibril formation times for SCA approaches).

| | **ICH** | **SCA1h** | **SCA4h** |
|---|---|---|---|
| Hyp [µg] | not detectable | 1.25 ± 0.1 | 14.13 ± 1.2 |
| Collagen [µg] | / | 9.26 ± 0.9 | 104.55 ± 8.9 |
| Collagen [%]* | / | 5.0 | 56 |

*Percentage of collagen correlated to the total collagen amount of the fibril formation solution

No Hyp and hence collagen was detectable for ICH functionalized sP(EO-*stat*-PO) coated scaffolds which was correlated to the detection limit of this assay of around 0.5 – 2.5 µg Hyp per mL[193] and to too low ICH amounts on these scaffolds (**Table 4**). For SCA functionalized sP(EO-*stat*-PO) coated scaffolds, the collagen amount increased from 5.0 % (SCA1h) concurrently with fibril formation durations to 56 % (SCA4h). This was in accordance to the expectations as the fibril formation of collagen was proven via turbidity measurements to proceed for at least 3 h. Prolonged fibril formation times result in a higher number of staggered fibrils[189, 190] and further complement the Hyp assay results.

Besides quantifying collagen on the scaffolds, the fibrillary collagen structure was also investigated with SEM analysis. Typically individual collagen fibrils align parallel and staggered to form the characteristic axial periodic D-banding pattern of collagen fibers.[189, 190] These fibers consist of closely packed thin collagen fibrils (30 – 100 nm) and the periodic D-banding pattern results from typical repeating units in the collagen fibers.[189, 190, 194] For visualization thereof collagen can be stained with heavy metal containing solutions, such as gold-palladium or phosphotungstic acid with uranyl acetate,[194] and analyzed with SEM or TEM microscopy. But also unstained collagen fibers allow the detection of this characteristic collagen feature. It was of interest if the collagen functionalized scaffolds would also display this D-banding pattern and SEM analysis was conducted without additionally staining the samples.

For ICH functionalized sP(EO-*stat*-PO) coated scaffolds thinner structures (~ 780 nm) than PCL fibers (~ 5 µm) were observable (**Figure 42 A**). But the characteristic D-banding pattern was not detectable, as depicted in the magnification in **Figure 42 B**. This was also not expected for this approach as the D-banding pattern results from multiple staggered collagen fibrils. But this figure demonstrates thinner structures located parallel on PCL fibers, which is different to previous observations for PCL or sP(EO-*stat*-PO) coated fibers.

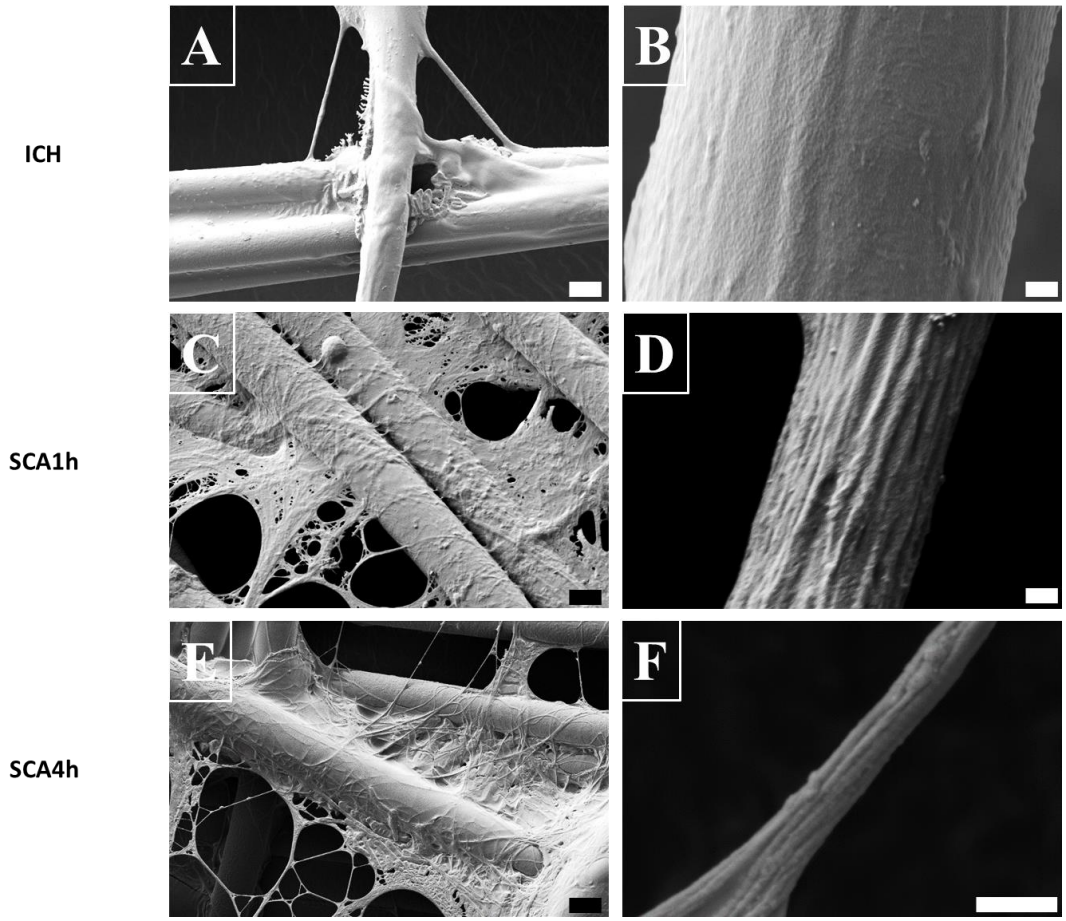


**Figure 42:** Representative SEM images of ICH (**A** and **B**) and SCA (SCA1h in **C** and **D**; and SCA4h in **E** and **F**) functionalized sP(EO-*stat*-PO) coated scaffolds. After aqueous pre-wetting, the pre-treatment of PCL scaffolds with 1 M NaOH for 5 min and washing of the scaffolds followed, prior to sP(EO-*stat*-PO) coating (2.0 wt.-% sP(EO-*stat*-PO), 10 min). Photoleucine solutions (1.34 x $10^{-5}$ mol in PBS) replaced the sP(EO-*stat*-PO) after 10 min for an overnight incubation. The scaffolds were washed with PBS and incubated in collagen type I solutions with 200 µg $mL^{-1}$ (1.67 x $10^{-9}$ mol in 0.5 M HAc) and irradiated (365 nm, 30 min). The samples were treated accordingly to ICH or to SCA approaches with fibril formation times of 1 h and 4 h. Prior to analysis the scaffolds were washed with PBS and dried. Scale bars represent 4 µm (**A**, **C** and **E**) and 400 nm (**B**, **D** and **F**).

However, collagen structures were clearly visible for SCA1h (**Figure 42 C**) and SCA4h (**Figure 42 E**) functionalized sP(EO-*stat*-PO) coated scaffolds. The thin fibrils detected for SCA1h could probably be correlated to collagen but the characteristic D-banding pattern was again not detectable (**Figure 42 D**). The lack of this for SCA1h could be explained by too little stacked fibrils. In accordance to this hypothesis, the results of the turbidity measurements already indicated the incompleteness of fibril formation after 60 min. For higher magnifications of SCA1h (**Figure 42 D**) more pronounced parallel aligned structures on PCL fibers were observable than compared to ICH (**Figure 42 B**). These

structures are hypothesized as indicators of immobilized collagen due to the comparable structures for both SCA1h (**Figure 42 D**) and SCA4h (**Figure 42 F**) and due to detectable D-banding patterns for SCA4h. The latter mentioned collagen bundles displayed sizes of around 280 nm and individual fibrils of 80 nm which is in good accordance to literature values of 80 – 200 nm[189, 190].

Analogous to the positive results of the fluorescence analysis and the Hyp assay, SEM analysis complemented the success of SCA formation on photoleucine functionalized sP(EO-*stat*-PO) coated scaffolds. Comparing SEM observations to the aforementioned PCL or sP(EO-*stat*-PO) coated fibers indirectly stressed that collagen was also successfully immobilized for the ICH approach.

### 3.1.4.4. Cell adhesion study

As a proof of principle for cell-material interaction studies on collagen functionalized sP(EO-*stat*-PO) coated scaffolds, a preliminary cell adhesion study with human mesenchymal stromal cells (hMSCs) was performed. These cells were chosen as they express DDR receptors[178, 179], which ultimately allow to distinguish between integrin or DDR mediated cell adhesion.

As controls for cellular adhesion, polystyrene- and collagen coated-wells were included. Two different well types were assessed to either allow (Nunclon™ Delta surface) or to inhibit attachment of hMSCs (Costar® non-treated surfaces). Collagen coating of both well types was performed by an overnight incubation with an acidified collagen type I solution (0.23 mg $mL^{-1}$ in 0.5 M HAc), followed by air drying and subsequent washing steps. This was performed to demonstrate the inhibition of cellular adhesion for non-collagen coated Costar® wells. Furthermore, the Costar® wells ensure selective cellular adhesion onto the scaffolds and were used for all scaffold containing experiments. Cells were seeded with 1.2 x $10^5$ cells per well, allowed to adhere for 6 h and cultured for up to 8 d. In this study cell adhesion was restricted to a limited time as prolonged durations potentially falsify the later analysis with Western Blot, due to the cellular production of collagen interfering in the DDR receptor activation. A Live/Dead staining was used for visualization purposes at 1 d and 8 d of culture. An overview of the results for the different well type controls is depicted in **Figure 43**.

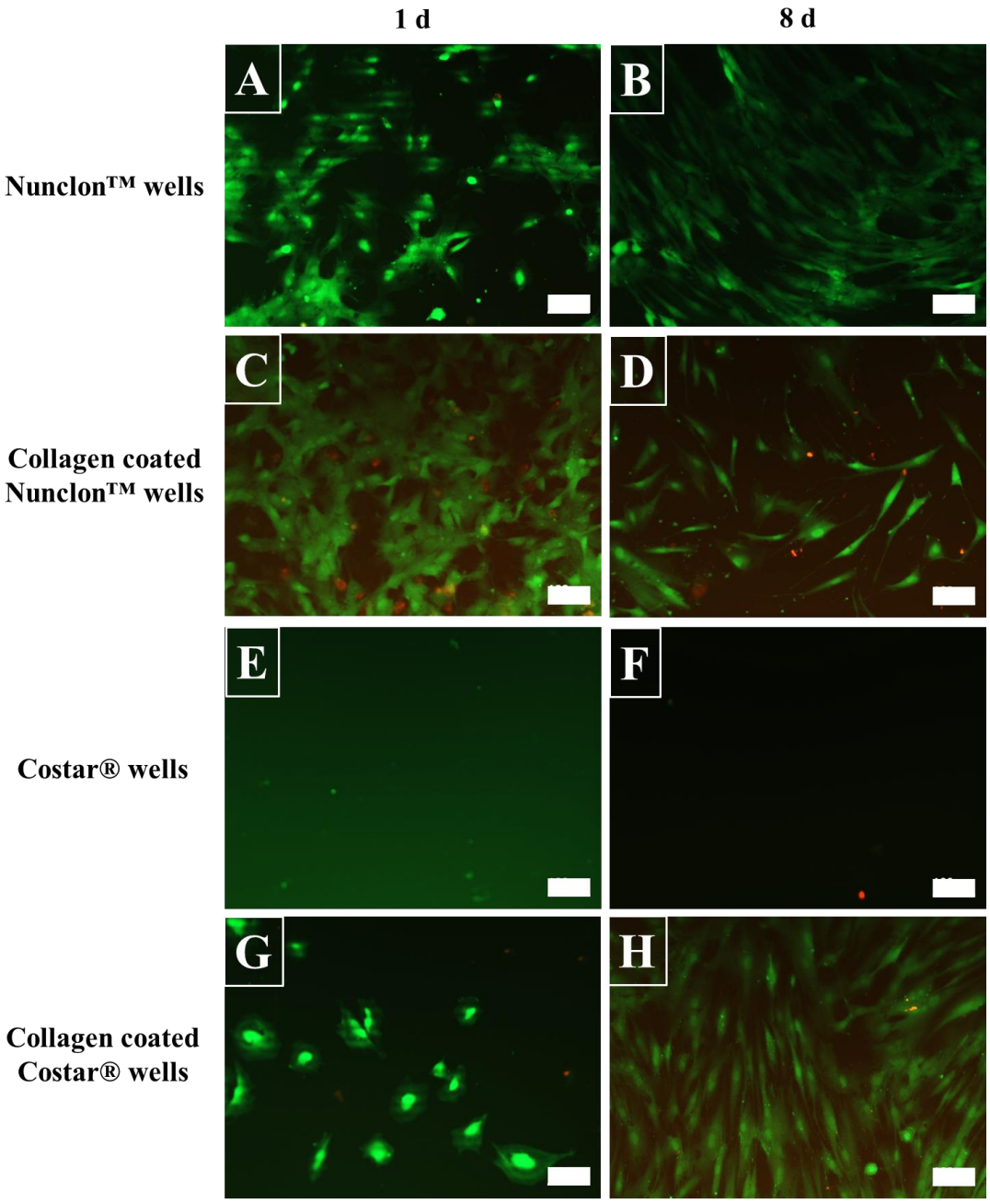


**Figure 43:** Representative Live/Dead images obtained from Nunclon™ wells (**A** and **B**) and the corresponding collagen coating of these wells (**C** and **D**). Costar® wells are depicted in **E** and **F** and collagen coated Costar® wells in **G** and **H**. Collagen coating of wells was achieved by an overnight incubation with 450 µL collagen type I (1/10 dilution of 5.0 mg $mL^{-1}$ collagen type I stock). After washing the wells with PBS, the wells were allowed to dry for 4 h prior to cell seeding (1.2 x $10^5$ hMSCs per well). Cells were allowed to adhere for 6 h. Live/Dead analysis after 1 d (*left column*) and 8 d (*right column*) in culture. Scale bars represent 100 µm.

As expected hMSCs adhered to Nunclon™ (**Figure 43 A** and **B**) and to collagen coated Nunclon™ (**Figure 43 C** and **D**) but not to Costar® wells (**Figure 43 E** and **F**). The absence

of cells on Costar® wells ensured the preferential cellular attachment on scaffolds rather than on polystyrene wells. Successful collagen coating of the wells was indirectly proven by adherent cells to collagen coated Costar® wells (**Figure 43 G** and **H**) and stressed the cell adhesion mediated by collagen. Comparing the well types, generally denser cell networks and more spread cells were detectable after 1 d in culture for Nunclon™ (**Figure 43 A**) and collagen coated Nunclon™ wells (**Figure 43 C**) than for Costar® wells (**Figure 43 E** and **G**). Moreover denser cell networks were found for prolonged culture times and suggested proliferating cells for Nunclon™ (**Figure 43 B**) and collagen coated Costar® wells (**Figure 43 H**).

Furthermore, different scaffold controls were included to assess the possibility of cellular attachments and to ensure the selective adherence of cells on collagen functionalized sP(EO-*stat*-PO) coated scaffolds. The controls therefore were PCL, NCO-hydrolyzed sP(EO-*stat*-PO) coated and irradiated photoleucine functionalized sP(EO-*stat*-PO) coated samples.

As expected hMSCs adhered to PCL scaffolds as these possess a rather hydrophobic surface resulting in unspecific protein adsorption from the cell media, which in turn is hypothesized to function as attractive site for cells (**Figure 44 A** and **B**). This was already proven by Hochleitner and coworkers.[11] The sP(EO-*stat*-PO) coating renders the scaffold surface more hydrophilic and thereby decreases potential protein adsorption, explaining the non-adherent cells for this control in **Figure 44 C** and **D**, which is also in good accordance to the previously cited work. Furthermore, no cell adherence was detectable for photoleucine functionalized sP(EO-*stat*-PO) coated scaffolds (**Figure 44 E** and **F**). The present amino acid derivative in these samples was not sufficient to function as attractive anchor for cellular adhesion. Generally, the cells proliferated throughout the culture period as suggested by denser cellular networks for 8 d (**Figure 44 B**) than for 1 d (**Figure 44 A**).

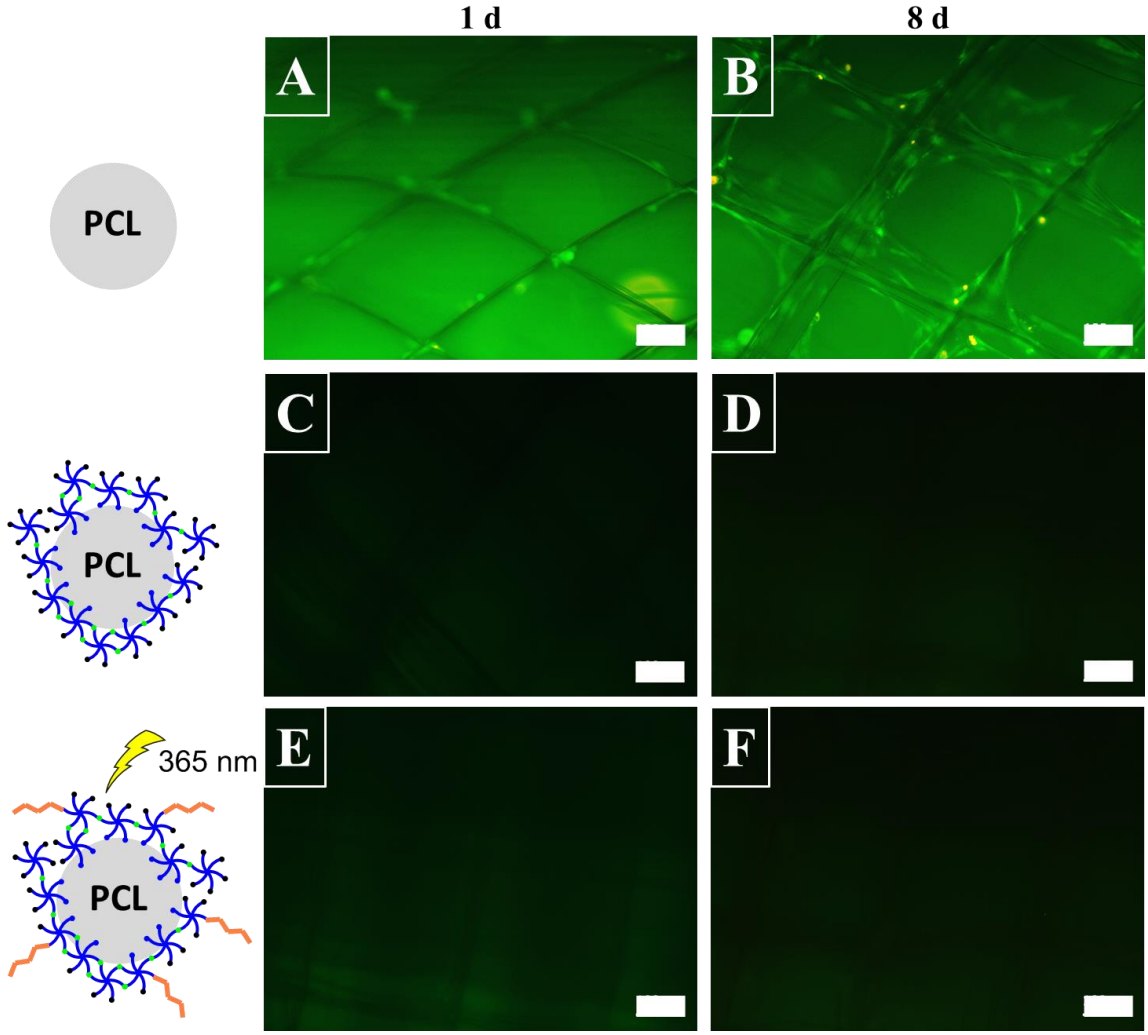


**Figure 44:** Representative Live/Dead images obtained from PCL control (**A** and **B**), NCO-hydrolyzed sP(EO-*stat*-PO) coated (**C** and **D**) and irradiated photoleucine functionalized sP(EO-*stat*-PO) coated scaffolds (**E** and **F**). All scaffolds were placed in Costar® wells. After aqueous pre-wetting, the pre-treatment of PCL scaffolds with 1 M NaOH for 5 min and washing of the scaffolds followed. Afterwards the sP(EO-*stat*-PO) coating was performed (2.0 wt.-% sP(EO-*stat*-PO), for 10 min **C** - **F**). The scaffolds were incubated in water overnight to allow NCO-hydrolysis (**C** and **D**) or the sP(EO-*stat*-PO) solution was replaced with photoleucine ($1.34 \times 10^{-5}$ mol in PBS) for an overnight incubation with subsequent washing with PBS and irradiation with 365 nm for 30 min (**E** and **F**). After washing the scaffolds with PBS, hMSCs were seeded ($1.2 \times 10^5$ cells per well) and allowed to adhere for 6 h. Live/Dead analysis after 1 d (*left column*) and 8 d (*right column*) in culture. Scale bars represent 100 µm.

As positive controls different approaches for the collagen conformation were compared and the cellular adhesion results are depicted in **Figure 45**.

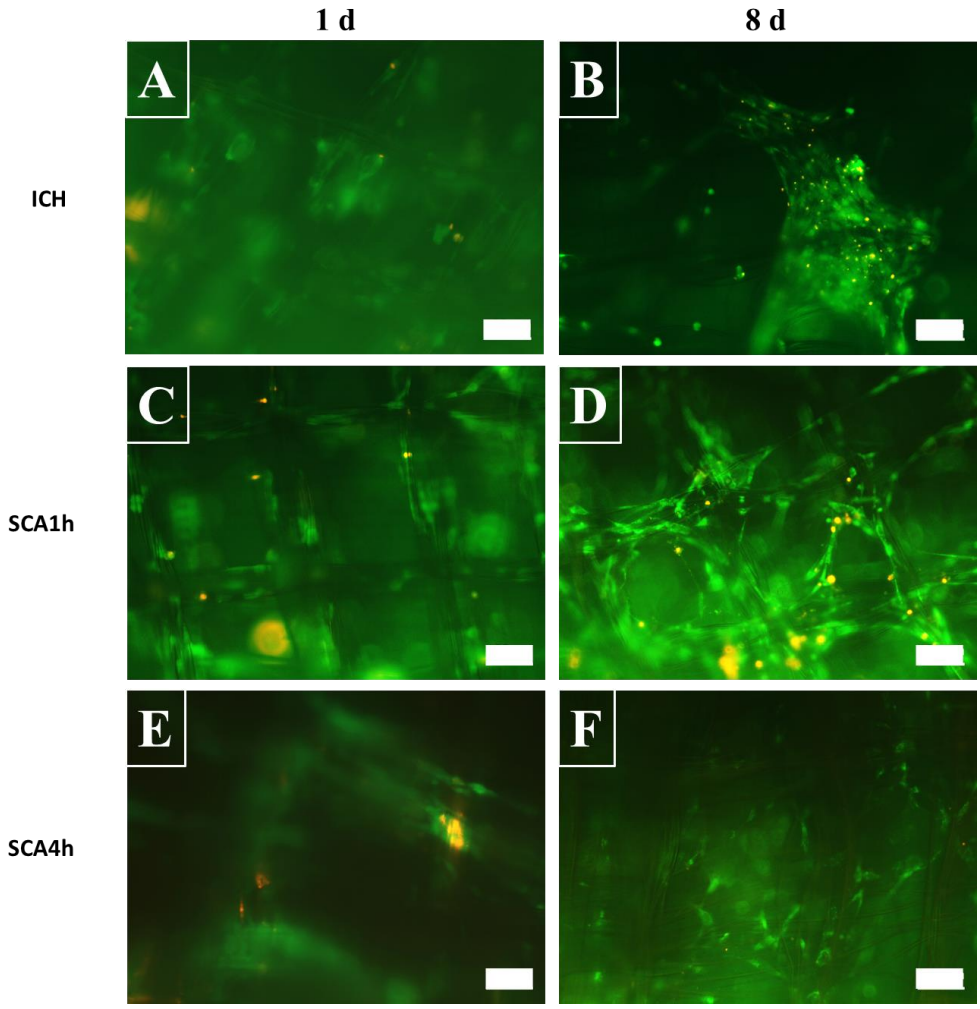


**Figure 45:** Representative Live/Dead images obtained from collagen functionalized sP(EO-*stat*-PO) coated scaffolds with either ICH (**A** and **B**) or SCA (SCA1h in **C** and **D**; and SCA4h in **E** and **F**). All scaffolds were placed in Costar® wells. After aqueous pre-wetting, the pre-treatment of PCL scaffolds with 1 M NaOH for 5 min and washing of the scaffolds followed, prior to sP(EO-*stat*-PO) coating (2.0 wt.-% sP(EO-*stat*-PO), 10 min). Photoleucine solutions ($1.34 \times 10^{-5}$ mol in PBS) replaced the sP(EO-*stat*-PO) after 10 min for an overnight incubation. The scaffolds were washed with PBS and incubated in collagen type I solutions with 200 µg $mL^{-1}$ ($1.67 \times 10^{-9}$ mol in 0.5 M HAc) and irradiated (365 nm, 30 min). The samples were treated accordingly to the ICH or to the SCA approach with fibril formation times of 1 h and 4 h. After washing the scaffolds with PBS, hMSCs were seeded ($1.2 \times 10^{5}$ cells per well) and allowed to adhere for 6 h. Live/Dead analysis after 1 d (*left column*) and 8 d (*right column*) in culture. Scale bars represent 100 µm.

Although in previous experiments ICH could not be quantified on scaffolds and only be detected on unblocked ICH functionalized sP(EO-*stat*-PO) coated scaffolds, an indirect proof of successful ICH functionalization was obtained by the cellular adhesion (**Figure 45 A** and **B**) in addition to the SEM analysis results. In contrast, the incorporation

of amino acid derivatives was not sufficient to induce cellular adhesion, as suggested by the results for irradiated photoleucine functionalized sP(EO-*stat*-PO) coated scaffolds.

The SCA functionalized sP(EO-*stat*-PO) coated scaffolds resulted in comparable cell adhesions without clear differences for the different fibril formation times (**Figure 45 C** and **D** for SCA1h; **Figure 45 E** and **F** for SCA4h). Spread cells were observable in all of the collagen containing samples, comparable to collagen coated wells, and seemed to proliferate during culture period (**Figure 45 D** and **F**).

This study proved the applicability of both collagen conformation approaches on photoleucine functionalized sP(EO-*stat*-PO) coated scaffolds for cell-material interaction studies in minimal protein adhesive environments. These scaffolds provide a platform to study in detail the cellular adhesion mediated by collagen via the activation of DDR receptors with suitable cells.

The advantages of the hydrogel coating with sP(EO-*stat*-PO) on PCL scaffolds are summarized in **Figure 46**.

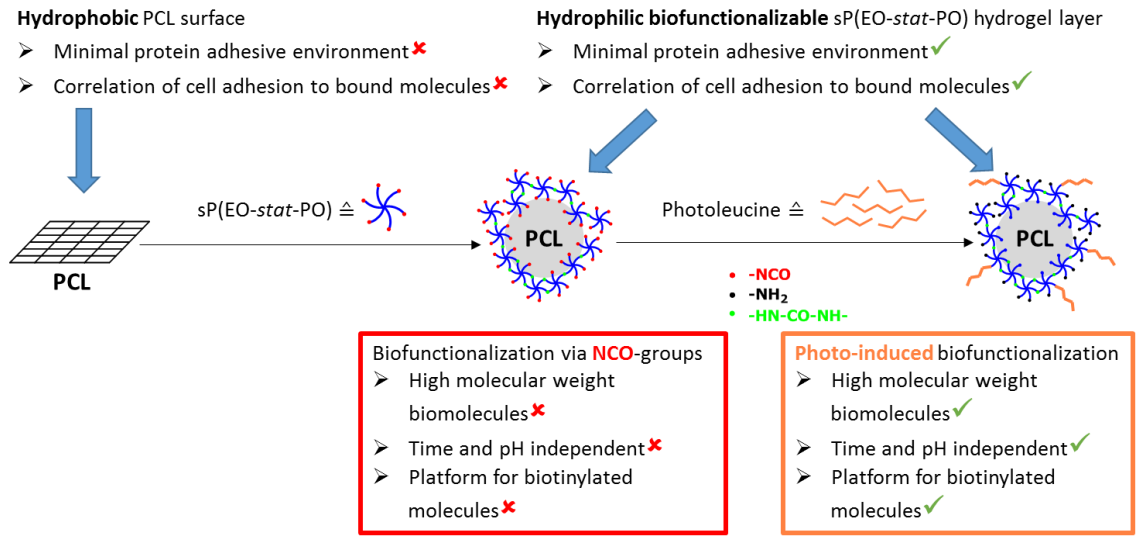


**Figure 46:** Hydrogel coating of PCL scaffolds and subsequent biofunctionalizations. The sP(EO-*stat*-PO) coating results in minimal protein adhesive environments, enabling the correlation of cell adhesion to incorporated molecules, which is contrary to PCL scaffolds. Different bio-functionalization possibilities were established and are based on NCO-reactive moieties of the biomolecules or on a photo-induced reaction. Advantages of the photo-reaction are the capability to bind high molecular weight biomolecules, the pH and time independency as well as the hypothesized provision of a platform to bind biotinylated molecules via streptavidin functionalized scaffolds.

Upon increasing the surface hydrophilicity of the scaffolds via the sP(EO-*stat*-PO) hydrogel coating, a minimal protein adhesive environment is obtained and allows to selectively study the interactions of cells with coupled molecules. To biofunctionalize sP(EO-*stat*-PO) coated scaffolds with low molecular weight molecules, a time and pH dependent reaction with sP(EO-*stat*-PO)-NCO groups is used. The restriction to low molecular weight biomolecules can be overcome by the application of photo-leucine functionalized sP(EO-*stat*-PO) coated scaffolds. Herein, the biofunctionalization is pH independent and decoupled from the limited time frame associated with biofunctionalizations via NCO-groups. Besides the possibility to investigate cellular adhesion on collagen functionalized sP(EO-*stat*-PO) coated scaffolds, the photo-induced reaction pathway is also hypothesized to represent a generic platform to bind any biotinylated molecules via streptavidin functionalized sP(EO-*stat*-PO) coated scaffolds.

## 3.2. Gelatin-based bioinks

In this chapter allyl-modified gelatin (GelAGE) products were combined with a variety of thiol-modified crosslinker to obtain hydrogels via thiol-ene click chemistry. A thorough characterization of GelAGE synthesis parameters, hydrogel characteristics and the applicability as a bioink platform for additive manufacturing (AM) techniques was assessed. Methacryloyl gelatin (GelMA) served as a reference material in this study.

Parts of this chapter are already published in:
S. Bertlein*, G. Brown*, K. S. Lim, T. Jungst, T. Boeck, T. Blunk, J. Tessmar, G. J. Hooper, T. B. F. Woodfield, J. Groll, Thiol-Ene Clickable Gelatin: a Platform Bioink for Multiple 3D Biofabrication Technologies, Advanced Materials, 29 (2017) 1703404.

This work was performed in cooperation with the Christchurch Regenerative Medicine and Tissue Engineering (CReaTE) group of Prof. Dr. Tim Woodfield at the Department of Orthopaedic Surgery and Musculoskeletal Medicine, University of Otago in Christchurch, New Zealand. Gabriella Brown at the aforementioned institute partially performed some of the GelAGE syntheses, the GelMA synthesis, the modification of poly(vinyl alcohol) with AGE, cellular viability and metabolic activity experiments (**Chapter 3.2.4**) and fabrication of GelAGE constructs with stereolithography in New Zealand as well as during an exchange visit in Würzburg.

As well Thomas Böck and Tomasz Jungst from the Department for Functional Materials in Medicine and Dentistry of Prof. Dr. Jürgen Groll at the University of Würzburg were involved in parts of the following experiments. With the help of Tomasz Jungst the extrusion-based printing experiments were conducted and Thomas Böck cultured the cells for GelAGE with macromolecular crosslinkers and performed Live/Dead staining experiments and biological evaluations of cast and printed constructs.

All TNBSA and hydrogel experiments were performed in triplicate ($n = 3$) and statistical evaluation was assessed by one-way ANOVA with post hoc Tukey (SigmaPlot 12.5). Values are presented as the mean ± standard deviation. Significant differences between represented groups are assigned with * ($p < 0.05$) and ** ($p < 0.001$).

### 3.2.1. Syntheses and characterizations of GelAGE

To obtain gelatin-based products which allow crosslinking via the thiol-ene click chemistry to hydrogels, gelatin was modified with allyl glycidyl ether (AGE) to yield GelAGE. The synthesis of GelAGE is based on modifications of previous published protocols for starch[195], chitosan[196, 197] and gelatin[198] and the alkaline-induced epoxide ring-opening. Under these reaction conditions gelatin can also undergo the known side-reaction of peptide-bond hydrolysis resulting in different extends of chain hydrolysis.[199] To gain a deeper insight into the correlation of the synthesis parameters to the products, already published protocols were used as a starting point to further elucidate the AGE functionalization of gelatin.

For this, gelatin was reacted with AGE for 1 – 24 h under alkaline conditions at 65 °C. The products were purified via intensive dialysis steps, finally obtained after freeze drying and stored under light exclusion at 4 °C. Products are termed corresponding to the reaction conditions, e.g. $GelAGE_{8LM}$ refers to an 8 h reaction time, low amounts of NaOH and medium amounts of AGE. Low (L), medium (M) and high (H) amounts correspond to 0.40 mmol, 2.0 mmol and 10 mmol NaOH per g gelatin and 2.4 mmol, 12 mmol and 60 mmol AGE per g gelatin, respectively. GelMA was included as a reference to the observed effects of GelAGE synthesis parameters and to the performance of GelAGE hydrogels.

Before investigating the correlation of the synthesis parameters to the substitution degree (SD) or to the apparent weight-averaged molar mass ($M_w$), the stability of gelatin under the applied reaction conditions was assessed.

#### 3.2.1.1. Degradation of gelatin under alkaline conditions

Important to note is that gelatin is generally obtained with either an acidic or alkaline treatment of collagen, resulting in the degradation of the triple helical collagen structure to individual and smaller gelatin fragments.[199] As the synthesis of GelAGE is conducted under slight to strong alkaline conditions[86, 198] the probability of degrading gelatin into even smaller fragments upon AGE modification has to be considered. Alkaline peptide-bond hydrolysis may occur[199], which could lead to an undesired decrease in chain length i.e. the molar mass and might also compromise latter analytics due to the generation of additional carboxylic acid- and amine-groups per peptide-bond cleavage. Molecular weight changes ultimately influence the mechanical properties of the resulting hydrogels as well

as the rheological properties of precursor solutions. Hence, this study is especially important regarding the optimization of GelAGE synthesis parameters, the later hydrogel properties and ultimately the applicability as bioink.

The gelatin degradation dependence on different synthesis parameters was first investigated with SEC analysis (**Figure 47**). Importantly, the coiling behavior of the samples influences their hydrodynamic radii and hence the SEC-derived $M_w$. To later exclude any potential interferences on the $M_w$ determination for GelAGE samples that could be related to the AGE modification and the introduction of new hydrophobic groups, which can in turn influence the coiling behavior, gelatin controls were first analyzed. Gelatin controls were treated with 2.0 mmol NaOH for 1 – 24 h at 65 °C without AGE ($Gelatin_{1\text{-}24M0}$), purified and lyophilized before being subjected to SEC-analysis.

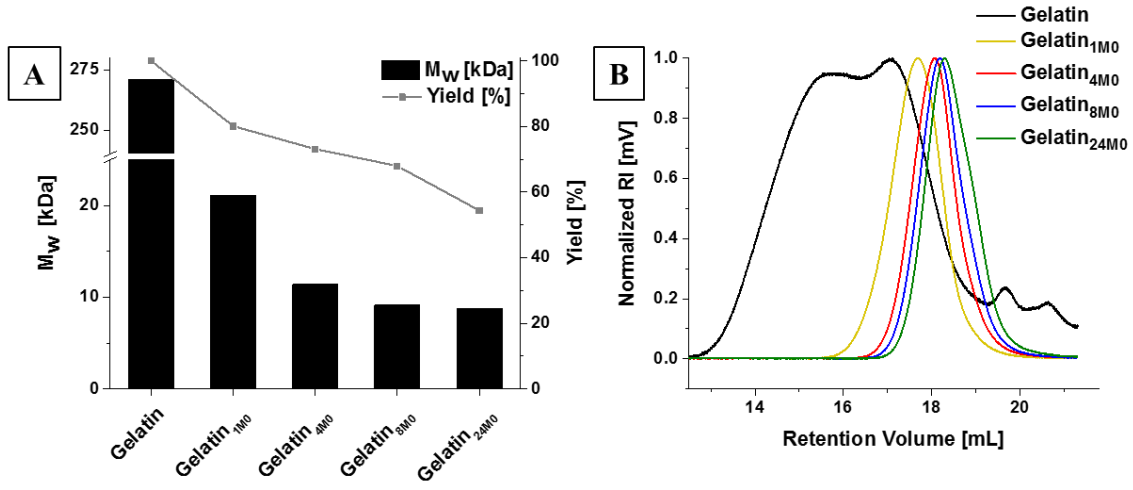


**Figure 47:** Representative apparent weight-averaged molar mass ($M_w$) plot of gelatin and gelatin controls ($Gelatin_{1\text{-}24M0}$) with the respective gelatin product yield (**A**). Black bars represent $M_w$ and grey dots correspond to the material yield. Representative elugrams of gelatin (black line) and gelatin controls with $Gelatin_{1M0}$ (yellow line), $Gelatin_{4M0}$ (red line), $Gelatin_{8M0}$ (blue line) and $Gelatin_{24M0}$ (green line) (**B**). Adapted with permission from Bertlein and coworkers[86]. Copyright (2017) John Wiley and Sons.

Increasing incubation times under alkaline conditions were accompanied by a clear drop of SEC-derived $M_w$ values and the material yield for gelatin controls (**Figure 47 A**). Even for the shortest incubation for $Gelatin_{1M0}$ the $M_w$ tremendously declined to 21 kDa, compared to 271 kDa for the reference gelatin, and only 80 % material was recovered. This trend was more pronounced for longer incubations and decreasing $M_w$ values ($Gelatin_{24M0}$ with 8.8 kDa) correlated with further reductions of the material yield ($Gelatin_{24M0}$ with 54 %) as the smaller reaction by-products were eventually removed during purification via dialysis.

These results were supported by a concurrent narrowing of the dispersity with increasing incubation times and a shift towards higher retention volumes (**Figure 47 B**) and suggest the pronounced degradation of gelatin under alkaline reaction conditions. This degradation was less prominent for $Gelatin_{1M0}$ than for other samples, due to the shortest incubation time.

To further investigate the molecular weight distribution, SDS-PAGE analysis was conducted. Whereas the samples are not denatured for SEC analysis, SDS-PAGE analysis is performed under additional reducing conditions i.e. addition of β-mercaptoethanol, heating to 95 °C and inclusion of the detergent sodium dodecyl sulfate (SDS). To break disulfide bridges β-mercaptoethanol is added and in combination with boiling and detergent, the proteins tertiary structure is disrupted and results in unfolded linear molecules. Moreover, SDS uniformly coats proteins with negative charges masking intrinsic charges of the proteins. These conditions ensure that linear, uniformly charged molecules can be separated by the applied electrical field in dependence on their molecular weight, which is proportional to the proteins length. In contrast to SEC analysis, which strongly depends on the hydrodynamic radii, SDS-PAGE analysis is rather independent from the molecular radii. This implies that no direct correlation of SEC-derived $M_w$ values to SDS-PAGE determined molecular weight distributions can be obtained, but the trend of alkaline induced degradation of gelatin during the simulated synthesis conditions should be maintained.

Compared to the gelatin reference (**Figure 48**, lane 2) the degradation of gelatin controls is reflected by a broadening of the migration patterns and a shift towards lower molecular weight distributions (**Figure 48**, lanes 3 – 6). The degradation seemed less prominent for the shortest incubation for $Gelatin_{1M0}$ and increased with longer incubation times.
Due to the broad migration pattern distributions no conclusion about defined molecular weight distributions were drawn, instead these results further supported the observations from SEC analysis and implied that a higher degree of gelatin degradation occurred for longer reaction times due to broader distributions and lower molecular weight distributions of the smallest gelatin fragments.

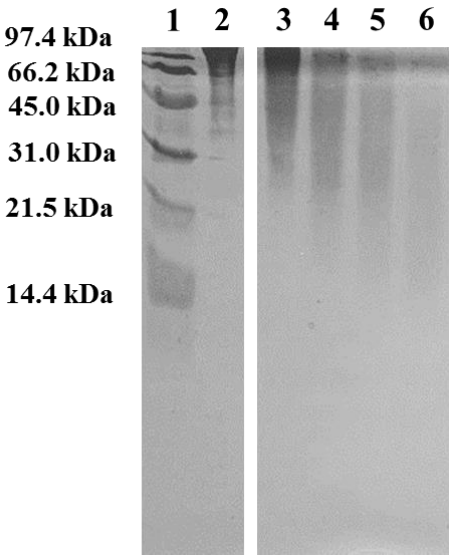


**Figure 48:** Representative SDS-PAGE gel (18.0 wt.-%) of gelatin and gelatin controls ($Gelatin_{1\text{-}24M0}$). Electrophoretic migration patterns of the low molecular weight marker (lane 1), gelatin (lane 2), $Gelatin_{1M0}$ (lane 3), $Gelatin_{4M0}$ (lane 4), $Gelatin_{8M0}$ (lane 5) and $Gelatin_{24M0}$ (lane 6). 8.0 µL marker were loaded from a 1/10 dilution with sample buffer. 15.0 µg of gelatinous samples were loaded per well. SDS-PAGE gels were stained with Coomassie blue R-250 and destained with a mixture of HAc/MeOH/water of 7.5/20/72.5 (v/v).

Moreover, gelatin controls were compared to the gelatin reference with $^{1}$H-NMR spectroscopy and with quantitative amino acid analysis (qASA) to assess possible compositional differences, resulting from alkaline hydrolyzed peptide bonds. Some amino acid sequences, e.g. bonds between hydrophobic amino acids are known to be rather stable to hydrolysis[200] and could result in the preferential loss of specific amino acid sequences.

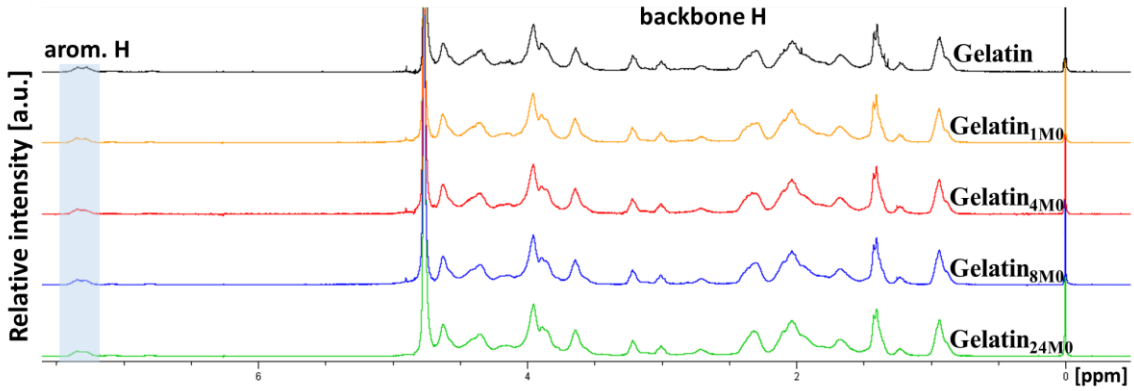


**Figure 49:** Representative $^{1}$H-NMR spectra of gelatin (black line) and gelatin controls with $Gelatin_{1M0}$ (yellow line), $Gelatin_{4M0}$ (red line), $Gelatin_{8M0}$ (blue line) and $Gelatin_{24M0}$ (green line). Blue box highlights the aromatic proton signals (7.4-7.3 ppm) arising from phenylalanine.

No differences of the $^{1}$H-NMR spectra between reference and gelatin controls (Gelatin$_{1\text{-}24M0}$) were observable (**Figure 49**) and suggested no preferential amino acid loss.

Quantitative amino acid analysis of gelatin and the gelatin controls (Gelatin$_{1\text{-}24M0}$) was performed by Frank Gutjahr Chromatographie (Balingen, Germany) (**Table 5**). Tryptophan is usually degraded during the acid hydrolysis procedure for qASA[201] and hence these Mol-% were neglected in the following table and account for the inequality to 100 Mol-%.

**Table 5:** Quantitative amino acid analysis (qASA) results for gelatin and gelatin controls (Gelatin$_{1\text{-}24M0}$).

| **Incubation [h] with medium (M) NaOH amounts** | **Gelatin** **/** | **Gelatin$_{1M0}$** **1** | **Gelatin$_{4M0}$** **4** | **Gelatin$_{8M0}$** **8** | **Gelatin$_{24M0}$** **24** |
|---|---|---|---|---|---|
| **Amino acid** | **[Mol-%]** | **[Mol-%]** | **[Mol-%]** | **[Mol-%]** | **[Mol-%]** |
| Aspartate | 4.45 | 4.48 | 4.49 | 4.63 | 4.55 |
| Threonine | 1.43 | 1.39 | 1.34 | 1.36 | 1.22 |
| Serine | 2.73 | 2.56 | 2.57 | 2.52 | 2.20 |
| Glutamate | 7.45 | 7.34 | 7.72 | 7.87 | 7.82 |
| Hydroxyproline | 8.05 | 7.73 | 8.46 | 8.23 | 8.19 |
| Proline | 13.7 | 14.0 | 13.8 | 13.8 | 13.9 |
| Glycine | 33.4 | 33.6 | 33.7 | 33.2 | 34.2 |
| Alanine | 11.7 | 11.8 | 11.7 | 11.5 | 11.7 |
| Valine | 2.34 | 2.53 | 2.25 | 2.30 | 2.23 |
| Methionine | 0.56 | 0.55 | 0.53 | 0.54 | 0.55 |
| Isoleucine | 0.93 | 0.92 | 0.90 | 0.96 | 0.88 |
| Leucine | 2.48 | 2.42 | 2.41 | 2.58 | 2.45 |
| Tyrosine | 0.36 | 0.31 | 0.32 | 0.45 | 0.38 |
| Phenylalanine | 1.32 | 1.34 | 1.31 | 1.40 | 1.35 |
| Histidine | 0.64 | 0.42 | 0.54 | 0.79 | 0.81 |
| Hydroxylysine | 0.59 | 0.55 | 0.53 | 0.55 | 0.51 |
| Lysine | 2.70 | 2.73 | 2.60 | 2.56 | 2.42 |
| Arginine | 4.93 | 4.95 | 4.66 | 4.65 | 4.42 |
| **Sum** | **99.8** | **99.5** | **99.8** | **99.9** | **99.8** |

The samples did not significantly differ in their amino acid composition as revealed by qASA results (**Table 5**).
Hence, both $^{1}$H-NMR spectra and qASA results suggest that no preferential amino acids were lost after alkaline treatment and the subsequent purification via dialysis.

To conclude the experiments regarding gelatins stability under simulated reaction conditions, the longer the incubation under alkaline conditions the smaller the gelatinous fragments and the lower the material yield. Reaction times longer than 4 h only led to minor reductions of the apparent $M_w$. Analysis with $^{1}$H-NMR spectroscopy and qASA could not further support any compositional differences between gelatin and gelatin controls, suggesting the alkaline treatment to solely determine the chain length, but not the composition which is later relevant to control the SD for GelAGE.

### 3.2.1.2. Reaction sites of gelatin for AGE functionalization

AGE functionalization of gelatin can involve multiple amino acids as all potentially nucleophilic side-chains are prone to bind AGE. The complex amino acid composition of gelatin results in the presence of a variety of functional groups.[202, 203] Herein, potentially reactive hydroxyl- (serine, threonine), carboxyl- (aspartic acid, glutamic acid) and nucleophilic nitrogen- (lysine, histidine and tryptophan) groups are of specific interest. Hence, model substances bearing these functional groups were used to elucidate possible reaction sites along the gelatin backbone and their reactivity towards AGE modification. Polyfunctional model polymers were namely pVA (poly(vinyl alcohol)), pAA (poly(acrylic acid) and pAAm (poly(allylamine)).

Although pAAm is not ideal to model histidine and tryptophan moieties, it was nonetheless judged as suitable as the histidine content (0.9 %) of gelatin is significantly lower than the lysine content (4.1 %)[203] and as the tryptophan content of gelatin remains arguable, due to the already mentioned problems associated with the qASA-detection. Hence, to include amine moieties for AGE functionalization of gelatin, pAAm seemed reasonable as model polymer. The molecular structures of the amino acids in comparison to pAAm are given in **Scheme 13**.

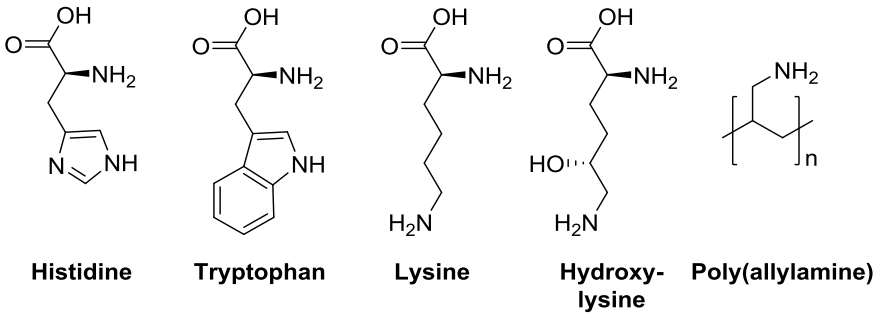


**Scheme 13:** Molecular structures of histidine, tryptophan, lysine, hydroxylysine and poly(allylamine) (pAAm).

A reaction time of 4 h at 65 °C and medium amounts of NaOH and AGE were used for the model polymer modifications (equally to $GelAGE_{4MM}$). Products were subsequently analyzed with $^{1}$H-NMR spectroscopy and in case of pAAm and pAAm-AGE via IR spectroscopy.

The pAAm-AGE product was rendered insoluble upon modification in $D_2O$, $CDCl_3$ and DMSO-*d6* and restricted the applicability of NMR spectroscopy. Therefore, no conclusions about the SD value could be drawn. However, a successful modification could be proven by IR spectroscopy via the appearance of additional bands in the region of 925 – 990 $cm^{-1}$, which can be assigned to allyl functionalities (**Figure 50**, red line for pAAm-AGE).

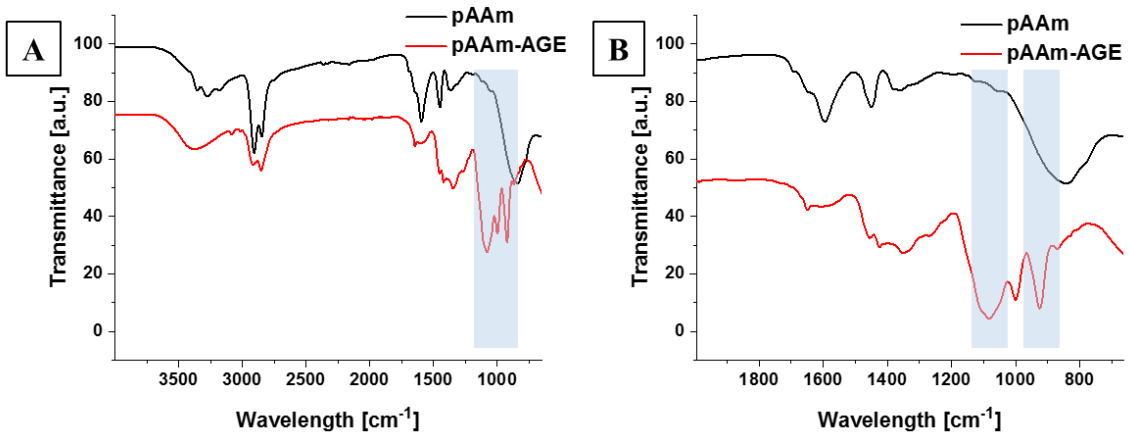


**Figure 50:** Overlay of representative IR spectra of pAAm (black line) and pAAm-AGE (red line) (**A**) and a more detailed view of the region from 2000 – 660 $cm^{-1}$ (**B**). Blue boxes highlight the wavelength area of allyl peaks at 925 – 990 $cm^{-1}$.

The insolubility of pAAm-AGE was attributed to an increase in hydrophobicity as a consequence of a high SD and to a premature crosslinking of this product. The other two

model polymer products, namely pVA-AGE and pAA-AGE, were soluble and accessible for $^{1}$H-NMR spectroscopy. In both cases peaks in the region from 6.1-5.8 ppm and 5.5-5.1 ppm could be correlated to allyl functionalities and corresponding SD values were determined to be 13.0 % for pVA-AGE (**Figure 51**) and 10.8 % for pAA-AGE (**Figure 52**).

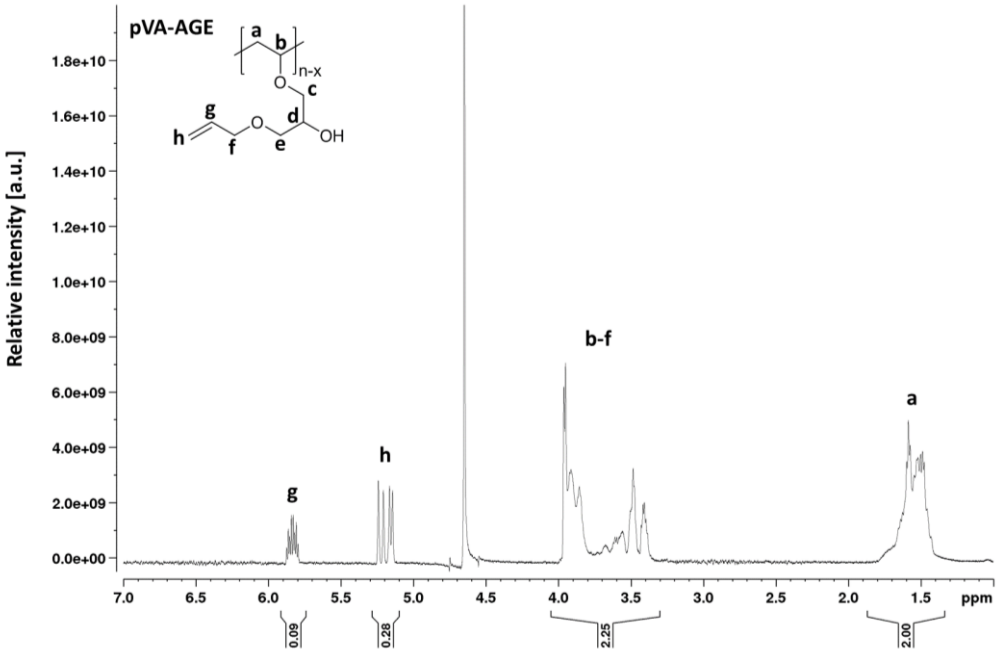


**Figure 51:** Representative $^{1}$H-NMR spectrum of pVA-AGE in $D_2O$. SD = 13.0 %.

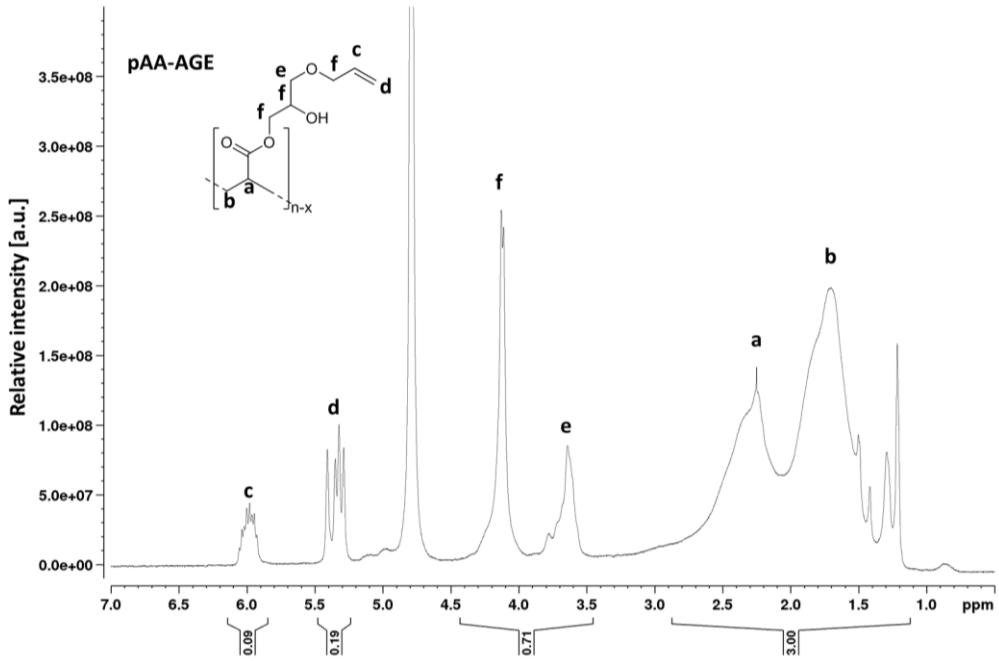


**Figure 52:** Representative $^{1}$H-NMR spectrum of pAA-AGE in $D_2O$. SD = 10.8 %.

Based on the hypothesized high SD of pAAm-AGE and the SD values for pVA-AGE and pAA-AGE, it could be suggested that amine functionalities possess the highest reactivity compared to hydroxyl and carboxyl groups under the given reaction conditions. This is in good accordance to the literature suggested epoxy-modification of gelatin via its amine groups.[198, 204, 205]

### 3.2.1.3. Functionalization of gelatin with AGE

An optimization study of AGE functionalization of gelatin was performed with varying reaction durations and molar ratios of reactants. Varied reaction conditions and corresponding SD values, as determined via $^{1}$H-NMR spectroscopy, are depicted in **Table 6**.

An exemplary $^{1}$H-NMR spectrum of $GelAGE_{1MM}$ with a SD of 42 % is demonstrated in **Figure 53** and the newly formed peaks in the region of 6.1-5.9 ppm and 5.4-5.2 ppm suggested the successful modification of gelatin with AGE. Calibration was performed based on the aromatic protons of phenylalanine.

**Table 6:** Different synthesis parameters for GelAGE and the corresponding SD values, as derived from $^{1}$H-NMR spectra. Adapted with permission from Bertlein and coworkers[86]. Copyright (2017) John Wiley and Sons.

| Sample | NaOH [mmol per g gelatin] | AGE [mmol per g gelatin] | Molar ratio NaOH:AGE | Reaction duration [h] | SD [%] |
|---|---|---|---|---|---|
| $GelAGE_{8LL}^{+)}$ | 0.40 | 2.4 | 1:6 | 8 | 24 |
| $GelAGE_{24LL}^{+)}$ | 0.40 | 2.4 | 1:6 | 24 | 25 |
| $GelAGE_{8LM}^{+)}$ | 0.40 | 12 | 1:30 | 8 | 35 |
| $GelAGE_{24LM}^{+)}$ | 0.40 | 12 | 1:30 | 24 | 36 |
| $GelAGE_{1MM}^{+)}$ | 2.0 | 12 | 1:6 | 1 | 42 |
| $GelAGE_{4MM}^{+)}$ | 2.0 | 12 | 1:6 | 4 | 62 |
| $GelAGE_{8MM}^{+)}$ | 2.0 | 12 | 1:6 | 8 | 69 |
| $GelAGE_{24MM}^{+)}$ | 2.0 | 12 | 1:6 | 24 | 72 |
| $GelAGE_{8MH}^{+)}$ | 2.0 | 60 | 1:30 | 8 | 92 |
| $GelAGE_{8HH}^{+)++)}$ | 10 | 60 | 1:6 | 8 | 124 |

$^{+)}$ L= low, m= medium, h= high amount; $^{++)}$ effect of additional N-termini on SD

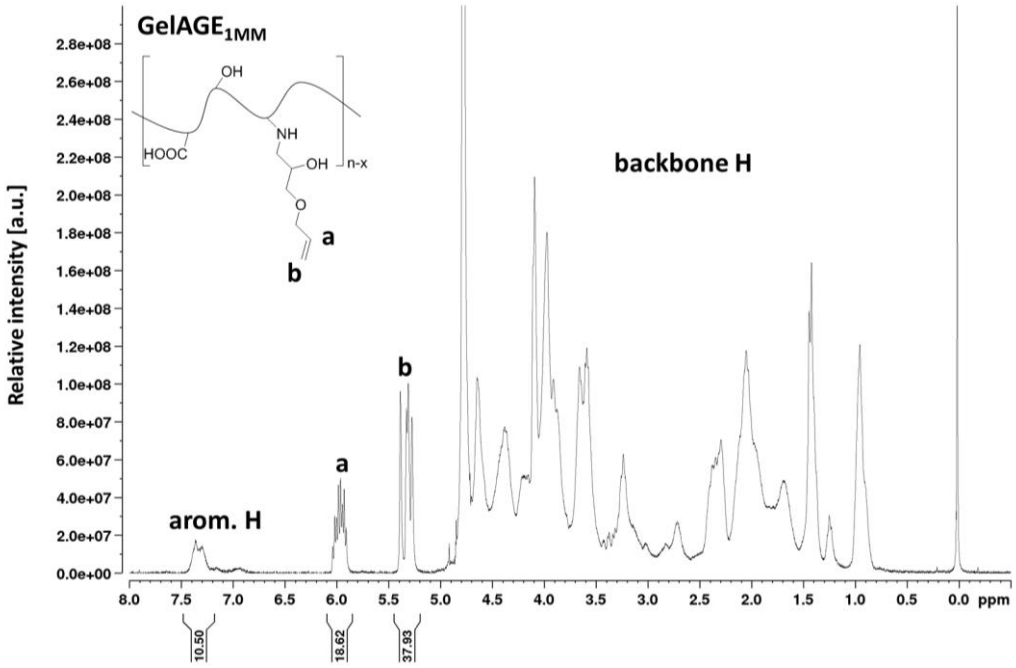


**Figure 53:** Representative $^{1}$H-NMR spectrum of GelAGE$_{1MM}$ in $D_2O$. SD = 42 %.

As previous results for model polymers and already published data for gelatin[198, 204, 205] both indicate the predominant functionalization of gelatin with AGE via amine functionalities, special interest gained the investigation of the extent of functionalized amines with the TNBSA assay.

Two parameters are crucial to determine the extent of AGE modification of GelAGE samples. As the already mentioned peptide-bond cleavage occurs during AGE modification, the amine and carboxylic content rise during the reaction course by increasing numbers of N-terminal amines and C-terminal carboxylic groups. Hence, first the amine-consumption of all amines, including newly formed N-terminal amines, was investigated with the TNBSA assay and this corresponds to the degree of amine-modification (percentage of functionalized amines). Second, the direct determination of newly introduced allyl-content is mandatory as well and was assessed with $^{1}$H-NMR spectroscopy. In this case only the theoretical number of available amines (lysine and hydroxylysine) and the nucleophilic nitrogen bearing amino acid histidine, based on the amino acid composition of gelatin, are taken into account without considering newly formed N-terminal amines. The amino acid composition of gelatin was based on the GMIA handbook[203] and the theoretical SD was calculated.

Determination of the amine-consumption of gelatin upon AGE modification with the TNBSA assay was used to quantify the percentage of functionalized amines including newly formed N-terminal amines, which were quantified from gelatin controls. To exemplarily obtain these percentages, the µmol $NH_2$ content per g gelatin of $GelAGE_{1\text{-}24MM}$ samples was correlated to the corresponding gelatin controls ($Gelatin_{1\text{-}24M0}$). After standard assay procedure the absorption was measured at 335 nm.

**A**

| Sample | $NH_2$ [µmol per g gelatin] |
|---|---|
| $Gelatin_{1M0}$ | 46.9 ± 5.5 |
| $Gelatin_{4M0}$ | 48.2 ± 6.3 |
| $Gelatin_{8M0}$ | 186.5 ± 68.6 |
| $Gelatin_{24M0}$ | 276.3 ± 18.2 |

**B**

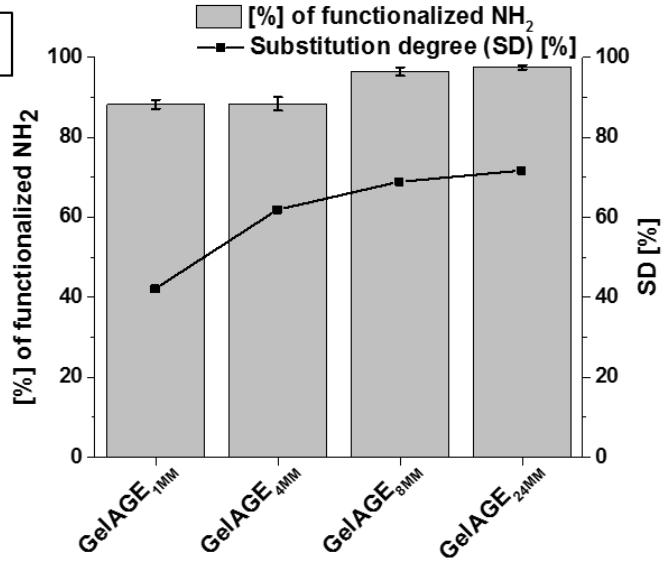


**Figure 54:** TNBSA assay results for the amine content of gelatin controls ($Gelatin_{1\text{-}24M0}$) (**A**). Representative overview of the percentage of functionalized amine groups of $GelAGE_{1\text{-}24MM}$ (grey bars) derived from the TNBSA assay and the corresponding SD values (black dots), as determined with $^1$H-NMR spectroscopy (**B**). Percentage of functionalized amines correlates to overall amine content of gelatin controls ($Gelatin_{1\text{-}24M0}$). Adapted with permission from Bertlein and coworkers[86]. Copyright (2017) John Wiley and Sons.

The amine content for gelatin controls ($Gelatin_{1\text{-}24M0}$) increased with longer reaction times (**Figure 54 A**, from $Gelatin_{1M0}$ with 46.9 ± 5.5 µmol $NH_2$ per g gelatin to $Gelatin_{24M0}$ with 276.3 ± 18.2 µmol $NH_2$ per g gelatin). These results supported the alkaline induced peptide-bond cleavage hypothesis and the concurrent rising number of available N-terminal amine moieties.

Considering the percentage of functionalized amines it could be concluded that all amines, including newly formed N-terminal amines, were almost equally efficient functionalized (**Figure 54 B**, 88 % for $GelAGE_{1MM}$ and 97 % for $GelAGE_{24MM}$ grey bars). However, the slight increase of this percentage with prolonged reaction times concurrent to an increased numbers of peptide-bond-cleaved N-terminal amines further supports the hypothesis of the predominant amine functionalization of gelatin with AGE. Generally, the SD increased concurrent with the reaction time from 42 % SD for $GelAGE_{1MM}$ to 72 % SD for $GelAGE_{24MM}$ (**Figure 54 B**, black dots). The SD clearly increased from $GelAGE_{1MM}$ (42 % SD) to $GelAGE_{4MM}$ (62 % SD), although the percentage of functionalized amines remained constant (88 % for both $GelAGE_{1MM}$ and $GelAGE_{4MM}$). This raise of SD values could be explained by the theoretical assumption of an amount of certain amino acids, which correlate to the number of available functional groups without taking newly formed N-terminal amines into account.

To conclude, longer reaction durations result in increased numbers of amine groups due to peptide-bond cleavages and consequently to higher SD values, but the degradation of gelatin can e.g. influence the hydrogels mechanical stiffness or the rheological behavior of the products, which is important for the application as bioink for distinct AM techniques.

Furthermore, the determination of amine-consumption of gelatin upon AGE modification was used to quantify residual free amines, which were not modified with AGE. A general overview of the TNBSA assay results of the µmol $NH_2$ per g gelatin of all other GelAGE samples is depicted in **Figure 55 A** without correlation to gelatin controls.

At constant molar ratios of reactants, the amine content of $GelAGE_{8LL}$ with 168.1 ± 40.7 µmol $NH_2$ per g gelatin decreased with prolonged reaction durations to $GelAGE_{24LL}$ with 93.0 ± 39.2 µmol $NH_2$ per g gelatin (**Figure 55 A**). The same trend was found for $GelAGE_{8LM}$ and $GelAGE_{24LM}$. For GelAGE samples which were treated with medium amounts of NaOH and AGE ($GelAGE_{1\text{-}24MM}$), no significant differences of the amine contents were detectable. These data were in good accordance to the obtained differences of SD values (**Table 6**). Only for the harsh reaction conditions for $GelAGE_{8HH}$ an increase in amine content was detectable and is later addressed in more detail (see p. 103).

Based on these results it was concluded that higher molar ratios of reactants and prolonged reaction durations resulted in a decrease of residual free amines and subsequently in a higher amount of functionalized amines.

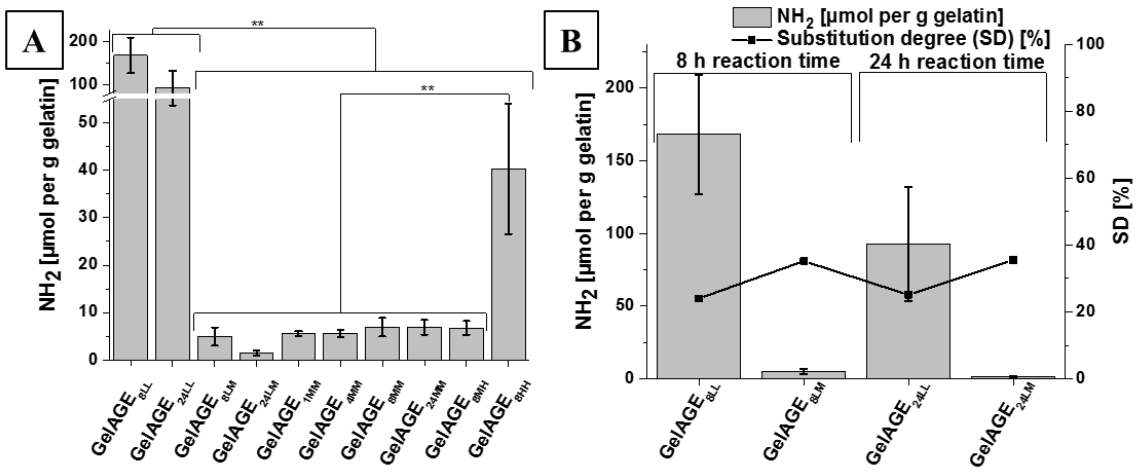


**Figure 55:** Overview of the TNBSA assay results of the amine content of GelAGE samples (**A**) and the direct comparison of the correlation of the SD (black dots) to the amine content of GelAGE (grey bars) (**B**). Adapted with permission from Bertlein and coworkers[86]. Copyright (2017) John Wiley and Sons.

GelAGE synthesis requires alkaline conditions, which are known to degrade gelatin and as a result of peptide-bond hydrolysis liberate additional amine functions[199] as already proven for gelatin controls ($Gelatin_{1\text{-}24M0}$). However, samples that were treated under constant alkaline conditions but with an increased amount of AGE, resulted in lower amine contents and higher SD values. This can be seen for e.g. $GelAGE_{8LL}$ with 168.1 ± 40.7 µmol $NH_2$ per g gelatin (24.0 % SD) compared to $GelAGE_{8LM}$ with 4.9 ± 1.9 µmol $NH_2$ per g gelatin (35.2 % SD) and for 24 h reaction times (**Figure 55 B**). The release of additional amines remains constant and can be neglected for these specific experimental conditions and further underlines the hypothesis of the predominant amine functionalization of gelatin with AGE, thereby reducing the amount of residual free amine groups.

It could be concluded that the functionalization of gelatin with AGE predominantly involves the amine functionalities and proved the SD calculations of GelAGE samples, which were based on the amounts of lysine, hydroxylysine and histidine to reflect the trend of AGE modification quite well (**Figure 56**).

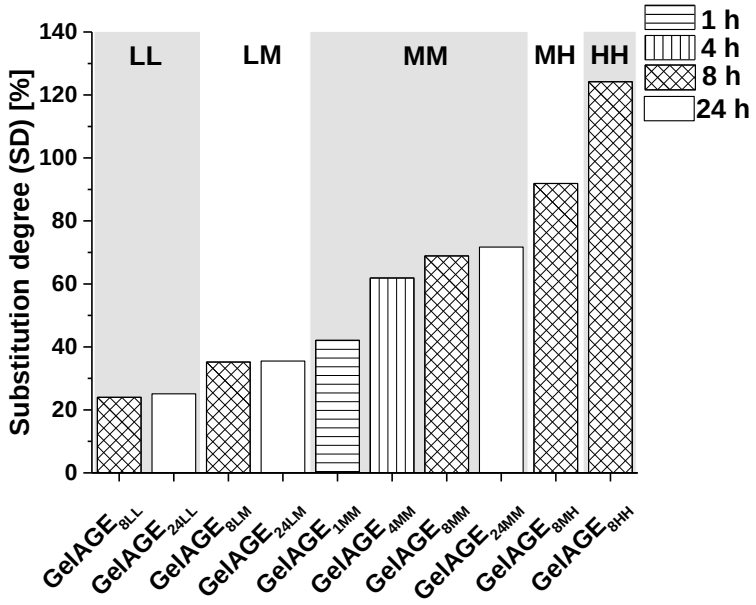


**Figure 56:** Representative correlation of SD values of GelAGE samples to different synthesis parameters. Reaction times are depicted by subscripted digits (1 h bars filled with horizontal stripes, 4 h with vertical stripes, 8 h with crosses and 24 h are represented by unfilled bars). The other subscripts refer to the amounts of NaOH and AGE. Low (L), medium (M) and high (H) amounts correlate to 0.40 mmol, 2.0 mmol and 10 mmol NaOH per g gelatin and to 2.4 mmol, 12 mmol and 60 mmol AGE per g gelatin.

The SD values of GelAGE samples ranged from 24.0 – 124 % and could be controlled by varying NaOH:AGE ratios and reaction intervals (**Table 6** and **Figure 56**). Whereas the highest increase in SD values was observable within the first 4 h reaction time ($GelAGE_{1MM}$ with 42 % SD to $GelAGE_{4MM}$ with 62 % SD), prolonged reaction durations from 8 h to 24 h could not clearly improve the SD values ($GelAGE_{8MM}$ with 69 % SD and $GelAGE_{24MM}$ with 72 % SD). Longer reaction intervals (24 h) could also not significantly improve SD values of GelAGE compared to 8 h with other combinations of NaOH:AGE ratios. Maintaining the alkaline conditions while increasing the AGE amount led to an increase in SD (e.g. $GelAGE_{8MM}$ with 69 % SD to $GelAGE_{8MH}$ with 92 % SD) suggesting a higher modification efficacy. Improved SD values were also obtained at constant AGE concentrations by increasing NaOH amounts ($GelAGE_{24LM}$ with 36 % SD and $GelAGE_{24MM}$ with 72 % SD). Various possibilities to control SD values were determined and suitable reaction condition combinations depend on the intended application of GelAGE samples, as higher amounts of NaOH and longer reaction times increase the peptide-bond hydrolysis rate and thus clearly reduce the $M_w$ as well as the viscosity of gelatin solutions.

Extreme alkaline conditions for $GelAGE_{8HH}$ resulted in an unusually high SD of 124 % (**Table 6** and **Figure 56**). This could be explained by the liberation of a high number of additional N-terminal amine groups as a result of peptide-bond hydrolysis.[199] To support this hypothesis another TNBSA assay experiment with non-modified $Gelatin_{8H0}$ was performed and compared to the untreated gelatin reference.

An increase of 68 % of additionally available amine groups was observed for $GelAGE_{8H0}$ (430 ± 19.8 µmol per g gelatin) compared to the reference gelatin (256 ± 58.0 µmol per g gelatin) and correlated to newly formed N-terminal residual amines as a consequence of peptide-bond hydrolysis. Another possibility to explain the high SD of $GelAGE_{8HH}$ is via multiple lysine conjugations as the monofunctionalization yields secondary amines, which are still prone to be modified with further AGE molecules. These monofunctionalized products in turn render the amine more nucleophilic after the first modification. The probability of multiple functionalization raises with increasing reaction durations and AGE amounts and no further optimization of the SD values with the harsh conditions for $GelAGE_{8HH}$ was performed.

However, it has to be noted that the results for the model polymers pVA-AGE and pAA-AGE also indicate that gelatin could in principle as well be modified via its hydroxyl and carboxylic groups. Especially for longer reaction times of 24 h an interplay of newly formed and functionalized amines together with modifications at hydroxyl and carboxylic groups could probably be expected. The complex amino acid composition of gelatin[202, 203] together with the aforementioned results, suggest the calculation of SD values based on the theoretical amounts of available amines to reflect the trend of increasing AGE modifications quite well.

IR spectroscopy was performed to further prove the successful allyl-functionalization of GelAGE products.

The successful modification of gelatin with AGE was characterized by the appearance of two additional peaks at around 925 $cm^{-1}$ and 990 $cm^{-1}$, which correspond to allyl functionalities (**Figure 57 A**). Additionally the trend to more intense bands concurrent with increasing SD values was detectable (**Figure 57 B**).

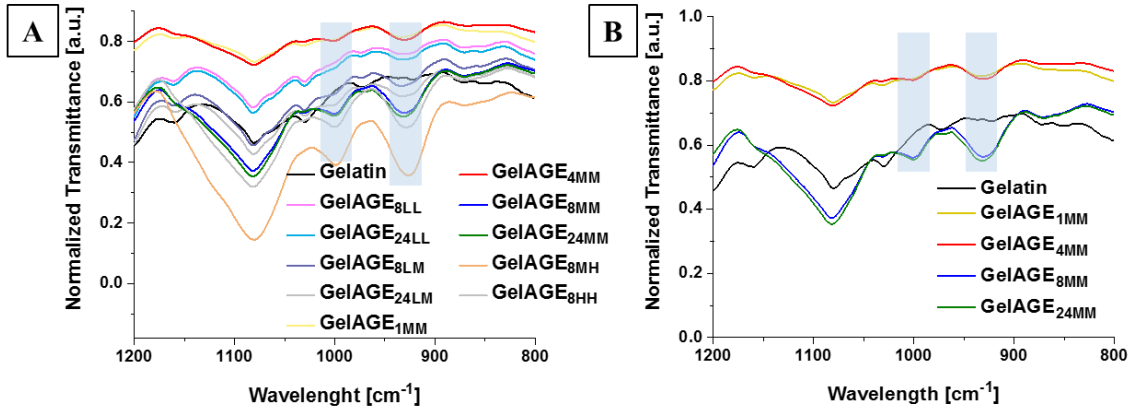


**Figure 57:** Representative IR spectra of gelatin and GelAGE samples (**A**). Comparison of gelatin (black line) with the complete time course of $GelAGE_{1\text{-}24MM}$ modifications in (**B**) with $GelAGE_{1MM}$ (yellow line), $GelAGE_{4MM}$ (red line), $GelAGE_{8MM}$ (blue line) and $GelAGE_{24MM}$ (green line). Blue boxes highlight the wavelength area of allyl peaks from 925 – 990 $cm^{-1}$.

Different GelAGE samples were furthermore investigated with SEC analysis to gain more insight into the correlation of the synthesis parameters to the corresponding SD values and to the apparent $M_w$ of GelAGE samples. GelMA was included as reference for the following experiments.

Considering first the comparison of both differently modified gelatin products, GelMA exhibited comparable high $M_w$ values as $GelAGE_{8LL}$ (**Figure 58 A**). This could be attributed to the rather neutral to slight acidic synthesis conditions of GelMA[125] and to the concurrent less pronounced gelatin backbone degradation, similar to the mildest reaction conditions for $GelAGE_{8LL}$. However, the sample coiling significantly influences the apparent $M_w$ determined by SEC analysis. GelMA and GelAGE are modified with distinct functional groups, which could result in different coiling behaviors further complicating conclusions on $M_w$-differences between these samples. Whereas, GelMA modification results in the introduction of amide groups, GelAGE functionalization results in secondary amine moieties and effects on the coiling behavior arising from differently protonated gelatin samples can most probably be neglected as the aqueous solvent was neutral (water supplemented with 0.1 M $NaNO_3$ and 0.02 wt.-% $NaN_3$).

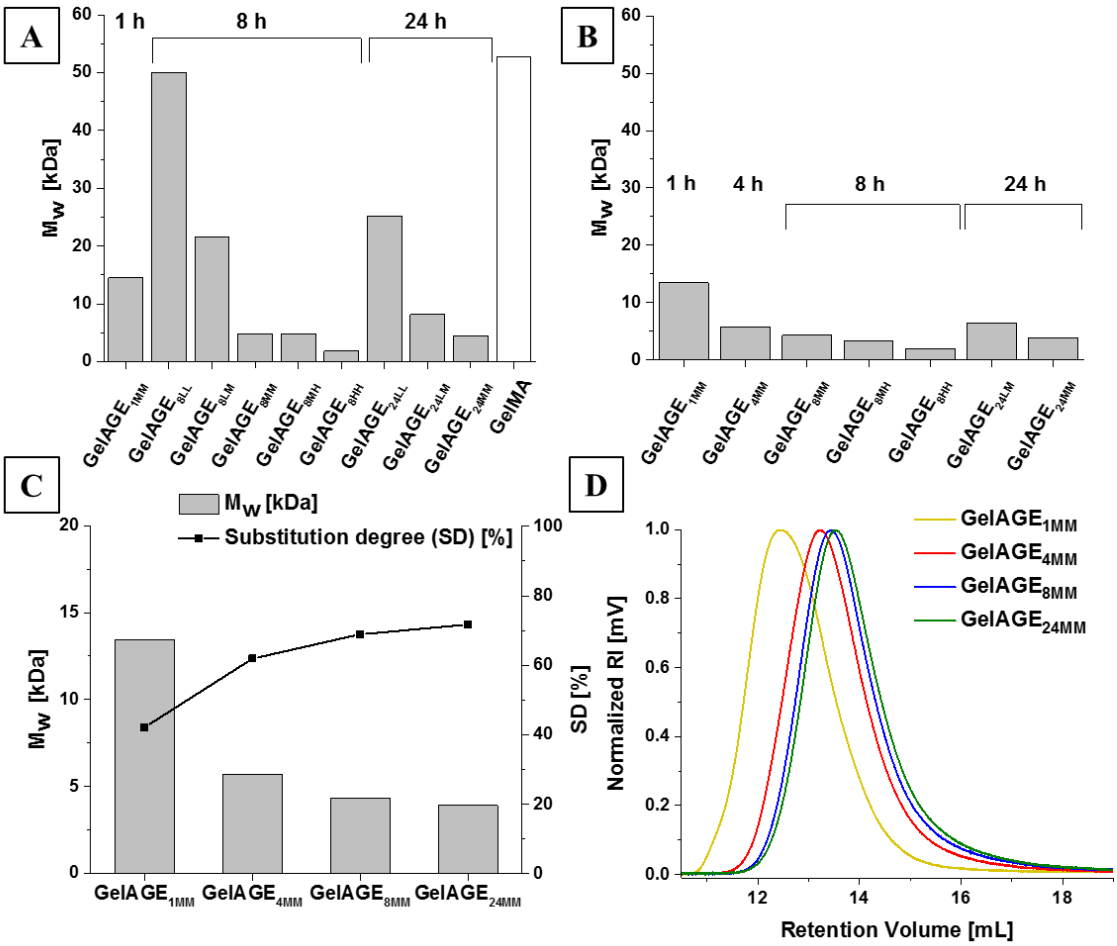


**Figure 58:** Representative results for the apparent weight-averaged molar mass ($M_w$) of GelAGE samples and GelMA on column set I (**A**) and on column set II (**B**). Grey bars represent $M_w$ of GelAGE samples and GelMA is represented with the white bar. The black dots in (**C**) represent SD values for the complete time course of GelAGE$_{1\text{-}24MM}$ and the grey bars the corresponding $M_w$ values. Elugrams (**D**) with GelAGE$_{1MM}$ (yellow line), GelAGE$_{4MM}$ (red line), GelAGE$_{8MM}$ (blue line) and GelAGE$_{24MM}$ (green line) in (**D**). Samples for **C** and **D** were analyzed with column set II. Adapted with permission from Bertlein and coworkers[86]. Copyright (2017) John Wiley and Sons.

It seemed that longer reaction times and increasing NaOH:AGE ratios led to a clear decrease in $M_w$ concurrent with increasing SD values (**Figure 58 A – C**). A slight dispersity narrowing and a shift towards higher retention volumes, similar to the gelatin controls without AGE modification (**Figure 47**, Gelatin$_{1\text{-}24M0}$) was detected for fixed NaOH:AGE ratios with varying reaction times (**Figure 58 D**). This correlation becomes more obvious by the comparison of GelAGE$_{1\text{-}24MM}$ samples, for which all parameters were kept constant except the reaction time was successively increased (**Figure 58 C**). Here the $M_w$ dropped from 13.4 kDa for GelAGE$_{1MM}$ (42.1 % SD) to 3.9 kDa for GelAGE$_{24MM}$ (71.7 % SD).

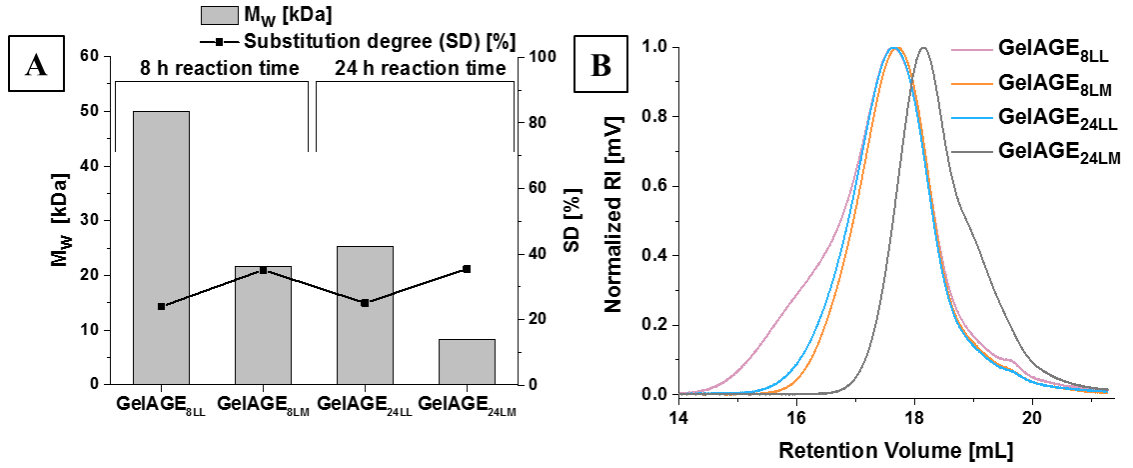


**Figure 59:** Representative comparison of the weight-averaged molar mass ($M_w$) values for GelAGE samples (grey bars) that were treated under the same reaction conditions but for distinct reaction times (8 h and 24 h) together with the SD values (black dots) in **A** and the corresponding elugrams in **B**. GelAGE$_{8LL}$ in light red, GelAGE$_{8LM}$ in orange, GelAGE$_{24LL}$ in light blue and GelAGE$_{24LM}$ in grey. Both graphs correlate to results from column set I. Adapted with permission from Bertlein and coworkers[86]. Copyright (2017) John Wiley and Sons.

Moreover, a slight increase in SD resulted in a drastic apparent $M_w$ decline of GelAGE products. This becomes obvious for the comparison of e.g. GelAGE$_{8LL}$ (50.0 kDa; 24.0 % SD) to GelAGE$_{8LM}$ (21.6 kDa; 35.2 % SD) (**Figure 59 A**) for which the same alkaline conditions were used and the different coiling behaviors of these samples are depicted in **Figure 59 B**. The influence of gelatin degradation on the $M_w$ can be neglected for these samples as the only difference was an increase in AGE quantities and a subsequently higher SD. Decreasing $M_w$ values could hence only be explained by a different coiling behavior of the modified products due to the increased hydrophobicity for higher AGE modification. This distinct coiling becomes evident by e.g. GelAGE$_{24LL}$ to GelAGE$_{24LM}$. However, comparing the influence of the reaction durations at constant NaOH:AGE ratios on the $M_w$ values, it becomes obvious that gelatin degradation also significantly influences these values. In case of GelAGE$_{8LL}$ the $M_w$ declined from 50.0 kDa to 25.2 kDa for GelAGE$_{24LL}$, although the SD values were almost equal with 24 % SD for GelAGE$_{8LL}$ and 25 % SD for GelAGE$_{24LL}$.

Hence, an interplay of peptide-bond hydrolysis in dependence on the reaction durations and of the introduction of a higher number of hydrophobic moieties with increasing SD values is suggested to account for the obtained $M_w$ values. SEC analysis provided a first insight into the $M_w$ distribution but the absolute $M_w$ values for GelMA and GelAGE require further

molar mass determination techniques, such as e.g. MALDI-ToF.

Similar to gelatin controls ($Gelatin_{1\text{-}24M0}$) an additional determination of the molecular weight distributions with SDS-PAGE analysis was conducted for all GelAGE samples (**Figure 60**).

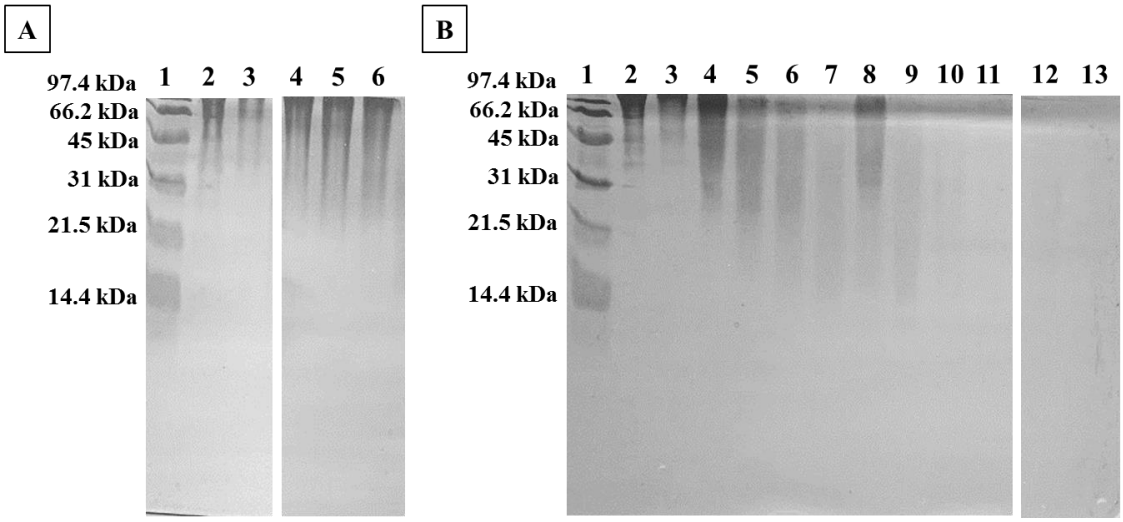


**Figure 60:** Representative 18.0 wt.-% SDS-PAGE gels of GelAGE samples. Electrophoretic migration patterns of the low molecular weight marker (lane 1), gelatin (lane 2), GelMA (lane 3), $GelAGE_{8LL}$ (lane 4), $GelAGE_{24LL}$ (lane 5) and $GelAGE_{8LM}$ (lane 6) (**A**); gelatin (lane 2), GelMA (lane 3), gelatin controls ($Gelatin_{1M0}$, lane 4; $Gelatin_{4M0}$ lane 5; $Gelatin_{8M0}$ lane 6; $Gelatin_{24M0}$ lane 7), $GelAGE_{1MM}$ (lane 8), $GelAGE_{4MM}$ (lane 9), $GelAGE_{8MM}$ (lane 10), $GelAGE_{24MM}$ (lane 11), $GelAGE_{8MH}$ (lane 12) and $GelAGE_{8HH}$ (lane 13) (**B**). 8.0 µL marker were loaded from a 1/10 dilution with sample buffer. 15.0 µg of gelatinous samples were loaded per well. SDS-PAGE gels were stained with Coomassie blue R-250 and destained with a mixture of HAc/MeOH/water of 7.5/20/72.5 (v/v).

GelMAs molecular weight distribution (**Figure 60 A**, lane 3) matched the distribution of the reference gelatin quite well (**Figure 60 A**, lane 2) and GelMA displayed molecular weight distributions at higher molecular weights than GelAGE samples. This suggested a less prominent degradation of gelatin which was correlated to the mild neutral to slightly acidic reaction conditions together with a short reaction time (1 h). Relatively mild synthesis parameters for $GelAGE_{8LL}$, $GelAGE_{24LL}$ and $GelAGE_{8LM}$ (**Figure 60 A**, lanes 4 – 6) resulted in similar migration patterns as for gelatin controls (**Figure 60 B**, $Gelatin_{8M0}$ and $Gelatin_{24M0}$ with lanes 5 and 6). The general SDS-PAGE analysis results of GelAGE samples are in good agreement to the conclusions from SEC analysis of these samples and the previously described gelatin controls. Increasing alkaline conditions and reaction times resulted in a more pronounced degradation of gelatin, which was reflected by broadened

migration patterns and a shift towards lower molecular mass.

Although the same amounts of samples were loaded per well, no migration patterns were observable for longer $GelAGE_{8MM}$ (**Figure 60 B**, lane 10) and harsher $GelAGE_{24MM}$ (**Figure 60 B**, lane 11), $GelAGE_{8MH}$ (**Figure 60 B**, lane 12) and $GelAGE_{8HH}$ synthesis conditions (**Figure 60 B**, lane 13) corresponding to the highest SD values from 72 – 124 %. Disappearing migration patterns could be explained based on the used Coomassie staining dye. This anionic dye predominantly interacts with positively charged groups, in the case of gelatin mainly with amines from lysine and hydroxylysine.[206] The main modification sites for AGE on the gelatin backbone are hypothesized to involve these amine functionalities and their consumption upon modification was previously demonstrated. However, these secondary amines are still prone for protonation and a steric hindrance of the interacting Coomassie dye could probably account for the diminished migration patterns. The extent of AGE modification together with the obtained low molecular weight distributions, which are prone to leach out of the SDS-PAGE gels, are hypothesized to account for diminishing GelAGE migration patterns. Also GelMA showed a less prominently stained migration pattern and this could be attributed to the modification of hydroxylysine resulting in amide groups which can no longer be protonated and hence lower amounts of Coomassie can interact with GelMA and indirectly further supports the hypothesis of diminishing migration patterns for GelAGE samples.

As a consequence of broad molecular weight distributions and partially diminished migration patterns, no conclusions about distinct molecular weight distributions were drawn based on SDS-PAGE analysis.

It can be concluded, that the amine content of gelatin decreased concurrently to increasing SD of GelAGE as predominantly amines were modified with AGE. $M_w$ values of gelatin controls and different GelAGE samples followed a similar declining trend with increasing SD values. Longer reaction times resulted generally in smaller gelatinous fragments. However, this cannot only be attributed to the degradation of gelatin, but its modification probably also alters the coiling behavior and influences SEC-derived $M_w$ values. Harsh reaction conditions for $GelAGE_{8HH}$ and the subsequent high SD were correlated to an increase in N-terminal amine content upon peptide-bond hydrolysis of gelatin. The molecular weight distributions from SDS-PAGE analysis further supported the trends of SEC results.

### 3.2.2. Free radical polymerization versus thiol-ene click chemistry

Before investigating crosslinked hydrogels, the different crosslinking chemistries of GelMA and GelAGE and their effects on the resulting polymeric networks are compared. Whereas the crosslinking of GelMA is based on the free radical random chain-growth polymerization of methacryloyl moieties[90, 93, 94, 207], the thiol-ene click chemistry[91, 92, 94, 95] accounts for GelAGE crosslinking. Based on the overall extend of methacryloyl functionalities of GelMA, non-degradable higher molecular weight components could be obtained as a result of the polymerization process of methacryloyl groups.[90, 94] Consequently, gelatin and the attached polymethacrylic acid bridges are hypothesized to form a rather heterogeneous polymer network within the hydrogels due to the uncontrolled length of these bridging chains.[90, 94] The thiol-ene click chemistry for GelAGE reflects a more controlled dimerization due to the formation of thioether bridges between one allyl- and one thiol-group and results in more homogeneous networks (**Figure 61**).[20, 91, 92, 95]

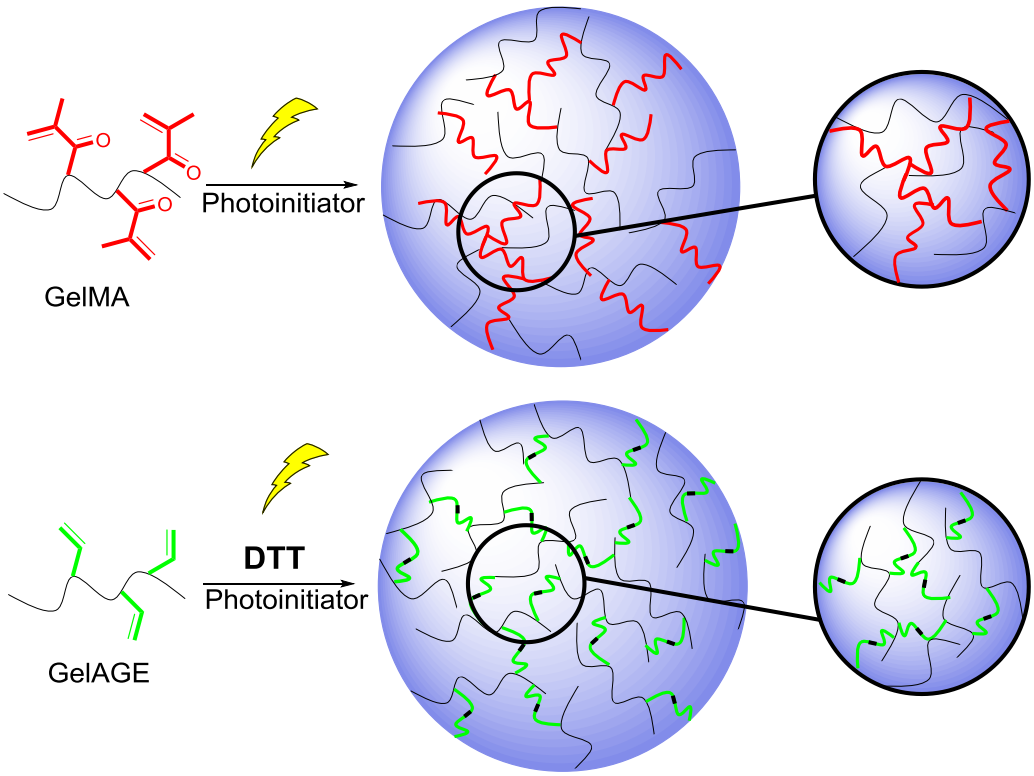


**Figure 61:** Schematic representations of the free radical polymerization of GelMA and the thiol-ene click chemistry for GelAGE with DTT. Both reactions are initiated by irradiation with UV- or Vis-light in the presence of suitable photoinitiators. Adapted with permission from Bertlein and coworkers[86]. Copyright (2017) John Wiley and Sons.

To further elucidate the aforementioned hypothesis, GelMA as well as $GelAGE_{1MM}$ hydrogels (both 20 wt.-%, Ene:SH = 1:12 for GelAGE) were crosslinked under the same UV-conditions (0.05 wt.-% I2959). A subsequent hydrolysis of the hydrogels was performed with 6 M HCl (95 °C, 12 h) and hydrolyzed products were characterized via SEC analysis.

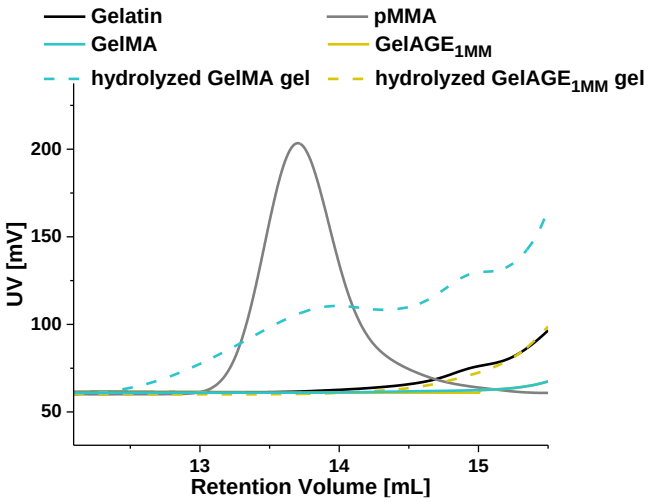


**Figure 62:** Representative SEC-UV-traces at 208 nm of gelatin (black line), pMMA (grey line; $M_w$ = 1.27 kDa), GelMA (light blue line) and $GelAGE_{1MM}$ (yellow line) and of hydrolyzed GelMA (light blue dashed line) and $GelAGE_{1MM}$ hydrogels (yellow dashed line). Adapted with permission from Bertlein and coworkers[86]. Copyright (2017) John Wiley and Sons.

The corresponding UV-traces at 208 nm of the polymeric fractions ($V_{ret}$ < 15 mL) are depicted in **Figure 62**. All samples, except for poly(methacrylic acid sodium salt) (pMMA), demonstrated a slight increase in mV for retention volumes larger than ~ 15.0 mL, which suggested the presence of rather small amino acid components and that both GelMA and GelAGE products were completely hydrolysable. A prominent band at 13.7 mL was observable for pMMA. Only hydrolyzed GelMA hydrogels possessed a peak in the same retention volume range, for which this peak was also broadened to lower retention volumes. These observations suggested the presence of higher molecular weight components solely in hydrolyzed GelMA hydrogels and could be correlated to polymerized methacrylates, which are eventually still decorated with residual amino acids.

However, no conclusions on the $M_w$ of these components were drawn, as the signal distribution was quite broad and no signal was detectable for the refractive index (RI)- or multi-angle light scattering (MALS)-detector. These results further underline the advantages of the thiol-ene click chemistry regarding the homogeneity and degradability of the crosslinked polymer networks.[20, 91, 92, 95]

### 3.2.3. Investigation of GelAGE hydrogel fabrication

To obtain GelAGE hydrogels, DTT was chosen as small bifunctional crosslinker and different Ene:SH ratios were investigated to optimize the hydrogel properties. Crosslinking was initiated with two different photoinitiators, one based upon UV-irradiation (I2959) and the other one upon irradiation with Vis-light (Ru/SPS). I2959 is known to be cytocompatible in a restrictive range (0.05 – 0.1 wt.-%)[89, 107-109, 115], hence, the following UV-experiments were solely performed with the lower concentration circumventing cytotoxicity arising from the photoinitiator. UV-irradiation remains controversial as potential long term damages on cellular DNA are being discussed.[110-112, 115]

As an alternative system the Ru/SPS initiator system was chosen which does not rely upon irradiation with UV-light. Previous studies had already proven this system to be biocompatible for concentrations of up to 1/10 mM Ru/SPS[113] and therefore represented the upper limit in the context of this study. The correlation between photoinitiator concentration and the tuning of the most promising hydrogel compositions was investigated over a wider concentration range (0.2/2 – 1/10 mM Ru/SPS). The concentration of 0.05 wt.-% I2959 (2.2 mM) was in a comparable range to the concentrations of the Ru/SPS system but a direct comparison of the radical generation remains prone to misinterpretations due to different mechanistic steps. Cell-free equilibrium swollen hydrogels (PBS, 2.0 mL, 24 h, 37 °C) were used to evaluate the mechanical stiffness, sol fraction, water content and the mass swelling ratio q. A comparison of GelAGE hydrogel performance to the gold standard GelMA hydrogels (10 wt.-%)[123, 207, 208] was conducted.

#### 3.2.3.1. Hydrogel formation using UV-light

Mechanical stiffness, mass swelling ratio q and the water content of the hydrogels (20 wt.-% GelAGE) were analyzed to correlate the differently degraded and functionalized GelAGE samples to one another. All hydrogels, including reference GelMA hydrogels (10 – 30 wt.-%), were initiated with 0.05 wt.-% I2959 and the same irradiation dosage.

GelAGE hydrogels were obtained for all different GelAGE products by adjusting Ene:SH ratios, except for $GelAGE_{8HH}$ regardless of the crosslinker concentration (**Figure 63**). The extent of gelatin degradation during these extreme alkaline synthesis conditions is suggested to prevent the gelation ability. No clear hydrogel property differences among the other degradation states of GelAGE samples were detectable and could be explained by the compensation of gelatin degradation with increasing SD values.

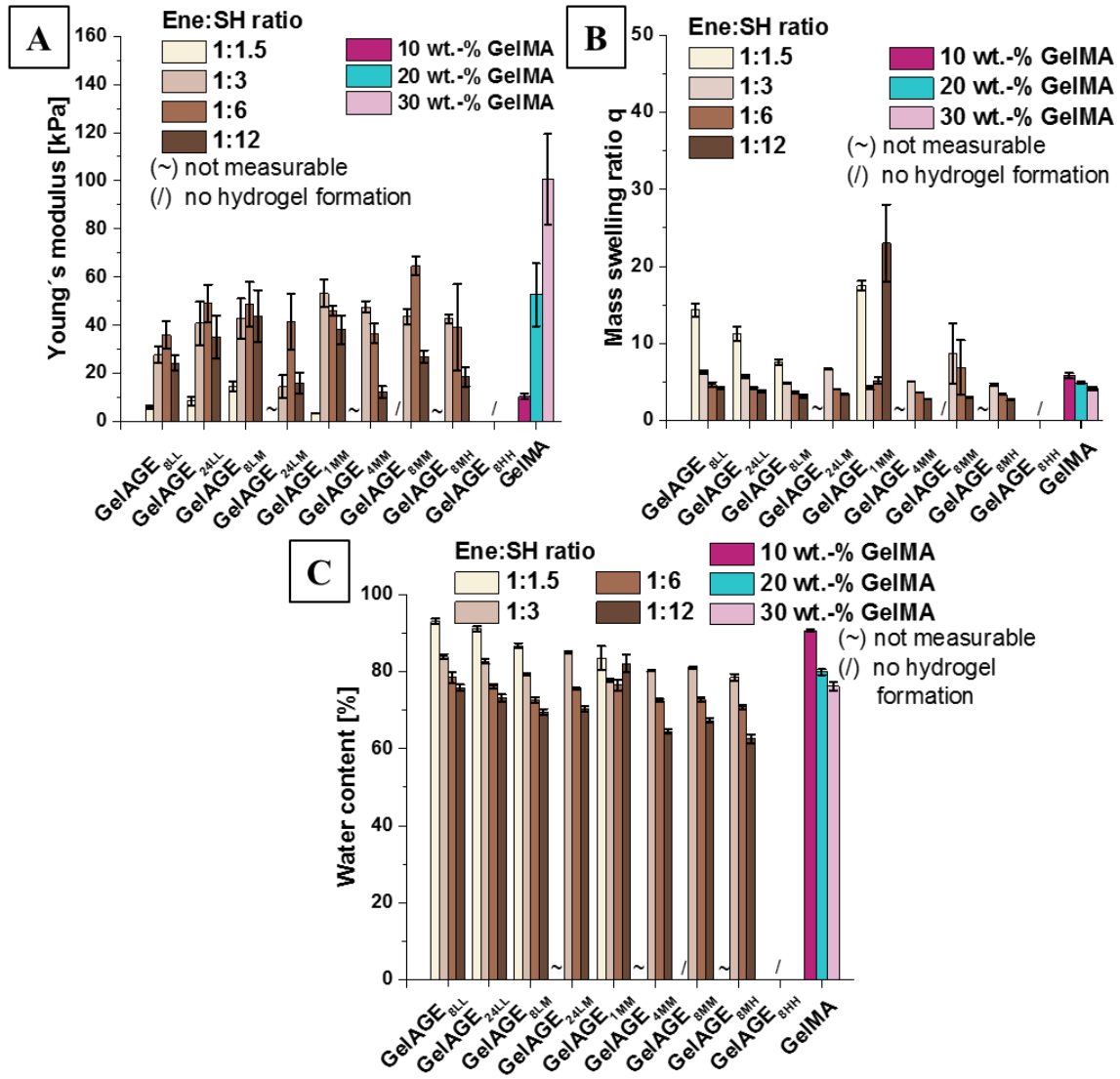


**Figure 63:** Young´s moduli (**A**), mass swelling ratio q (**B**) and water content (**C**) of 20 wt.-% GelAGE hydrogels crosslinked with DTT (Ene:SH = 1:1.5 – 1:12). GelAGE and GelMA reference hydrogels (10 – 30 wt.-%) were initiated with 0.05 wt.-% I2959. Ene:SH ratios of 1:1.5 (yellow bars), 1:3 (light brown bars), 1:6 (brown bars) and 1:12 (dark brown bars) and 10 wt.-% GelMA (magenta bars), 20 wt.-% GelMA (turquoise bars) and 30 wt.-% GelMA hydrogels (light magenta bars). Conditions marked with (~) represent non-measurable hydrogels (too soft) and (/) correlates to lack of gelation. For clarity purposes the statistical differences between the groups are not presented. Adapted with permission from Bertlein and coworkers[86]. Copyright (2017) John Wiley and Sons.

Generally, the mechanical stiffness of GelAGE hydrogels increased concurrent with crosslinker concentrations, whereas the mass swelling ratio q decreased (**Figure 63 A** and **B**). Both observations suggest the trend towards higher crosslinked polymer networks. Young´s moduli for GelAGE gels could be controlled in the range of 3.4 – 65 kPa using 20 wt.-% hydrogels with Ene:SH ratios between 1:1.5 and 1:12. Optima

for Ene:SH ratios of 1:3 and 1:6 were observable for the mechanical strength (**Figure 63 A**).

The lowest Ene:SH ratio (1:1.5) resulted in the softest hydrogels between 3.4 – 15 kPa, followed by the highest ratio (1:12) with Young´s moduli of 16 – 44 kPa. Incompletely crosslinked hydrogels due to insufficient crosslinker amounts for the lowest ratio and a coupling of an excess of DTT to the allyl groups without further crosslinking but rather saturating AGE groups for the highest Ene:SH ratio were hypothesized.

The Young´s moduli of the GelAGE system (20 wt.-%, Ene:SH = 1:3 – 1:12) with values of 15.9 – 64.6 kPa were superior to the standard 10 wt.-% GelMA hydrogels with 10.9 ± 1.4 kPa, in a comparable range to 20 wt.-% GelMA hydrogels with 55.5 ± 13.7 kPa and lower than 30 wt.-% GelMA hydrogels (106 ± 19.9 kPa). Only the lowest Ene:SH ratio of 1:1.5 resulted in hydrogels with a lower mechanical stiffness (< 15 kPa) and a higher mass swelling ratio (q > 7.5) than all GelMA hydrogels (10 – 106 kPa and q = 4.1 – 5.9). Water contents of all hydrogels were in the range of 64 – 93 % (**Figure 63 C**).

The high mechanical strength of $GelAGE_{1MM}$ hydrogels (Ene:SH = 1:3) with 53 ± 5.8 kPa and the narrow standard deviation combined with a good balance between high $M_w$ and SD values render this gel composition the most suitable for follow-up studies. Moreover, as previously demonstrated with the example of unmodified gelatin controls ($Gelatin_{1\text{-}24M0}$), the highest material yield coincided with the shortest alkaline incubation time and further completed the advantages of $GelAGE_{1MM}$.

### 3.2.3.2. Hydrogel formation using Vis-light

The alternative Vis-light system (Ru/SPS) was examined with $GelAGE_{1MM}$ (20 wt.-%) and GelMA reference hydrogels (10 – 30 wt.-%). Constant Ene:SH ratios (1:1.5 – 1:12) and the same irradiation dosages as for UV-experiments were used, whereas photoinitiator concentrations were chosen between 0.2/2 mM and 1/10 mM Ru/SPS.

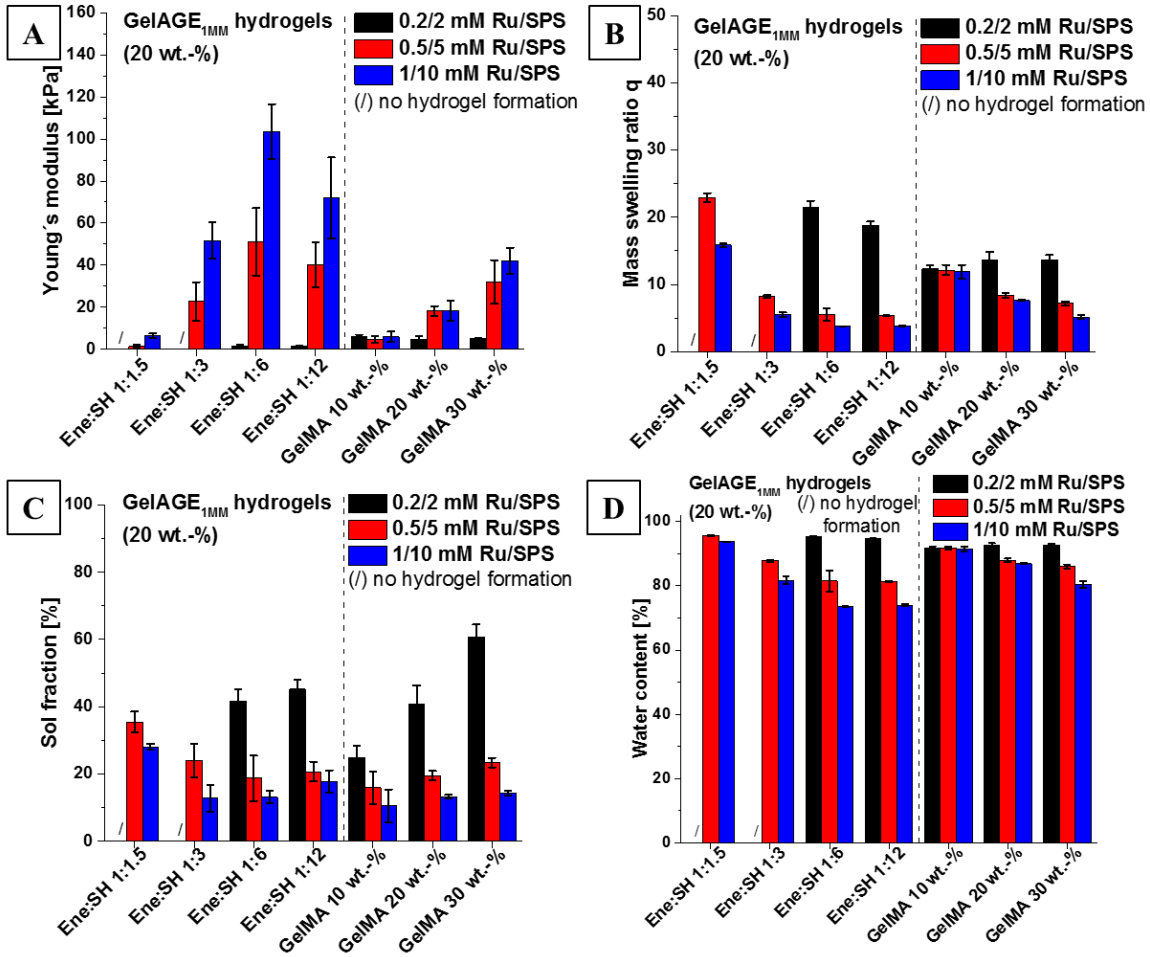


**Figure 64:** Young´s moduli (**A**), mass swelling ratio q (**B**), sol fraction (**C**) and water content (**D**) of 20 wt.-% GelAGE$_{1MM}$ hydrogels crosslinked with DTT (Ene:SH = 1:1.5 – 1:12). GelAGE$_{1MM}$ and 10 – 30 wt.-% GelMA reference hydrogels were initiated with 0.2/2 – 1/10 mM Ru/SPS. Vis-initiation with 0.2/2 mM Ru/SPS is represented by black bars, 0.5/5 mM Ru/SPS by red bars and 1/10 mM Ru/SPS by blue bars. Conditions marked with (/) represent lack of gelation. For clarity purposes the statistical differences between the groups are not presented. Adapted with permission from Bertlein and coworkers[86]. Copyright (2017) John Wiley and Sons.

Increasing Ru/SPS concentrations clearly increased the mechanical stiffness while decreasing the mass swelling ratio q, the sol fraction and the water content for 20 wt.-% GelAGE$_{1MM}$ hydrogels (**Figure 64**). These results suggested most efficiently crosslinked hydrogels for the highest photoinitiator concentrations (1/10 mM Ru/SPS). At constant Ene:SH ratios of 1:6 and polymer weight percentages of 20 wt.-%, the Vis-system allowed tuning of the GelAGE$_{1MM}$ Young´s moduli in the range of 1.4 – 110 kPa solely with varying photoinitiator concentrations (**Figure 64 A**). Furthermore, a tuning of the mechanical properties can be achieved with varying Ene:SH ratios, analogous to the UV-system. The lowest Ene:SH ratio of 1:1.5 led to the softest GelAGE$_{1MM}$ hydrogels

(1.4 – 6.4 kPa) with the highest mass swelling ratio (up to q = 23) and sol fraction (25 – 36 %) similar to the described trend for UV-experiments. Moreover, the lowest initiator concentration (0.2/2 mM Ru/SPS) was insufficient to yield hydrogels for 1:1.5 and 1:3 Ene:SH ratios. Contrary to UV-initiated crosslinking with optima for Ene:SH ratios of 1:3 and 1:6, a clear optimum in hydrogel properties was herein reflected by Ene:SH of 1:6. The highest Ene:SH ratio (1:12) did not improve the hydrogel properties and similar to the UV-conditions the high excess of thiols is hypothesized to result in the saturation of $GelAGE_{1MM}$ with DTT rather than in efficient crosslinking.

The $GelAGE_{1MM}$ system (20 wt.-%) was superior to GelMA hydrogels (10 – 30 wt.-%) with respect to all hydrogel properties, except for the lowest initiator concentration of 0.2/2 mM Ru/SPS and Ene:SH ratios of 1:1.5 and 1:3. In this case the mass swelling ratio (q > 18) and the sol fraction (42 – 45 %) for $GelAGE_{1MM}$ were higher than for GelMA hydrogels (q < 14, sol fraction 25 – 61 %), suggesting less crosslinked $GelAGE_{1MM}$ hydrogels (**Figure 64 B** and **C**). The water content of $GelAGE_{1MM}$ hydrogels was in the range of 73 – 95 % (**Figure 64 D**) and comparable to GelMA hydrogels (81 – 93 %) and to UV-experiments (64 – 93 %) (**Figure 63 C**).

These observations suggested the tunability of the Vis-initiating system in cytocompatible photoinitiator concentration ranges at constant Ene:SH ratios and polymer weight percentages.

### 3.2.3.3. Comparison of UV- and Vis-initiated hydrogels

Hydrogel properties of UV- and Vis-initiated hydrogels were directly compared for $GelAGE_{1MM}$ (20 wt.-%) with Ene:SH ratios of 1:3 – 1:12 and for 10 – 30 wt.-% GelMA. To ensure comparability amongst the hydrogels the same irradiation dosages were applied. The increase in overall polymer content represented for UV-conditions the only possibility to tune the hydrogel properties of GelMA hydrogels due to the restricted cytocompatible concentration of I2959. Hence, a comparison of 30 wt.-% $GelAGE_{1MM}$ (Ene:SH = 1:3) to GelMA (30 wt.-%) was conducted for both initiating systems.

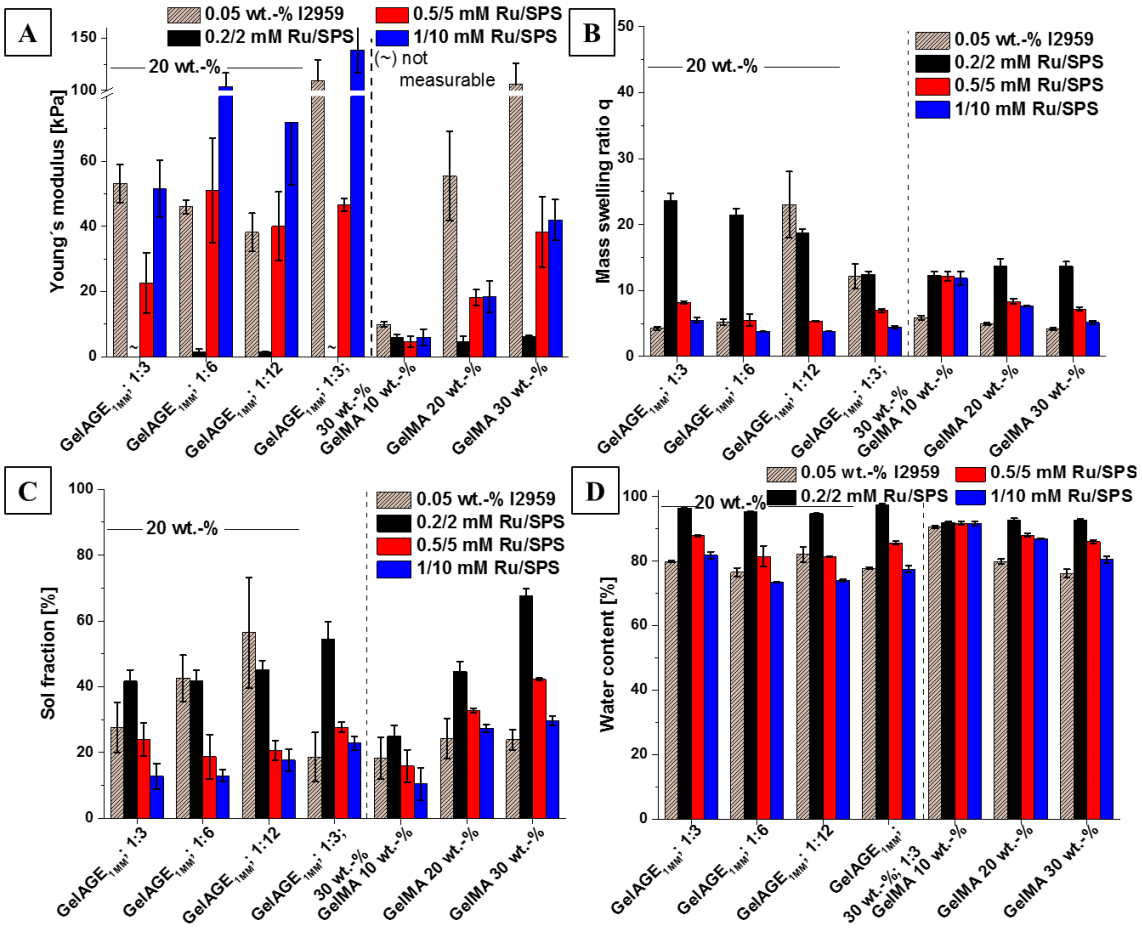


**Figure 65:** Young´s moduli (**A**), mass swelling ratio q (**B**), sol fraction (**C**) and water content (**D**) of 20 wt.-% GelAGE$_{1MM}$ hydrogels crosslinked with DTT (Ene:SH = 1:3 – 1:12) and 30 wt.-% GelAGE$_{1MM}$ crosslinked with DTT at an Ene:SH ratio of 1:3. GelAGE$_{1MM}$ and GelMA reference hydrogels (10 – 30 wt.-%) were initiated with 0.05 wt.-% I2959 or 0.2/2 – 1/10 mM Ru/SPS. UV-initiation with 0.05 wt.-% I2959 is represented by grey lined bars and Vis-initiation with 0.2/2 mM Ru/SPS by black bars, 0.5/5 mM Ru/SPS by red bars and 1/10 mM Ru/SPS by blue bars. Conditions marked with (~) represent non-measurable hydrogels (too soft). For clarity purposes the statistical differences between the groups are not presented. Adapted with permission from Bertlein and coworkers[86]. Copyright (2017) John Wiley and Sons.

30 wt.-% GelAGE$_{1MM}$ hydrogels (Ene:SH = 1:3) possessed superior mechanical strengths compared to 30 wt.-% GelMA hydrogels at 1/10 mM Ru/SPS while this property remained similar for lower Ru/SPS concentrations (**Figure 65 A**). Generally, Vis-initiated GelAGE$_{1MM}$ hydrogels were stiffer than corresponding GelMA hydrogels, except for the lowest Ru/SPS concentration. The UV-initiated hydrogel stiffnesses of GelAGE$_{1MM}$ (20 – 30 wt.-%) were in a comparable range to the GelMA system (20 – 30 wt.-%) and superior to 10 wt.-% GelMA hydrogels. Furthermore, UV-conditions were superior to the lowest Ru/SPS concentration, as reflected by higher mechanical stiffness, lower mass

swelling ratio q, water content and sol fraction (**Figure 65 A – D**). The hydrogels water content ranged between 74 – 98 % (**Figure 65 D**). Besides these observations, the hydrogel properties followed the trends that were already discussed in the previous chapters.
The direct comparison of both initiating systems underlines the advantageous tunability of the $GelAGE_{1MM}$ hydrogels initiated with the Vis-system compared to UV-initiation. Hydrogels over a wide mechanical stiffness range can easily be obtained by adjusting the concentration of the Vis-system upon retaining Ene:SH ratios and the polymer weight percentages.
The GelAGE system is accordingly more tunable with respect to the hydrogel properties due to the additional crosslinker compared to GelMA hydrogels.

### 3.2.4. Cell compatibility of GelAGE hydrogels

Cell compatibility of $GelAGE_{1MM}$ hydrogels crosslinked with DTT was investigated with human articular chondrocytes (hAChs). 20 wt.-% $GelAGE_{1MM}$ hydrogels with Ene:SH ratios of 1:1.5 – 1:12 and 30 wt.-% $GelAGE_{1MM}$ with Ene:SH ratio of 1:3 were compared to 10 wt.-% GelMA hydrogels. Cells were encapsulated in UV- or Vis-light initiated hydrogels and cultured for one week. Photoinitiator concentrations were 0.05 wt.-% for I2959 and 1/10 mM for Ru/SPS and the constructs were irradiated with the same dosage. Viability was quantified by imaging live and dead cells and the metabolic activity was quantified with an AlamarBlue® assay. The change in metabolic activity was calculated based on the correlation of metabolic activity of 7 d to 1 d.

GelMA hydrogels supported cell survival (70 – 79 %) and metabolic activity for both initiating systems (**Figure 66**), which is in good accordance to literature.[113, 209] Below the highest Ene:SH ratio of 1:12 the $GelAGE_{1MM}$ system also exhibited high cell survival rates with 72 – 91 % (1 d) and 68 – 89 % (7 d) independent on differences in mechanical stiffnesses of 3.4 – 104 kPa of the hydrogels (**Figure 66 A** and **B**). For the metabolic activity the same trend was observable (**Figure 66 C**). The highest Ene:SH ratio decreased cellular viability to 60 – 63 % for UV- and to 66 % for Vis-initiation and the change in metabolic activity concurrently declined. This correlates to the previous hypothesis of incomplete crosslinked hydrogels for high excess of DTT, which results in the presence of a high amount of uncrosslinked and cytotoxic thiol functionalities.

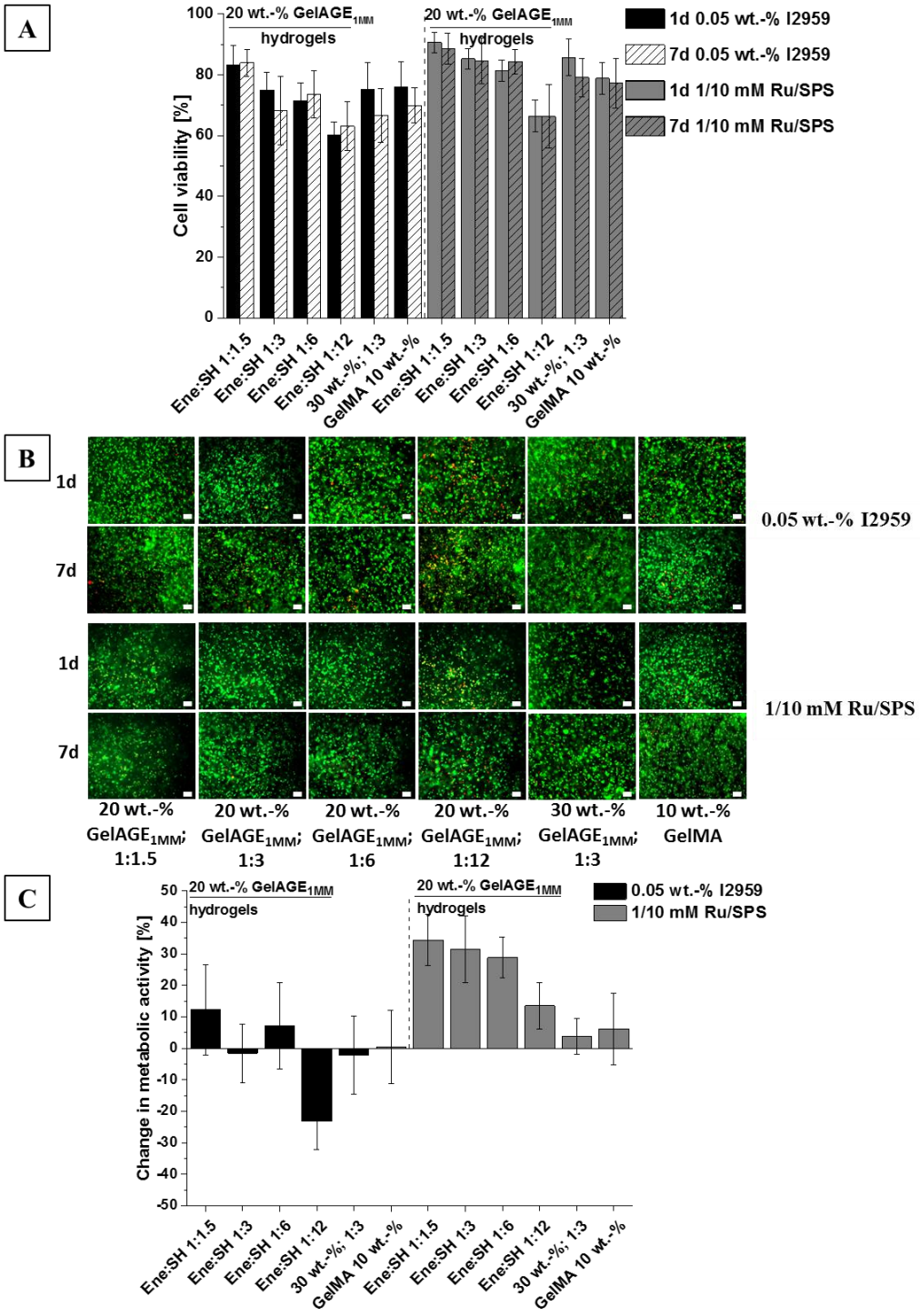


**Figure 66:** Cell viability after 1 d and 7 d in culture for $GelAGE_{1MM}$ hydrogels (20 wt.-%, Ene:SH = 1:1.5 – 1:12 and 30 wt.-%, Ene:SH = 1:3) and for 10 wt.-% GelMA hydrogels (**A**). Black bars for 1 d and black lined bars for 7 d (0.05 wt.-% I2959) and grey bars for 1 d and grey lined bars after 7 d (1/10 mM Ru/SPS) in culture. Representative corresponding Live/Dead images from the center of different hydrogels (**B**). Scale bars represent 100 µm. Change in metabolic activity was correlated from metabolic activity of 7 d to 1 d (**C**). Black bars for 0.05 wt.-% I2959 and grey bars for 1/10 mM Ru/SPS. 15 x $10^6$ hAChs $mL^{-1}$ were encapsulated in the hydrogels prior to initiation. Adapted with permission from Bertlein and coworkers[86]. Copyright (2017) John Wiley and Sons.

The Vis-system displayed slightly increased cellular viabilities together with a drastic increase in metabolic activity over time compared to the UV-system. This further underlines the advantages of this initiation system, together with the tunable hydrogel properties and can most probably be correlated to the lack of irradiation with UV-light rather than to the toxicity of the photoinitiators.[113]

### 3.2.5. Versatility of GelAGE as bioink

Bioinks are usually developed for one specific biofabrication technology as they demand different bioink properties, e.g. liquids are needed for stereolithographic approaches[86], whereas more viscous materials are necessary for extrusion-based bioprinting[14, 210, 211]. The synthesis parameters for GelAGE control the degradation of gelatin and in turn influence the rheological properties of the products. Two GelAGE samples were assessed for their applicability as bioinks, namely $GelAGE_{1MM}$ and $GelAGE_{8MM}$.

Whereas the stronger degraded $GelAGE_{8MM}$ remained liquid (10 – 30 wt.-%) even upon cooling to 4 °C, the less degraded $GelAGE_{1MM}$ (30 wt.-%) exhibited a more pronounced thermoresponsive behavior and an increase in viscosity upon cooling. Due to these distinct properties $GelAGE_{8MM}$ was used for SLA with digital light processing (DLP) and $GelAGE_{1MM}$ for extrusion-based printing.

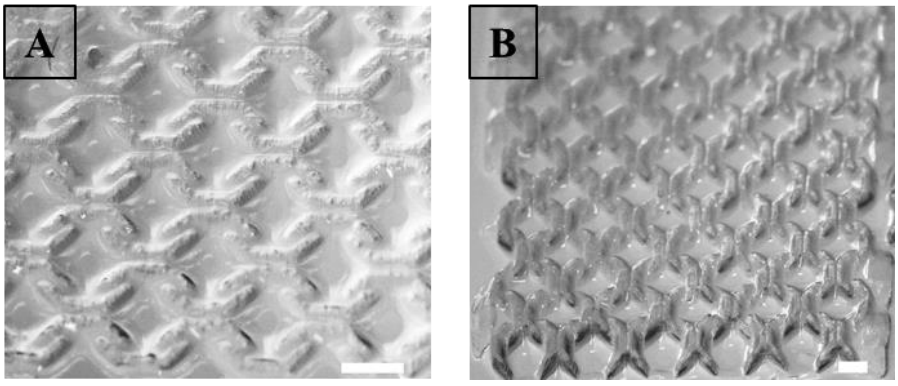


**Figure 67:** Representative microscopic images from 10 wt.-% $GelAGE_{8MM}$ constructs (Ene:SH = 1:12, one layer, **A**) and 20 wt.-% $GelAGE_{8MM}$ (Ene:SH = 1:12, two layers, **B**), both samples were initiated with 0.5/5 mM Ru/SPS and fabricated with stereolithography (SLA) with digital light processing (DLP). Scale bars represent 1 mm. Adapted with permission from Bertlein and coworkers[86]. Copyright (2017) John Wiley and Sons.

A porous construct geometry (250 µm diameter strands) was fabricated stereolithographically with 10 wt.-% $GelAGE_{8MM}$ (**Figure 67 A**) and 20 wt.-% $GelAGE_{8MM}$ (**Figure 67 B**). Both formulations contained an Ene:SH ratio of 1:12 and were initiated under Vis-conditions with 0.5/5 mM Ru/SPS. Notably no additives, such as Orasol Orange G, which are commonly used to control radical propagation[212], were needed to fabricate $GelAGE_{8MM}$ into structurally defined constructs. Herein, the stronger degraded gelatin backbone of the GelAGE product is advantageous compared to GelMA as the formation of physical crosslinks renders a 10 wt.-% GelMA solution too viscous for this fabrication technique.

The thermoresponsive behavior of the 30 wt.-% $GelAGE_{1MM}$ precursor solution (Ene:SH = 1:3) was investigated with respect to the rheological properties. To ensure sterile conditions, which are required for extrusion-based bioprinting, a sterile-filtered, lyophilized and re-dissolved $GelAGE_{1MM}$ formulation was compared to a non-sterile solution. To mimic shear stress in the printing needle, the shear rate was estimated according to the following equation:

$$\gamma = \frac{8\nu}{d} \qquad \textbf{(Equation 1)}$$

with $\gamma$= shear rate [$s^{-1}$], $\upsilon$= printing velocity [0.33 mm $s^{-1}$] and d= needle diameter [0.33 mm].[213]

A shear rate of around 8 $s^{-1}$ was determined for the processing parameters and was accordingly used for the temperatures sweep experiments.

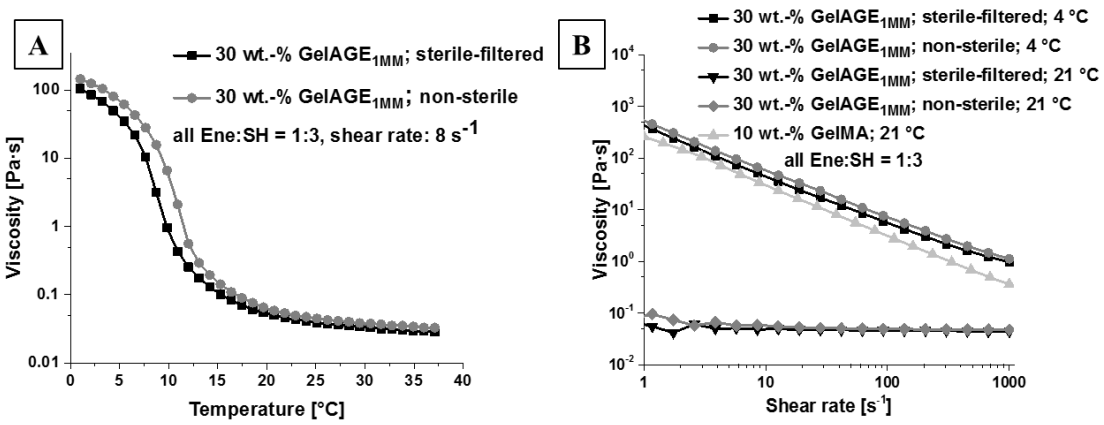


**Figure 68:** Representative temperature sweep from 1 – 37 °C with 1 °C $min^{-1}$ of sterile-filtered and non-sterile 30 wt.-% $GelAGE_{1MM}$ (Ene:SH = 1:3) precursor solutions at a constant shear rate of 8 $s^{-1}$ (**A**) and the viscosity in dependence on different shear rates at 4 °C and 21 °C (**B**) compared to 10 wt.-% GelMA. Adapted with permission from Bertlein and coworkers[86]. Copyright (2017) John Wiley and Sons.

The temperature sweep, depicted in **Figure 68 A**, clearly demonstrates the thermoresponsive and well documented behavior of gelatin[125, 214] without clear differences between sterile-filtered and non-sterile solutions.

The shear-thinning at 4 °C of $GelAGE_{1MM}$ was comparable to the most commonly used 10 wt.-% GelMA at 21 °C (**Figure 68 B**). The comparability of both $GelAGE_{1MM}$-based solutions regarding their shear-thinning properties and the liquidity of $GelAGE_{1MM}$ at room temperature were demonstrated.

Macroscopically observations and the rheological results demonstrated the increase in viscosity of $GelAGE_{1MM}$ solutions upon cooling, hence, the extrusion-based printer was equipped with two cooling loops that enabled the separate cooling of the syringe and the printing plate to 4 – 7 °C. The applicability of this precursor solution (30 wt.-% $GelAGE_{1MM}$; Ene:SH = 1:3) was investigated for both photoinitiator systems at minimal exposure times for UV-irradiation with a 2 s interval irradiation per construct layer and a final irradiation with 3 x 2 s after the extrusion-based printing process to circumvent potential damages on cellular DNA for later bioprinting. Irradiation with the Vis-system was performed for 3 min post-fabrication due to the lack of DNA damaging UV-light. Photoinitiator concentrations were 0.05 wt.-% I2959 for UV- and 1/10 mM Ru/SPS for Vis-irradiation.

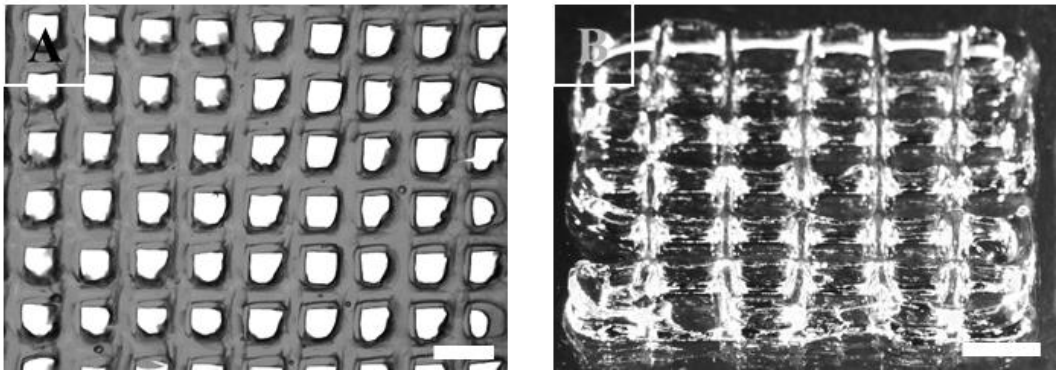


**Figure 69:** Representative microscopic images of a four-layered 30 wt.-% $GelAGE_{1MM}$ construct (Ene:SH = 1:3, 0.05 wt.-% I2959, **A**) and an eight-layered construct (1/10 mM Ru/SPS, **B**) both obtained by extrusion-based printing. UV-irradiation was performed with 2 s intervals per layer and a final irradiation of 3 x 2s while the Vis-irradiation was conducted after the printing for 3 min. Scale bars represent 2 mm. Adapted with permission from Bertlein and coworkers[86]. Copyright (2017) John Wiley and Sons.

The high shape fidelity constructs derived from both initiator systems for extrusion-based printing are depicted in **Figure 69**. Without collapse of the construct structure, four-layered UV- (**Figure 69 A**) and eight-layered Vis-initiated constructs (**Figure 69 B**) were fabricated. Construct sizes were 21 x 21 $mm^2$ (UV) and 12 x 12 $mm^2$ (Vis) with strand distances of 1194 ± 35 µm and fiber diameters of 876 ± 43 µm for the UV-system and strand distances of 1317 ± 32 µm and fiber diameters of 643 ± 13 µm for the Vis-system.

As a proof of principle this bioink composition was tested for extrusion-based bioprinting with porcine chondrocytes (pCh). The more cell compatible Vis-system (1/10 mM Ru/SPS) was used to initiate crosslinking for an irradiation of 3 min after the printing process. 3.0 x $10^6$ pCh $mL^{-1}$ were encapsulated in the precursor formulations and the constructs were analyzed for cellular viability for up to 23 d.

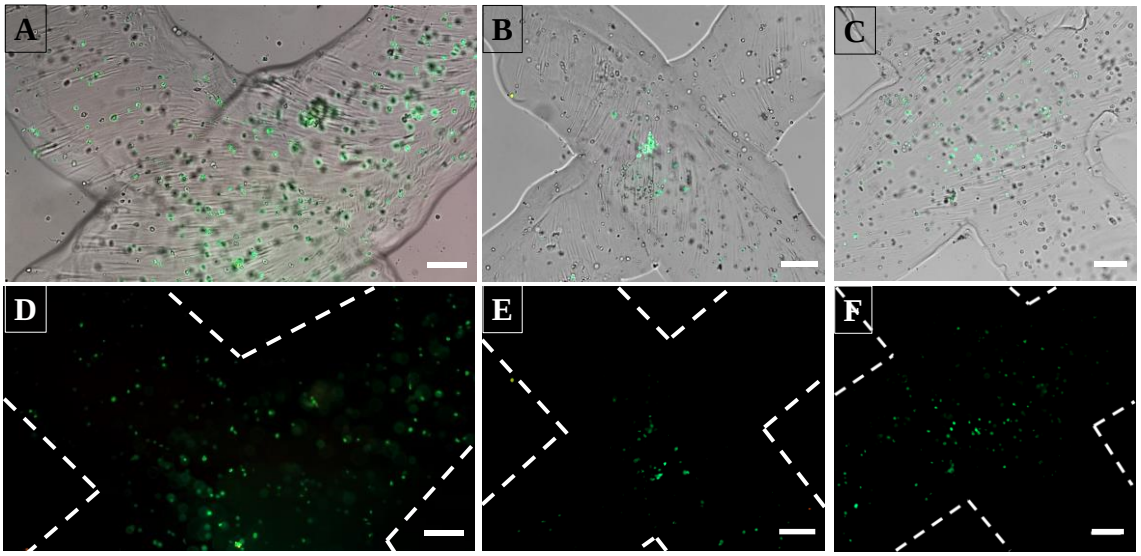


**Figure 70:** Representative Live/Dead images from porcine chondrocytes (3.0 x $10^6$ pCh $mL^{-1}$) encapsulated in 30 wt.-% $GelAGE_{1MM}$ constructs (Ene:SH = 1:3, 1/10 mM Ru/SPS, one layer) after 7 d (**A** and **D**), 14 d (**B** and **E**) and 21 d (**C** and **F**) in culture. **A** – **C** images represent merged fluorescence images with bright field and **D** – **F** fluorescence images only. Scale bars represent 100 µm.

The cells remained viable throughout the culture period of 23 d further stressing the applicability of the $GelAGE_{1MM}$ formulation as a bioink for extrusion-based bioprinting (**Figure 70**). No quantification of cellular viability was conducted as the cell numbers were too low in the hydrogel constructs.

For more detailed images these constructs were additionally analyzed with a confocal microscope at 23 d (**Figure 71**) and proved a homogeneous distribution of viable pChs.

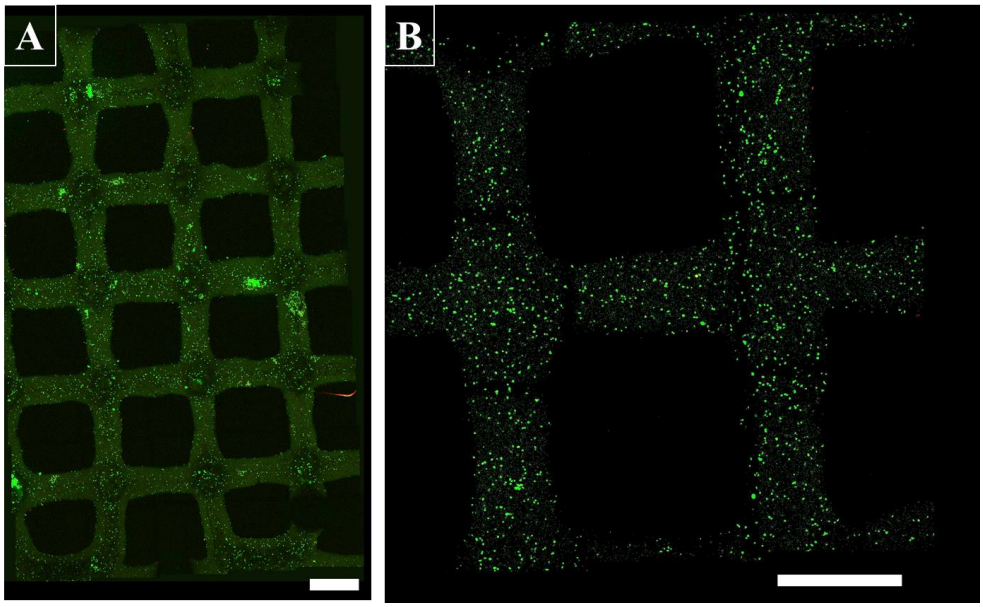


**Figure 71:** Representative Live/Dead confocal images from porcine chondrocytes (3.0 x $10^6$ pCh $mL^{-1}$) encapsulated in a 30 wt.-% $GelAGE_{1MM}$ construct (Ene:SH = 1:3, 1/10 mM Ru/SPS, one layer) after 23 d in culture. Scale bars represent 1 mm. Adapted with permission from Bertlein and coworkers[86]. Copyright (2017) John Wiley and Sons.

These extrusion-based printing results together with the synthesis control over GelAGE properties and hydrogels prepared thereof underline the applicability for biofabrication approaches. Additionally, the versatility of this system for other AM techniques was demonstrated.

### 3.2.6. GelAGE hydrogels with macromolecular crosslinkers

Multifunctional macromolecular crosslinkers were investigated to enable a reduction of the potentially cytotoxic thiols, while maintaining hydrogel properties similar to DTT crosslinked hydrogels, due to their multivalence and backbone flexibility. The previously studied DTT on the other hand, as a small bifunctional compound, is hypothesized to require a higher overall amount of thiols to efficiently crosslink available allyl functionalities. An improvement of the rheological behavior and consequently on the extrusion-based printability of these macromolecular crosslinker containing $GelAGE_{1MM}$ precursor formulations was speculated. Different molecular structures of the crosslinkers were included to evaluate effects on the precursor solution or hydrogel properties. Therefore, eight-armed star-shaped PEG thiols (sPEGSH, 10 kDa) and a linear multifunctional thiol-modified low molecular weight hyaluronic acid (LHASH) were examined in the following studies.

### 3.2.6.1. Hydrogel properties

While eight-armed star-shaped sPEGSH is commercially available, LHASH was synthesized according to previous established protocols[142, 147] with a SD of 25 % as confirmed by $^{1}$H-NMR spectroscopy (for detailed synthesis and characterizations see **Chapter 3.3.1**). Based on the assumption of statistically distributed thiol groups, the molecular weight of the educt and the multiplicity of the disaccharides repeating unit, an estimated amount of functional groups per kDa with 0.7 groups per kDa was obtained. This amount is comparable to sPEGSH with 0.8 groups per kDa and enables the comparison of crosslinking densities within the hydrogels, without taking the flexibility and the distribution of thiols on the crosslinkers into account.
To allow comparability of the macromolecular crosslinked hydrogels to DTT crosslinked hydrogels, the applied weight percentages of the hydrogels refer to the entire polymer content, although the gelatin content is consequently lower for macromolecular crosslinked hydrogels. Weight percentages of the precursor compositions are later addressed in more detail for rheological experiments. In order to improve the readability, $GelAGE_{1MM}$ which is used throughout this crosslinker study, is abbreviated as GelAGE only.

GelAGE hydrogels were subsequently obtained with different Ene:SH ratios of macromolecular crosslinkers and hydrogel formation was initiated with 0.05 wt.-% of the UV-initiator I2959. Comparability to the previous results was ensured via the same irradiation dosages. An Ene:SH ratio of 1:3 represented the optimum hydrogel properties for DTT crosslinked hydrogels and was chosen as upper limit for this study. The lower Ene:SH ratio of 1:1.5 was investigated to detect the macromolecular crosslinkers influence on maintained or improved hydrogel properties with low thiol quantities.

Although the gelatin content of macromolecular crosslinked hydrogels was lowered, a clear increase in Young´s modulus was detectable (18 – 240 kPa sPEGSH and 30 – 365 kPa LHASH) for both Ene:SH ratios, compared to DTT crosslinked hydrogels (0.7 – 110 kPa) (**Figure 72 A**) and the theory of maintained hydrogel properties for macromolecular crosslinked hydrogels, with reduced thiol amounts, compared DTT-derived hydrogel properties was verified. Hydrogels containing macromolecular crosslinkers were in a similar stiffness range throughout the tested conditions without clear differences amongst each other.

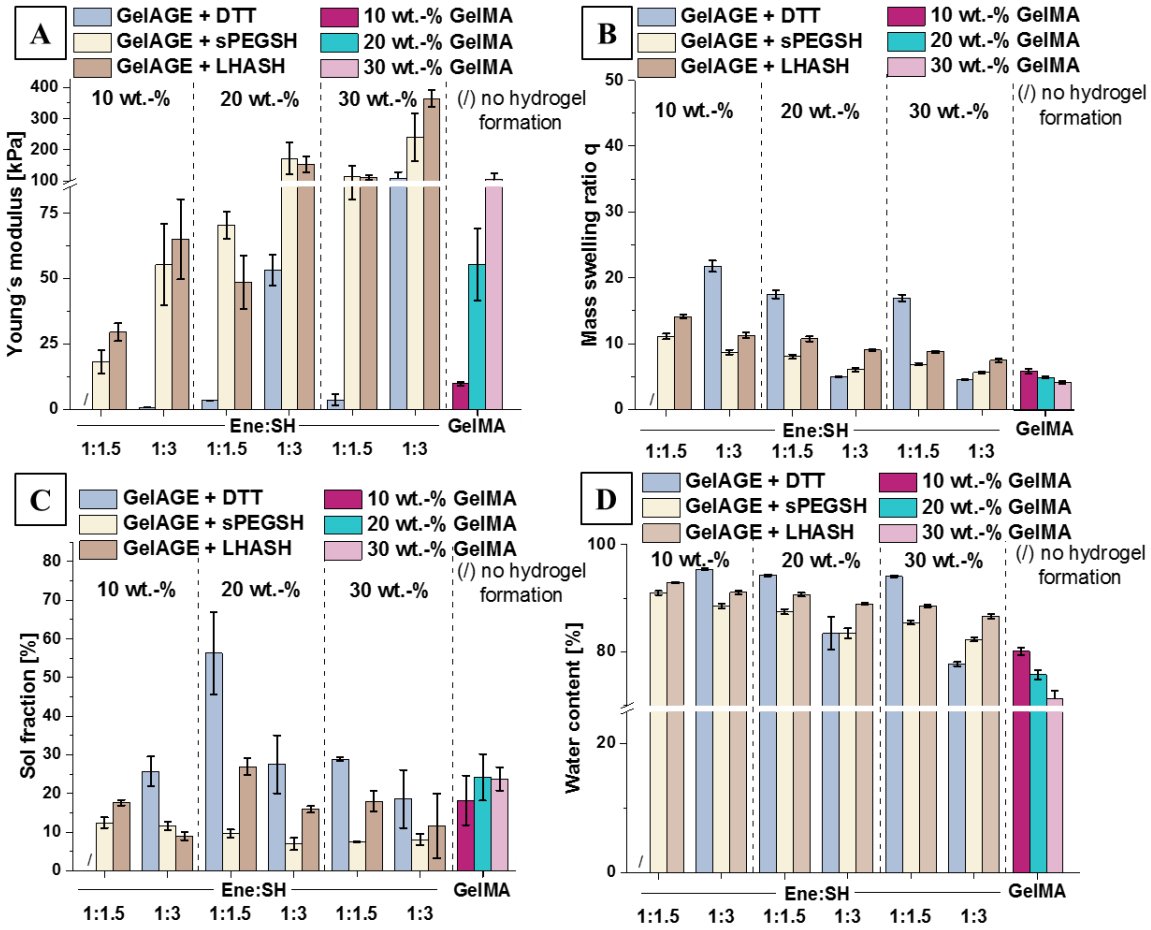


**Figure 72:** Young´s moduli (**A**), mass swelling ratio q (**B**), sol fraction (**C**) and water content (**D**) of GelAGE hydrogels (10 – 30 wt.-%), crosslinked with DTT, sPEGSH or LHASH (Ene:SH = 1:1.5 – 1:3) and initiated with 0.05 wt.-% I2959. GelMA reference hydrogels (10 – 30 wt.-%) were also initiated with 0.05 wt.-% I2959. GelAGE + DTT crosslinked hydrogels are represented in light blue, GelAGE + sPEGSH in yellow and GelAGE + LHASH in light brown and 10 wt.-% GelMA in magenta, 20 wt.-% GelMA in turquoise and 30 wt.-% GelMA hydrogels in light magenta. Conditions marked with (/) represent lack of gelation. For clarity purposes the statistical differences between the groups are not presented.

Moreover, the Young´s moduli of 10 wt.-% GelAGE hydrogels (18 ± 4.5 kPa sPEGSH and 30 ± 3.4 kPa LHASH) even at the lowest Ene:SH ratio were superior to the standard 10 wt.-% GelMA hydrogels (10 ± 0.8 kPa). However, this Ene:SH ratio for 20 – 30 wt.-% macromolecular crosslinked GelAGE hydrogels (71 – 115 kPa sPEGSH and 49 – 111 kPa LHASH) yielded only comparable stiffnesses to GelMA hydrogels with 56 ± 14 kPa for 20 wt.-% and 106 ± 20 kPa for 30 wt.-% hydrogels. Superior mechanical strengths were observable for an Ene:SH ratio of 1:3 for 20 – 30 wt.-% GelAGE hydrogels with 172 – 240 kPa for sPEGSH and 150 – 365 kPa for LHASH than for 30 wt.-% GelMA hydrogels.

The mass swelling ratio q and sol fractions were also improved for sPEGSH (q < 11, sol fraction 7 – 12 %) and LHASH (q < 14, sol fraction 9 – 27 %) crosslinked hydrogels compared to DTT crosslinking (**Figure 72 B**, q < 21; **Figure 72 C**, sol fraction 19 – 57 %). Depending on the molecular weight of macromolecular crosslinkers for GelAGE hydrogels, the mass swelling ratio was similar to GelMA hydrogels (q < 6) whereas the sol fraction was consistently lower than for GelMA hydrogels with sol fractions of 18 – 24 %. Both mass swelling ratio q and sol fractions decreased with increasing weight percentages and Ene:SH ratios for GelAGE hydrogels. The declined mass swelling ratio q and sol fractions for GelAGE (sPEGSH and LHASH) suggested more efficiently crosslinked polymer networks than for DTT and similar efficacy to GelMA hydrogels. Generally, sPEGSH crosslinking led to higher crosslinked networks than LHASH, as represented by decreasing mass swelling ratio q and sol fractions. Contributing to the higher mass swelling ratios q for GelAGE + LHASH is the polyanionic character of HA which results in a higher water attraction. The water content of GelAGE hydrogels was in the range of 78 – 95 % and higher than for GelMA hydrogels (76 – 84 %) (**Figure 72 D**).

These results supported the advantages of macromolecular crosslinkers regarding the hydrogel properties. Even at lower Ene:SH ratios improved hydrogel properties were detectable, such as mechanical stiffness, mass swelling ratio q and sol fraction, compared to DTT crosslinked hydrogels.

### 3.2.6.2. Influence on rheological properties

The effect of macromolecular crosslinkers on the rheological properties and the applicability for extrusion-based (bio)printing was of interest. First, the effect of sPEGSH and LHASH on the viscosity of 30 wt.-% GelAGE precursor solutions was investigated and compared to the previous printed 30 w.-% GelAGE with DTT (Ene:SH = 1: 3). For this, an Ene:SH ratio of 1:1.5 was chosen as this was demonstrated to yield mechanical properties for sPEGSH (115 ± 34.5 kPa) and LHASH (111 ± 7.57 kPa) crosslinked hydrogels equally to an Ene:SH ratio of 1:3 for DTT crosslinked hydrogels (109 ± 19.8 kPa) and allowed to decrease the potential cytotoxic thiol functionalities. At a fixed Ene:SH ratio of 1:1.5 the macromolecular crosslinkers were compared to DTT with an overall polymer content of 20 wt.-% to evaluate the possibility to (bio)print these precursor compositions.

Precursor solutions and hydrogels were matched according to the entire polymer content and the differences in gelatin content of these precursor formulations is depicted in **Table 7**.

**Table 7:** Content of 30 wt.-% GelAGE precursor formulations in dependency on different crosslinkers and Ene:SH ratios.

| GelAGE with | Ene:SH | Gelatin [wt.-%] | Crosslinker [wt.-%] | Gelatin:Crosslinker [%] | SH [mM] |
|---|---|---|---|---|---|
| DTT | 1:1.5 | 29.2 | 0.8 | 97:3 | 79 |
| | 1:3 | 28.4 | 1.6 | 95:5 | 158 |
| sPEGSH | 1:1.5 | 24.6 | 5.4 | 82:18 | 59 |
| LHASH | 1:1.5 | 24.0 | 6.0 | 80:20 | 57 |

While the gelatin content decreased to around 24 – 25 wt.-% for macromolecular precursor solutions compared to almost 30 wt.-% of DTT containing compositions, the crosslinker content concurrently increased to maximum 6.0 wt.-% for GelAGE + LHASH (**Table 7**). The gelatin:crosslinker ratios reflected these trends. Although the crosslinker weight percentage increased at fixed Ene:SH ratios, the concentration of thiols in the hydrogels decreased by approximately 25 % to 59 mM as compared to GelAGE + DTT with 79 mM. Most importantly the mechanical stiffnesses of the hydrogels could be retained upon more than halving the thiol concentration for macromolecular crosslinker compositions, compared to GelAGE + DTT (Ene:SH = 1:3) with a thiol concentration of 158 mM.

The temperature sweep was investigated with the previously calculated shear rate of 8 $s^{-1}$ to mimic the shear rate in the needle while printing.

30 wt.-% GelAGE (DTT and sPEGSH) displayed a similar thermoresponsive behavior and resulted at room temperature in equal liquidities (**Figure 73 A**). In contrast, exclusively below 15 °C, 30 wt.-% GelAGE + LHASH exhibited a similar responsiveness to temperature changes, however, shifted towards higher viscosities. Above 15 °C this solution remained also more viscous than the other solutions and not as sensitive towards temperature changes. This can most probably be attributed to the initially more viscous, literature known[139, 140, 215], behavior of HA which interferes with gelatins thermoresponsiveness, as the crosslinkers weight percentages were in similar ranges (5.4 wt.-% sPEGSH and 6.0 wt.-% LHASH). In this case the viscosity measurements were

limited to above 8 °C as the solution was too viscous at the applied shear rate and resulted in removal of the material from the plate-plate geometry of the rheometer.

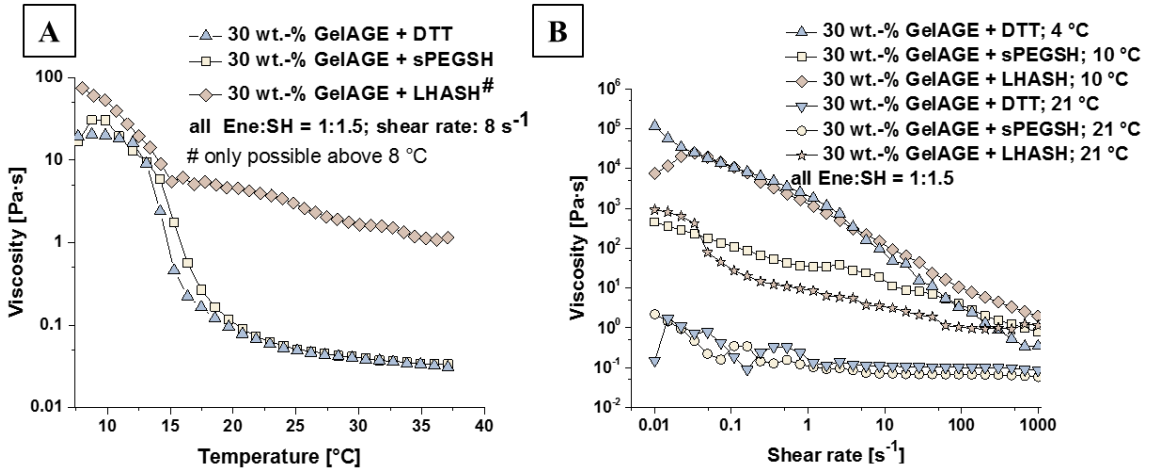


**Figure 73:** Representative temperature sweep from 8 – 37 °C with 1 °C $min^{-1}$ at a constant shear rate of 8 $s^{-1}$ (**A**) and the viscosity in dependence on different shear rates at 4 °C, 10 °C and 21 °C (**B**) of 30 wt.-% GelAGE (Ene:SH = 1:1.5) containing DTT (light blue), sPEGSH (yellow) or LHASH as crosslinker (light brown). For GelAGE + LHASH temperature sweep measurements only above 8 °C were possible (# in **A**).

The viscosity dependence on different shear rates and temperatures is depicted in **Figure 73 B**. Important to note is that neither sPEGSH nor LHASH containing GelAGE solutions could be measured below 10 °C due to similar experimental problems as already stated. Upon increasing the temperature to 10 °C GelAGE + LHASH was comparable to GelAGE + DTT at 4 °C, while sPEGSH containing formulations displayed a shear-thinning behavior with lower viscosities. Nevertheless, all formulations showed shear-thinning properties under cooled conditions and GelAGE + LHASH demonstrated this behavior also at room temperature. Further increasing the temperature for DTT and sPEGSH containing formulations rendered these liquid. Although the precursor formulations slightly differed in their shear-thinning at a shear rate of 8 $s^{-1}$, no direct correlation of the shear-thinning properties of macromolecular crosslinkers to DTT containing precursor formulations was possible due to different experimental temperatures.

It was furthermore of interest if a lower overall polymer content of the precursor compositions would still be applicable for extrusion-based printing, as biocompatibility is associated with decreasing polymer contents[6]. Hence, the same rheological experiments were conducted with 20 wt.-% precursor compositions (Ene:SH = 1:1.5). The differences

in gelatin content of the potential bioinks is depicted in **Table 8**.

**Table 8:** Content of 20 wt.-% GelAGE precursor formulations in dependency on different crosslinkers at an Ene:SH ratio of 1:1.5.

| GelAGE with | Ene:SH | Gelatin [wt.-%] | Crosslinker [wt.-%] | Gelatin:Crosslinker [%] | SH [mM] |
|---|---|---|---|---|---|
| DTT | 1:1.5 | 19.5 | 0.5 | 97:3 | 52 |
| sPEGSH | 1:1.5 | 16.4 | 3.6 | 82:18 | 40 |
| LHASH | 1:1.5 | 16.0 | 4.0 | 80:20 | 38 |

Equal observations as for the 30 wt.-% GelAGE formulations were found for lower weight percentage precursor solutions. The gelatin content of macromolecular precursor solutions decreased to 16 % while the crosslinker content increased to 4 % compared to DTT containing solutions (19.5 wt.-% gelatin and 0.5 wt.-% DTT), which was reflected by the gelatin:crosslinker ratios (**Table 8**). The thiol concentration decreased to around 40 mM for macromolecular precursor formulations than compared to GelAGE + DTT with 52 mM.

Similar rheological correlations as for the 30 wt.-% formulations were observable for 20 wt.-% solutions. Solutions containing DTT and sPEGSH, exhibited the same thermoresponsive behavior, whereas the combination with LHASH resulted in a higher viscosity within the range of 16 – 37 °C (**Figure 74 A**). In contrast to 30 wt.-% GelAGE + LHASH, the corresponding 20 wt.-% solution was measurable over the temperature range of 1 – 37 °C. This enables a direct comparison of the viscosity in dependence on different shear rates at 4 °C and (**Figure 74 B**). Shear-thinning properties for all formulations were clearly observable at 4 °C and are all in comparable ranges especially at the calculated shear rate of 8 $s^{-1}$. Increasing the temperature to 21 °C resulted in more pronounced liquidities for GelAGE + DTT and GelAGE + sPEGSH than for GelAGE + LHASH, which demonstrated the highest viscosity at room temperature.

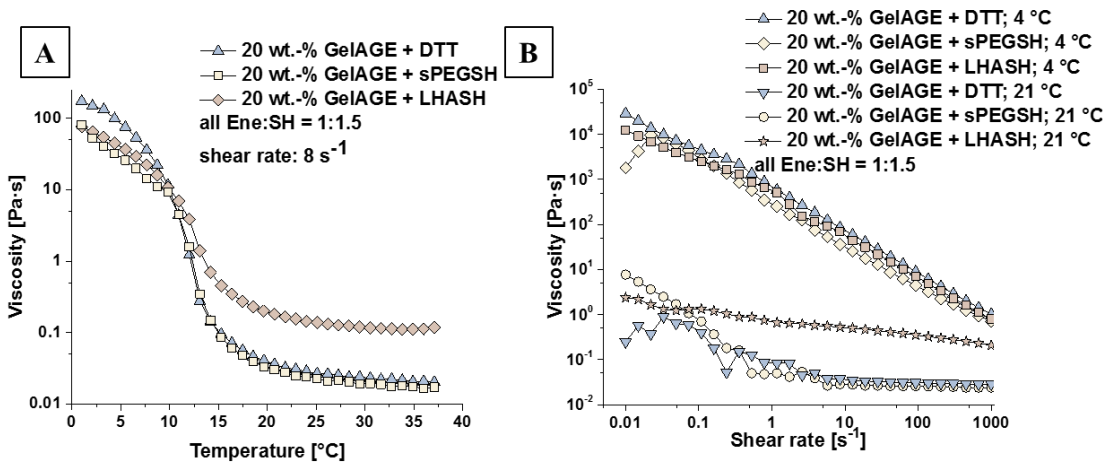


**Figure 74:** Representative temperature sweep from 1 – 37 °C with 1 °C $min^{-1}$ at a constant shear rate of 8 $s^{-1}$ (**A**) and the viscosity in dependence from different shear rates at 4 °C and 21 °C (**B**) of 20 wt.-% GelAGE (Ene:SH = 1:1.5) containing DTT (light blue), sPEGSH (yellow) or LHASH as crosslinker (light brown).

These rheological investigations suggest the applicability of macromolecular crosslinker formulations for extrusion-based (bio)printing even at lower entire polymer percentages and lower thiol concentrations than for DTT containing solutions. Only 20 wt.-% solutions were further investigated regarding the processability with extrusion-based printing, due to to-be-expected enhanced biocompatibility of lower weight percentage solutions.[6] Although the rheological properties of 20 wt.-% GelAGE (DTT, Ene:SH = 1:1.5) were comparable to macromolecular solutions, this composition yielded hydrogels with a low overall mechanical stiffness (3.4 ± 0.1 kPa) and a high sol fraction (56 ± 11 %), which do not support high shape fidelity constructs and consequently this formulation was not further analyzed.

### 3.2.6.3. Bioinks for extrusion-based bioprinting

For extrusion-based printing of GelAGE with sPEGSH and LHASH (both 20 wt.-% and Ene:SH = 1:1.5) the same printing setup as for 30 wt.-% GelAGE (DTT; Ene:SH = 1:3) was used. To optimize the sagging of extruded strands, the G Code was slightly adjusted with decreased velocities (from GelAGE + DTT with 20 mm $min^{-1}$ to GelAGE + sPEGSH/LHASH with 15 mm $min^{-1}$). This adjustment consequently results in a slightly lower calculated shear rate of 6 $s^{-1}$, but the previously determined rheological observations were also similar for this shear rate. For all constructs the applied pressure on the printing needle was in the range of 2.1 – 2.7 bar. Construct irradiation in the presence of 0.05 wt.-%

I2959 was performed while printing with 2 s intervals per layer followed by 3 x 2 s intervals after printing, equal to GelAGE + DTT extrusion-based printing. The irradiation with short intervals was conducted to reduce the risk of cellular DNA damages arising from UV-irradiation for following biofabrication approaches.

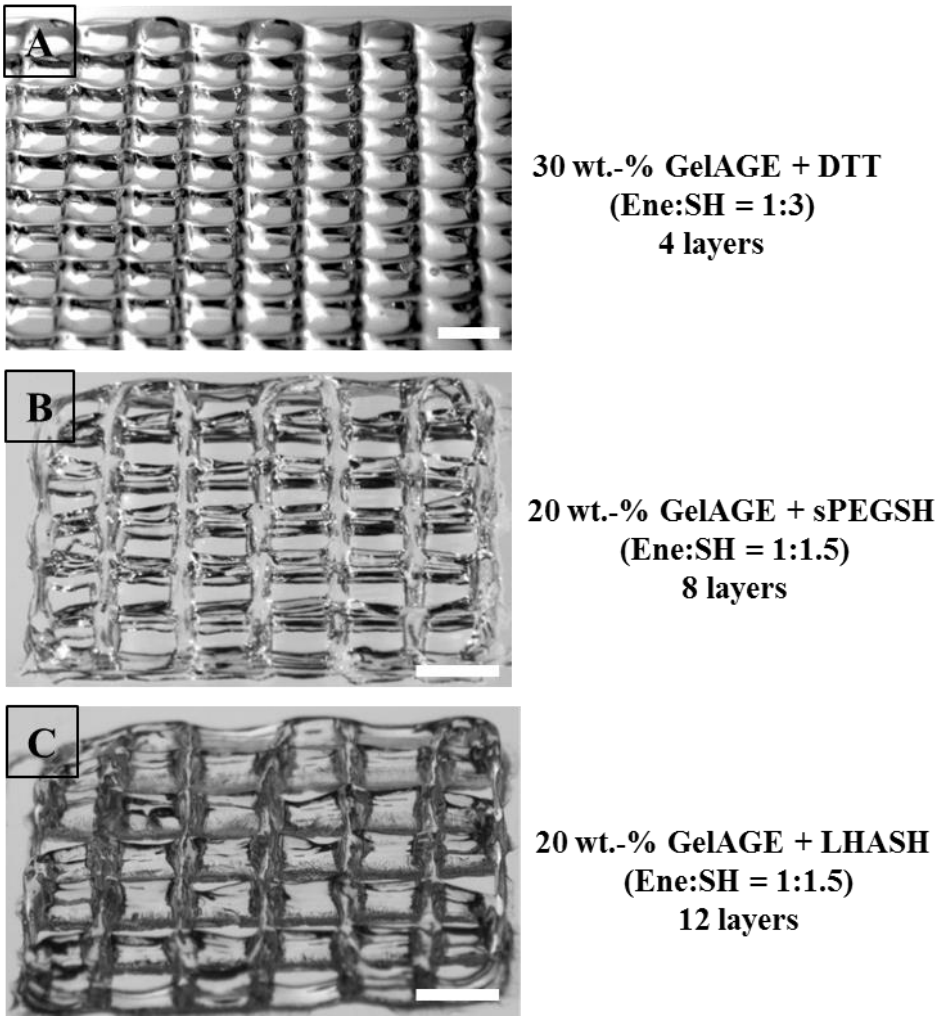


**Figure 75:** Representative microscopic images of 30 wt.-% GelAGE + DTT (Ene:SH = 1:3, four layers in **A**), 20 wt.-% GelAGE + sPEGSH (Ene:SH = 1:1.5, eight layers in **B**) and of 20 wt.-% GelAGE + LHASH (Ene:SH = 1:1.5, twelve layers in **C**) constructs. All precursor formulations were initiated with 2 s intervals per layer and a final irradiation of 3 x 2 s (0.05 wt.-% I2959). Scale bars represent 2 mm.

Comparing DTT- with sPEGSH- or LHASH-crosslinked constructs indicate that both macromolecular crosslinkers supported the ease of fabricating mechanically stable constructs with lower overall polymer percentages. Four-layered 30 wt.-% GelAGE + DTT (Ene:SH = 1:3) constructs are depicted in **Figure 75 A** and eight-layered 20 wt.-% GelAGE + sPEGSH (**Figure 75 B**, Ene:SH = 1:1.5) and twelve-layered 20 wt.-%

GelAGE + LHASH (**Figure 75 C**, Ene:SH = 1:1.5) displayed similar shape fidelities although the layer number was considerable increased. Macromolecular crosslinked constructs possessed final sizes of 12 x 12 $mm^2$ and both macromolecular crosslinked systems performed equally under the applied printing conditions without clear differences. Strand distances of 1666 ± 80 µm and fiber diameters of 347 ± 13 µm for GelAGE + sPEGSH and 919 ± 16 µm strand distances with fiber diameters of 383 ± 21 µm were obtained for GelAGE + LHASH and suggested slightly higher resolutions for GelAGE + sPEGSH.

The reduced polymer content and lower Ene:SH ratios render the macromolecular GelAGE formulations interesting for extrusion-based bioprinting due to the already mentioned beneficial properties of lower polymer contents[6] and to the lower amounts of thiol groups. For this, porcine chondrocytes (pCh) were encapsulated in the hydrogel precursor solutions, to ensure comparability to the previously described results for GelAGE + DTT. A comparison of cast versus printed hydrogels was conducted to evaluate the influence of the shear stress during printing on cellular viability and was analyzed via Live/Dead staining after 1 d and 21 d in culture.

An overview of the percentage of viable pChs is given in **Figure 76 A** after 1 d and 21 d in culture and the corresponding microscopic Live/Dead hydrogel images are depicted in **Figure 76 B**. Slightly higher cell viabilities were detectable for cast sPEGSH crosslinked hydrogels with 77 ± 3 % than for LHASH crosslinked hydrogels with 73 ± 1 % after 1 d in culture. Printed GelAGE + LHASH hydrogels possessed significantly lower cell viabilities of 54 ± 2 % than compared to 72 ± 4 % for printed GelAGE + sPEGSH hydrogels after 1 d. This trend continued over the culture time with 60 ± 8 % (cast) and 57 ± 4 % (printed) viabilities for sPEGSH crosslinked hydrogels and values of 51 ± 11 % (cast) and 43 ± 10 % (printed) for LHASH crosslinked hydrogels. For sPEGSH crosslinked hydrogels, minor differences between cast and printed hydrogels were observable throughout the culture period.

In LHASH containing hydrogels pChs seemed to be more sensitive towards shear stress during extrusion-based printing, as represented by declining cell viabilities. This could not directly be correlated to differences of the rheological properties of the individual hydrogel systems, as these were proven to be similar under cell-free conditions (**Figure 74**).

The highest printing pressure of 2.7 bar was required for extrusion-based printing of cell-laden LHASH containing precursor solutions, which increases shear stress during printing and can affect cell viabilities. The hydrogel composition, more specifically the crosslinker in combination with the printing pressure, were hypothesized to account for this difference.

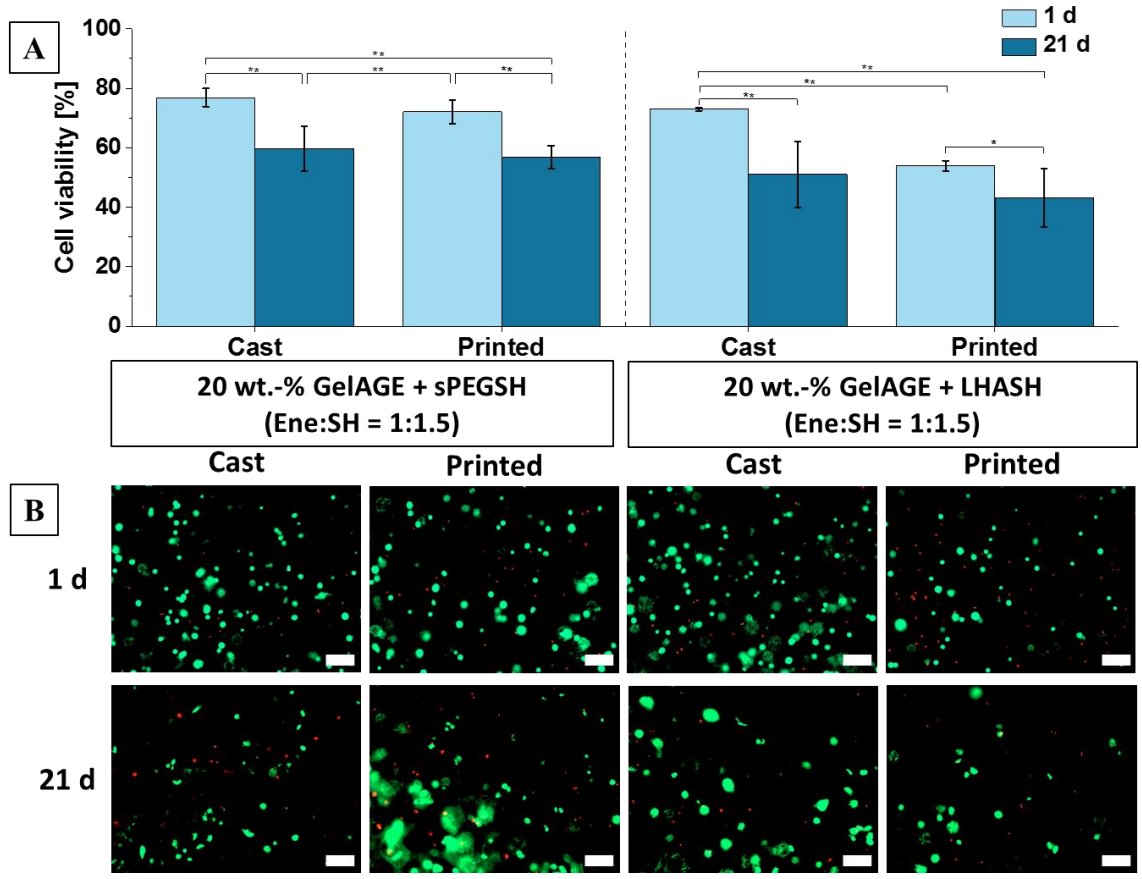


**Figure 76:** Viability of encapsulated pChs (4.0 x $10^6$ cells $mL^{-1}$) in GelAGE + sPEGSH and GelAGE + LHASH hydrogels (both 20 wt.-% and Ene:SH = 1:1.5) after 1 d (light blue) and 21 d (dark blue) in culture (**A**). Hydrogels were either cast or extrusion-based bioprinted and crosslinking was initiated with 0.05 wt.-% I2959 at constant irradiation dosages. Representative Live/Dead images from the center of hydrogel constructs after 1 d and 21 d in culture (**B**). Scale bars represent 100 µm.

Besides chondrocytes, mesenchymal stromal cells (MSCs) are among the most commonly used cells for extrusion-based bioprinting. A comparison of both cell types was conducted to evaluate most suitable cells for the individual bioink formulations. Chondrocytes were derived from porcine donors, while MSCs were derived from human donors (hMSCs). Moreover, cast and printed constructs were included to ensure analogy to the aforementioned results. Construct crosslinking was initiated with 0.05 wt.-% I2959 and the same irradiation dosages as previously were used.

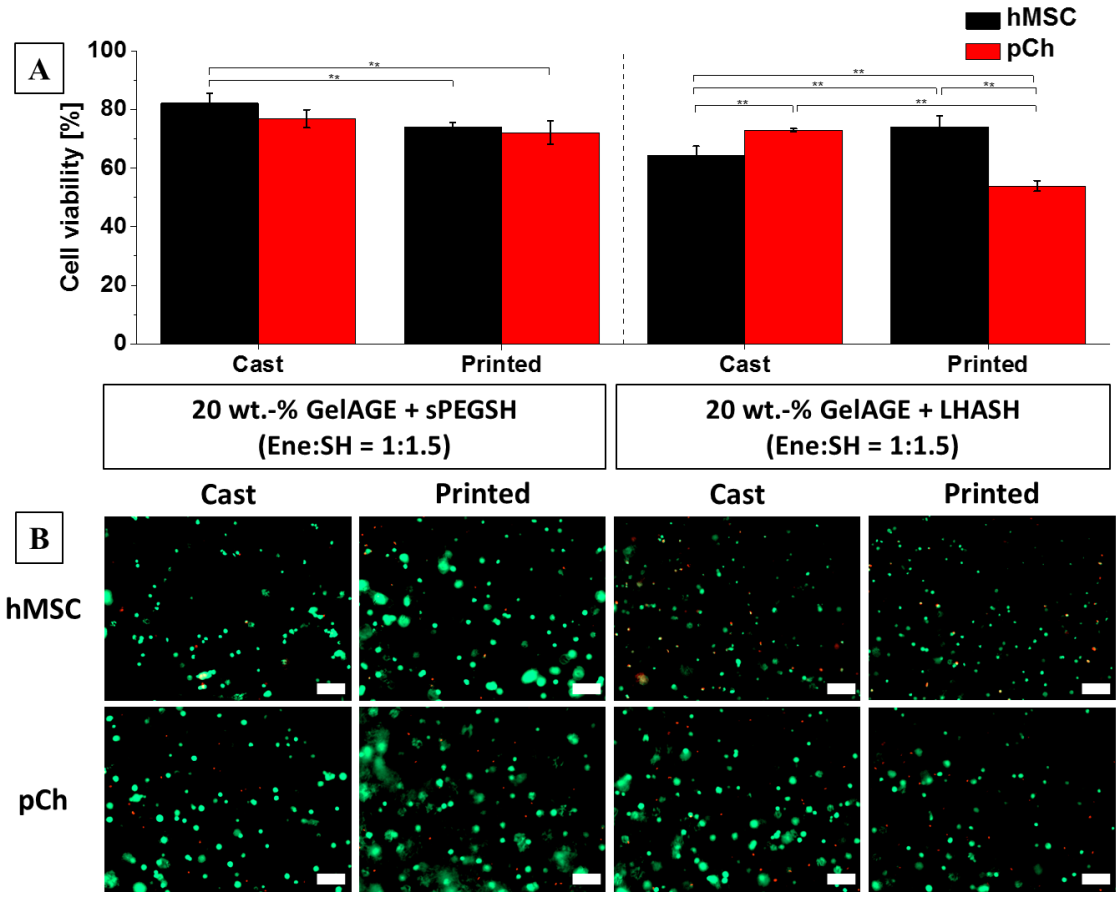


**Figure 77:** Percentage of viable encapsulated hMSCs (black) compared to pCh (red) after 1 d culture (**A**). Both cells types were encapsulated with 4.0 x $10^6$ cells $mL^{-1}$ in GelAGE + sPEGSH and in GelAGE + LHASH precursor solutions (both 20 wt.-% and Ene:SH = 1:1.5) prior to casting or extrusion-based bioprinting. Crosslinking of the hydrogels was initiated with 0.05 wt.-% I2959 with constant irradiation dosages. Representative Live/Dead images from the center of different hydrogel constructs after 1 d in culture (**B**). Scale bars represent 100 µm.

For sPEGSH crosslinked hydrogels only minor viability differences were detectable comparing hMSCs with 82 ± 3 % to pChs with 77 ± 3 % for cast or for printed hydrogels with 74 ± 2 % for hMSCs and 72 ± 4 % for pChs (**Figure 77 A**). For cast LHASH containing hydrogels significant differences of cell viabilities with 64 ± 3 % for hMSCs and 73 ± 1 % for pChs were detected. Superior hMSC viabilities were observable for printed GelAGE + LHASH constructs with 74 ± 4 % compared to pChs. Furthermore, the sensitivity of cells towards shear stress during printing was most pronounced for the combination of LHASH containing hydrogels with encapsulated pChs, whereas both cell types were less affected in printed sPEGSH constructs, which can be explained with the highest printing pressure. The corresponding microscopic Live/Dead images are shown in **Figure 77 B**. These results further underline that suitable cells for extrusion-based

bioprinting have to be evaluated individually for each bioink system.

To gain more detailed images and a concurrent higher resolution of the cellular distribution within extrusion-based printed constructs, confocal microscopic images after 1 d culture were obtained. This was exemplarily performed for constructs with encapsulated hMSCs, as these were proven to possess comparable or slightly higher viabilities in printed hydrogels than pChs.

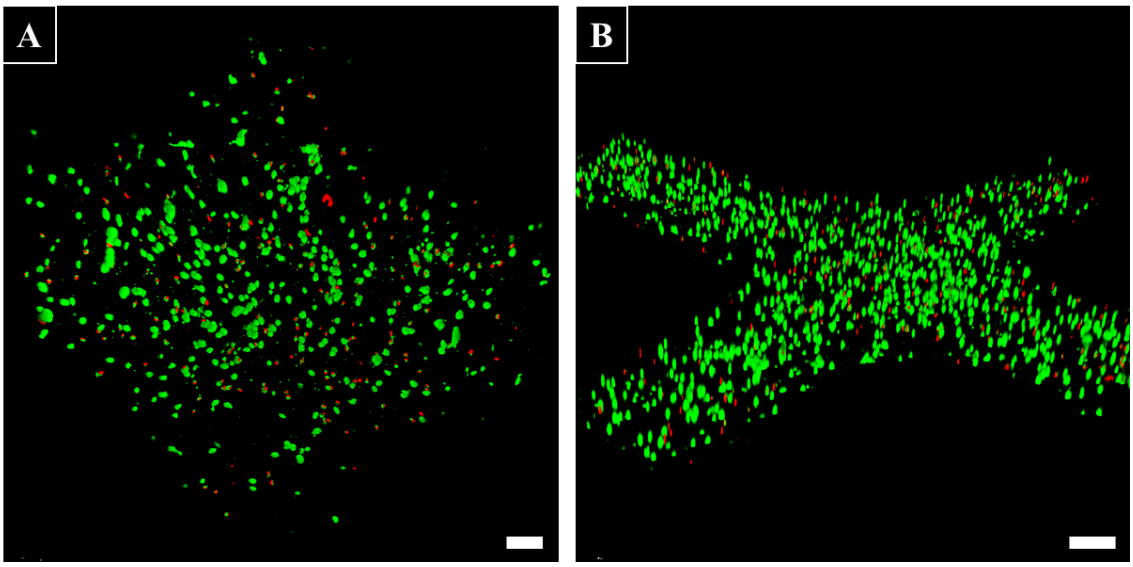


**Figure 78:** Representative Live/Dead confocal images from encapsulated hMSCs (4.0 x $10^6$ cells $mL^{-1}$) in one-layered 20 wt.-% GelAGE + sPEGSH (Ene:SH = 1:1.5) in **A** and 20 wt.-% GelAGE + LHASH (Ene:SH = 1:1.5) constructs in **B** after 1 d. Crosslinking of the hydrogels was initiated with 0.05 wt.-% I2959 at constant irradiation dosages. Scale bars represent 100 µm (**A**) and 200 µm (**B**).

For both macromolecular bioink formulations no differences of hMSC distribution were detectable. 20 wt.-% GelAGE + sPEGSH (**Figure 78 A**, Ene:SH = 1:1.5) and 20 wt.-% GelAGE + LHASH (**Figure 78 B**, Ene:SH = 1:1.5) demonstrated homogeneously distributed viable hMSCs and further complemented the analysis of the applicability of macromolecular crosslinker GelAGE formulations for extrusion-based bioprinting.

Beneficial properties of these macromolecular crosslinker containing bioinks compared to DTT-based ones are the reduced thiol content, while maintaining physico-chemical hydrogel properties and are summarized in **Figure 79**.

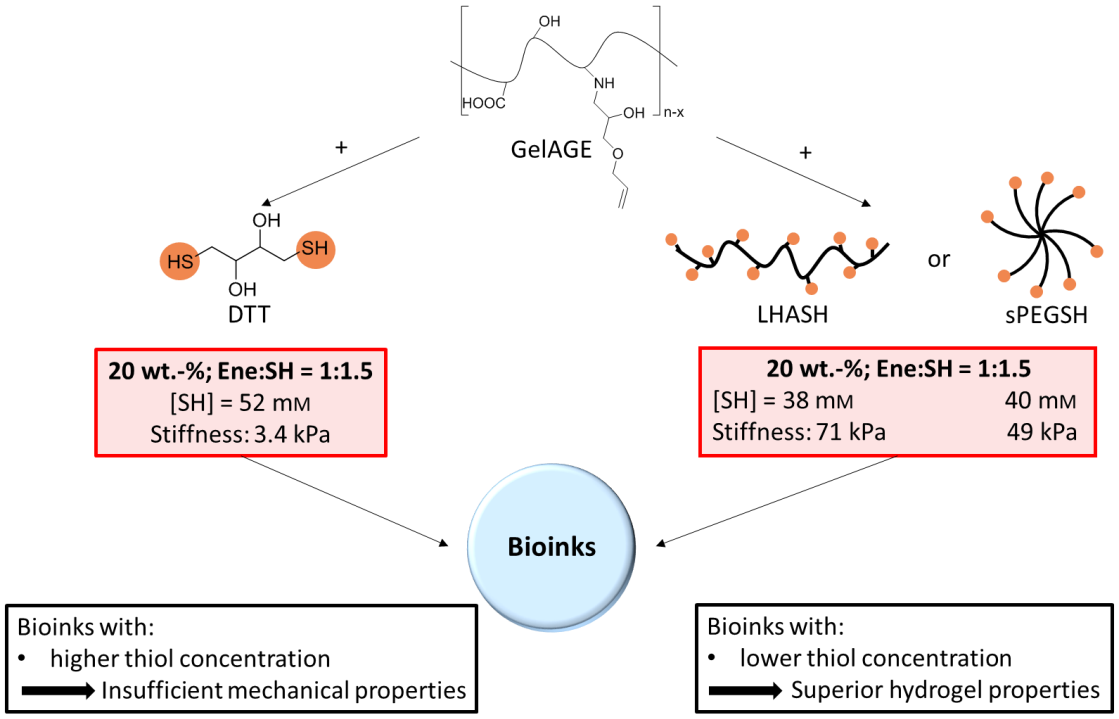


**Figure 79:** Schematic presentation of the improved GelAGE bioink compositions by comparing the small bifunctional crosslinker DTT to multifunctional macromolecular crosslinkers (LHASH and sPEGSH). Reduced thiol content resulted in superior hydrogel properties while maintaining the processability with extrusion-based bioprinting.

The thiol content of the bioinks is clearly reduced for formulations with LHAS or sPEGSH. Keeping the polymer content and Ene:SH ratio fixed for DTT containing bioinks results in constructs with only very low mechanical stiffness and these are hence unsuitable for biofabrication purposes. Only increasing polymer contents to 30 wt.-% and Ene:SH ratio to 1:3 allows to biofabricate mechanically stable constructs for DTT formulations. A direct comparisons of cell viabilities between DTT- (hAChs) and macromolecular crosslinkers- (hMSCs or pChs) constructs was not conducted as this is prone to misinterpretations due to the different cell types.

## 3.3. Hyaluronic acid-based bioinks

In this chapter hyaluronic acid (HA) was modified with pentenoate- and thiol-groups (HAPA and HASH, respectively) to enable crosslinking to pure hyaluronic acid hydrogels via the thiol-ene click chemistry. Crosslinking of the products was initiated with the most commonly used UV-initiator. Hydrogel properties were systematically investigated with varying polymer concentrations and Ene:SH ratios. Moreover, pure HA precursor formulations were compared to gelatin/HA hybrid formulations and examined for their applicability for extrusion-based bioprinting.

This work was performed with the help of Thomas Böck and Tomasz Jungst from the Department for Functional Materials in Medicine and Dentistry of Prof. Dr. Jürgen Groll at the University of Würzburg. Tomasz Jungst supported the extrusion-based printing experiments and Thomas Böck cultured the cells used for extrusion-based printing and performed the Live/Dead staining experiments and analysis of cast and printed constructs.

All hydrogel experiments were performed in triplicate ($n = 3$) and statistical evaluation was assessed by one-way ANOVA with post hoc Tukey (SigmaPlot 12.5). All values are presented as the mean ± standard deviation. Significant differences between represented groups are assigned with * ($p < 0.05$) and ** ($p < 0.001$).

### 3.3.1. Syntheses and characterizations of modified hyaluronic acid products

To enable thiol-ene click crosslinking to pure HA hydrogels, HA was modified according to literature protocols[216] with pentenoate functionalities via the hydroxyl groups of HA (**Scheme 14 A**). This esterification of HA was conducted with low and high molecular weight HA (LHA with 27.3 kDa and HHA with 1.36 MDa, respectively) and an excess of pentenoate anhydride in DMF/water mixtures under slight alkaline conditions. Products were precipitated with EtOH and purified via dialysis. After freeze-drying the products, LHAPA and HHAPA, were stored under exclusion of light at 4 °C.

To obtain fully HA-based hydrogels, the same low molecular weight thiol-modified HA crosslinker (LHASH; SD 25 %), was used as for the GelAGE-based system. In this case, the modification of HA is based on the reaction of carboxyl functionalities with disulfide bridged dihydrazides and the subsequent reduction with TCEP yields thiol-bearing products (**Scheme 14 B**). After dialysis and freeze-drying, LHASH was stored under inert gas atmosphere in a glovebox.

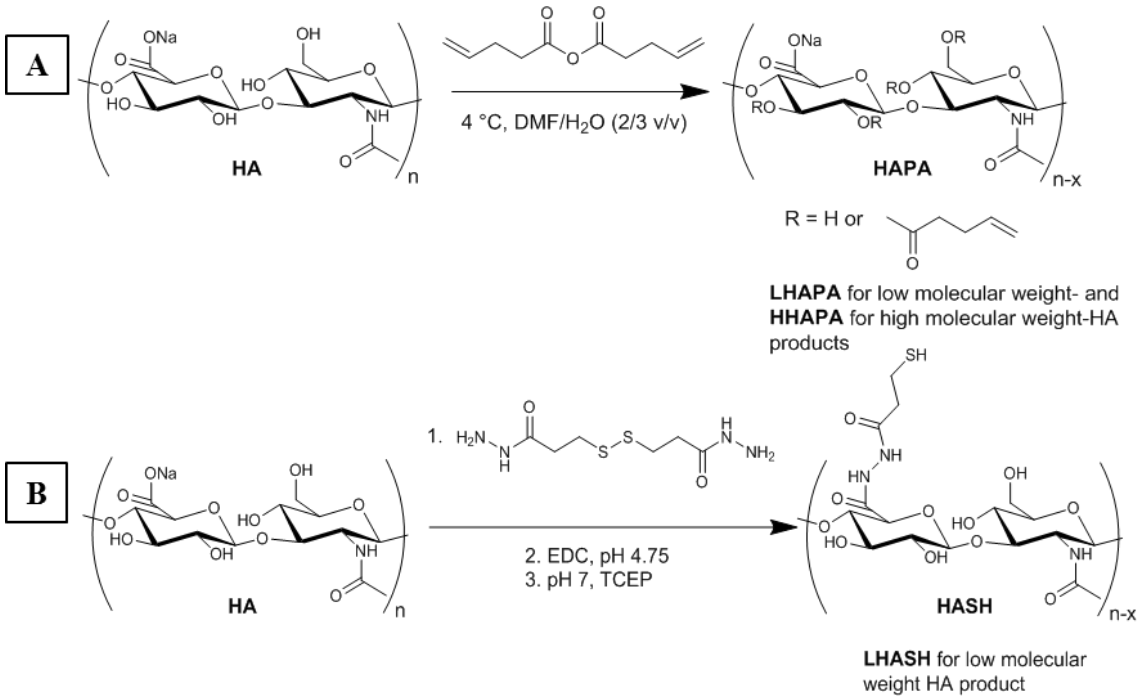


**Scheme 14:** Synthesis of pentenoate-modified hyaluronic acid (HAPA) in (**A**) and of thiol-modified hyaluronic acid (HASH) in (**B**).

Via $^{1}$H-NMR spectroscopy the SD of modified HA-products was determined and $M_w$ values by SEC analysis.

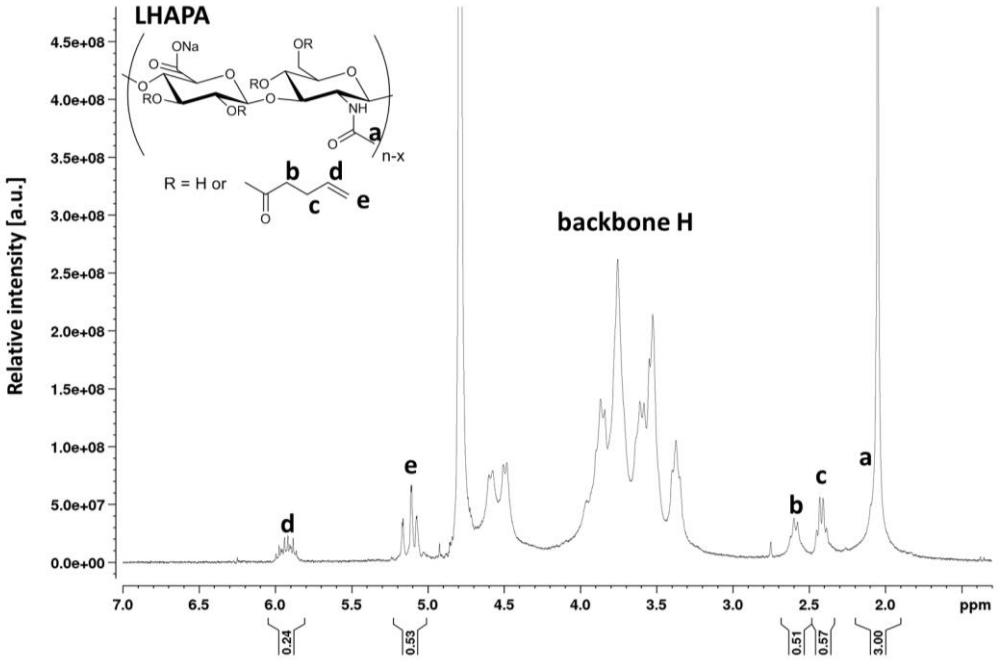


**Figure 80:** Representative $^{1}$H-NMR spectrum of LHAPA in $D_2O$. SD = 26 %.

For LHAPA, newly introduced peaks in the region from 6.0-5.8 ppm and 5.2-5.0 ppm were assigned to Ene-groups and confirmed the successful synthesis (**Figure 80**) with a calculated SD of 26 %.

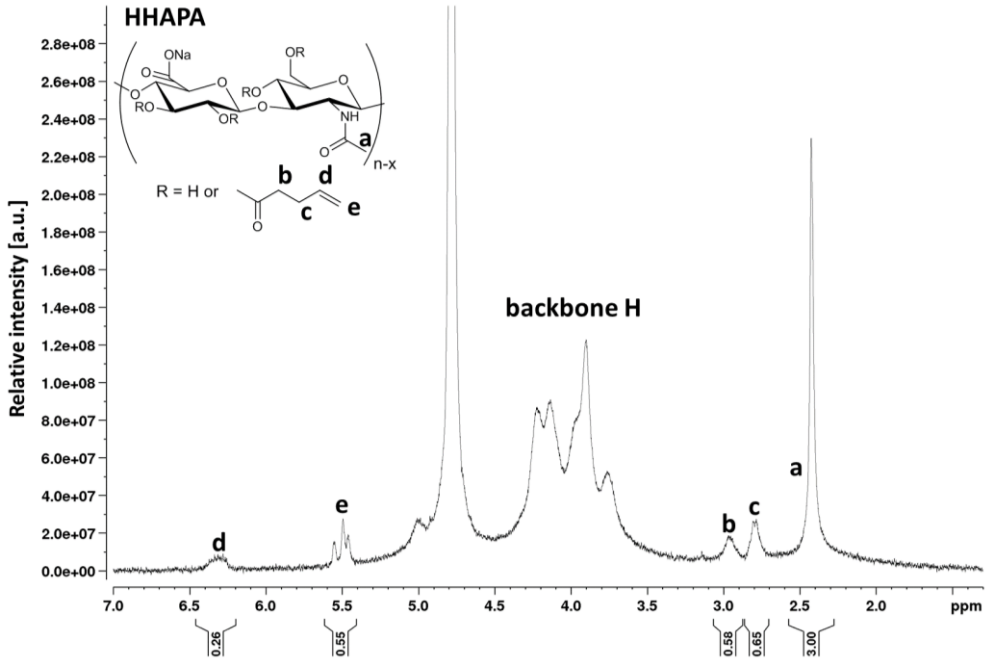


**Figure 81:** Representative $^{1}$H-NMR spectrum of HHAPA in $D_2O$ at 60 °C. SD = 32 %.

Due to the high viscosity of HHAPA solutions, the $^{1}$H-NMR spectrum of this sample was measured at 60 °C, which compared to LHAPA resulted in a shift of the Ene peaks of around 0.4 ppm (**Figure 81**). Peaks from 6.4-6.2 ppm and 5.6-5.4 ppm were assigned to the introduced Ene-moieties and the SD was estimated to be 32 %.

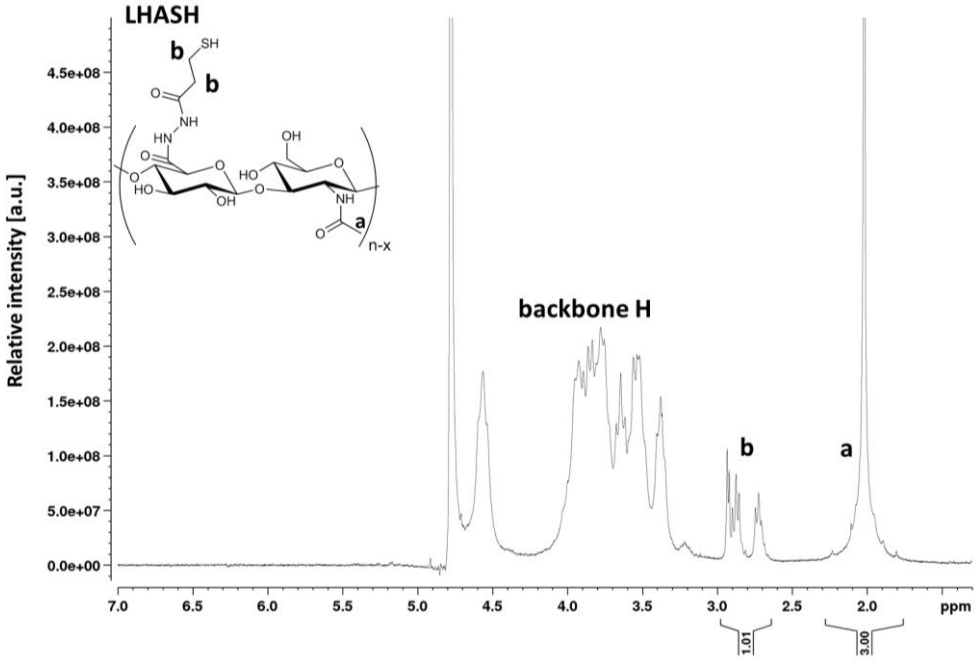


**Figure 82:** Representative $^{1}$H-NMR spectrum of LHASH in $D_2O$. SD = 25 %.

The successful synthesis of LHASH was verified via the introduction of peaks in the region of 3.0-2.6 ppm and correlated to a SD of 25 % as already described (**Figure 82**).

Differences in SEC-derived $M_w$ values for HA educts and products, as depicted in **Table 9**, can on the one side be attributed to different coiling behaviors of the products upon modification, altering the hydrodynamic radii and therefore the elution time during SEC measurements. On the other side changing molar mass as a consequence of the modification or the degradation of the HA backbone could also account for these differences. Functional group modifications with hydrophobic moieties and the extent of these functionalizations potentially influence the coiling behavior as already discussed for gelatin materials.
For thiol modification of HA, it is acknowledged that HA degrades due to the acidic synthesis and purification conditions.[138, 217, 218] However, the $M_w$ of LHA (65.4 kDa) and LHASH (78.3 kDa) were comparable and correlated to different coiling behaviors of these samples.

**Table 9:** Substitution degree (SD) values based on $^{1}$H-NMR spectroscopy and the corresponding weight-averaged molar mass ($M_w$) of HA educts and products as derived from SEC analysis.

| Sample | SD [%] | $M_w$ [kDa] |
|---|---|---|
| LHA | / | 65.4 |
| LHAPA | 26 | 71.0 |
| LHASH | 25 | 78.3 |
| HHA | / | 5294.0 |
| HHAPA | 32 | 4860.0 |

No clear trend among pentenoate functionalizations was observable as the $M_w$ values of the high molecular weight HA educt and product displayed a reversed trend with higher $M_w$ values for HHA (5294 kDa) than for HHAPA (4860 kDa) as compared to the unmodified LHA and the LHAPA product. The lower $M_w$ value of LHAPA (71.0 kDa) compared to LHASH could most probably be attributed to different coiling behaviors resulting from the introduction of distinct functionalities. Generally only minor $M_w$ value differences were detected and no conclusions about defined $M_w$ values for HA samples were drawn as both unmodified educts displayed significantly higher values than expected (27.3 kDa for LHA and 1.36 MDa for HHA) due to the calibration with poly(ethylene glycol) standards.

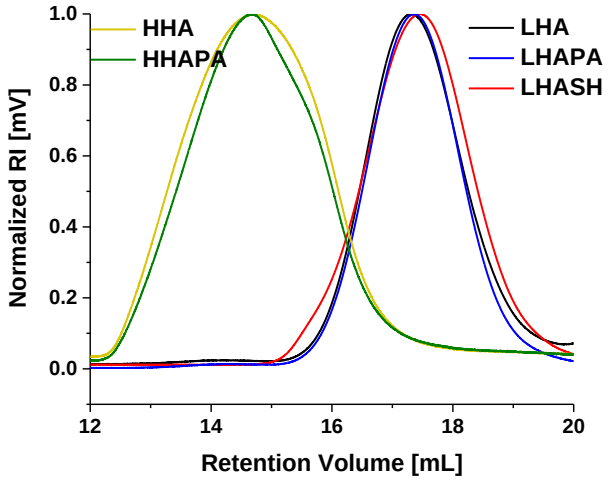


**Figure 83:** Representative elugrams of high molecular weight hyaluronic acid (HHA, yellow line) and a product with HHA, namely, HHAPA (green line) and of low molecular weight hyaluronic acid (LHA, black line) and products with LHA, namely, LHAPA (blue line) and LHASH (red line) as obtained by SEC analysis with column set I.

Considering the elugrams of HA samples, it becomes obvious that the broadening of the signals could contribute to falsifications of the obtained $M_w$ values (**Figure 83**). High molecular weight samples (HHA and HHAPA) displayed molar mass distributions in the lower retention volume range, suggesting higher molar mass components than for other samples. The molar mass distributions of the educts and products, depending on the molecular weight of HA, were in similar ranges.

### 3.3.2. Hydrogel properties

The performance of pure HA hydrogels was compared to hybrid hydrogels of gelatin with HA ($GelAGE_{1MM}$ + LHASH). Varying polymer weight percentages were used to evaluate differences between the distinct weighty HAPA products on the mechanical and physico-chemical properties of the hydrogels. Lower weight percentage hydrogels, compared to the previous studied $GelAGE_{1MM}$ + LHASH system were analyzed due to the viscosity of high molecular weight HA[138, 139, 217, 218] and due to higher functional group densities of both LHAPA and HHAPA. It has to be noted that all HA products have similar theoretical amounts of functional groups of 0.7 groups per kDa. The calculations are based on the educts molecular weight and the corresponding multiplicity of the disaccharides repeating unit. These values are roughly four times higher than directly compared to the previous investigated $GelAGE_{1MM}$ product with 0.2 groups per kDa and could account for hydrogel property differences when comparing both systems. Ene:SH ratios were chosen according to the $GelAGE_{1MM}$ + LHASH system (1:1.5 – 1:3) and 0.05 wt.-% I2959 was used to initiate crosslinking under equal irradiation dosages as previously used.

For simplification the obtained hydrogels are termed GelAGE + LHASH ($GelAGE_{1MM}$ + LHASH), LHAPA + LHASH and HHAPA+ LHASH in the context of this study. Importantly, HHAPA + LHASH hydrogels possessed a limited weight percentage range of max. 5.0 wt.-%, due to their high viscosity and manageability, whereas LHAPA + LHASH hydrogels could easily be fabricated up to 7.5 wt.-%. Besides low polymer weight percentages for GelAGE + LHASH hydrogels (2.5 – 7.5 wt.-%) also high weight percentages of 10 – 30 wt.-% were included in this study.

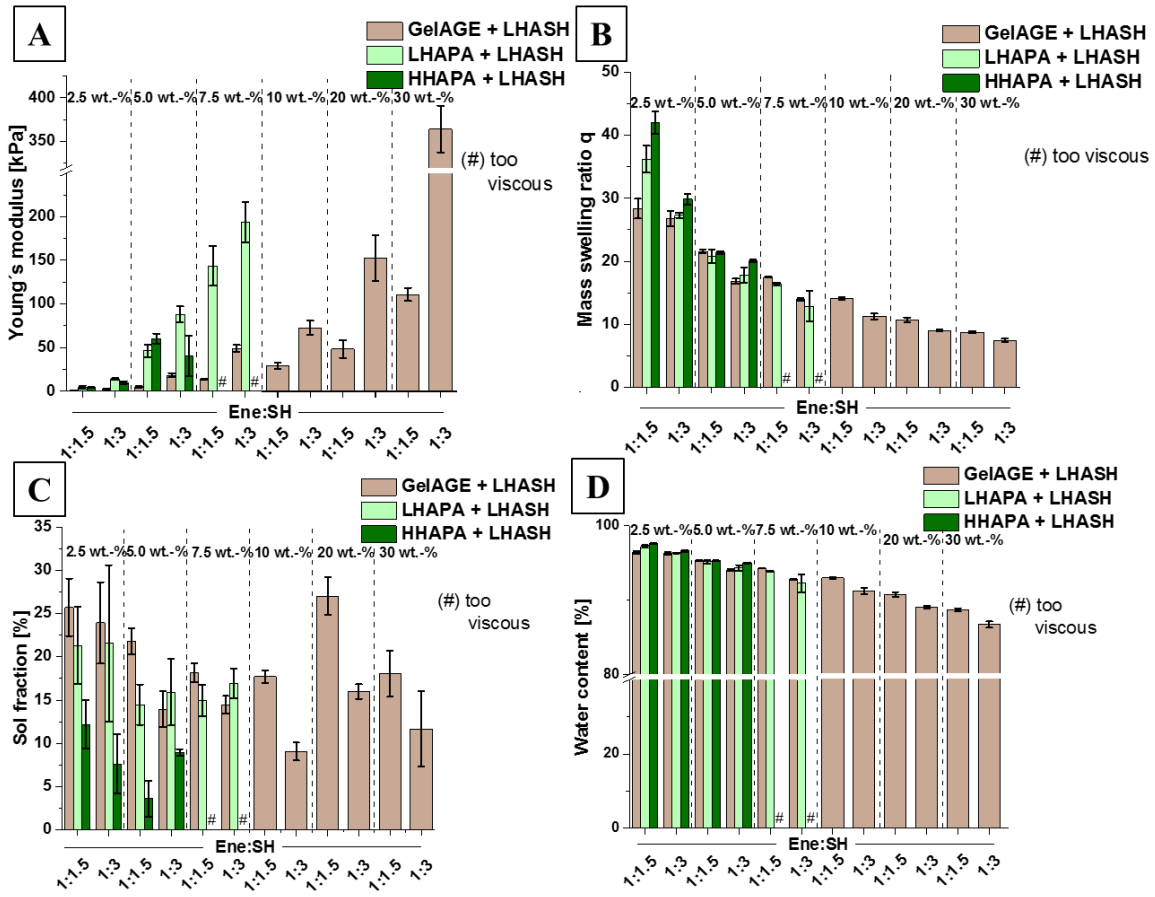


**Figure 84:** Young´s moduli (**A**) of GelAGE + LHASH, LHAPA + LHASH and HHAPA + LHASH hydrogel compositions with varying weight percentages, the corresponding mass swelling ratio q (**B**), sol fraction (**C**) and water content of the hydrogels (**D**). Crosslinking was initiated with 0.05 wt.-% I2959. GelAGE + LHASH hydrogels are represented by brown bars, LHAPA + LHASH by light green bars and HHAPA + LHASH by dark green bars. Conditions marked with (#) represent too viscous precursor solutions to be manageable. For clarity purposes the statistical differences between the groups are not presented.

A general trend of increasing mechanical stiffness with increasing polymer weight percentages, which allows for higher crosslinking densities, was observable (**Figure 84 A**). The Ene:SH ratio exhibited similar characteristics, where an increase of this ratio led to improvements of the overall hydrogel properties by increasing mechanical stiffnesses while decreasing mass swelling ratios q, sol fractions and water contents (**Figure 84**). Comparing 2.5 – 7.5 wt.-% hydrogels with one another it becomes obvious that GelAGE + LHASH hydrogels (0.6 – 48 kPa) exhibited lower mechanical strengths as HA hydrogels (4.5 – 193 kPa for LHAPA + LHASH and 4.7 – 60 kPa for HHAPA + LHASH). Moreover, even HA hydrogels with maximal 7.5 wt.-% possessed already superior mechanical properties compared to 2.5 – 20 wt.-% GelAGE + LHASH hydrogels. These observations

can probably be correlated to different densities in functional groups per kDa, which in turn increase the number of possible crosslinks. An increase in SD for GelAGE was previously demonstrated not to improve the hydrogels mechanical stability, as this was compensated by the proceeding degradation of the gelatin backbone. Mass swelling ratios q of all hydrogels decreased concurrent with increasing polymer content and was lower for an Ene:SH ratio of 1:3 due to more efficiently crosslinked networks (**Figure 84 B**). Both HA systems reached similar values throughout the tested conditions of 2.5 – 7.5 wt.-% ($q < 36$ for LHAPA + LHASH and $q < 42$ for HHAPA + LHASH), which were slightly higher than for corresponding GelAGE + LHASH hydrogels ($q < 28$) and could be correlated to the polyanionic character of HA and the concurrent water attraction. Sol fractions for all HHAPA + LHASH hydrogels varied between 3 – 12 % and were lower than for the LHAPA + LHASH hydrogels, which possessed values in the range of 14 – 22 % (**Figure 84 C**). The lower sol fraction of HHAPA + LHASH hydrogels could be explained by a limited diffusion possibility of HHAPA, due to the higher molecular weight. Most efficiently crosslinked hydrogels were reached for 5.0 wt.-% HA hydrogels and 7.5 wt.-% LHAPA + LHASH hydrogels with Ene:SH ratios of 1:3 as reflected by the lowest mass swelling ratios q and sol fractions. Water contents of the hydrogels were comparable for the different systems and ranged between 87 – 98 % (**Figure 84 D**).

In general, only 30 wt.-% GelAGE + LHASH possessed superior properties than HA hydrogels (maximum 7.5 wt.-%). The mechanical and physico-chemical properties of HA hydrogels were slightly increased compared to GelAGE + LHASH hydrogels (10 – 20 wt.-%). Especially noteworthy is the decrease in required weight percentages to achieve similar or even improved hydrogel properties as for GelAGE + LHASH, which is depicted in **Table 10**.

For HA hydrogels only half or less of the polymer content and lower Ene:SH ratios were required to obtain similar hydrogel properties than for GelAGE + LHASH hydrogels (**Table 10**). GelAGE + LHASH hydrogels for the same weight percentages as HA compositions resulted in strongly decreased hydrogel properties. For example 7.5 wt.-% LHAPA + LHASH resulted in Young´s moduli of around 143 kPA, whereas 7.5 wt.-% GelAGE + LHASH yielded approximately 14 kPa and were hence unsuitable for mechanically stable constructs with high shape fidelities. Comparable mechanical stiffness was found for 20 wt.-% GelAGE + LHASH (152 kPA) with more than the doubled polymer

content than for LHAPA + LHASH. Similar correlations were found for HHAPA + LHASH compositions. Swelling ratios and water contents remained constant and lower sol fraction were detectable for HA hydrogels compared to identical weight percentages of GelAGE + LHASH compositions.

**Table 10:** Comparison of Ene:SH ratio, thiol content, mechanical and physico-chemical properties of GelAGE + LHASH, LHAPA + LHASH and HHAPA + LHASH hydrogels.

| LHASH with | Ene:SH ratio | SH [mM] | Young´s Modulus [kPa] | Mass swelling ratio q | Sol fraction [%] | Water content [%] |
|---|---|---|---|---|---|---|
| 20 wt.-% GelAGE | 1:3 | 60 | 152 ± 26 | 9.1 ± 0.1 | 16 ± 0.9 | 89 ± 0.2 |
| 7.5 wt.-% GelAGE | 1:1.5 | 14 | 14 ± 0.1 | 18 ± 0.1 | 18 ± 1.1 | 94 ± 0.1 |
| 7.5 wt.-% LHAPA | 1:1.5 | 25 | 143 ± 22 | 16 ± 0.2 | 14 ± 1.8 | 94 ± 0.4 |
| 10 wt.-% GelAGE | 1:3 | 30 | 73 ± 8.0 | 14 ± 0.3 | 9.0 ± 1.0 | 92 ± 0.4 |
| 5.0 wt.-% GelAGE | 1:1.5 | 9.6 | 4.8 ± 0.6 | 22 ± 0.3 | 22 ± 1.5 | 94 ± 0.2 |
| 5.0 wt.-% HHAPA | 1:1.5 | 19 | 60 ± 5.5 | 21 ± 0.2 | 3.6 ± 2.1 | 95 ± 0.1 |

Mechanical and physico-chemical properties of pure HA and hybrid gelatin-HA hydrogels were controlled by varying Ene:SH ratios, polymer weight percentages and molecular weights of HA components. The HA system allowed to significantly reduce the polymer and thiol content while maintaining the overall hydrogel properties (e.g. 20 wt.-% GelAGE with 60 mM SH and 7.5 wt.-% LHAPA with 25 mM SH). This was attributed to higher functional group densities and the maintained molecular mass of HA-polymers. In contrast, increasing the SD for GelAGE products could not improve the physico-chemical properties of the hydrogels as this was compensated by the degradation of gelatin and further underlines the importance of the control over the polymers molecular mass.

### 3.3.3. Rheological properties and extrusion-based bioprinting

HA-based precursor solutions were analyzed with rheological experiments, analogous to the GelAGE system, to assess their applicability as bioinks for extrusion-based (bio)printing.

Rheological analysis of LHAPA containing precursor solutions was not possible with the highest polymer content of 7.5 wt.-% as this system was too liquid to enable the detection

of stable measurement points. Exchanging low with high molecular weight HAPA component resulted in a significant increased viscosity, which is in accordance to literature[139, 217] and enabled rheological investigations. As previously mentioned the upper limit for manageability of HHAPA-based solutions was 5.0 wt.-% and this solution was compared to printable 20 wt.-% GelAGE + LHASH at constant Ene:SH ratios of 1:1.5.

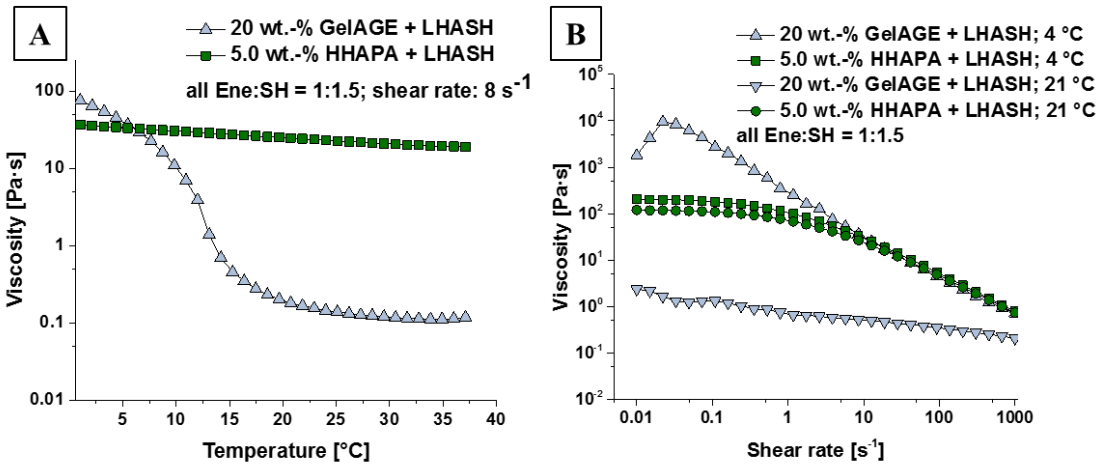


**Figure 85:** Representative temperature sweep from 1 – 37 °C with 1 °C $min^{-1}$ at a constant shear rate of 8 $s^{-1}$ (**A**) and the viscosity in dependence from different shear rates at 4 °C and 21 °C (**B**) of 20 wt.-% GelAGE + LHASH (light blue) compared to 5.0 wt.-% HHAPA + LHASH (dark green) both with Ene:SH = 1:1.5.

Comparing 5.0 wt.-% HHAPA + LHASH solution to the printable 20 wt.-% GelAGE + LHASH system, at a fixed Ene:SH ratio of 1:1.5, it becomes obvious that no thermoresponsiveness was detectable for HHAPA + LHASH (**Figure 85 A**). This was also not expected as in contrast to gelatin, HA is not known to exhibit a thermoresponsive behavior[219]. Hence, the shear-thinning behavior of HHAPA + LHASH was independent on the different temperatures, whereas GelAGE + LHASH solutions clearly demonstrated a decrease in viscosity with rising temperatures (**Figure 85 B**). At the previously determined printing shear rates of approximately 6 – 8 $s^{-1}$ both solutions were in similar ranges independent on the temperature except for 21 °C with GelAGE + LHASH.

These observations indicate the applicability of 5.0 wt.-% HHAPA + LHASH solutions (Ene:SH = 1:1.5) for extrusion-based (bio)printing. Extrusion-based printing with HHAPA + LHASH could theoretically be performed either at room temperature or under cooled conditions. However, to ensure comparability of this solution to the previous obtained results for extrusion-based bioprinting and the concurrent cellular viability for

GelAGE-based formulations, the same printing parameters as for GelAGE + LHASH were applied and the printing was conducted under cooled conditions.

Notably the pure HA system could be processed with only 1.25 bar, whereas for GelAGE + LHASH 2.1 – 2.7 bar were applied. The G Code remained the same and constructs were irradiated, in the presence of 0.05 wt.-% I2959, while printing with 2 s intervals per layer and afterwards with 3 x 2 s, similar to previous printed constructs in order to minimize potential damages on cellular DNA during UV-irradiation.

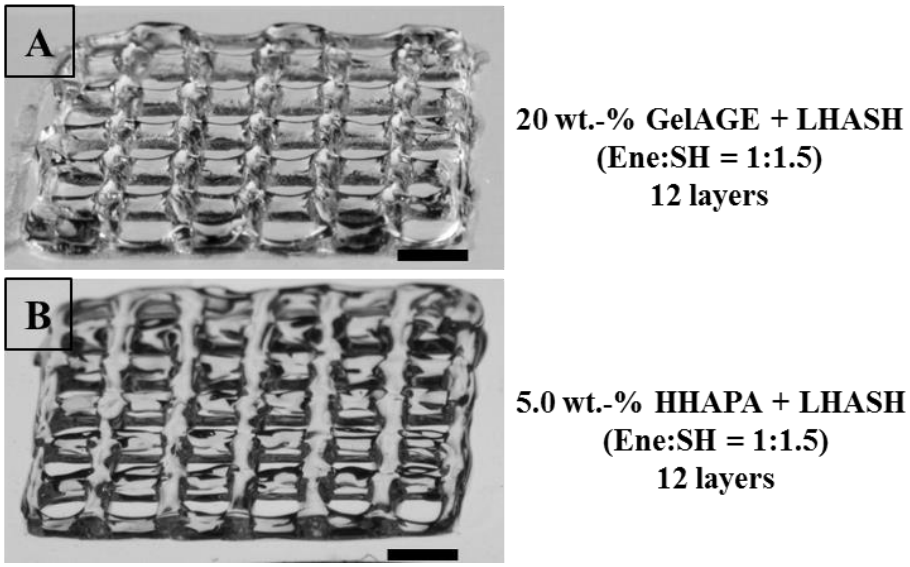


**Figure 86:** Representative microscopic images of a 20 wt.-% GelAGE + LHASH (Ene:SH = 1:1.5) construct (**A**) and of a 5.0 wt.-% HHAPA + LHASH (Ene:SH = 1:1.5) construct (**B**). For both twelve-layered constructs the crosslinking was initiated with 0.05 wt.-% I2959 with 2 s intervals per layer and a final irradiation of 3 x 2 s. Scale bars represent 2 mm.

5.0 wt.-% HHAPA + LHASH constructs with a high shape fidelity of up to twelve layers were fabricated (**Figure 86 A**), similar to 20 wt.-% GelAGE + LHASH (**Figure 86 B**) at constant Ene:SH ratios of 1:1.5. Strand distances of 880 ± 41 µm and fiber diameters of 430 ± 40 µm were obtained for HHAPA + LHASH and are in comparable ranges to GelAGE + LHASH with 919 ± 16 µm strand distances and 383 ± 21 µm fiber diameters. Compared to GelAGE + LHASH, HHAPA + LHASH enabled processing with lower thiol amounts and only one-fourth of the entire polymer content at lower printing pressures, which represent factors that are hypothesized to increase the biocompatibility of the system.[6]

To further evaluate the applicability of 5.0 wt.-% HHAPA + LHASH (Ene:SH = 1:1.5) as a bioink for extrusion-based bioprinting the cell viability of encapsulated pChs was compared for cast and printed hydrogels, similar to previous obtained results for GelAGE + LHASH. Live/Dead staining was used to assess the cellular viability after 1 d and 21 d in culture.

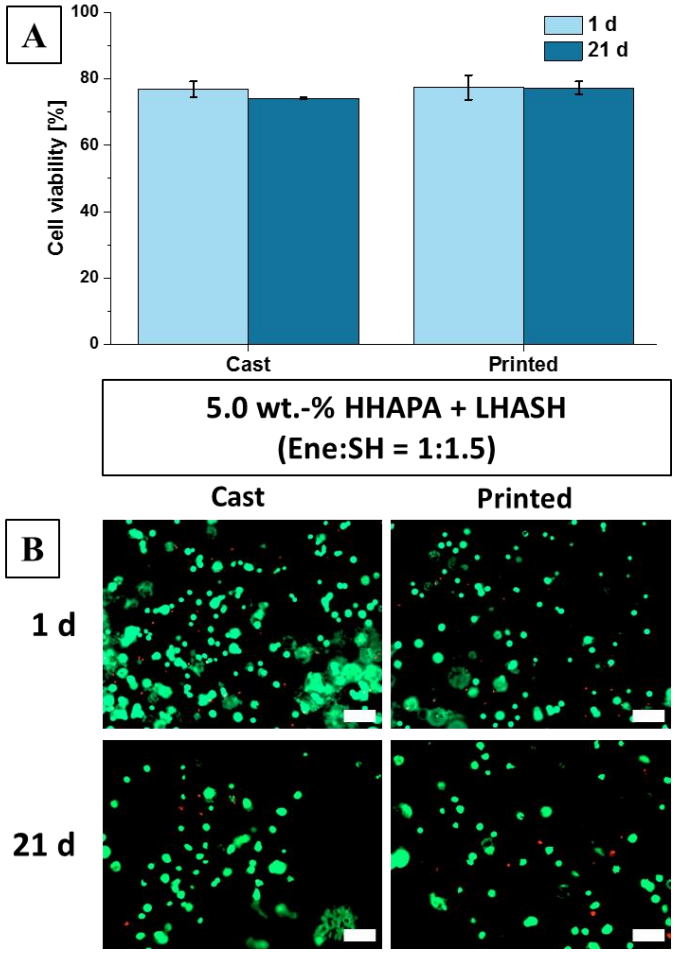


**Figure 87:** Viability of encapsulated pChs (4.0 x $10^6$ cells $mL^{-1}$) in 5.0 wt.-% HHAPA + LHASH hydrogels (Ene:SH = 1:1.5) after 1 d (light blue) and 21 d (dark blue) in culture (**A**). Hydrogels were either cast or extrusion-based bioprinted and crosslinking was initiated with 0.05 wt.-% I2959 with constant irradiation dosages. Concurrent representative Live/Dead images from the center of hydrogel constructs after 1 d and 21 d of culture (**B**). Scale bars represent 100 µm. No significant differences between the investigated groups were detectable.

No significant differences of cell viabilities were detectable for cast with 77 ± 2 % or printed HHAPA + LHASH hydrogels with 77 ± 4 % after 1 d of culture and throughout the culture period with viabilities of 74 ± 0.3 % in cast and 77 ± 2 % in printed hydrogels

(**Figure 87 A**). Corresponding Live/Dead images of the constructs are depicted in **Figure 87 B**. For HHAPA + LHASH the reduction of the printing pressure to 1.25 bar, compared to 2.1 – 2.7 bar for GelAGE + LHASH, significantly improved the cellular viability by reducing the shear stress during extrusion-based printing. This effect is most prominent after the culture period with values of around 77 % for HHAPA + LHASH and 43 % for GelAGE + LHASH.

Moreover, cellular viabilities of hMSCs were compared to pChs after a culture period of 1 d to assess the most suitable cells for this hydrogel composition, similar to the evaluation for GelAGE + LHASH.

A slight increased viability of pChs with 77 ± 2 % was detectable as compared to 71 ± 6 % for hMSCs both in cast and printed hydrogels with 77 ± 4 % for pChs and 71 ± 3 % for hMSCs (**Figure 88 A**). No viability restricting effects arising from extrusion-based bioprinting were observable. Again this was attributed to the reduction of required printing pressure and further underlines the applicability of 5.0 wt.-% HHAPA + LHASH (Ene:SH = 1:1.5) as bioink for extrusion-based printing purposes. The concurrent Live/Dead images are given in **Figure 88 B**.

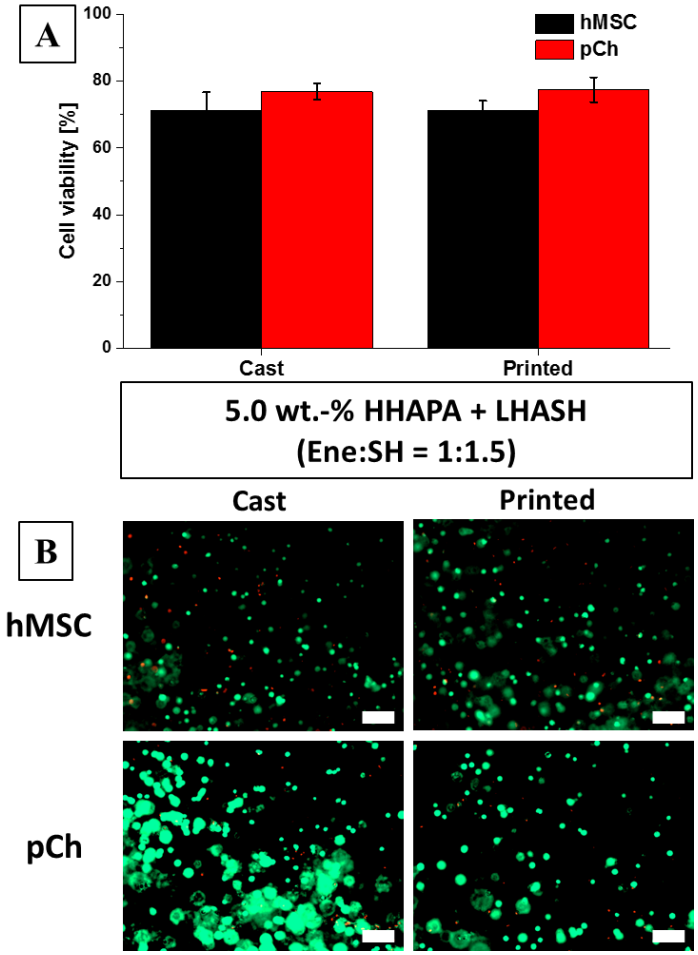


**Figure 88:** Percentage of viable encapsulated hMSCs (black) compared to pChs (red) after 1 d culture (**A**). Both cells types were encapsulated with 4.0 x $10^6$ cells $mL^{-1}$ in 5.0 wt.-% HHAPA + LHASH precursor solutions (Ene:SH = 1:1.5) prior to casting or extrusion-based bioprinting. Crosslinking of the hydrogels was initiated with 0.05 wt.-% I2959 with constant irradiation dosages. Representative Live/Dead images from the center of the different hydrogel constructs after 1 d in culture (**B**). Scale bars represent 100 µm. No significant differences between the investigated groups were detectable.

The beneficial properties of pure HA bioinks (HHAPA + LHASH) compared to hybrid bioinks with GelAGE are summarized in **Figure 89**.

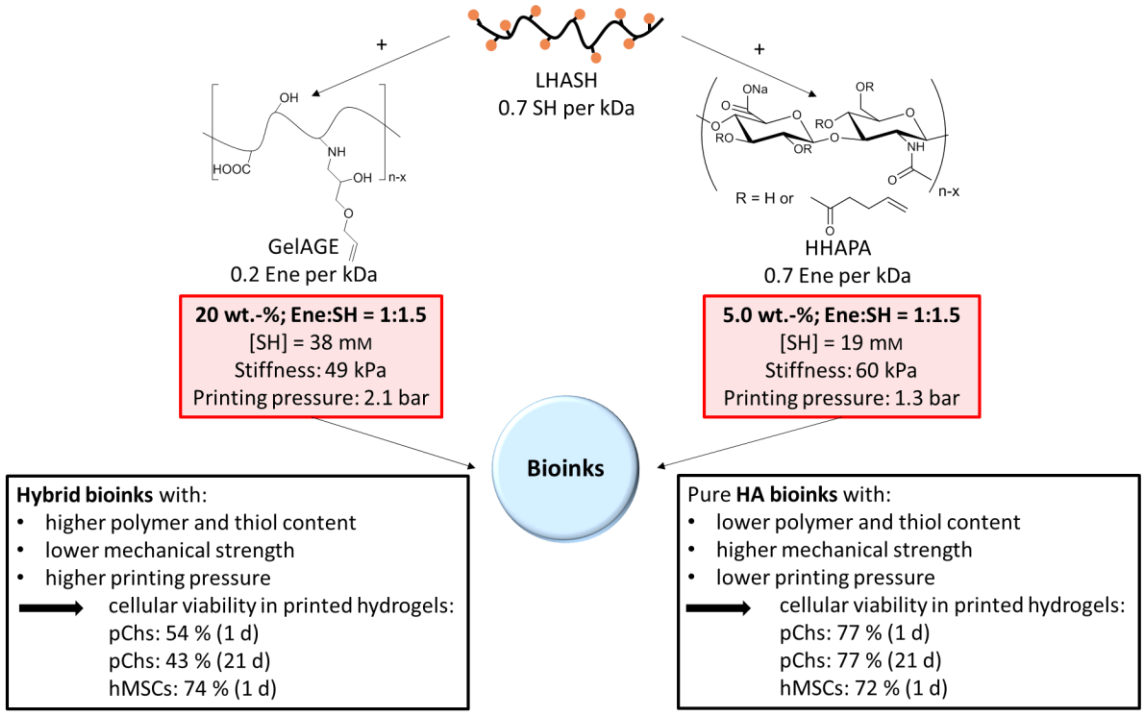


**Figure 89:** Schematic presentation of the bioink compositions of hybrid and pure HA bioinks. With LHASH as constant crosslinker molecule and fixed Ene:SH ratios of 1:1.5, superior hydrogel properties were detectable for pure HA bioinks than compared to hybrid bioinks with GelAGE. The lower printing pressure together with a reduction of the polymer and thiol content resulted in increased cell viabilities in bioprinted constructs.

Only one-fourth of the polymer content compared to GelAGE + LHASH systems is required for the pure HA bioink with HHAPA to obtain high shape fidelity constructs and this reduction together with the lower thiol content was proven to increase the cellular viability of encapsulated pChs and hMSCs. Herein, a direct comparison between cellular viabilities is enabled due to the same cell sources and underlines the advantageous of pure HA bioinks, further stressing the applicability as a bioink for biofabrication approaches.

# 4. Summary/Zusammenfassung

# Summary

**Aim of this thesis** was the development of functionalizable hydrogel coatings for melt electrowritten PCL scaffolds and of bioprintable hydrogels for biofabrication.

Hydrogel coatings of melt electrowritten scaffolds enabled to control the surface hydrophilicity, thereby allowing cell-material interaction studies of biofunctionalized scaffolds in minimal protein adhesive environments. For this purpose, a hydrophilic star-shaped crosslinkable polymer was used and the coating conditions were optimized. Moreover, newly developed photosensitive scaffolds facilitated a time and pH independent biofunctionalization.

Bioprintable hydrogels for biofabrication were based on the allyl-functionalization of gelatin (GelAGE) and modified hyaluronic acid-products, to enable hydrogel crosslinking by means of the thiol-ene click chemistry. Optimization of GelAGE hydrogel properties was achieved through an in-depth analysis of the synthesis parameters, varying Ene:SH ratios, different crosslinking molecules and photoinitiators. Homogeneity of thiol-ene crosslinked networks was compared to free radical polymerized hydrogels and the applicability of GelAGE as bioink for extrusion-based bioprinting was investigated. Purely hyaluronic acid-based bioinks were hypothesized to maintain mechanical- and rheological properties, cell viabilities and the processability, upon further decreasing the overall hydrogel polymer and thiol content.

**Hydrogel coatings:** Highly structured PCL scaffolds were fabricated with MEW and subjected to coatings with six-armed star-shaped crosslinkable polymers (sP(EO-*stat*-PO)). Crosslinking results from the aqueous induced hydrolysis of reactive isocyanate groups (NCO) of sP(EO-*stat*-PO) and increased the surface hydrophilicity and provided a platform for biofunctionalizations in minimal protein adhesive environments. Not only the coating procedure was optimized with respect to sP(EO-*stat*-PO) concentrations and coating durations, instead scaffold pre-treatments were developed, which were fundamental to enhance the final hydrophilicity to completely avoid unspecific protein adsorption on sP(EO-*stat*-PO) coated scaffolds. The sP(EO-*stat*-PO) layer thickness of around 100 nm generally allows *in vitro* studies not only in dependence on the scaffold biofunctionalization but also on the scaffold architecture. The hydrogel coating extent was assessed via an indirect quantification of the NCO-hydrolysis products. Knowledge of NCO-hydrolysis kinetics enabled to achieve a balance of sufficiently coated scaffolds while maintaining the

presence of NCO-groups that were exploited for subsequent biofunctionalizations. However, this time and pH dependent biofunctionalization was restricted to small biomolecules. In order to overcome this limitation and to couple high molecular weight biomolecules another reaction route was developed. This route was based on the photolysis of diazirine moieties and enabled a time and pH independent scaffold biofunctionalization with streptavidin and collagen type I. The fibril formation ability of collagen was used to obtain different collagen conformations on the scaffolds and a preliminary *in vitro* study demonstrated the applicability to investigate cell-material interactions.

The herein developed scaffolds could be applied to gain deeper insights into the fundamentals of cellular sensing. Especially the complexity by which cells sense e.g. collagen remain to be further elucidated. Therefore, different hierarchies of collagen-like conformations could be coupled to the scaffolds, e.g. gelatin or collagen-derived peptide sequences, and the activation of DDR receptors in dependence on the complexity of the coupled substances could be determined. Due to the strong streptavidin-biotin bond, streptavidin functionalized scaffolds could be applied as a versatile platform to allow immobilization of any biotinylated molecules.

**Gelatin-based bioinks**: First the GelAGE products were synthesized with respect to molecular weight distributions and amino acid composition integrity. A detailed study was conducted with varying molar ratios of reactants and synthesis durations and implied that gelatin degradation was most dominant for high alkaline synthesis conditions with long reaction times. Gelatin possesses multiple functionalizable groups and the predominant functionalization of amine groups was confirmed via different model substances and analyses. Polymer network homogeneity was proven for the GelAGE system compared to free radical polymerized hydrogels with GelMA. A detailed analysis of hydrogel compositions with varying functional group ratios and UV- or Vis-light photoinitiators was executed. The UV-initiator concentration is restricted due to cytotoxicity and potential cellular DNA damages upon UV-irradiation, whereas the more cytocompatible Vis-initiator system enabled mechanical stiffness tuning over a wide range by controlling the photoinitiator concentration at constant Ene:SH ratios and polymer weight percentages. Versatility of the GelAGE bioink for different AM techniques was proved by exploiting the thermo-gelling behavior of differently degraded GelAGE products for stereolithography and extrusion-based printing. Moreover, the viability of cell-laden

GelAGE constructs was demonstrated for extrusion-based bioprinting. By applying different multifunctional thiol-macromolecular crosslinkers the mechanical and rheological properties improved concurrently to the processability. Importantly, lower thiol-crosslinker concentrations were required to yield superior mechanical strengths and physico-chemical properties of the hydrogels as compared to the small bis-thiol-crosslinker. Extrusion-based bioprinting with distinct encapsulated cells underlined the need for individual optimization of cell-laden hydrogel formulations.

Not only the viability of encapsulated cells in extrusion-based bioprinted constructs should be assessed, instead other parameters such as cell morphology or production of collagen or glycosaminoglycans should be considered as these represent some of the crucial prerequisites for cartilage Tissue Engineering applications. Moreover, these studies should be expanded to the stereolithographic approach and ultimately the versatility and cytocompatibility of formulations with macromolecular crosslinkers would be of interest. Macromolecular crosslinkers allowed reducing polymer weight percentages and amounts of thiol groups and are thus expected to contribute to increased cytocompatibility, especially in combination with the more cytocompatible Vis-initiator system, which remains to be elucidated.

**Hyaluronic acid-based bioinks:** Different molecular weight hyaluronic acid (HA) products were synthesized to bear ene- (HAPA) or thiol-functionalities (LHASH) to enable pure HA thiol-ene crosslinked hydrogels. Depending on the molecular weight of modified HA products, polymer weight percentages and Ene:SH ratios, a wide range of mechanical stiffness was covered. However, the manageability of high molecular weight HA (HHAPA) product solutions (HHAPA + LHASH) was restricted to 5.0 wt.-% as a consequence of the high viscosity. Based on the same HA thiol component (LHASH), hybrid hydrogels of HA with GelAGE were compared to pure HA hydrogels. Although the overall polymer weight percentage of HHAPA + LHASH hydrogels was significantly lowered compared to hybrid hydrogels (GelAGE + LHASH), similar mechanical and physico-chemical properties of pure HA hydrogels were determined with maintained Ene:SH ratios. Low viscous low molecular weight HA precursor solutions (LHAPA + LHASH) prevented the applicability for extrusion-based bioprinting, whereas the non-thermoresponsive HHAPA + LHASH system could be bioprinted with only one-fourth of the polymer content of hybrid formulations. The high viscous behavior of HHAPA + LHASH solutions, lower polymer

weight percentages, decreased printing pressures and consequently declined shear stress during printing, were hypothesized to contribute to high cell viabilities in extrusion-based bioprinted constructs compared to the hybrid bioink.

The low molecular weight HA precursor formulation (LHAPA + LHASH) was not applicable for extrusion-based printing, but this system has potential for other AM techniques such as stereolithography. Similar to the GelAGE system a more detailed study on the functions of encapsulated cells would be useful to further develop this system. Moreover, the initiation with the Vis-initiator should be conducted.

# Zusammenfassung

**Ziel dieser Arbeit** war die Entwicklung von funktionalisierbaren Hydrogel Beschichtungen für Schmelz-elektrogeschriebene PCL Gerüste und von Bio-druckbaren Hydrogelen für die Biofabrikation.

Hydrogel Beschichtungen von Schmelz-elektrogeschriebenen Konstrukten ermöglichten die Kontrolle der Oberflächen-Hydrophilie und damit Zell-Material Interaktionsstudien in minimal Protein-adhäsiven Umgebungen. Zu diesem Zweck wurde ein hydrophiles sternförmiges vernetzbares Polymer verwendet und eine Optimierung der Beschichtungsbedingungen durchgeführt. Außerdem boten neu entwickelte photosensitive Konstrukte eine Zeit- und pH-unabhängige Biofunktionalisierung.

Bio-druckbare Hydrogele für die Biofabrikation basierten auf der Allyl-Funktionalisierung von Gelatine (GelAGE) und modifizierten Hyaluronsäure-Produkten, die das Hydrogel-Vernetzen mittels Thiol-En Click Chemie ermöglichen. Die Optimierung der GelAGE Hydrogel-Eigenschaften wurde durch eine detaillierte Analyse der Syntheseparameter, variierender En:SH Verhältnisse, unterschiedlicher Vernetzungsmoleküle und Photoinitiatoren erreicht. Die Homogenität der Thiol-En Netzwerke wurde mit denen der freien radikalischen Polymerisation verglichen und die Verwendbarkeit von GelAGE als Bio-Tinte für den Extrusions-basierten Bio-Druck wurde untersucht. Es wurde angenommen, dass reine Hyaluronsäure-basierte Bio-Tinten eine Beibehaltung der mechanischen und rheologischen Eigenschaften, der Zellviabilität und der Prozessierbarkeit ermöglichen trotz geringerem Polymer- und Thiol-Anteil der Hydrogele.

**Hydrogel-Beschichtungen:** Hoch definierte PCL Gerüste wurden mittels MEW hergestellt und anschließend mit sechs armigen sternförmigen vernetzbaren Polymeren (sP(EO-*stat*-PO)) beschichtet. Die Vernetzung wird durch die wässrig-induzierte Hydrolyse reaktiver Isocyanatgruppen (NCO) von sP(EO-*stat*-PO) bedingt. Diese Beschichtung erhöhte die Oberflächen-Hydrophilie und stellte eine Plattform für weitere Biofunktionalisierungen, in minimal Protein-adhäsiven Umgebungen, dar. Nicht nur das Beschichtungsprotokoll wurde hinsichtlich der sP(EO-*stat*-PO) Konzentrationen und der Beschichtungsdauern optimiert, sondern auch Vorbehandlungen der Gerüste wurden entwickelt. Diese waren essentiell um die finale Hydrophilie von sP(EO-*stat*-PO) beschichteten Gerüste so zu erhöhen, dass unspezifische Protein-Adhäsionen vollständig unterbunden wurden. Die sP(EO-*stat*-PO) Schichtdicke, von ungefähr 100 nm, ermöglicht

generell *in vitro* Studien nicht nur in Abhängigkeit der Gerüst-Biofunktionalisierung, sondern auch in Abhängigkeit der Gerüst-Architektur durchzuführen. Das Ausmaß der Hydrogel-Beschichtung wurde mittels einer indirekten Quantifizierung der NCO-Hydrolyse-Produkte ermittelt. Kenntnis über die NCO-Hydrolyse-Kinetik ermöglichte ein Gleichgewicht zwischen ausreichend beschichteten Gerüsten und der Präsenz der NCO-Gruppen herzustellen, welche für die anschließenden Biofunktionalisierungen genutzt wurden. Diese Zeit- und pH-abhängige Biofunktionalisierung war jedoch nur für kleine Biomoleküle möglich. Um diese Beschränkung zu umgehen und auch hochmolekulare Biomoleküle kovalent anzubinden, wurde ein anderer Reaktionsweg entwickelt. Dieser basierte auf der Photolyse von Diazirin-Gruppen und ermöglichte eine Zeit- und pH-unabhängige Biofunktionalisierung der Gerüste mit Streptavidin und Kollagen Typ I. Die Fibrillen bildende Eigenschaft von Kollagen wurde genutzt um auf den Gerüsten verschiedene Kollagen-Konformationen zu erhalten und eine erste *in vitro* Studie bestätigte die Anwendbarkeit für Zell-Material Interaktionsstudien.

Die hier entwickelten Gerüste könnten verwendet werden um tiefere Einblicke in die Grundlagen der zellulären Wahrnehmung zu erhalten. Insbesondere die Komplexität mit der Zellen z.B. Kollagen wahrnehmen bleibt weiterhin klärungsbedürftig. Hierfür könnten diverse Hierarchien von Kollagen-ähnlichen Konformationen an die Gerüste gebunden werden, z.B. Gelatine oder Kollagen-abgeleitete Peptidsequenzen. Dann könnte die Aktivierung der DDR-Rezeptoren in Abhängigkeit der Komplexität der angebundenen Substanzen bestimmt werden. Aufgrund der starken Streptavidin-Biotin Bindung könnten Streptavidin funktionalisierte Gerüste eine vielseitige Plattform für die Immobilisierung von jeglichen biotinylierten Molekülen darstellen.

**Gelatine-basierte Bio-Tinten:** Zuerst wurden die GelAGE-Produkte hinsichtlich der Molekulargewichts-Verteilung und der Integrität der Aminosäuren-Zusammensetzung synthetisiert. Eine detailliert Studie, mit variierenden molaren Edukt-Verhältnissen und Synthese-Zeitspannen, wurde durchgeführt und implizierte, dass der Gelatine Abbau am deutlichsten für stark alkalische Synthesebedingungen mit langen Reaktionszeiten war. Gelatine beinhaltet mehrere funktionalisierbare Gruppen und anhand diverser Model-Substanzen und Analysen wurde die vorrangige Amingruppen-Funktionalisierung ermittelt. Die Homogenität des GelAGE-Polymernetzwerkes, im Vergleich zu frei radikalisch polymerisierten GelMA-Hydrogelen, wurde bestätigt. Eine ausführliche

Analyse der Hydrogel-Zusammensetzungen mit variierenden funktionellen Gruppen Verhältnissen und UV- oder Vis-Licht induzierbaren Photoinitiatoren wurde durchgeführt. Die UV-Initiator Konzentration ist aufgrund der Zell-Toxizität und der potenziellen zellulären DNA-Beschädigung durch UV-Bestrahlung eingeschränkt. Das Zell-kompatiblere Vis-Initiator System hingegen ermöglichte, durch die kontrollierte Photoinitiator-Konzentration bei konstanten En:SH Verhältnissen und Polymeranteilen, die Einstellung der mechanischen Eigenschaften über eine große Spanne hinweg. Die Flexibilität der GelAGE Bio-Tinte für unterschiedliche additive Fertigungstechniken konnte, durch Ausnutzung des temperaturabhängigen Gelierungsverhaltens unterschiedlich stark degradierter GelAGE Produkte, für Stereolithographie und Extrusions-basiertem Druck bewiesen werden. Außerdem wurde die Viabilität zellbeladener GelAGE Konstrukte bewiesen, die mittels Extrusions-basiertem Bio-Druck erhalten wurden. Die Verwendung diverser multifunktioneller und makromolekularer Thiol-Vernetzungsmoleküle ermöglichte eine Verbesserung der mechanischen und rheologischen Eigenschaften und ebenso der Prozessierbarkeit. Verglichen mit dem kleinen bis-Thiol-funktionellen Vernetzungsmolekül waren geringere Thiol-Vernetzer-Konzentrationen notwendig um bessere mechanische Festigkeiten und physikochemische Eigenschaften der Hydrogele zu erhalten. Der Extrusions-basierte Bio-Druck unterschiedlicher eingekapselter Zellen verdeutlichte die Notwendigkeit der individuellen Optimierung von Zell-beladenen Hydrogel-Formulierungen.

Nicht nur die Zellviabilität von eingekapselten Zellen in Extrusions-basierten biogedruckten Konstrukten sollte bewertet werden, sondern auch andere Parameter wie die Zellmorphologie oder die Kollagen- oder Glykosaminoglykan-Produktion, da diese einige der essentiellen Voraussetzungen für die Verwendung in Knorpel Tissue Engineering Konzepten darstellen. Außerdem sollten diese Studien auf die stereolithographischen Ansätze erweitert werden und letztlich wäre die Flexibilität und Zellkompatibilität der Formulierungen mit makromolekularen Vernetzern von Interesse. Makromolekulare Vernetzer ermöglichten die Reduktion des Polymeranteils und des Thiol-Gehalts und können, insbesondere in Kombination mit dem Zell-kompatibleren Vis-Initiator-System, voraussichtlich zu einer gesteigerten Zellkompatibilität beitragen, was zu klären bleibt.

**Hyaluronsäure-basierte Bio-Tinten:** Unterschiedliche Hyaluronsäure-Produkte (HA) wurden synthetisiert, sodass diese En- (HAPA) oder Thiol-Funktionalitäten (LHASH)

beinhalteten, um reine HA Thiol-En vernetzte Hydrogele zu erhalten. In Abhängigkeit des Molekulargewichts der HA-Produkte, der Polymeranteile und des En:SH Verhältnisses, konnte eine große Spanne an mechanischen Festigkeiten abgedeckt werden. Aufgrund der hohen Viskosität war allerdings im Falle von hochmolekularen HA (HHAPA) Produkt-Lösungen (HHAPA + LHASH) die Handhabbarkeit auf 5.0 wt.-% beschränkt. Die Verwendung der gleichen HA Thiol-Komponenten (LHASH) ermöglichte Hybrid-Hydrogele, mit HA und GelAGE, mit reinen HA-Hydrogelen zu vergleichen. Obwohl der Polymeranteil von HHAPA + LHASH Hydrogelen signifikant geringer war, als im Vergleich zu Hybrid-Hydrogelen (GelAGE + LHASH), wurden für gleiche En:SH Verhältnisse ähnliche mechanische und physikochemische Eigenschaften reiner HA-Hydrogele bestimmt. Aufgrund der geringen Viskosität niedermolekularer HA Lösungen (LHAPA + LHASH) konnten diese nicht für den Extrusions-basierten Druck verwendet werden. Das nicht temperaturabhängige HHAPA + LHASH System hingegen konnte mit nur einem Viertel des Polymeranteils der Hybrid Formulierungen gedruckt werden. Im Vergleich zu der Hybrid Bio-Tinte wurde angenommen, dass das hoch viskose Verhalten von HHAPA + LHASH Lösungen, der geringere Polymeranteil, der geringere Druck für das Drucken und eine demzufolge geringere Scherspannung, maßgeblich zu der hohen Zellviabilität in Extrusions-basiert-biogedruckten Konstrukten beisteuerten.

Die niedrigmolekulare HA Formulierung (LHAPA + LHASH) konnte zwar nicht für den Extrusions-basierten Druck verwendet werden, allerdings besitzt dieses System Potential für andere additive Fertigungstechniken wie z.B. der Stereolithographie. Um dieses System weiterzuentwickeln wäre, analog zu dem GelAGE System, eine detailliertere Studie zu den Funktionen eingekapselter Zellen hilfreich. Außerdem sollte die Initiierung dieses Systems mit dem Vis-Initiator untersucht werden.

# 5. Experimental Section

## 5.1. Materials

Gelatin (porcine skin, type A, gel strength 300), ethanolamine (≥98 %), biocytin (≥98 %), trans-4-hydroxy-L-proline (≥99 %), chloramine T trihydrate (98 %), isopropanol (≥99.5 %), Trizma® base (≥99.9 %), Tween® 20, 4-(dimethylamino)benzaldehyde (DMAB) (≥99 %), sodium acetate (>99 %), citric acid monohydrate (≥98 %), iodine solution ($I_2$) (volumetric, 0.05 M $I_2$), L-proline, L-ascorbic acid-2-phosphate sesquimagnesium salt (AsAp), allyl glycidyl ether (AGE) (≥99 %), acetic acid (HAc) (≥99.8 %), methanol (MeOH) (p.a.), ethanol (EtOH) (p.a.), hydrochloric acid (HCl) (37 %), dimethylformamide (DMF) (>99.8 %), tris(2-carboxyethyl)phosphine hydrochloride (TCEP) (≥98 %), 4-pentenoic anhydride (PA) (98 %), sodium chloride (NaCl) (≥99 %), sodium hydroxide (NaOH) (>98 %), poly(acrylic acid sodium salt) (pAA) ($M_w$ ~ 5.1 kDa), poly(allylamine) (pAAm) (20 wt.-% in $H_2O$, $M_w$ = 17 kDa), poly(methacrylic acid sodium salt) (pMMA) ($M_w$ = 1.27 kDa; analytical standard for SEC), tris(2,2´-bipyridyl)dichlororuthenium(II) hexahydrate (Ru) (99.95 %), tetramethylsilane (TMS; analytical NMR standard), sodium persulfate (SPS) (≥98 %) and ß-mercaptoethanol were purchased from Sigma-Aldrich (St. Louis, MO, USA). Phosphate buffered saline was prepared by mixing NaCl (8.00 g, 136 mmol), potassium dihydrogen phosphate (0.20 g, 1.47 mmol), sodium phosphate dibasic dodecahydrate (2.80 g, 7.82 mmol) and potassium chloride (0.20 g, 2.68 mmol) in 1 L deionized water and adjusted to pH 7.4 (all salts from Sigma-Aldrich). DMEM/Ham`s F-12 + GlutaMAX™–I medium, fetal calf serum (FCS), penicillin and streptomycin were obtained from Life Technologies GmbH (Darmstadt, Germany). Bovine serum albumin (BSA), Molecular Probes calcein acetoxymethyl ester (calcein-AM), ethidium homodimer 1 (EthD-1), Texas Red™ labelled bovine serum albumin (TRBSA), Alexa Fluor™ 647 Streptavidin (AFSA), 24 well plates (Nunclon™ Delta surface), L-photo-leucine and 2,4,6-trinitrobenzene sulfonic acid (TNBSA) (5.0 wt.-% in MeOH) were purchased from Thermo Fisher Scientific (Darmstadt, Germany). Acrylamide/bis solution (30 %, 37.5:1), ammonium persulfate (APS), tetramethylethylene-diamine (TEMED), bromophenol blue and low range SDS-PAGE standard were obtained from Bio-Rad (Munich, Germany). Disodium hydrogen phosphate ($Na_2HPO_4$), sodium bicarbonate ($NaHCO_3$), barium chloride ($BaCl_2$), anti-collagen type I antibody (AB758) and perchloric acid ($HClO_4$) (70 %) were purchased from Merck Millipore (Darmstadt, Germany). Deuterium oxide ($D_2O$), deuterated chloroform ($CDCl_3$) and DMSO-*d6* were obtained from Deutero GmbH (Kastellaun, Germany). Sodium

dodecyl sulfate (SDS) and Coomassie brilliant blue were purchased from Serva (Heidelberg, Germany). Dithiothreitol (DTT) (AppliChem, Darmstadt, Germany), type II collagenase (Worthington Biochemical Corporation, Lakewood, USA), 1 kDa dialysis tubing (biotech cellulose ester dialysis membrane, SpectrumLabs, Germany), sodium nitrate ($NaNO_3$) (99.5 %) (Gruessing, Filsum, Germany), 1-ethyl-3-(3-dimethylaminopropyl)carbodiimide hydrochloride (EDC) (Carbo-Synth, Compton, UK), dithiobis(propanoic dihydrazide) (DTP) (Arkè Organics, Calcinaia, Italy), low molecular weight hyaluronic acid (LHA, 27.3 kDa) and high molecular weight hyaluronic acid (HHA, 1.36 MDa) (BaccaraRose, Aplen, Germany), NCO-poly(ethylene oxide-*stat*-propylene oxide, $M_w$ = 12 kDa) (sP(EO-*stat*-PO)) (DWI Leibnitz-Institute for Interactive Materials, Aachen, Germany), milk powder (blotting grade from Carl Roth GmbH + Co. KG, Karlsruhe, Germany), poly-ε-caprolactone (PCL) (PURASORB PC 12, Corbion Inc., Gorinchem, Netherlands), biotin-SP AffiniPure donkey anti-goat IgG antibody (Jackson ImmunoResearch Inc., PA, USA) and eight-armed star-shaped PEG thiol (hexaglycerol core) (sPEGSH, $M_w$ = 10 kDa) (JenKem Technology USA, Plano, Texas, USA) were used as received. 2-hydroxy-1-[4-(hydroxyethoxy)-phenyl]-2-methyl-1-propanone (I2959) was obtained from BASF (Ludwigshafen, Germany). 24 well plates (Costar® non-treated) were purchased from (OmniLab, Bremen, Germany) and Collagen (5.0 mg $mL^{-1}$ in 0.017 N HAc, from calf hides) from Symatese (Chaponost, France).

## 5.2. Methods

### 5.2.1. $^1$H-NMR spectroscopy

$^1$H-NMR spectra were recorded on a Bruker Fourier 300 at 300 MHz with 128 scans (Bruker, Billerica, MA, USA) with $D_2O$ as solvent. TMS was used as internal reference. $^1$H-NMR spectra were used to calculate the SD for GelAGE, which represents the percentage of gelatins modified reactive amino acids (lysine for GelMA and lysine, hydroxylysine and histidine for GelAGE) and for the SD of HA modified groups (hydroxyl or carboxyl functionalities for LHAPA and HHAPA or LHASH, respectively). The amino acid composition of gelatin was acquired from the gelatin handbook of the gelatin manufacturer's institute of America (GMIA).[203] Phenylalanine peaks at $\delta$ = 7.4-7.3 ppm served as reference signals for modifications of gelatin. For LHAPA and HHAPA the newly introduced protons at 6.0-5.8 ppm and 5.2-5.0 ppm (LHAPA) and 6.4-6.2 ppm and 5.6-5.4 ppm (HHAPA) were calibrated to three protons from the *N*-acetyl methyl group (2.1-1.9 ppm). $^1$H-NMR spectra for HHAPA were recorded at 60 °C due to its high viscosity. For LHASH the signals at 3.0-2.6 ppm were calibrated to three protons from the *N*-acetyl methyl group (2.1-1.9 ppm). The following abbreviations were used: d: doublet; t: triplet; m: multiplett; arom: aromatic protons.

### 5.2.2. IR spectroscopy

Substances were analyzed with an ATR-FT-IR spectrometer (Nicolet iS10, Thermo Fisher Scientific, Darmstadt, Germany). The following abbreviations were used: w: weak; m: middle; s: strong; ν: stretching or bonding vibrations; δ: bending or deformation vibrations; as: asymmetric; s: symmetric.

## 5.3. Experiments for biofunctionalizations of PCL scaffolds

### 5.3.1. PCL scaffold production via MEW

The custom-built machine used for the scaffold production is based on a commercially available CNC platform as already presented elsewhere.[148] Programmable logic controllers (Bosch Rexroth AG, Lohr am Main, Germany) were connected to the x-y slide system (Bosch Rexroth AG, Lohr am Main, Germany). Disposable syringes (Optimum 3cc, Nordson EFD Deutschland GmbH, Pforzheim, Germany) were filled with PCL and the temperature within the syringes was controlled by an electrical heating unit (Nordson EFD Deutschland GmbH, Pforzheim, Germany). To control the air pressure during the production of the scaffolds, a digitally controlled air pressure system (Bosch Rexroth AG, Lohr am Main, Germany) was connected to the syringe. The high voltage electrode was supplied by a positive high voltage source (LNC 10000-5 pos, Heinzinger Electronic GmbH, Rosenheim, Germany). The scaffolds were collected on a grounded stainless steel platform (200 × 175 mm), which was attached to the x-y slide system. 200 µm filament spaced scaffolds (4.2 x 4.2 $cm^2$) with a fiber diameter of around 5 – 7 µm were fabricated with an accelerating voltage of 5.6 kV, a collector distance of 4.5 mm and a heating temperature of 96 °C. The feeding air pressure was kept constant at 1.9 bar. The spinneret diameter was 25 G (Nordson EFD Deutschland GmbH, Pforzheim, Germany) and the axis velocity 3500 mm $min^{-1}$. Box-structured scaffolds were obtained by alternating layer deposition at 0° and 90° with 16 layer (200 µm filament spacing, 6 µm fiber diameter) or 50 layer (300 µm filament spacing, 5 – 7 µm fiber diameter for cell adhesion experiments were provided from Gernot Hochleitner) per direction. The scaffold geometry was further analyzed with a stereomicroscope (SteREO Discovery.V20, Carl Zeiss Microscope, Jena, Germany).

### 5.3.2. Gelation ability of sP(EO-*stat*-PO) solutions and coating procedure

Different amounts of sP(EO-*stat*-PO) were weighed and dissolved in deionized water to obtain final sP(EO-*stat*-PO) concentrations of 0.3 – 7.5 wt.-% to record gelation times of the scaffold-free solutions.

The scaffolds were cut into smaller pieces (1.2 x 1.2 $cm^2$) with razor blades (Hartenstein, Würzburg, Germany), mounted on a stainless steel block (1.2 cm width) equipped with a handle. Afterwards the scaffolds were transferred to 24 well plates (Nunclon™ Delta

surface) and placed into a sandwich between two serological pipette rings (25 mL, CELLSTAR, Greiner bio-one, cut to 4 mm and 9 mm height) for fixation. Pre-wetting of the scaffolds was achieved by the addition of deionized water (2.0 mL per well) and followed by a pre-treatment (5 min) with deionized water or 1 M or 5 M NaOH (2.0 mL per well). Then the scaffolds were washed with deionized water (5 x 5 min, each 2.0 mL per well). SP(EO-*stat*-PO) was dissolved for 5 min in deionized water and added to the scaffolds (1.0 mL per scaffold) for different incubation times. Complete hydrolysis of the reactive NCO-groups was achieved by incubating the scaffolds in deionized water overnight (2.0 mL per well), followed by washing 5 times with 20 min incubation in deionized water or PBS (2.0 mL per well).

### 5.3.3. SP(EO-*stat*-PO) coating concentration

The pre-wetted (deionized water, 2.0 mL) scaffolds were pre-treated for 5 min in 1 M NaOH, which was followed by washing steps (5 times, deionized water, 2.0 mL each). 1.0 – 4.0 wt.-% sP(EO-*stat*-PO) solutions were used to coat the scaffolds for 15 min. These samples were subsequently dried prior to IR analysis. Complete hydrolysis of reactive NCO-groups was achieved via an overnight incubation in water (deionized water, 2.0 mL) prior to IR analysis of dried scaffolds.

### 5.3.4. Contact angle measurements

The scaffolds were pre-wetted (deionized water, 2.0 mL) and pre-treated with deionized water, 1 M or 5 M NaOH for 5 min and washed 5 times with 2.0 mL deionized water (2.0 mL each). The coating with sP(EO-*stat*-PO) (2.0 wt.-%, 10 min) was followed by an overnight incubation for complete NCO-hydrolysis as previously described. After the coating or the overnight incubation the scaffolds were washed (5 times, deionized water, 2.0 mL each) and dried under a constant air stream in the lids of cut Eppendorf-tubes. Water droplets (3 µL) were placed onto the scaffolds, images taken after 2 s of the deposition and left and right contact angles measured (Contact Angle System OCA, DataPhysics Instruments GmbH, Filderstadt, Germany).

### 5.3.5. Protein adsorption

After pre-wetting (deionized water, 2.0 mL) and pre-treating the scaffolds with deionized water, 1 M or 5 M NaOH for 5 min, washing cycles with deionized water (5 times, 2.0 mL

each) followed. The sP(EO-*stat*-PO) coating was performed for 10 min (2.0 wt.-% sP(EO-*stat*-PO)) and an overnight incubation in water was conducted. After complete NCO-hydrolysis, 850 µL of TRBSA (50 µg $mL^{-1}$ in PBS) were added to each of the scaffolds. After 3 h incubation at RT in the dark, the scaffolds were extensively washed via discarding the solution and refilling the wells (2.0 mL, PBS) for 3 times followed by an incubation of 20 min in the last washing solution. This procedure was repeated 5 times in total prior to analysis of dried samples with fluorescence microscopy (Zeiss Axio Imager.M1, Carl Zeiss, Jena, Germany).

### 5.3.6. SP(EO-*stat*-PO) coating duration optimization

The pre-wetted (deionized water, 2.0 mL) scaffolds were pre-treated with 1 M NaOH for 5 min and this was followed by washing cycles (5 times, deionized water, 2.0 mL for 5 min each). The scaffolds were then incubated for different time intervals (5 – 112 min) in 2.0 wt.-% sP(EO-*stat*-PO) solutions. Drying of the scaffolds (1 min) was conducted with a constant air stream prior to IR analyses. Additionally the washing of the scaffolds after the sP(EO-*stat*-PO) coating was investigated for sP(EO-*stat*-PO) coating times of 5 – 75 min with 5 cycles of each 2.0 mL deionized water (3 min in total) before being dried and analyzed with IR spectroscopy. IR spectra were recorded at different locations within the samples.

### 5.3.7. SEM- and EDX-analysis of sP(EO-*stat*-PO) coated samples

The pre-wetted (deionized water, 2.0 mL) scaffolds were pre-treated with 1 M NaOH for 5 min and this was followed by washing cycles (5 times, deionized water, 2.0 mL for 5 min each). Coating of the scaffolds was conducted with 2.0 wt.-% sP(EO-*stat*-PO) solution for 10 min. A subsequent overnight hydrolysis (2.0 mL, deionized water) with washing steps was performed (5 times, deionized water, 2.0 mL for 5 min each). The samples were sputtered with 4 nm platinum (Plano GmbH, Wetzlar, Germany) and visualized using a Crossbeam 340 SEM (Carl Zeiss Microscopy, Oberkochen, Germany). FIB cutting of the scaffold fibers was performed with a Ga-beam, operated with a beam voltage of 30 kV and beam currents of 10 – 50 pA. EDX-analysis of the nitrogen content of the cut surface was conducted. Additionally a sP(EO-*stat*-PO) staining with $BaCl_2$ and $I_2$ was performed according to Skoog *et al*.[157, 159] for which sP(EO-*stat*-PO) coated scaffolds were placed in 100 µL deionized water per well and 400 µL perchloric acid (0.1 M), 100 µL $BaCl_2$ (5.0 %

w/v in water) and 50 µL iodine solution (0.1 M in 7:3 EtOH/deionized water) were added. Scaffolds were washed 3 times (deionized water, 1.0 mL, 10 s) and dried prior to EDX analysis.

### 5.3.8. TNBSA assay for quantification of sP(EO-*stat*-PO) on PCL scaffolds

Ethanolamine solutions with concentrations from 0.5 µg $mL^{-1}$ to 11.88 µg $mL^{-1}$ (in 0.1 M $NaHCO_3$, pH 8.5) were used for calibration. SP(EO-*stat*-PO) was dissolved in deionized water at a concentration of 2.0 wt.-% to serve as additional calibration reference. To ensure complete NCO-hydrolysis an overnight incubation at RT was performed. Further concentrations ranging from 0.0025 – 1.0 wt.-% sP(EO-*stat*-PO) were diluted with $NaHCO_3$ (0.1 M, pH 8.5). Scaffolds were pre-wetted (deionized water, 2.0 mL) and then pre-treated for 5 min in 1 M NaOH, washed (5 times, deionized water, 2.0 mL, 5 min) and coated with 2.0 wt.-% sP(EO-*stat*-PO) for 10 min or overnight. To ensure comparability of the distinct sP(EO-*stat*-PO) coating times, the shorter incubation was allowed to hydrolyze overnight. The scaffolds and PCL controls were washed 5 times (20 min, deionized water, 2.0 mL for 5 min each) and dried before being incubated in 6 M HCl (65 °C, 2 h, 200 µL) (Thermomixer 5436, Eppendorf AG, Hamburg, Germany). Ethanolamine controls were treated equally or left untreated in 0.1 M $NaHCO_3$ (pH 8.5). To 50 µL of sample volume, 25 µL of TNBSA (0.01 % in 0.1 M $NaHCO_3$, pH 8.5) were added into the wells of 96 well plate and the plates were incubated at 37 °C for 2 h (Type ULE 500, Memmert, Schwabach, Germany). Finally, SDS (25 µL, 10 wt.-%) and 1 M HCl (12.5 µL) were added to the samples and the absorbance recorded at 335 nm (Tecan Infinite M200, Maennedorf, Switzerland).

### 5.3.9. Biofunctionalizations of PCL scaffolds via NCO-groups

Pre-wetting (deionized water, 2.0 mL), pre-treatment (1 M NaOH, 2.0 mL, 5 min) and washing cycles were performed as previously described for all following scaffolds. For the biofunctionalization via the reactive sP(EO-*stat*-PO)-NCO-groups, the sP(EO-*stat*-PO) solution was removed after 10 min coating and replaced by the desired coupling substances, which are described in the following sections and represented by the schemes depicted in **Figure 90**.

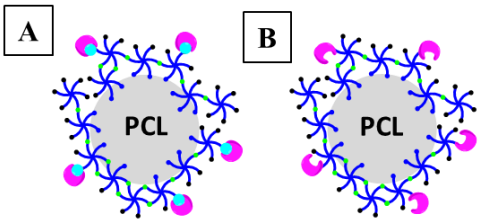


**Figure 90:** Overview of the different schemes correlating to the experimental procedures for biocytin- (**A**) and AFSA-functionalized sP(EO-*stat*-PO) coated scaffolds (**B**).

950 µL of biocytin solutions (5.37 x $10^{-7}$ mol, 2.68 x $10^{-6}$ mol and 1.34 x $10^{-5}$ mol in PBS) replaced the sP(EO-*stat*-PO) coating solution and were left with gentle shaking on a rocker (Rocker-shaker PMR-100, Grant Instruments, Cambridge, UK) overnight. The scaffolds were then washed in the wells 5 times for 20 min with PBS (2.0 mL) before being incubated overnight in an AFSA solution (1.67 x $10^{-10}$ mol in PBS, 1.0 mL). Prior to fluorescence microscopy (Keyence BZ-9000, Biorevo, Neu-Isenburg, Germany) the scaffolds were washed 5 times for 20 min with PBS (2.0 mL) (**Figure 90 A**). Dried biocytin functionalized sP(EO-*stat*-PO) coated scaffolds coupled with AFSA were analyzed with IR spectroscopy. 1.0 mL AFSA solution (1.67 x $10^{-10}$ mol in PBS, 1.0 mL) replaced the sP(EO-*stat*-PO) coating solution and was incubated with gentle shaking overnight on a rocker (Rocker-shaker PMR-100, Grant Instruments, Cambridge, UK). The scaffolds were then washed 5 times for 20 min with PBS (2.0 mL) and analyzed with fluorescence microscopy (Keyence BZ-9000, Biorevo, Neu-Isenburg, Germany) (**Figure 90 B**).

### 5.3.10. Photo-induced biofunctionalizations of PCL scaffolds

Pre-wetting (deionized water, 2.0 mL), pre-treatment (1 M NaOH, 2.0 mL, 5 min) and washing cycles were performed as previously described for all following photoleucine functionalized sP(EO-*stat*-PO) coated scaffolds.

For the photoleucine functionalization via the reactive sP(EO-*stat*-PO)-NCO-groups, the sP(EO-*stat*-PO) solution was removed after 10 min coating and replaced by 1.0 mL photoleucine solution (1.34 x $10^{-5}$ mol in PBS) and was left with gentle moving on a rocker (Rocker-shaker PMR-100, Grant Instruments, Cambridge, UK) overnight. The scaffolds were then washed 5 times for 20 min with PBS (2.0 mL) and were then irradiated (**Figure 91 A**) in 950 µL of AFSA solutions (1.67 x $10^{-10}$ mol in PBS or 0.5 M HAc) for 30 min at 365 nm (UV-LED cubes, Polymerschmiede, Aachen, Germany). Finally, the scaffolds were washed 5 times for 20 min (2.0 mL, PBS) before being analyzed with

fluorescence microscopy (Keyence BZ-9000, Biorevo, Neu-Isenburg, Germany). Photoleucine functionalized sP(EO-*stat*-PO) coated scaffolds were irradiated in a collagen type I solution (200 µg $mL^{-1}$, 1.67 x $10^{-9}$ mol; 0.5 M HAc, 1.0 mL). Afterwards the scaffolds were either washed under acidic conditions (5 times for 20 min, with 2.0 mL 0.5 M HAc) to remove excess of unbound collagen and to achieve ICH (**Figure 91 B**) or incubated at 37 °C (Type ULE 500, Memmert, Schwabach, Germany) for 1 h or 4 h in a freshly neutralized collagen solution type I solution (200 µg $mL^{-1}$, 1.67 x $10^{-9}$ mol; 0.5 M HAc, 1.0 mL, 520 µL 1 M NaOH) to achieve SCA1h and SCA4h, respectively (**Figure 91 C**). The scaffolds were either blocked with TBST (TBS consisting of 140 mM NaCl and 10 mM Trizma® base, pH 8.0, with 0.05 % Tween) supplemented with 5.0 wt.-% milk powder overnight at 4 °C or they were left non-blocked. All scaffolds were then washed 5 times with TBST (pH 8.0, 2.0 mL, 10 min each) and incubated with goat anti-collagen type I antibody (1:500 in TBST) at RT for 4 h under gentle shaking (Rocker-shaker PMR-100, Grant Instruments, Cambridge, UK). After washing the scaffolds with TBST (pH 8.0, 2.0 mL, 5 times, 10 min) under gentle shaking, the constructs were incubated with the secondary antibody (donkey anti-goat biotin labelled; 1:1666 in TBST) at 4 °C overnight with gentle shaking (Rocking-Shaker DRS-12, neoLAB Migge GmbH, Heidelberg, Germany). Washing of the scaffolds (3 times, 2.0 mL, 10 min) was followed by the incubation with AFSA solutions overnight (10 µg $mL^{-1}$, 1.67 x $10^{-10}$ mol in PBS) at 4 °C under gentle shaking (Rocking-Shaker DRS-12, neoLAB Migge GmbH, Heidelberg, Germany). Finally, the constructs were washed with PBS (3 times, 2.0 mL, 10 min) and further analyzed with fluorescence (Keyence BZ-9000, Biorevo, Neu-Isenburg, Germany) or confocal microscopy (LEICA TCS SP8, Leica Microsystems AG, Wetzlar, Germany). Both collagen conformation approaches on photoleucine functionalized sP(EO-*stat*-PO) coated scaffolds were investigated with SEM as previously described.

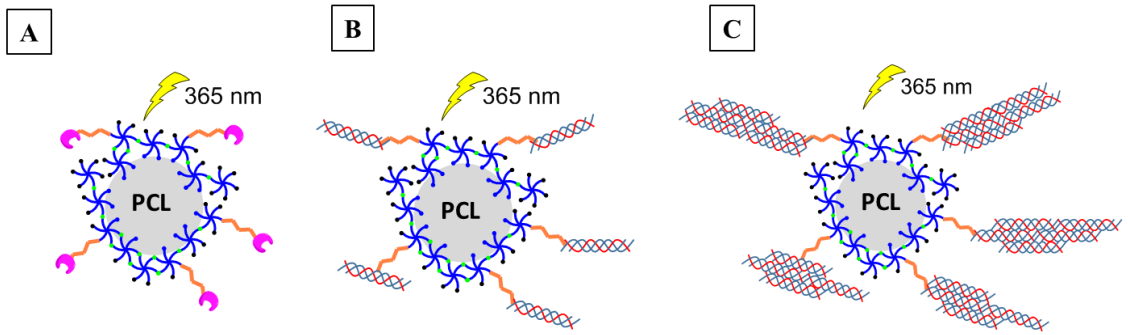


**Figure 91:** AFSA- (**A**) and collagen-functionalized sP(EO-stat-PO) coated scaffolds for ICH (**B**) or for SCA (**C** with fibril formation times of 1 h and 4 h).

### 5.3.11. Controls for biofunctionalizations of PCL scaffolds

All controls were firstly pre-wetted (deionized water, 2.0 mL) and pre-treated as already described. Controls included the incubation of PCL scaffolds in biocytin solutions ($5.37 \times 10^{-7}$ mol, $2.68 \times 10^{-6}$ mol and $1.34 \times 10^{-5}$ mol in PBS; 950 µL each) after which the subsequent incubation in AFSA solution ($1.67 \times 10^{-10}$ mol in PBS, 1.0 mL) followed accordingly to the procedure of biocytin functionalized sP(EO-*stat*-PO) coated scaffolds (**Figure 92 A**). These samples are referred to as biocytin treated PCL scaffolds.

Furthermore, PCL scaffolds were incubated in AFSA solutions ($1.67 \times 10^{-10}$ mol in PBS, 1.0 mL) which was followed by the previously described procedures and termed AFSA treated PCL scaffolds (**Figure 92 B**).

The incubation of PCL scaffolds in photoleucine solutions ($1.34 \times 10^{-10}$ mol in PBS, 950 µL) was followed by incubation in AFSA ($1.67 \times 10^{-10}$ mol in PBS, 1.0 mL) in which the scaffolds were irradiated for 30 min at 365 nm. The same procedure as for AFSA functionalized sP(EO-*stat*-PO) coated scaffolds was conducted and these controls are referred to as photoleucine treated PCL scaffolds **(Figure 92 C**).

Additionally NCO-hydrolyzed sP(EO-*stat*-PO) coated scaffolds were treated with biocytin and AFSA ($1.67 \times 10^{-10}$ mol in PBS, 1.0 mL) solutions (**Figure 92 D**), similar to biocytin treated PCL scaffolds and are referred to as biocytin treated sP(EO-*stat*-PO) coated scaffolds.

Not completely NCO-hydrolyzed sP(EO-*stat*-PO) coated scaffolds were treated with AFSA solutions, by replacing the sP(EO-*stat*-PO) solution after 10 min with AFSA ($1.67 \times 10^{-10}$ mol in PBS, 1.0 mL) (**Figure 92 E**) and are termed AFSA treated NCO-hydrolyzed sP(EO-*stat*-PO) coated scaffolds.

Another set of controls was represented by photoleucine functionalized sP(EO-*stat*-PO) coated scaffolds which were not irradiated while being incubated in AFSA solutions ($1.67 \times 10^{-10}$ mol in PBS, 1.0 mL) (**Figure 92 F**) and are termed AFSA treated unirradiated sP(EO-*stat*-PO) coated scaffolds.

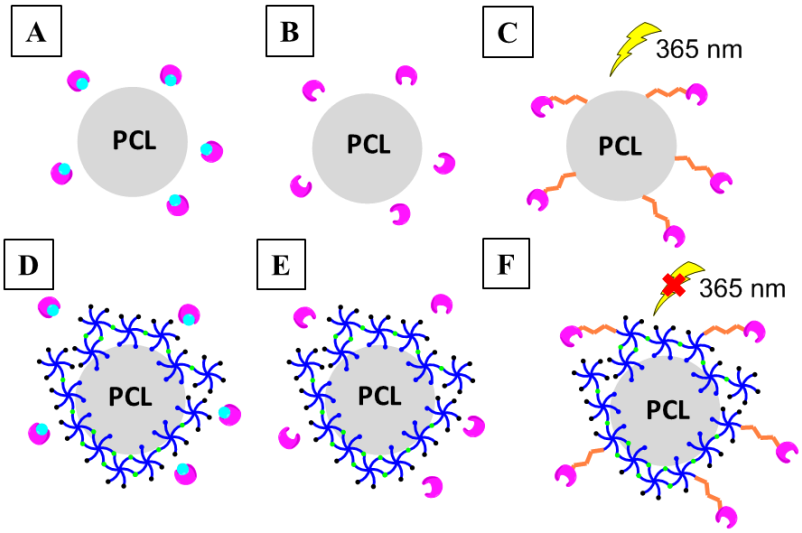


**Figure 92:** Overview of the controls for biocytin treated PCL (**A**), AFSA treated PCL (**B**) or photo-leucine treated PCL scaffolds (**C**). Controls for biocytin treated NCO-hydrolyzed scaffolds (**D**). AFSA treated NCO-hydrolyzed sP(EO-*stat*-PO) coated scaffolds (**E**). AFSA treated unirradiated photoleucine functionalized sP(EO-*stat*-PO) coated scaffolds (**F**).

For simplification the controls for both collagen conformation approaches are represented in **Figure 93**. Controls included the incubation of PCL (collagen treated PCL scaffolds) (**Figure 93 A**) and NCO-hydrolyzed sP(EO-*stat*-PO) coated scaffolds (collagen treated NCO-hydrolyzed sP(EO-*stat*-PO) coated scaffolds) in collagen solutions (200 µg $mL^{-1}$, 1.67 x $10^{-9}$ mol in 0.5 M HAc, 1.0 mL, **Figure 93 B**) with a subsequent irradiation (30 min, 365 nm, UV-LED cubes). Additionally PCL scaffolds were treated with photoleucine (1.34 x $10^{-5}$ mol in PBS) and collagen (200 µg $mL^{-1}$ 1.67 x $10^{-9}$ mol in 0.5 M HAc, 1.0 mL) and irradiated (30 min, 365 nm, UV-LED cubes **Figure 93 C**) to yield collagen/photoleucine treated PCL scaffolds. Photoleucine functionalized sP(EO-*stat*-PO) coated scaffolds were treated with collagen (200 µg $mL^{-1}$, 1.67 x $10^{-9}$ mol in 0.5 M HAc, 1.0 mL) but without an irradiation and are termed collagen treated unirradiated photoleucine functionalized sP(EO-*stat*-PO) coated scaffolds (**Figure 93 D**). Other than that all the scaffolds were treated equally to the biofunctionalization approaches with photoleucine by washing or blocking steps and incubation in antibody solutions.

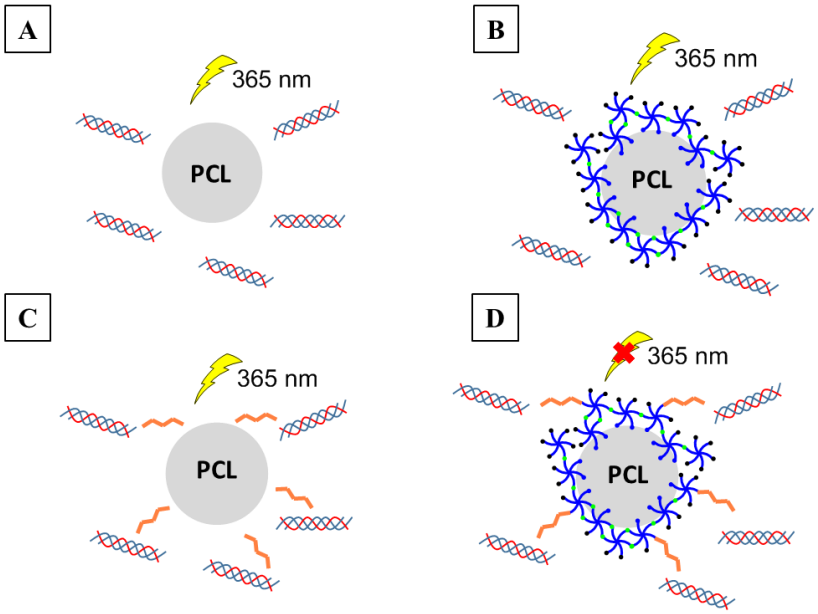


**Figure 93:** Controls for the collagen-modified scaffolds. Incubation of collagen treated PCL (**A**) or collagen treated NCO-hydrolyzed sP(EO-*stat*-PO) coated scaffolds (**B**) in collagen solutions. PCL scaffolds were treated with photoleucine and subsequently with collagen (collagen/photoleucine treated PCL scaffolds) (**C**). Samples **A** – **C** were irradiated for 30 min at 365 nm. Collagen treated unirradiated photoleucine functionalized sP(EO-*stat*-PO) coated scaffolds were incubated in collagen solution but without irradiation (**D**).

### 5.3.12. Photobleaching of AFSA solutions

AFSA solutions of 1.67 x $10^{-10}$ mol were prepared in PBS (pH 7.4) or in 0.5 M HAc (pH 2.5). 200 µL of these solutions were irradiated for different time intervals (0 min, 5 min, 15 min and 30 min, 365 nm, UV-LED cubes) and the intensity of the fluorescence at 665 nm was measured with a fluorescence spectrometer (SQ-2000-4, Photon Technology International, New Jersey, USA) with a xenon lamp (75 W) and photomultiplier (R928P) in a quartz cuvette.

### 5.3.13. SP(EO-*stat*-PO) coating under acidic conditions

sP(EO-*stat*-PO) was dissolved in 0.5 M HAc to give a final concentration of 2.0 wt.-%. The scaffolds were treated with the previously used pre-wetting and pre-treatment (1 M NaOH, 5 min) and subsequently washed (5 times, deionized water, 2.0 mL, 5 min) before being incubated in acidified sP(EO-*stat*-PO) solutions (10 min, 20 min, 60 min and 160 min). The samples were then either dried with a constant air stream or the samples were neutralized with 1 M NaOH prior to the drying process. IR spectra were recorded at different locations within the dried scaffolds.

### 5.3.14. Turbidity measurements of collagen solutions

Acidic collagen solutions (5.0 mg $mL^{-1}$ in 0.5 M HAc) were neutralized with 0.5 M NaOH. The 96 well plates were then incubated at 37 °C and the absorbance at 313 nm was recorded every minute for 3 h (Tecan Infinite M200, Maennedorf, Switzerland).

### 5.3.15. Hydroxyproline assay

The amount of immobilized collagen on the collagen functionalized sP(EO-*stat*-PO) coated scaffolds was analyzed with the hydroxyproline (Hyp) assay using a slightly modified Woessner method.[193] Briefly, PCL scaffolds, both collagen conformation approaches on the collagen functionalized sP(EO-*stat*-PO) coated scaffolds and Hyp controls (0.05 – 8.0 µg Hyp) were completely hydrolyzed at 95 °C (Thermomixer 5436, Eppendorf AG, Hamburg, Germany) for 12 h in 6 M HCl (200 µL). Excess of HCl was removed upon heating to 95 °C (Thermomixer 5436, Eppendorf AG, Hamburg, Germany) and dried samples were re-dissolved in 350 µL deionized water. 100 µL of the samples were mixed with 50 µL chloramine T reagent (70.5 mg chloramine T in 4.0 mL pH 6 buffer (18.0 g sodium acetate, 12.5 g citric acid monohydrate, 3.0 mL HAc were filled up to 250 mL) with the addition of 0.5 mL isopropanol and incubated for 20 min at RT. Then, 50 µL of DMAB (0.75 g in 3 mL isopropanol with 1.3 mL perchloric acid) were added. This mixture was then incubated for 30 min at 65°C, cooled and the absorbance was measured at 560 nm (Tecan Infinite M200, Maennedorf, Switzerland). Converting the hydroxyproline amount by a factor of 7.4 enables the correlation to the collagen amount.[192]

### 5.3.16. Collagen coating of polystyrene wells

100 µL of the collagen stock solution (5.0 mg $mL^{-1}$ in 0.017 N HAc) were diluted with 900 µL 0.5 M HAc. 450 µL of this solution were placed in the wells of both well type plates (24 well plates, Nunclon™ and Costar®) and incubated at RT overnight. Then 1.0 mL PBS was added to the wells and removed after 1 h. This step was repeated twice and the solutions were allowed to evaporate for 1 d.

### 5.3.17. Cell adhesion experiments and Live/Dead staining

To sterilize the scaffolds, these were placed for 30 min in 70 % EtOH and washed with autoclaved deionized water. The pre-treatment of PCL scaffolds and sP(EO-*stat*-PO) coating thereof were performed as previously described. For cellular adhesion on scaffolds,

the scaffolds were placed in Costar® wells. Additionally cells were seeded as reference on Nunclon™ and Costar® wells. Primary hMSCs were provided from the König Ludwig Haus (Würzburg, Germany) and were originally isolated from trabecular bone from the femoral head of patients undergoing total hip arthroplasty.[220] Cells were seeded at an initial density of 1.2 x $10^5$ per well in 40 µL but diluted after 30 min with 500 µL medium (DMEM/Hams´s F-12 + GlutaMAX™-I supplemented with 10 % FCS, 100 U $mL^{-1}$ penicillin, 100 mg $mL^{-1}$ streptomycin and 50 µg $mL^{-1}$ AsAp) per well. Cell attachment was allowed to proceed for 6 h at 37°C. The medium was removed, the scaffolds were washed twice with 1.0 mL 1x PBS (pH 7.4) and cultured for 8 d in a humidified atmosphere of 5 % $CO_2$ at 37 °C.

The cells were stained with calcein-AM (2.0 µM) and EthD-1 (1.0 µM) in PBS. 300 µL of this staining solution were added per well and incubated for 45 min at RT and the scaffolds were analyzed with fluorescence microscopy (Zeiss Axio Imager.M1, Carl Zeiss, Jena, Germany).

## 5.4. Experiments for bioprintable hydrogels

### 5.4.1. Syntheses of GelAGE

The modification of gelatin with AGE (GelAGE) was based on modifications of protocols for AGE functionalization of starch[195], chitosan[196, 197] and gelatin[198]. After dissolving gelatin (10 wt.-%) in deionized water at 65 °C, different amounts of AGE (0.40 – 10 mmol) and 2 M NaOH (2.4 – 60 mmol) were added to the reaction solution (see **Table 11**). After different time points (1 – 24 h) the reaction solutions were dialyzed (MWCO 1 kDa) against deionized water. The products were then lyophilized (Alpha 1-2 LD, Christ, Osterode am Harz, Germany) and stored at 4 °C under exclusion of light until use.

In order to obtain control groups ($Gelatin_{1\text{-}24M0}$), gelatin was incubated for 1 – 24 h with medium amounts of NaOH (2.0 mmol) but without AGE. After designated time points the controls were dialyzed (MWCO 1 kDa) against deionized water. Afterwards the products were lyophilized and stored at 4 °C until use.

**Table 11:** Overview of the varying synthesis parameters for GelAGE products.

| Sample | NaOH [mmol per g gelatin] | AGE [mmol per g gelatin] | Time [h] |
|---|---|---|---|
| $GelAGE_{8LL}$ | 0.40 | 2.4 | 8 |
| $GelAGE_{24LL}$ | 0.40 | 2.4 | 24 |
| $GelAGE_{8LM}$ | 0.40 | 12 | 8 |
| $GelAGE_{24LM}$ | 0.40 | 12 | 24 |
| $GelAGE_{1MM}$ | 2.0 | 12 | 1 |
| $GelAGE_{4MM}$ | 2.0 | 12 | 4 |
| $GelAGE_{8MM}$ | 2.0 | 12 | 8 |
| $GelAGE_{24MM}$ | 2.0 | 12 | 24 |
| $GelAGE_{8MH}$ | 2.0 | 60 | 8 |
| $GelAGE_{8HH}$ | 10 | 60 | 8 |

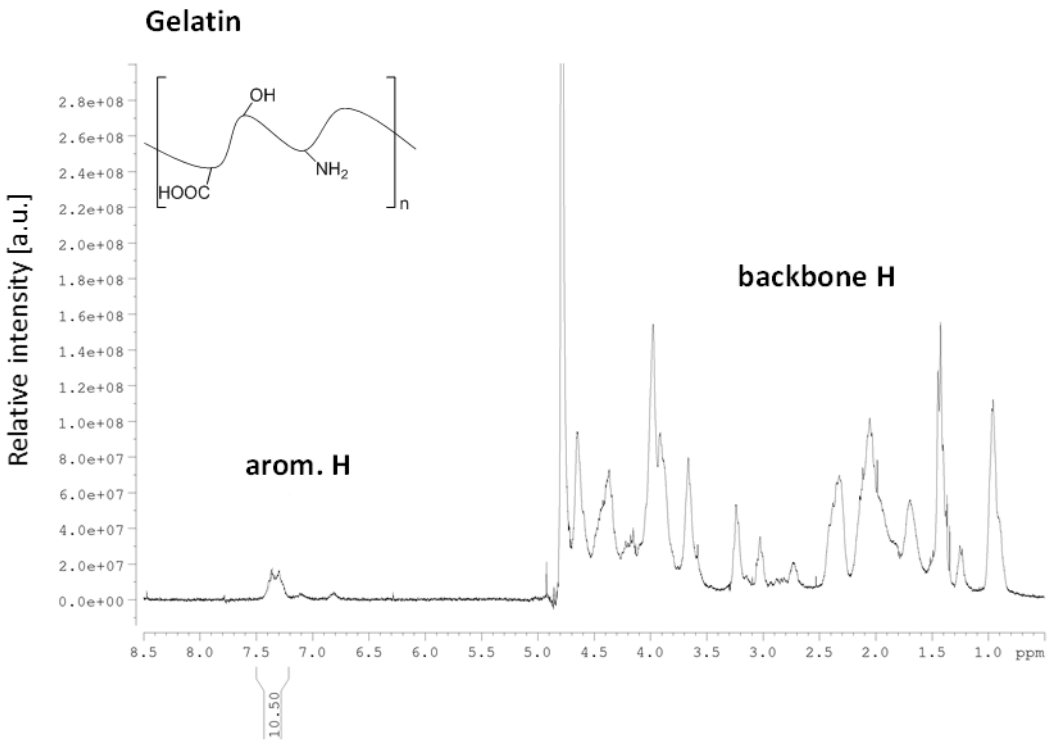


**Figure 94:** Representative $^{1}$H-NMR spectrum of gelatin in $D_2O$.

$^{1}$H-NMR (300 MHz, $D_2O$, gelatin, δ): 7.4-7.3 (10.5 H, d, arom. –C*H*), 4.6-0.8 (m, backbone) ppm.

$^{1}$H-NMR (300 MHz, $D_2O$, $GelAGE_{1MM}$, δ): 7.4-7.3 (10.5 H, d, arom. –C*H*) 6.1-5.9 (18.6 H, m, $H^a$), 5.4-5.2 (37.9 H, t, $H^b$), 4.6-0.8 (m, backbone) ppm.
SD ($GelAGE_{1MM}$): 42 %.

IR (gelatin): ν = 3278 (m; ν(-NH)), 3073 (w; ν(-OH)), 2936 (w; ν(-OH)), 2874 (w; ν(-CH)), 1630 (s; C=O), 1530 (s), 1447 (s; δ(-CH)), 1389 (s; δ(-CH)), 1333 (m; δ(-OH)), 1233 (s), 1201 (s), 1079 (s), 1029 (s) $cm^{-1}$.
IR (GelAGE): ν = 3278 (m; ν(-NH)), 3073 (w; ν(-OH)), 2936 (w; ν(-OH)), 2874 (w; ν(-CH)), 1630 (s; C=O), 1530 (s), 1447 (s; δ(-CH)), 1389 (s; δ(-CH)), 1333 (m; δ(-OH)), 1233 (s), 1201 (s), 1079 (s), 1029 (s), 997 (m; δ(C=C)), 925 (m; δ(C=C)) $cm^{-1}$.

### 5.4.2. Syntheses of modified hyaluronic acid products

Pentenoate-modified low and high molecular weight hyaluronic acid (LHAPA and HHAPA, respectively) were synthesized using protocols described elsewhere.[216] Briefly, LHA (27.3 kDa) and HHA (1.36 MDa), both 2.0 wt.-% (3.0 g, 7.5 mmol), were dissolved

in deionized water at 4 °C overnight. DMF was added to give a DMF/water ratio of 2/3 (v/v). PA (0.4 mL, 2.10 mmol) was added to the reaction solution while maintaining the pH between 8 and 9 by addition of 0.5 M NaOH aliquots for 5 h. After overnight stirring at 4 °C, NaCl was added to give a final concentration of 0.5 M and followed by the addition of EtOH (water/EtOH ratio of 2/3 (v/v)) to precipitate the products. The solution was stirred for 1 h, the supernatant was discarded and the precipitate was washed with cold mixtures of water/EtOH (3/7, 1/4, 1/9 (v/v)). The products were finally dissolved in deionized water and dialyzed (MWCO 1 kDa) against deionized water with 100 mM NaCl and 1/100 EtOH/water (v/v). After three dialysis cycles the products were extensively dialyzed against deionized water, finally lyophilized and stored under exclusion of light at 4 °C until use.

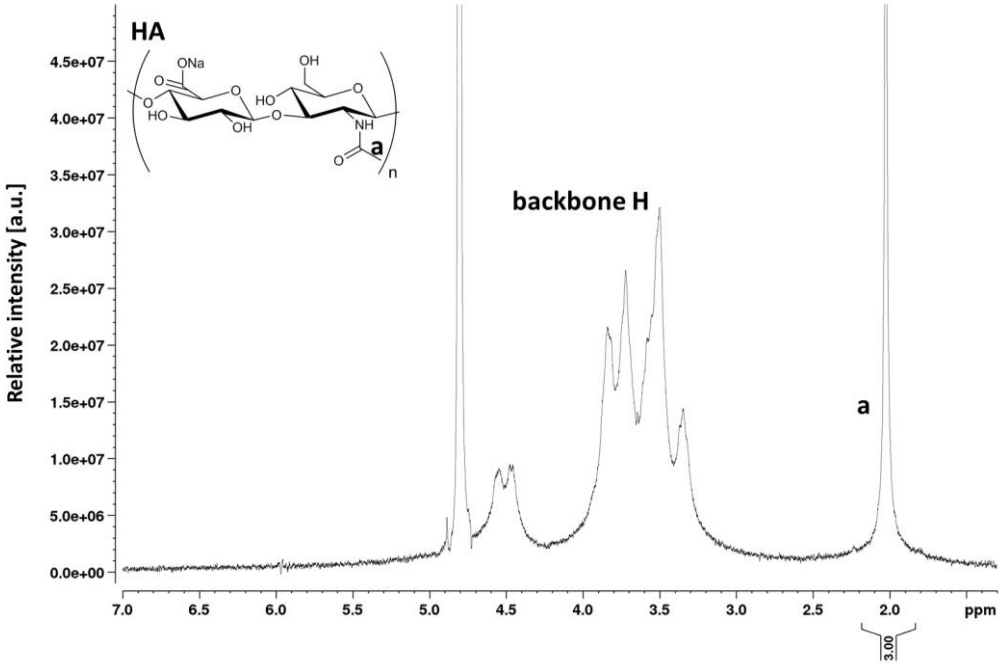


**Figure 95:** Representative $^{1}$H-NMR spectrum of HA in $D_2O$.

$^{1}$H-NMR (300 MHz, $D_2O$, HA, δ): 4.6-4.3 (m, backbone), 4.1-3.3 (m, backbone), 2.1-1.9 (3 H, s, $H^a$) ppm.

$^{1}$H-NMR (300 MHz, $D_2O$, LHAPA, δ): 6.0-5.8 (0.2 H, m, $H^d$), 5.2-5.0 (0.5 H, t, $H^e$), 4.6-4.3 (m, backbone), 4.1-3.3 (m, backbone), 2.6-2.5 (0.5 H, m, $H^b$), 2.5-2.3 (0.6 H, m, $H^c$), 2.1-1.9 (3 H, s, $H^a$) ppm.

SD (LHAPA): 26 %.

$^1$H-NMR (300 MHz, $D_2O$, HHAPA, δ): 6.4-6.2 (0.3 H, m, $H^d$), 5.6-5.4 (0.6 H, t, $H^e$), 5.2-4.8 (m, backbone), 4.4-3.5 (m, backbone), 3.1-2.9 (0.6 H, m, $H^b$), 2.9-2.7 (0.7 H, m, $H^c$), 2.6-2.3 (3 H, s, $H^a$) ppm.
SD (HHAPA): 32 %.

Low molecular weight thiol-modified hyaluronic acid (LHASH) was prepared as previously described.[142] LHA (27.3 kDa, 5.00 g, 12.5 mmol) was dissolved in deionized water and DTP (0.490 g, 2.10 mmol) was added under continuous stirring. After adjusting the pH of the reaction mixture to 4.75 with 1 M HCl aliquots, EDC (660 mg, 3.40 mmol) was added. The pH was maintained at 4.75 (1 M HCl) and the solution was stirred overnight. The solution was subsequently degassed with Ar and neutralized (0.5 M NaOH) before addition of TCEP (0.88 mg, 3.10 mmol). The pH was adjusted to 6 and the solution was subsequently stirred overnight. Afterwards the solution was dialyzed (MWCO 3.5 kDa) against acidified water (pH 4) for three dialysis cycles and then exhaustively against water. The product was finally lyophilized and stored under inert atmosphere in a glovebox until use.

$^1$H-NMR (300 MHz, $D_2O$, LHASH, δ): 4.6-4.4 (m, backbone), 4.2-3.2 (m, backbone), 3.0-2.6 (1.1 H, m, $H^b$), 2.1-1.9 (3 H, s, $H^a$) ppm.
SD (LHASH): 25 %.

### 5.4.3. Reaction sites of GelAGE - model polymers

Reaction parameters for $GelAGE_{4MM}$ (see **Table 11**) were used and transferred to the functionalization of the model substances pAA and pAAm. After 4 h the products were dialyzed against deionized water (MWCO 1 kDa). The products were subsequently lyophilized and stored at 4 °C under exclusion of light until use.

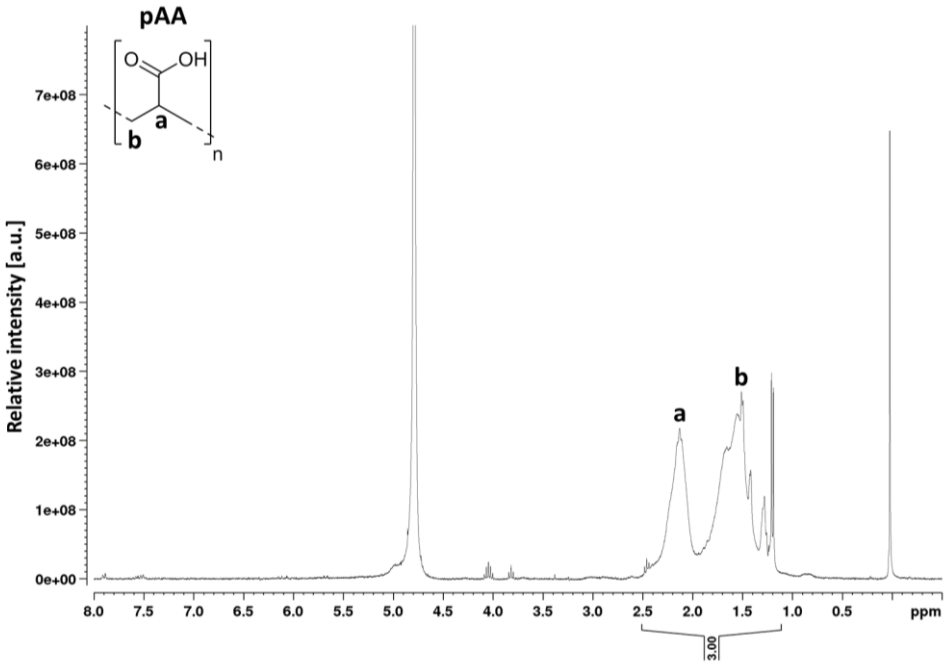


**Figure 96:** Representative $^{1}$H-NMR spectrum of pAA in $D_2O$.

$^{1}$H-NMR (300 MHz, $D_2O$, pAA, δ): 2.5-1.1 (3 H, m, $H^a$ and $H^b$) ppm.
$^{1}$H-NMR (300 MHz, $D_2O$, pAA-AGE, δ): 6.1-5.9 (0.1 H, m, $H^e$), 5.3-5.2 (0.2 H, m, $H^f$), 4.3-4.0 (0.4 H, d, $H^c$), 3.9-3.5 (0.2 H, m, $H^d$), 2.5-1.1 (3 H, m, $H^a$ and $H^b$) ppm.
SD (pAA-AGE): 10.8 %.

IR (pAAm): $\nu$ = 3356 (w; $\nu_{as}$(-$NH_2$)), 3278 (w; $\nu_s$(-$NH_2$)), 3176 (w), 2909 (m; $\nu$(C-H)), 2851 (m; $\nu$(C-H)), 1598 (m; $\delta$(-$NH_2$)), 1452 (m; $\delta$(CH)), 1369 (w; $\delta_s$(CH)), 835 (s) $cm^{-1}$.
IR (pAAm-AGE): ν = 3380 (w; $\nu_{as}$(-$NH_2$)), 3078 (w), 2909 (m, C-H), 2851 (m; $\nu$(C-H)), 1644 (m; $\delta$(-$NH_2$)), 1452 (m; $\delta$(CH)), 1417 (m; $\delta$(CH)), 1350 (m; $\delta_s$(CH)), 1083 (s), 994 (s; δ(C=C)), 922 (s; δ(C=C)), 862 (w) $cm^{-1}$.

### 5.4.4. SEC analysis

A Malvern system (Herrenberg, Germany) was used to conduct aqueous SEC analysis for GelAGE samples, HA products and the corresponding educts with 0.1 M $NaNO_3$, 0.02 wt.-% $NaN_3$ and with 0.3 M NaCl, 20 mM $Na_2HPO_4$, pH 8.3 for UV-detection of hydrolyzed hydrogels and the corresponding references. The system consisted of a Viskotek GPCmax (in-line degasser, 2 piston-pump and auto sampler), column oven (35 °C), refractive index- (Viskotek), UV- (Viskotek; 208 nm) and MALS- (Viskotek SEC-MALS 20) detector. Two different column sets (length = 300 mm, width = 8 mm, porous

poly hydroxymethacrylate polymer, particle size A6000M = 13 µm, A3000 = 6 µm and A2000 = 8 µm) were used, namely set I (2 x A6000M) and set II (A3000/A2000). Set I was used for gelatin and its controls ($Gelatin_{1\text{-}24M0}$), GelMA, $GelAGE_{8\text{-}24LL}$, $GelAGE_{8\text{-}24LM}$, $GelAGE_{1MM}$, $GelAGE_{8\text{-}24MM}$, $GelAGE_{8MH}$ and $GelAGE_{8HH}$ whereas set II was used for $GelAGE_{24LM}$, $GelAGE_{1\text{-}24MM}$, $GelAGE_{8MH}$, $GelAGE_{8HH}$ and HA educts and products. The flow rate was set to 0.7 mL $min^{-1}$. For calibration poly(ethylene glycol) standards (Malvern, Herrenberg, Germany) were used. Samples were allowed to dissolve overnight (3.0 mg $mL^{-1}$), except for LHASH to reduce the probability of thiol oxidation, in the corresponding eluent and filtered through a syringe filter (0.45 µm regenerated cellulose, Thermo Scientific, Darmstadt, Germany) before being subjected to analysis.

### 5.4.5. Hydrogel fabrication and characterization

GelMA, GelAGE, GelAGE/HA hybrid and HA hydrogels were prepared in PBS at different polymer weight percentages. Allylated product hydrogel solutions were mixed with the corresponding crosslinker to obtain functional group ratios of 1:1.5; 1:3; 1:6 and 1:12 (Ene:SH) for DTT and 1:1.5 and 1:3 for sPEGSH and LHASH. The photoinitiators (0.05 wt.-%, 2.2 mM I2959 or 0.2/2 – 1/10 mM of Ru/SPS) were added to the precursor solutions. GelMA precursor solutions were covered with a glass slide to reduce oxygen inhibition effects before and during irradiation. All other hydrogels were polymerized in an open environment. Crosslinking was initiated via irradiation with either UV-light (bluepoint 4, Dr. Hoehnle AG, Munich, Germany) or Vis-light (bluepoint 4, Dr. Hoehnle AG, Munich, Germany equipped with 390 – 500 nm filter from Dr. Hoehnle AG) for 3 min at 30 mW $cm^{-2}$. Cylindrical constructs (h = 2 mm, Ø = 6 mm) were prepared in silicon molds.

#### 5.4.5.1. Hydrolysis of gelatin-based hydrogels and SEC analysis

20 wt.-% GelMA (0.05 wt.-% I2959) and 20 wt.-% $GelAGE_{1MM}$ (Ene:SH = 1:12; 0.05 wt.-% I2959) hydrogels were prepared as previously described. References, hydrogels and pMMA were incubated for 30 min at 300 W in 6 M HCl (200 µL) in a microwave (CEM discover SP-D, Kamp-Lintfort, Germany). Drying of the hydrolyzed solutions was performed by heating the samples in a thermomixer (Thermomixer 5436, Eppendorf, Hamburg, Germany) to 95 °C for 12 h. The residues were dissolved (0.3 M NaCl, 20 mM $Na_2HPO_4$, pH 8.3) and filtered before being subjected to SEC analysis as previously

described (column set II).

### 5.4.5.2. Physico-chemical properties of hydrogels

Crosslinked hydrogels were weighed ($m_{initial,t0}$) and triplets were lyophilized to obtain the initial dry weights ($m_{dry,t0}$) of the hydrogels to calculate the actual macromer fraction, which is defined according to the following equation:

$$Actual\ macromer\ fraction = \frac{m_{dry,t0}}{m_{initial,t0}} \qquad \textbf{(Equation 2)}$$

The calculation of the initial dry weight of the remaining samples was based on the actual macromer fraction together with the initial weights. To obtain the swollen weights ($m_{swollen}$) of the remaining samples, the hydrogels were allowed to swell in PBS (2.0 mL) at 37 °C for 1 d. Afterwards the hydrogels were lyophilized to obtain the freeze dried weights ($m_{dry}$). The mass swelling ratio q is represented by the following equation:

$$q = \frac{m_{swollen}}{m_{dry}} \qquad \textbf{(Equation 3)}$$

The sol fraction of the hydrogels is defined as the percentages of polymer that were not covalently incorporated into the hydrogel network and represents the mass loss after equilibrium swelling (t = 24 h).

$$Sol\ fraction = \frac{m_{dry,t0} - m_{dry}}{m_{dry,t0}}\ x\ 100 \qquad \textbf{(Equation 4)}$$

Additionally the water content of the hydrogels was calculated according to the following equation:

$$Water\ content = \frac{m_{swollen} - m_{dry}}{m_{swollen}}\ x\ 100 \qquad \textbf{(Equation 5)}$$

### 5.4.5.3. Mechanical testing

Prior to mechanical compression testing experiments, triplets of the individual hydrogel compositions were swollen in PBS (2.0 mL) at 37 °C to equilibrium (24 h). Mechanical

testing of the hydrogels was performed with a dynamical mechanical testing machine (BOSE 5500 system, ElectroForce, Eden Prairie, MN, USA) equipped with a load cell (2.45 N or 22.2 N). Cylindrical samples (h = 2 mm, Ø = 6 mm) were loaded parallel to their long axis and investigated at a constant cross head displacement rate of 0.01 mm $sec^{-1}$. The slope of the true stress-strain curve in the linear elastic range (strain: 0 – 10 %) represents the Young´s modulus.

### 5.4.6. Rheology

Rheological properties of the precursor solutions were analyzed with a Physica MCR301 rheometer (Anton Paar, Ostfildern, Germany) in plate-plate geometry (plate diameter 25 mm, distance 0.5 mm) equipped with a solvent trap to prevent drying effects. For all investigations rotating measurements were performed on precursor solutions without photoinitiator. In order to mimic the shear rate while extrusion-based printing the following equation was chosen to estimate the corresponding shear rate in the needle:

$$\gamma = \frac{8\upsilon}{d} \qquad \textbf{(Equation 1)}$$

with γ= shear rate [$s^{-1}$], υ= printing velocity [0.33 mm $s^{-1}$ and 0.25 mm $s^{-1}$] and d= needle diameter [0.33 mm] and a corresponding shear rate of 6 – 8 $s^{-1}$.[213]

Temperature sweeps from 1 – 37 °C (1 °C $min^{-1}$) were recorded at 8 $s^{-1}$. Viscosity over shear rate was investigated at different temperatures between 0.01 – 1 000 $s^{-1}$.

### 5.4.7. Extrusion-based (bio)printing

Robotic dispensing was conducted with a 3D discovery printer (RegenHU, Villaz-St-Pierre, Switzerland) equipped with a DD-135N syringe dispenser print head. The apparatus was set in a laminar flow hood to ensure sterile conditions. Two separate cooling loops were equipped to the syringe and the printing plate and enabled cooling of the system to 4 – 7 °C. After preparing the precursor solutions as previously described, these were transferred to 3 mL syringes and allowed to cool for 30 min. The solutions were then printed with a 23 G (0.33 mm) needle tip and 1.25 bar, 2.1 bar, 2.5 bar and 2.7 bar (HHAPA (LHASH; Ene:SH = 1:1.5), GelAGE (DTT; Ene:SH = 1:3), GelAGE (sPEGSH; Ene:SH = 1:1.5) and GelAGE (LHASH; Ene:SH = 1:1.5), respectively). For I2959 mediated crosslinking the constructs were irradiated while printing (1 x 2 s per layer with

additional 3 x 2 s intervals after printing) with UV-light. For Vis-light irradiation of 30 wt.-% GelAGE (DTT; Ene:SH = 1:3) the constructs were irradiated after the printing process for 3 min at 30 mW $cm^{-2}$. The constructs were finally imaged using a stereomicroscope (SteREO Discovery.V20, Carl Zeiss microscope, Jena, Germany).

For extrusion-based bioprinting stock solutions of Ru and SPS (50 mM and 1 M, respectively) were prepared and sterile filtered (0.2 µm). To obtain sterile precursors, $GelAGE_{1MM}$ and HHAPA were dissolved in deionized water, sterile filtered, subsequently lyophilized and stored at 4 °C until use. For sterilization of thiol bearing components an irradiation with UV-light at 245 nm (UVL hand lamp with filter, A. Hartenstein, Würzburg, Germany) for 10 min prior to use was conducted.

### 5.4.8. TNBSA assay for gelatin, GelMA and GelAGE samples

Different amounts of ethanolamine (0.5 – 10 µg $mL^{-1}$) were used for calibration. Each gelatin-derived sample was dissolved (1.0 mg $mL^{-1}$) and further diluted with 0.1 M $NaHCO_3$ (1:1; 1:4 and 1:10 (v/v)). 100 µL of the samples were transferred to 96 well plates and 50 µL of TNBSA (0.01 %, 0.09 µmol in 0.1 M $NaHCO_3$) were added to each well. After an incubation for 2 h at 37 °C, 50 µL SDS (10 wt.-%) were added followed by the addition of 25 µL HCl (1 M). The produced $CO_2$ was removed by gently shaking the well plate. The absorption was measured at 335 nm (Infinite M200 Pro, Tecan, Maennedorf, Switzerland).

### 5.4.9. SDS-PAGE

The SDS-PAGE analysis was performed according to the procedure of Laemmli.[221] Samples were heated to 95 °C for 5 min under reducing conditions in the sample buffer (62.5 mM Trizma Base, 10 wt.-% glycerin, 2.0 wt.-% SDS, 5.0 wt.-% β-mercaptoethanol). The low molecular weight marker was diluted 1/10 with sample buffer and 8 µL were loaded per well. 15.0 µg of the samples were deposited in the wells, and the migration was induced at 40 mA until the migration front reached the end of the resolving gel. The gels (18 wt.-%) were stained with Coomassie blue R-250 (0.1 wt.-% in MeOH/HAc/water 20/7.5/72.5 (v/v)) over night and destained with a mixture of HAc/MeOH/water (7.5/20/72.5 (v/v)).

# 6. Literature

[1] K. Y. Lee, D. J. Mooney, Hydrogels for Tissue Engineering, Chemical Reviews, 101 (2001) 1869-1880.

[2] B. V. Slaughter, S. S. Khurshid, O. Z. Fisher, A. Khademhosseini, N. A. Peppas, Hydrogels in Regenerative Medicine, Advanced Materials, 21 (2009) 3307-3329.

[3] F. P. W. Melchels, M. A. N. Domingos, T. J. Klein, J. Malda, P. J. Bartolo, D. W. Hutmacher, Additive Manufacturing of Tissues and Organs, Progress in Polymer Science, 37 (2012) 1079-1104.

[4] D. W. Hutmacher, P. D. Dalton, Melt Electrospinning, Chemistry – An Asian Journal, 6 (2011) 44-56.

[5] D. W. Hutmacher, Scaffolds in Tissue Engineering Bone and Cartilage, Biomaterials, 21 (2000) 2529-2543.

[6] J. Malda, J. Visser, F. P. Melchels, T. Jüngst, W. E. Hennink, W. J. A. Dhert, J. Groll, D. W. Hutmacher, 25$^{th}$ Anniversary Article: Engineering Hydrogels for Biofabrication, Advanced Materials, 25 (2013) 5011-5028.

[7] E. L. Ritman, Micro-Computed Tomography - Current Status and Developments, Annual Review of Biomedical Engineering, 6 (2004) 185-208.

[8] H. G. Potter, B. J. Nestor, C. M. Sofka, S. T. Ho, L. E. Peters, E. A. Salvati, Magnetic Resonance Imaging after Total Hip Arthroplasty: Evaluation of Periprosthetic Soft Tissue, Journal of Bone and Joint Surgery, 86 (2004) 1947-1954.

[9] T. Liu, J. D. Houle, J. Xu, B. P. Chan, S. Y. Chew, Nanofibrous Collagen Nerve Conduits for Spinal Cord Repair, Tissue Engineering: Part A, 18 (2012) 1057-1066.

[10] B. Mammadov, M. Sever, M. O. Guler, A. B. Tekinay, Neural Differentiation on Synthetic Scaffold Materials, Biomaterials Science, 1 (2013) 1119-1137.

[11] G. Hochleitner, T. Jüngst, T. D. Brown, K. Hahn, C. Moseke, F. Jakob, P. D. Dalton, J. Groll, Additive Manufacturing of Scaffolds with Sub-Micron Filaments via Melt Electrospinning Writing, Biofabrication, 7 (2015) 035002.

[12] D. F. Williams, Definitions in Biomaterials: Proceedings of a Consensus Conference of the European Society for Biomaterials, Chester, England, March 3-5, 1986, Elsevier.

[13] T. D. Brown, A. Slotosch, L. Thibaudeau, A. Taubenberger, D. Loessner, C. Vaquette, P. D. Dalton, D. W. Hutmacher, Design and Fabrication of Tubular Scaffolds via Direct Writing in a Melt Electrospinning Mode, Biointerphases, 1 (2012) 1-16.

[14] T. Jungst, W. Smolan, K. Schacht, T. Scheibel, J. Groll, Strategies and Molecular Design Criteria for 3D Printable Hydrogels, Chemical Reviews, 116 (2016) 1496-1539.

[15] F. P. W. Melchels, J. Feijen, D. W. Grijpma, A Review on Stereolithography and its Applications in Biomedical Engineering, Biomaterials, 31 (2010) 6121-6130.

[16] R. Langer, J. P. Vacanti, Tissue Engineering, Science, 260 (1993) 920-926.

[17] A. Rossi, L. Wistlich, K.-H. Heffels, H. Walles, J. Groll, Isotropic Versus Bipolar Functionalized Biomimetic Artifical Basement Membranes and Their Evaluation in Long-Term Human Cell Co-Culutre, Advanced Healthcare Materials, 5 (2016) 1939-1948.

[18] N. Annabi, A. Tamayol, J. A. Uquillas, M. Akbari, L. E. Bertassoni, C. Cha, G. Camci-Unal, M. R. Dokmeci, N. A. Peppas, A. Khademhosseini, 25$^{th}$ Anniversary Article: Rational Design and Applications of Hydrogels in Regenerative Medicine, Advanced Materials, 26 (2014) 85-124.

[19] S. Gorgieva, V. Kokol, Collagen- vs. Gelatine-Based Biomaterials and Their Biocompatibility: Review and Perspectives, Biomaterials Applications for Nanomedicine, Prof. Rosario Pignatello (Ed.), InTech, (2011) DOI: 10.5772/24118.

[20] S. Stichler, T. Jungst, M. Schamel, I. Zilkowski, M. Kuhlmann, T. Böck, T. Blunk, J. Teßmar, J. Groll, Thiol-Ene Clickable Poly(Glycidol) Hydrogels for Biofabrication, Annals of Biomedical Engineering, 45 (2016) 273-285.

[21] M. Bongio, J. J. Van den Beucken, M. R. Nejadnik, S. C. Leeuwenburgh, L. A. Kinard, F. K. Kasper, A. G. Mikos, J. A. Jansen, Biomimetic Modification of Synthetic Hydrogels by Incorporation of Adhesive Peptides and Calcium Phosphate Nanoparticles: In Vitro Evaluation of Cell Behavior, European Cells and Materials, 22 (2011) 359-376.

[22] M. Lutolf, J. L. Lauer-Fields, H. G. Schmoekel, A. T. Metters, F. E. Weber, G. B. Fields, J. A. Hubbell, Synthetic Matrix Metalloproteinase-Sensitive Hydrogels for the Conduction of Tissue Regeneration: Engineering Cell-Invasion Characteristics, Proceedings of the National Academy of Science, 100 (2003) 5413-5418.

[23] T. P. Kraehenbuehl, P. Zammaretti, A. J. Van der Vlies, R. G. Schoenmakers, M. P. Lutolf, M. E. Jaconi, J. A. Hubbell, Three-Dimensional Extracellular Matrix-Directed Cardioprogenitor Differentiation: Systematic Modulation of a Synthetic Cell-Responsive PEG-Hydrogel, Biomaterials, 29 (2008) 2757-2766.

[24] X. Jia, K. L. Kiick, Hybrid Multicomponent Hydrogels for Tissue Engineering, Macromolecular Bioscience, 9 (2009) 140-156.

[25] Z.-M. Huang, Y. Z. Zhang, M. Kotaki, S. Ramakrishna, A Review on Polymer Nanofibres by Electrospinning and their Applications in Nanocomposites, Composites Science and Technology, 63 (2003) 2223-2253.

[26] P. D. Dalton, C. Vaquette, B. L. Farrugia, T. R. Dargaville, T. D. Brown, D. W. Hutmacher, Electrospinning and Additive Manufacturing: Converging Technologies, Biomaterials Science, 1 (2013) 171-185.

[27] Q. P. Pham, U. Sharma, A. G. Mikos, Electrospun Poly(ε-Caprolactone) Microfiber and Multilayer Nanofiber/Mircofiber Scaffolds: Characterizaion of Scaffolds and Measurement of Cellular Infiltration, Biomacromolecules, 7 (2006) 2796-2805.

[28] T. D. Brown, P. D. Dalton, D. W. Hutmacher, Direct Writing by Way of Melt Electrospinning, Advanced Materials, 23 (2011) 5651-5657.

[29] T. D. Brown, F. Edin, N. Detta, A. D. Skelton, D. W. Hutmacher, P. D. Dalton, Melt Electrospinning of Poly(ε-Caprolactone) Scaffolds: Phenomenological Observations Associated with Collection and Direct Writing, Materials Science and Engineering: C, 45 (2014) 698-708.

[30] C. Wei, J. Dong, Direct Fabrication of High-Resolution Three-Dimensional Polymeric Scaffolds Using Electrohydrodynamic Hot Jet Plotting, Journal of Micromechanics and Microengineering, 23 (2013) 025017.

[31] B. L. Farrugia, T. D. Brown, Z. Upton, D. W. Hutmacher, P. D. Dalton, T. R. Dargaville, Dermal Fibroblast Infiltration of Poly(ε-Caprolactone) Scaffolds Fabricated by Melt Electrospinning in a Direct Writing Mode, Biofabrication, 5 (2013) 025001.

[32] J. Visser, F. P. W. Melchels, J. E. Jeon, E. M. van Bussel, L. S. Kimpton, H. M. Byrne, W. J. A. Dhert, P. D. Dalton, D. W. Hutmacher, J. Malda, Reinforcement of Hydrogels Using Three-Dimensionally Printed Microfibres, Nature Communications, 6 (2015) 6933.

[33] N. Ristovski, N. Bock, S. Liao, S. K. Powell, J. Ren, G. T. Kirby, K. A. Blackwood, M. A. Woodruff, Improved Fabrication of Melt Electrospun Tissue Engineering Scaffolds Using Direct Writing and Advanced Electric Field Control, Biointerphases, 10 (2015) 011006.

[34] G. Hochleitner, J. F. Hümmer, R. Luxenhofer, J. Groll, High Definition Fibrous Poly(2-Ethyl-2-Oxazoline) Scaffolds Through Melt Electrospinning Writing, Polymer, 55 (2014) 5017-5023.

[35] F. J. v. Natta, J. W. Hill, W. H. Carothers, Studies of Polymerization and Ring Formation. XXIII. ε-Caprolactone and its Polymers, Journal of the American Chemical Society, 56 (1934) 455-457.

[36] R. Chandra, R. Rustgi, Biodegradable Polymers, Progress in Polymer Science, 23 (1998) 1273-1335.

[37] I. Zein, D. W. Hutmacher, K. C. Tan, S. H. Teoh, Fused Deposition Modeling of Novel Scaffold Architectures for Tissue Engineering Application, Biomaterials, 23 (2002) 1169-1185.

[38] H. Huang, S. Oizumi, N. Kojima, T. Niino, Y. Sakai, Avidin-Biotin Binding-Based Cell Seeding and Perfusion Culture of Liver-Derived Cells in a Porous Scaffold with Three-Dimensional Interconnected Flow-Channel Network, Biomaterials, 28 (2007) 3815-3823.

[39] L. S. Nair, C. T. Laurencin, Biodegradable Polymers as Biomaterials, Progress in Polymer Science, 32 (2007) 762-798.

[40] A. Luciani, V. Coccoli, S. Orsi, L. Ambrosio, P. A. Netti, PCL Microspheres Based Functional Scaffolds by Bottom-Up Approach with Predefined Microstructural Properties and Release Profiles, Biomaterials, 29 (2008) 4800-4807.

[41] C. Marrazzo, E. Di Maio, S. Iannace, Conventional and Nanometric Nucleating Agents in Poly(ε-Caprolactone) Foaming: Crystals vs. Bubbles Nucleation, Polymer Engineering & Science, 48 (2008) 336-344.

[42] Y. Lu, H. Jiang, K. Tu, L. Wang, Mild Immobilization of Diverse Macromolecular Bioactive Agents onto Multifunctional Fibrous Membranes Prepared by Coaxial Electrospinning, Acta Biomaterialia, 5 (2009) 1562-1574.

[43] V. Thomas, M. V. Jose, S. Chowdhury, J. F. Sullivan, D. R. Dean, Y. K. Vohra, Mechano-Morphological Studies of Aligned Nanofibrous Scaffolds of Polycaprolactone Fabricated by Electrospinning, Journal of Biomaterials Science. Polymer Edition, 17 (2006) 969-984.

[44] H. Yoshimoto, Y. M. Shin, H. Terai, J. P. Vacanti, A Biodegradable Nanofiber Scaffold by Electrospinning and its Potential for Bone Tissue Engineering, Biomaterials, 24 (2003), 2077-2082.

[45] M. A. Woodruff, D. W. Hutmacher, The Return of a Forgotten Polymer - Polycaprolactone in the 21st Century, Progress in Polymer Science, 35 (2010) 1217-1256.

[46] C. X. F. Lam, D. W. Hutmacher, J.-T. Schantz, M. A. Woodruff, S. H. Teoh, Evaluation of Polycaprolactone Scaffold Degradation for 6 Months In Vitro and In Vivo, Journal of Biomedical Materials Research Part A, 90 (2009) 906-919.

[47] W. J. Li, K. G. Danielson, P. G. Alexander, R. S. Tuan, Biological Response of Chondrocytes Cultured in Three-Dimensional Nanofibrous Poly(ε-Caprolactone) Scaffolds, Journal of Biomedical Materials Research Part A, 67 (2003) 1105-1114.

[48] M. Vert, Degradable and Bioresorbable Polymers in Surgery and in Pharmacology: Beliefs and Facts, Journal of Materials Science: Materials in Medicine, 20 (2009) 437-446.

[49] S. C. Woodward, P. S. Brewer, F. Moatamed, A. Schindler, C. G. Pitt, The Intracellular Degradation of Poly(ε-Caprolactone), Journal of Biomedical Materials Research Part A, 19 (1985) 437-444.

[50] R. M. Ginde, R. K. Gupta, In Vitro Chemical Degradation of Poly(Glycolic Acid) Pellets and Fibers, Journal of Applied Polymer Science, 33 (1987) 2411-2429.

[51] J. E. Bergsma, W. De Bruijn, F. Rozema, R. Bos, G. Boering, Late Degradation Tissue Response to Poly(L-Lactide) Bone Plates and Screws, Biomaterials, 16 (1995) 25-31.

[52] D. W. Hutmacher, Scaffold Design and Fabrication Technologies for Engineering Tissues - State of the Art and Future Perspectives, Journal of Biomaterials Science. Polymer Edition, 12 (2001) 107-124.

[53] C. X. F. Lam, M. M. Savalani, S.-H. Teoh, D. W. Hutmacher, Dynamics of In Vitro Polymer Degradation of Polycaprolactone-Based Scaffolds: Accelerated versus Simulated Physiological Conditions, Biomedical Materials, 3 (2008) 034108.

[54] H. J. Milton, Introduction to Biotechnical and Biomedical Applications of Poly(Ethylene Glycol) in Poly(Ethylene Glycol) Chemistry: Biotechnical and Biomedical Applications, (Ed: J. M. Harris), Springer US, Boston, MA 1992, 1-14.

[55] M. Bartneck, K.-H. Heffels, Y. Pan, M. Bovi, G. Zwadlo-Klarwasser, J. Groll, Inducing Healing-Like Human Primary Macrophage Phenotypes by 3D Hydrogel Coated Nanofibers, Biomaterials, 33 (2012) 4136-4146.

[56] U. Hersel, C. Dahmen, H. Kessler, RGD Modified Polymers: Biomaterials for Simulated Cell Adhesion and Beyond, Biomaterials, 24 (2003) 4385-4415.

[57] E. Ostuni, R. G. Chapman, R. E. Holmlin, S. Takayama, G. M. Whitesides, A Survey of Structure-Property Relationships of Surfaces that Resist the Adsorption of Protein, Langmuir, 17 (2001) 5605-5620.

[58] K. Klinkhammer, J. Bockelmann, C. Simitzis, G. A. Brook, D. Grafahrend, J. Groll, M. Möller, J. Mey, D. Klee, Functionalization of Electrospun Fibers of Poly(ε-Caprolactone) with Star Shaped NCO-Poly(Ethylene Glycol)-stat-Poly(Propylene Glycol) for Neuronal Cell Guidance, Journal of Materials Science: Materials in Medicine, 21 (2010) 2637-2651.

[59] S. I. Jeon, J. H. Lee, J. D. Andrade, P. G. De Gennes, Protein-surface interactions in the presence of polyethylene oxide: I. Simplified theory, Journal of Colloid and Interface Science, 142 (1991), 149-158.

[60] J. Satulovsky, M. Carignano, I. Szleifer, Kinetic and Thermodynamic Control of Protein Adsorption, Proceedings of the National Academy of Sciences, 97 (2000) 9037-9041.

[61] S. Sofia, E. Merill, J. Harris, S. Zalipsky, Poly(Ethylene Glycol): Chemistry and Biological Applications, American Chemical Society, Washington DC, 1997.

[62] I. Szleifer, Protein Adsorption on Surfaces with Grafted Polymers: a Theoretical Approach, Biophysical Journal, 72 (1997) 595-612.

[63] T. McPherson, A. Kidane, I. Szleifer, K. Park, Prevention of Protein Adsorption by Tethered Poly(Ethylene Oxide) Layers: Experiments and Single-Chain Mean-Field Analysis, Langmuir, 14 (1998) 176-186.

[64] K. Feldman, G. Hähner, N. Spencer, P. Harder, M. Grunze, Probing Resistance to Protein Adsorption of Oligo(Ethylene Glycol)-Terminated Self-Assembled Monolayers by Scanning Force Microscopy, Journal of the American Chemical Society, 121 (1999) 10134-10141.

[65] J. Groll, T. Ameringer, J. P. Spatz, M. Moeller, Ultrathin Coatings from Isocyanate-Terminated Star PEG Prepolymers: Layer Formation and Characterization, Langmuir, 21 (2005) 1991-1999.

[66] I. Szleifer, M. Carignano, Tethered Polymer Layers: Phase Transitions and Reduction of Protein Adsorption, Macromolecular Rapid Communications, 21 (2000) 423-448.

[67] H. Götz, U. Beginn, C. F. Bartelink, H. J. M. Grünbauer, M. Möller, Preparation of Isophorone Diisocyanate Terminated Star Polyethers, Macromolecular Materials and Engineering, 287 (2002) 223-230.

[68] D. J. Irvine, A. M. Mayes, L. Griffith-Cima, Self-Consistent Field Analysis of Grafted Star Polymers, Macromolecules, 29 (1996) 6037-6043.

[69] B. J. Bauer, L. J. Fetters, W. W. Graessley, N. Hadjichristidis, G. F. Quack, Chain Dimensions in Dilute Polymer Solutions: a Light-Scattering and Viscometric Study of Multiarmed Polyisoprene Stars in Good and θ Solvents, Macromolecules, 22 (1989) 2337-2347.

[70] S. J. Sofia, V. Premnath, E. W. Merrill, Poly(Ethylene Oxide) Grafted to Silicon Surfaces: Grafting Density and Protein Adsorption, Macromolecules, 31 (1998) 5059-5070.

[71] J. Groll, E. V. Amirgoulova, T. Ameringer, C. D. Heyes, C. Röcker, G. U. Nienhaus, M. Möller, Biofunctionalized, Ultrathin Coatings of Cross-Linked Star-Shaped Poly(Ethylene Oxide) Allow Reversible Folding of Immobilized Proteins, Journal of the American Chemical Society, 126 (2004) 4234-4239.

[72] P. Gasteier, A. Reska, P. Schulte, J. Salber, A. Offenhäusser, M. Moeller, J. Groll, Surface Grafting of PEO-Based Star-Shaped Molecules for Bioanalytical and Biomedical Applications, Macromolecular Bioscience, 7 (2007) 1010-1023.

[73] C. D. Heyes, J. Groll, M. Möller, G. U. Nienhaus, Synthesis, Patterning and Applications of Star-Shaped Poly(Ethylene Glycol) Biofunctionalized Surfaces, Molecular BioSystems, 3 (2007) 419-430.

[74] J. Groll, H. Rong, P. Greiwe, M. Flach, Star performers, European Coatings Journal, 5 (2007) 162.

[75] F. Topuz, M. Möller, J. Groll, Covalently Layer-by-Layer Assembled Homogeneous Nanolayers with Switchable Wettability, Polymer Chemistry, 6 (2015) 4690-4697.

[76] A. A. Caraculacu, S. Coseri, Isocyanates in Polyaddition Processes. Structure and Reaction Mechanisms, Progress in Polymer Science, 26 (2001) 799-851.

[77] S. Sinn, M. Eichler, L. Müller, D. Bünger, J. Groll, G. Ziemer, F. Rupp, H. Northoff, J. Geis-Gerstorfer, F. K. Gehring, NCO-sP(EO-stat-PO) Coatings on Gold Sensors – a QCM Study of Hemocompatibility, Sensors, 11 (2011) 5253-5269.

[78] J. Groll, J. Fiedler, E. Engelhard, T. Ameringer, S. Tugulu, H. A. Klok, R. E. Brenner, M. Moeller, A Novel Star PEG-Derived Surface Coating for Specific Cell Adhesion, Journal of Biomedical Materials Research Part A, 74 (2005) 607-617.

[79] J. Salber, S. Gräter, M. Harwardt, M. Hofmann, D. Klee, J. Dujic, H. Jinghuan, J. Ding, S. Kippenberger, A. Bernd, Influence of Different ECM Mimetic Peptide Sequences Embedded in a Nonfouling Environment on the Specific Adhesion of Human-Skin Keratinocytes and Fibroblasts on Deformable Substrates, Small, 3 (2007) 1023-1031.

[80] D. Grafahrend, K. H. Heffels, M. Möller, D. Klee, J. Groll, Electrospun, Biofunctionalized Fibers as Tailored In Vitro Substrates for Keratinocyte Cell Culture, Macromolecular Bioscience, 10 (2010) 1022-1027.

[81] G. Böhm, Y. Ushakova, H. P. Alizai, T. Braunschweig, C. Lente, K. H. Heffels, J. Groll, U. P. Neumann, K. Junge, Biocompatibility of PLGA/sP(EO-stat-PO)-Coated Mesh Surfaces under Constant Shearing Stress, European Surgical Research, 47 (2011) 118-129.

[82] D. Grafahrend, K.-H. Heffels, M. V. Beer, P. Gasteier, M. Möller, G. Boehm, P. D. Dalton, J. Groll, Degradable Polyester Scaffolds with Controlled Surface Chemistry Combining Minimal Protein Adsorption with Specific Bioactivation, Nature Materials, 10 (2011) 67-73.

[83] L. Wistlich, J. Kums, K. Heffels, H. Wajant, J. Groll, A One-step Approach for Multimodal Functionalization of Electrospun Nanofibers and their Application for Immune-regulatory Surfaces, Tissue Engineering Part A, 21 (2015) S50-S55.

[84] C. C. Chang, E. D. Boland, S. K. Williams, J. B. Hoying, Direct-Write Bioprinting Three-Dimensional Biohybrid Systems for Future Regenerative Therapies, Journal of Biomedical Materials Research Part B: Applied Biomaterials, 98 (2011) 160-170.

[85] T. Billiet, E. Gevaert, T. De Schryver, M. Cornelissen, P. Dubruel, The 3D Printing of Gelatin Methacrylamide Cell-Laden Tissue-Engineered Constructs with High Cell Viability, Biomaterials, 35 (2014) 49-62.

[86] S. Bertlein, G. Brown, K. S. Lim, T. Jungst, T. Boeck, T. Blunk, J. Tessmar, G. J. Hooper, T. B. F. Woodfield, J. Groll, Thiol-Ene Clickable Gelatin: A Platform Bioink for Multiple 3D Biofabrication Technologies, Advanced Materials, 29 (2017) 1703404.

[87] S. Wüst, R. Müller, S. Hofmann, Controlled Positioning of Cells in Biomaterials - Approaches Towards 3D Tissue Printng, Journal of Functional Biomaterials, 2 (2011) 119-154.

[88] D. Buenger, F. Topuz, J. Groll, Hydrogels in Sensing Applications, Progress in Polymer Science, 37 (2012) 1678-1719.

[89] T. Billiet, M. Vandenhaute, J. Schelfhout, S. Van Vlierberghe, P. Dubruel, A Review of Trends and Limitations in Hydrogel-Rapid Prototyping for Tissue Engineering, Biomaterials, 33 (2012) 6020-6041.

[90] J. J. Roberts, S. J. Bryant, Comparison of Photopolymerizable Thiol-Ene PEG and Acrylate-Based PEG Hydrogels for Cartilage Development, Biomaterials, 34 (2013) 9969-9979.

[91] C. E. Hoyle, C. N. Bowman, Thiol-Ene Click Chemistry, Angewandte Chemie International Edition, 49 (2010) 1540-1573.

[92] M. J. Kade, D. J. Burke, C. J. Hawker, The Power of Thiol-Ene Chemistry, Journal of Polymer Science Part A: Polymer Chemistry, 48 (2010) 743-750.

[93] K. Yue, G. Trujillo-de Santiago, M. M. Alvarez, A. Tamayol, N. Annabi, A. Khademhosseini, Synthesis, Properties, and Biomedical Applications of Gelatin Methacryloyl (GelMA) Hydrogels, Biomaterials, 73 (2015) 254-271.

[94] Z. Mũnoz, H. Shih, C.-C. Lin, Gelatin Hydrogels Formed by Orthogonal Thiol-Norbornene Photochemistry for Cell Encapsulation, Biomaterials Science, 2 (2014) 1063-1072.

[95] A. B. Lowe, Thiol-Ene "Click" Reactions and Recent Applications in Polymer and Materials Synthesis: A First Update, Polymer Chemistry, 5 (2014) 4820-4870.

[96] H. Lu, J. A. Carioscia, J. W. Stansbury, C. N. Bowman, Investigations of Step-Growth Thiol-Ene Polymerizations for Novel Dental Restoratives, Dental Materials, 21 (2005) 1129-1136.

[97] B. H. Northrop, R. N. Coffey, Thiol-Ene Click Chemistry: Computational and Kinetic Analysis of the Influence of Alkene Functionality, Journal of the American Chemical Society, 134 (2012) 13804-13817.

[98] C.-C. Lin, A. Raza, H. Shih, PEG Hydrogels Formed by Thiol-Ene Photo-Click Chemistry and their Effect on the Formation and Recovery of Insulin-Secreting Cell Spheroids, Biomaterials, 32 (2011) 9685-9695.

[99] K. T. Nguyen, J. L. West, Photopolymerizable Hydrogels for Tissue Engineering Applications, Biomaterials, 23 (2002) 4307-4314.

[100] A. B. Scranton, C. N. Bowman, R. W. Peiffer, Photopolymerization: Fundamentals and Applications, ACS Publications, 1997.

[101] J.-P. Fouassier, Photoinitiation, Photopolymerization, and Photocuring: Fundamentals and Applications, Hanser, 1995.

[102] J. W. Nichol, S. Koshy, H. Bae, C. M. Hwang, S. Yamanlar, A. Khademhosseini, Cell-Laden Microengineered Gelatin Methacrylate Hydrogels, Biomaterials, 31 (2010) 5536-5544.

[103] H. Bae, A. F. Ahari, H. Shin, J. W. Nichol, C. B. Hutson, M. Masaeli, S.-H. Kim, H. Aubin, S. Yamanlar, A. Khademhosseini, Cell-Laden Microengineered Pullulan Methacrylate Hydrogels Promote Cell Proliferation and 3D Cluster Formation, Soft Matter, 7 (2011) 1903-1911.

[104] M. Bartnikowski, N. J. Bartnikowski, M. A. Woodruff, K. Schrobback, T. J. Klein, Protective Effects of Reactive Functional Groups on Chondrocytes in Photocrosslinkable Hydrogel Systems, Acta Biomaterialia, 27 (2015) 66-76.

[105] B. J. Klotz, D. Gawlitta, A. J. W. P. Rosenberg, J. Malda, F. P. W. Melchels, Gelatin-Methacryloyl Hydrogels: Towards Biofabrication-Based Tissue Repair, Trends in Biotechnology, 34 (2016) 394-407.

[106] M. Liu, M.-D. Li, J. Xue, D. L. Phillips, Time-Resolved Spectroscopic and Density Functional Theory Study of the Photochemistry of Irgacure-2959 in an Aqueous Solution, The Journal of Physical Chemistry A, 118 (2014) 8701-8707.

[107] N. E. Fedorovich, M. H. Oudshoorn, D. van Geemen, W. E. Hennink, J. Alblas, W. J. A. Dhert, The Effect of Photopolymerization on Stem Cells Embedded in Hydrogels, Biomaterials, 30 (2009) 344-353.

[108] C. G. Williams, A. N. Malik, T. K. Kim, P. N. Manson, J. H. Elisseeff, Variable Cytocompatibility of Six Cell Lines with Photoinitiators Used for Polymerizing Hydrogels and Cell Encapsulation, Biomaterials, 26 (2005) 1211-1218.

[109] S. J. Bryant, C. R. Nuttelman, K. S. Anseth, Cytocompatibility of UV and Visible Light Photoinitiating Systems on Cultured NIH/3T3 Fibroblasts In Vitro, Journal of Biomaterials Science. Polymer Edition, 11 (2000) 439-457.

[110] U. P. Kappes, D. Luo, M. Potter, K. Schulmeister, T. M. Rünger, Short- and Long-Wave UV Light (UVB and UVA) Induce Similar Mutations in Human Skin Cells,

Journal of Investigative Dermatology, 126 (2006) 667-675.

[111] R. P. Sinha, D.-P. Hader, UV-induced DNA Damage and Repair: A Review, Photochemical & Photobiological Sciences, 1 (2002) 225-236.

[112] C. A. Jones, E. Huberman, M. L. Cunningham, M. J. Peak, Mutagenesis and Cytotoxicity in Human Epithelial Cells by Far- and Near-Ultraviolet Radiations: Action Spectra, Radiation Research, 110 (1987) 244-254.

[113] K. S. Lim, B. S. Schon, N. V. Mekhileri, G. C. J. Brown, C. M. Chia, S. Prabakar, G. J. Hooper, T. B. F. Woodfield, New Visible-Light Photoinitiating System for Improved Print Fidelity in Gelatin-Based Bioinks, ACS Biomaterials Science & Engineering, 2 (2016) 1752-1762.

[114] H. Shih, C. C. Lin, Visible-Light-Mediated Thiol-Ene Hydrogelation Using Eosin-Y as the Only Photoinitiator, Macromolecular Rapid Communications, 34 (2013) 269-273.

[115] B. D. Fairbanks, M. P. Schwartz, C. N. Bowman, K. S. Anseth, Photoinitiated Polymerization of PEG-Diacrylate with Lithium Phenyl-2,4,6-Trimethylbenzoylphosphinate: Polymerization Rate and Cytocompatibility, Biomaterials, 30 (2009) 6702-6707.

[116] D. A. Fancy, C. Denison, K. Kim, Y. Xie, T. Holdeman, F. Amini, T. Kodadek, Scope, Limitations and Mechanistic Aspects of the Photo-Induced Cross-Linking of Proteins by Water-Soluble Metal Complexes, Chemistry & Biologoy, 7 (2000) 697-708.

[117] K. L. Spiller, S. A. Maher, A. M. Lowman, Hydrogels for the Repair of Articular Cartilage Defects, Tissue Engineering. Part B, 17 (2011) 281-299.

[118] N. C. Hunt, L. M. Grover, Cell Encapsulation Using Biopolymer Gels for Regenerative Medicine, Biotechnology Letters, 32 (2010) 733-742.

[119] P. H. Maurer, II. Antigenicity of Gelatin in Rabbits and Other Species, The Journal of Experimental Medicine, 100 (1954) 515-523.

[120] Q. Feng, K. Wei, S. Lin, Z. Xu, Y. Sun, P. Shi, G. Li, L. Bian, Mechanically Resilient, Injectable, and Bioadhesive Supramolecular Gelatin Hydrogels Crosslinked by Weak Host-Guest Interactions Assist Cell Infiltration and In Situ Tissue Regeneration, Biomaterials, 101 (2016) 217-228.

[121] W. Schuurman, P. A. Levett, M. W. Pot, P. R. van Weeren, W. J. A. Dhert, D. W. Hutmacher, F. P. W. Melchels, T. J. Klein, J. Malda, Gelatin-Methacrylamide

Hydrogels as Potential Biomaterials for Fabrication of Tissue-Engineered Cartilage Constructs, Macromolecular Bioscience, 13 (2013) 551-561.

[122] M. Nikkhah, N. Eshak, P. Zorlutuna, N. Annabi, M. Castello, K. Kim, A. Dolatshahi-Pirouz, F. Edalat, H. Bae, Y. Yang, A. Khademhosseini, Directed Endothelial Cell Morphogenesis in Micropatterned Gelatin Methacrylate Hydrogels, Biomaterials, 33 (2012) 9009-9018.

[123] L. E. Bertassoni, J. C. Cardoso, V. Manoharan, A. L. Cristino, N. S. Bhise, W. A. Araujo, P. Zorlutuna, N. E. Vrana, A. M. Ghaemmaghami, M. R. Dokmeci, A. Khademhosseini, Direct-Write Bioprinting of Cell-Laden Methacrylated Gelatin Hydrogels, Biofabrication, 6 (2014) 024105.

[124] M. B. Chen, S. Srigunapalan, A. R. Wheeler, C. A. Simmons, A 3D Microfluidic Platform Incorporating Methacrylated Gelatin Hydrogels to Study Physiological Cardiovascular Cell–Cell Interactions, Lab on a Chip, 13 (2013) 2591-2598.

[125] A. I. Van Den Bulcke, B. Bogdanov, N. De Rooze, E. H. Schacht, M. Cornelissen, H. Berghmans, Structural and Rheological Properties of Methacrylamide Modified Gelatin Hydrogels, Biomacromolecules, 1 (2000) 31-38.

[126] E. Kaemmerer, F. P. Melchels, B. M. Holzapfel, T. Meckel, D. W. Hutmacher, D. Loessner, Gelatine Methacrylamide-Based Hydrogels: an Alternative Three-Dimensional Cancer Cell Culture System, Acta Biomaterialia, 10 (2014) 2551-2562.

[127] A. Serafim, C. Tucureanu, D.-G. Petre, D.-M. Dragusin, A. Salageanu, S. Van Vlierberghe, P. Dubruel, I.-C. Stancu, One-Pot Synthesis of Superabsorbent Hybrid Hydrogels Based on Methacrylamide Gelatin and Polyacrylamide. Effortless Control of Hydrogel Properties Through Composition Design, New Journal of Chemistry, 38 (2014) 3112-3126.

[128] Y. Fan, F. Xu, G. Huang, T. J. Lu, W. Xing, Single Neuron Capture and Axonal Development in Three-Dimensional Microscale Hydrogels, Lab on a Chip, 12 (2012) 4724-4731.

[129] F. Xu, C.-A. M. Wu, V. Rengarajan, T. D. Finley, H. O. Keles, Y. Sung, B. Li, U. A. Gurkan, U. Demirci, Three-Dimensional Magnetic Assembly of Microscale Hydrogels, Advanced Materials, 23 (2011) 4254-4260.

[130] B. Zamanian, M. Masaeli, J. W. Nichol, M. Khabiry, M. J. Hancock, H. Bae, A. Khademhosseini, Interface-Directed Self-Assembly of Cell-Laden Microgels,

Small, 6 (2010) 937-944.

[131] H.-Y. Hsieh, G. Camci-Unal, T.-W. Huang, R. Liao, T.-J. Chen, A. Paul, F.-G. Tseng, A. Khademhosseini, Gradient Static-Strain Stimulation in a Microfluidic Chip for 3D Cellular Alignment, Lab on a Chip, 14 (2014) 482-493.

[132] N. Annabi, S. Selimovic, J. P. Acevedo Cox, J. Ribas, M. Afshar Bakooshli, D. Heintze, A. S. Weiss, D. Cropek, A. Khademhosseini, Hydrogel-Coated Microfluidic Channels for Cardiomyocyte Culture, Lab on a Chip, 13 (2013) 3569-3577.

[133] M. J. Hancock, F. Piraino, G. Camci-Unal, M. Rasponi, A. Khademhosseini, Anisotropic Material Synthesis by Capillary Flow in a Fluid Stripe, Biomaterials, 32 (2011) 6493-6504.

[134] D. B. Kolesky, R. L. Truby, A. S. Gladman, T. A. Busbee, K. A. Homan, J. A. Lewis, 3D Bioprinting of Vascularized, Heterogeneous Cell-Laden Tissue Constructs, Advanced Materials, 26 (2014) 3124-3130.

[135] L. E. Bertassoni, M. Cecconi, V. Manoharan, M. Nikkhah, J. Hjortnaes, A. L. Cristino, G. Barabaschi, D. Demarchi, M. R. Dokmeci, Y. Yang, A. Khademhosseini, Hydrogel Bioprinted Microchannel Networks for Vascularization of Tissue Engineering Constructs, Lab on a Chip, 14 (2014) 2202-2211.

[136] J. R. E. Fraser, T. C. Laurent, U. B. G. Laurent, Hyaluronan: its Nature, Distribution, Functions and Turnover, Journal of Internal Medicine, 242 (1997) 27-33.

[137] J. A. Burdick, G. D. Prestwich, Hyaluronic Acid Hydrogels for Biomedical Applications, Advanced Materials, 23 (2011) H41-H56.

[138] Y. Tokita, A. Okamoto, Degradation of Hyaluronic Acid—Kinetic Study and Thermodynamics, European Polymer Journal, 32 (1996) 1011-1014.

[139] E. Shimada, G. Matsumura, Viscosity and Molecular Weight of Hyaluronic Acids, The Journal of Biochemistry, 78 (1975) 513-517.

[140] A. G. Ogston, J. E. Stanier, The Physiological Function of Hyaluronic Acid in Synovial Fluid; Viscous, Elastic and Lubricant Properties, The Journal of Physiology, 119 (1953) 244-252.

[141] S. Stichler, T. Böck, N. Paxton, S. Bertlein, R. Levato, V. Schill, W. Smolan, J. Malda, J. Teßmar, T. Blunk, J. Groll, Double Printing of Hyaluronic Acid/Poly(Glycidol) Hybrid Hydrogels with Poly(ε-Caprolactone) for MSC Chondrogenesis, Biofabrication, 9 (2017) 044108.

[142] X. Z. Shu, Y. Liu, Y. Luo, M. C. Roberts, G. D. Prestwich, Disulfide Cross-Linked Hyaluronan Hydrogels, Biomacromolecules, 3 (2002) 1304-1311.

[143] X. Z. Shu, Y. Liu, F. Palumbo, G. D. Prestwich, Disulfide-Crosslinked Hyaluronan-Gelatin Hydrogel Films: a Covalent Mimic of the Extracellular Matrix for In Vitro Cell Growth, Biomaterials, 24 (2003) 3825-3834.

[144] P. A. Levett, F. P. W. Melchels, K. Schrobback, D. W. Hutmacher, J. Malda, T. J. Klein, A Biomimetic Extracellular Matrix for Cartilage Tissue Engineering Centered on Photocurable Gelatin, Hyaluronic Acid and Chondroitin Sulfate, Acta Biomaterialia, 10 (2014) 214-223.

[145] H. Wang, L. Zhou, J. Liao, Y. Tan, K. Ouyang, C. Ning, G. Ni, G. Tan, Cell-Laden Photocrosslinked GelMA–DexMA Copolymer Hydrogels with Tunable Mechanical Properties for Tissue Engineering, Journal of Materials Science: Materials in Medicine, 25 (2014) 2173-2183.

[146] G. Camci-Unal, D. Cuttica, N. Annabi, D. Demarchi, A. Khademhosseini, Synthesis and Characterization of Hybrid Hyaluronic Acid-Gelatin Hydrogels, Biomacromolecules, 14 (2013) 1085-1092.

[147] X. Z. Shu, S. Ahmad, Y. Liu, G. D. Prestwich, Synthesis and Evaluation of Injectable, In Situ Crosslinkable Synthetic Extracellular Matrices for Tissue Engineering, Journal of Biomedical Materials Research Part A, 79A (2006) 902-912.

[148] G. Hochleitner, A. Youssef, A. Hrynevich, N. Haigh Jodie, T. Jungst, J. Groll, P. D. Dalton, Fibre Pulsing During Melt Electrospinning Writing, BioNanoMaterials, 17 (2016) 159-171.

[149] P. D. Dalton, C. Hostert, K. Albrecht, M. Moeller, J. Groll, Structure and Properties of Urea-Crosslinked Star Poly[(Ethylene Oxide)-ran-(Propylene Oxide)] Hydrogels, Macromolecular Bioscience, 10 (2008) 923-931.

[150] F. R. Tay, D. H. Pashley, M. C. Williams, R. Raina, R. J. Loushine, R. N. Weller, W. F. Kimbrough, N. M. King, Susceptibility of a Polycaprolactone-Based Root Canal Filling Material to Degradation. I. Alkaline Hydrolysis, Journal of Endodontics, 31 (2005) 593-598.

[151] C. X. F. Lam, S. H. Teoh, D. W. Hutmacher, Comparison of the Degradation of Polycaprolactone and Polycaprolactone–(β-Tricalcium Phosphate) Scaffolds in Alkaline Medium, Polymer International, 56 (2007) 718-728.

[152] M. Hesse, H. Meier, B. Zeeh, Spektroskopische Methoden in der organischen Chemie, Georg Thieme Verlag, 2005.

[153] V. A. Schulte, M. Diez, Y. Hu, M. Möller, M. C. Lensen, Combined Influence of Substrate Stiffness and Surface Topography on the Antiadhesive Properties of Acr-sP(EO-stat-PO) Hydrogels, Biomacromolecules, 11 (2010) 3375-3383.

[154] E. V. Amirgoulova, J. Groll, C. D. Heyes, T. Ameringer, C. Röcker, M. Möller, G. U. Nienhaus, Biofunctionalized Polymer Surfaces Exhibiting Minimal Interaction Towards Immobilized Proteins, ChemPhysChem, 5 (2004) 552-555.

[155] F. Eggert, Standardfreie Elektronenstrahl-Mikroanalyse: mit dem EDX im Rasterelektronenmikroskop; ein Handbuch für die Praxis, BoD–Books on Demand, 2005.

[156] J. Rudloff-Grund, F. E. Brenker, K. Marquardt, F. V. Kaminsky, A. Schreiber, STEM EDX Nitrogen Mapping of Nanoinclusions in Milky Diamonds from Juina, Brazil, Using a Windowless Silicon Drift Detector System, Analytical Chemistry, 88 (2016) 5804-5808.

[157] B. Skoog, Determination of Polyethylene Glycols 4000 and 6000 in Plasma Protein Preparations, Vox Sanguinis, 37 (1979) 345-349.

[158] R. Monacelli, M. Doretti, Separation of Polyoxyethylene Glycol in Ice Creams, Boll. Lab. Chim. Prov.(Bologna), 15 (1964) 235-238.

[159] M. M. Kurfürst, Detection and Molecular Weight Determination of Polyethylene Glycol-Modified Hirudin by Staining after Sodium Dodecyl Sulfate-Polyacrylamide Gel Electrophoresis, Analytical Biochemistry, 200 (1992) 244-248.

[160] C. E. Childs, The Determination of Polyethylene Glycol in γ Globulin Solutions, Microchemical Journal, 20 (1975) 190-192.

[161] J. Groll, Z. Ademovic, T. Ameringer, D. Klee, M. Moeller, Comparison of Coatings from Reactive Star Shaped PEG-stat-PPG Prepolymers and Grafted Linear PEG for Biological and Medical Applications, Biomacromolecules, 6 (2005) 956-962.

[162] J. Hoffmann, J. Groll, J. Heuts, H. Rong, D. Klee, G. Ziemer, M. Moeller, H. P. Wendel, Blood Cell and Plasma Protein Repellent Properties of Star-PEG-Modified Surfaces, Journal of Biomaterials Science. Polymer Edition, 17 (2006) 985-996.

[163] N. M. Green, Avidin, Advances in Protein Chemistry, 29 (1975) 85-133.

[164] J. Wong, A. Chilkoti, V. T. Moy, Direct Force Measurements of the Streptavidin–Biotin Interaction, Biomolecular Engineering, 16 (1999) 45-55.

[165] P. C. Weber, D. H. Ohlendorf, J. J. Wendoloski, F. R. Salemme, Structural Origins of High-Affinity Biotin Binding to Streptavidin, Science, 243 (1989) 85-88.

[166] Y. L. Jeyachandran, J. A. Mielczarski, E. Mielczarski, B. Rai, Efficiency of Blocking of Non-Specific Interaction of Different Proteins by BSA Adsorbed on Hydrophobic and Hydrophilic Surfaces, Journal of Colloid and Interface Science, 341 (2010) 136-142.

[167] Z. Péterfi, B. Kocsis, Comparison of Blocking Agents for an ELISA for LPS, Journal of Immunoassay, 21 (2000) 341-354.

[168] L. Dubinsky, B. P. Krom, M. M. Meijler, Diazirine Based Photoaffinity Labeling, Bioorganic & Medicinal Chemistry, 20 (2012) 554-570.

[169] V. Mogal, V. Papper, A. Chaurasia, G. Feng, R. Marks, T. Steele, Novel On-Demand Bioadhesion to Soft Tissue in Wet Environments, Macromolecular Bioscience, 14 (2014) 478-484.

[170] A. Blencowe, W. Hayes, Development and Application of Diazirines in Biological and Synthetic Macromolecular Systems, Soft Matter, 1 (2005) 178-205.

[171] J. Brunner, H. Senn, F. M. Richards, 3-Trifluoromethyl-3-Phenyldiazirine. A New Carbene Generating Group for Photolabeling Reagents, Journal of Biological Chemistry, 255 (1980) 3313-3318.

[172] Y. Chevolot, J. Martins, N. Milosevic, D. Léonard, S. Zeng, M. Malissard, E. G. Berger, P. Maier, H. J. Mathieu, D. H. G. Crout, H. Sigrist, Immobilisation on Polystyrene of Diazirine Derivatives of Mono- and Disaccharides: Biological Activities of Modified Surfaces, Bioorganic & Medicinal Chemistry, 9 (2001) 2943-2953.

[173] A. F. Gomes, F. C. Gozzo, Chemical Cross-Linking with a Diazirine Photoactivatable Cross-Linker Investigated by MALDI- and ESI-MS/MS, Journal of Mass Spectrometry, 45 (2010) 892-899.

[174] Alexa Fluor 647® FLUORONANOGOLD™-Streptavidin Conjugates from Nanoprobes, Product Information, 95 Horseblock Road, Unit 1, Yaphank NY 11980-9710, Revision: 1.0 (08/16).

[175] M. D. Pierschbacher, E. Ruoslahti, Cell Attachment Activity of Fibronectin Can be Duplicated by Small Synthetic Fragments of the Molecule, Nature, 309 (1984) 30-33.

[176] W. F. Vogel, R. Abdulhussein, C. E. Ford, Sensing Extracellular Matrix: An Update on Discoidin Domain Receptor Function, Cell Signalling, 18 (2006) 1108-1116.

[177] S. Ricard-Blum, The Collagen Family, Cold Spring Harbor Perspectives in Biology, 3 (2011) a004978.

[178] K. Johnson, S. Zhu, M. S. Tremblay, J. N. Payette, J. Wang, L. C. Bouchez, S. Meeusen, A. Althage, C. Y. Cho, X. Wu, A Stem Cell–Based Approach to Cartilage Repair, Science, 336 (2012) 717-721.

[179] Y. Zhang, J. Su, J. Yu, X. Bu, T. Ren, X. Liu, L. Yao, An Essential Role of Discoidin Domain Receptor 2 (DDR2) in Osteoblast Differentiation and Chondrocyte Maturation via Modulation of Runx2 Activation, Journal of Bone and Mineral Research, 26 (2011) 604-617.

[180] J. Dejmek, K. Leandersson, J. Manjer, A. Bjartell, S. O. Emdin, W. F. Vogel, G. Landberg, T. Andersson, Expression and Signaling Activity of Wnt-5a/Discoidin Domain Receptor-1 and Syk Plays Distinct but Decisive Roles in Breast Cancer Patient Survival, Clinical Cancer Research, 11 (2005) 520-528.

[181] W. F. Vogel, A. Aszódi, F. Alves, T. Pawson, Discoidin Domain Receptor 1 Tyrosine Kinase Has an Essential Role in Mammary Gland Development, Molecular and Cellular Biology, 21 (2001) 2906-2917.

[182] W. Vogel, G. D. Gish, F. Alves, T. Pawson, The Discoidin Domain Receptor Tyrosine Kinases are Activated by Collagen, Molecular Cell, 1 (1997) 13-23.

[183] A. Shrivastava, C. Radziejewski, E. Campbell, L. Kovac, M. McGlynn, T. E. Ryan, S. Davis, M. P. Goldfarb, D. J. Glass, G. Lemke, G. D. Yancopoulos, An Orphan Receptor Tyrosine Kinase Family Whose Members Serve as Nonintegrin Collagen Receptors, Molecular Cell, 1 (1997) 25-34.

[184] H. Boedtker, P. Doty, The Native and Denatured States of Soluble Collagen, Journal of the American Chemical Society, 78 (1956) 4267-4280.

[185] K. A. Piez, E. A. Eigner, M. S. Lewis, The Chromatographic Separation and Amino Acid Composition of the Subunits of Several Collagens, Biochemistry, 2 (1963) 58-66.

[186] L. Chaiet, T. Miller, F. Tausig, F. Wolf, Antibiotic MSD-235. II. Separation and Purification of Synergistic Components, Antimicrobial Agents and Chemotherapy, 161 (1963) 28-32.

[187] D. Jackson, J. Fessler, Isolation and Properties of a Collagen Soluble in Salt Solution at Neutral pH, Nature, 176 (1955) 69-70.

[188] J. Gross, J. Highberger, F. Schmitt, Collagen Structures Considered a State of Aggregation of a Kinetic Unit. The Tropocollagen Molecule, Proceeding of the Society for Experimental Biology and Medicine, 80 (1952) 462.

[189] K. E. Kadler, D. F. Holmes, J. A. Trotter, J. A. Chapman, Collagen Fibril Formation, Biochemical Journal, 316 (1996) 1-11.

[190] B. R. Williams, R. A. Gelman, D. C. Poppke, K. A. Piez, Collagen Fibril Formation. Optimal In Vitro Conditions and Preliminary Kinetic Results, Journal of Biological Chemistry, 253 (1978) 6578-6585.

[191] U. Hansen, P. Bruckner, Macromolecular Specificity of Collagen Fibrillogenesis: Fibrils of Collagens I and XI Contain A Heterotypic Alloyed Core and a Collagen I Sheath, Journal of Biological Chemistry, 278 (2003) 37352-37359.

[192] R. E. Neuman, M. A. Logan, The Determination of Collagen and Elastin in Tissues, Journal of Biological Chemistry, 186 (1950) 549-556.

[193] J. F. Woessner, The Determination of Hydroxyproline in Tissue and Protein Samples Containing Small Proportions of this Imino Acid, Archives of Biochemistry and Biophysics, 93 (1961) 440-447.

[194] J. A. Chapman, M. Tzaphlidou, K. M. Meek, K. E. Kadler, The Collagen Fibril—A Model System for Studying the Staining and Fixation of a Protein, Electron Microscopy Reviews, 3 (1990) 143-182.

[195] J. Duanmu, E. K. Gamstedt, A. Rosling, Synthesis and Preparation of Crosslinked Allylglycidyl Ether-Modified Starch-Wood Fibre Composites, Starch – Stärke, 59 (2007) 523-532.

[196] N. Flores-Ramírez, E. A. Elizalde-Peña, S. R. Vásquez-García, J. González-Hernández, A. Martinez-Ruvalcaba, I. C. Sanchez, G. Luna-Bárcenas, R. B. Gupta, Characterization and Degradation of Functionalized Chitosan with Glycidyl Methacrylate, Journal of Biomaterials Science. Polymer Edition, 16 (2005) 473-488.

[197] S.-P. Zhao, F. Zhou, L.-Y. Li, PH- and Temperature-Responsive Behaviors of Hydrogels Resulting from the Photopolymerization of Allylated Chitosan and N-Isopropylacrylamide, and their Drug Release Profiles, Journal of Polymer Research, 19 (2012) 9944.

[198] T. D. Li, X. L. Tang, X. D. Yang, H. Guo, Y. Z. Cui, J. Xu, Studies on the Reaction of Allyl Glycidyl Ether with Gelatin by Van Slyke Method, Asian Journal of Chemistry, 25 (2013) 858-860.

[199] R. J. Croome, Acid and Alkaline Hydrolysis of Gelatin, Journal of Applied Chemistry, 3 (1953) 280-286.

[200] I. Davidson, Hydrolysis of Samples for Amino Acid Analysis Protein Sequencing Protocols, (Ed: B. J. Smith), Humana Press, Totowa, NJ 1997, 119.

[201] R. J. Simpson, M. R. Neuberger, T. Y. Liu, Complete Amino Acid Analysis of Proteins from a Single Hydrolysate, Journal of Biological Chemistry, 251 (1976) 1936-1940.

[202] J. E. Eastoe, The Amino Acid Composition of Mammalian Collagen and Gelatin, Biochemical Journal, 61 (1955) 589-600.

[203] G. N. A. Atlantic Gelatin/Kraft Foods Global Inc., Nitta Gelatin Canada Inc., PB Leiner, Rousselot Inc., Weishardt International, 2012, 25.

[204] S. Liu, X. Yang, S. Wang, X. Dai, T. Li, Y. Wang, Interaction Between EPTAC-Modified Gelatin and Surfactants: Surface Tension and Conductivity Methods, Journal of Dispersion Science and Technology, 36 (2015) 731-739.

[205] L. Yue, J. Li, Y. Ding, J. Xu, T. Li, Heterogeneous Reaction Kinetics Between Mono Epoxy–Terminated Polydimethylsiloxane and Gelatin: Effect of Material Ratio and Temperature, International Journal of Polymer Analysis and Characterization, 21 (2016) 198-206.

[206] R. W. Congdon, G. W. Muth, A. G. Splittgerber, The Binding Interaction of Coomassie Blue with Proteins, Analytical Biochemistry, 213 (1993) 407-413.

[207] J. A. Benton, C. A. DeForest, V. Vivekanandan, K. S. Anseth, Photocrosslinking of Gelatin Macromers to Synthesize Porous Hydrogels That Promote Valvular Interstitial Cell Function, Tissue Engineering. Part A, 15 (2009) 3221-3230.

[208] K. W. M. Boere, J. Visser, H. Seyednejad, S. Rahimian, D. Gawlitta, M. J. van Steenbergen, W. J. A. Dhert, W. E. Hennink, T. Vermonden, J. Malda, Covalent Attachment of a Three-Dimensionally Printed Thermoplast to a Gelatin Hydrogel for Mechanically Enhanced Cartilage Constructs, Acta Biomaterialia, 10 (2014) 2602-2611.

[209] X. Li, S. Chen, J. Li, X. Wang, J. Zhang, N. Kawazoe, G. Chen, 3D Culture of Chondrocytes in Gelatin Hydrogels with Different Stiffness, Polymers, 8 (2016)

269.

[210] D. Chimene, K. K. Lennox, R. R. Kaunas, A. K. Gaharwar, Advanced Bioinks for 3D Printing: A Materials Science Perspective, Annals of Biomedical Engineering, 44 (2016) 2090-2102.

[211] K. Hölzl, S. Lin, L. Tytgat, S. V. Vlierberghe, L. Gu, A. Ovsianikov, Bioink Properties Before, During and After 3D Bioprinting, Biofabrication, 8 (2016) 032002.

[212] F. P. W. Melchels, J. Feijen, D. W. Grijpma, A Poly(D,L-Lactide) Resin for the Preparation of Tissue Engineering Scaffolds by Stereolithography, Biomaterials, 30 (2009) 23-24.

[213] K. W. M. Boere, M. M. Blokzijl, J. Visser, J. E. A. Linssen, J. Malda, W. E. Hennink, T. Vermonden, Biofabrication of Reinforced 3D-Scaffolds Using Two-Component Hydrogels, Journal of Materials Chemistry B, 3 (2015) 9067-9078.

[214] L. Klouda, A. G. Mikos, Thermoresponsive Hydrogels in Biomedical Applications, European Journal of Pharmaceutics and Biopharmaceutics, 68 (2008) 34-45.

[215] J. Necas, L. Bartosikova, P. Brauner, J. Kolar, Hyaluronic Acid (Hyaluronan): a Review, Veterinarni Medicina, 53 (2008) 397-411.

[216] J. Mergy, A. Fournier, E. Hachet, R. Auzély-Velty, Modification of Polysaccharides via Thiol-Ene Chemistry: A Versatile Route to Functional Biomaterials, Journal of Polymer Science Part A: Polymer Chemistry, 50 (2012) 4019-4028.

[217] Y. Tokita, A. Okamoto, Hydrolytic Degradation of Hyaluronic Acid, Polymer Degradation and Stability, 48 (1995) 269-273.

[218] K. Tømmeraas, C. Melander, Kinetics of Hyaluronan Hydrolysis in Acidic Solution at Various pH Values, Biomacromolecules, 9 (2008) 1535-1540.

[219] D. A. Gibbs, E. W. Merrill, K. A. Smith, E. A. Balazs, Rheology of Hyaluronic Acid, Biopolymers, 6 (1968) 777-791.

[220] S. E. Haynesworth, J. Goshima, V. M. Goldberg, A. I. Caplan, Characterization of Cells with Osteogenic Potential from Human Marrow, Bone, 13 (1992) 81-88.

[221] U. K. Laemmli, Cleavage of Structural Proteins During the Assembly of the Head of Bacteriophage T4, Nature, 227 (1970) 680-685.